UNIVERSITE DE GRENOBLE

Ecole doctorale de physique

Développement de techniques nano-sondes pour la mesure du travail de sortie et application aux matériaux en microélectronique

T H E S E

Preparée au CEA - LETI - MINATEC

Présentée à l'Université de Grenoble

pour obtenir le grade de

Docteur de l'Université de Grenoble

spécialité: nano-physique

par

Khaled KAJA

soutenue le 18 Juin 2010 devant le jury composé par :

Président :	**René-Louis Inglebert**	-	Polytech (Grenoble)
Rapporteurs :	**Thierry Melin**	-	CNRS - IEMN (Lille)
	Nick Barrett	-	CEA - IRAMIS (Saclay)
Directeur de thèse :	**Guy Feuillet**	-	CEA - LETI (Grenoble)
Examinateurs:	**Brice Gautier**	-	INL - INSA (Lyon)
	Benjamin Grevin	-	CNRS - SPrAM (Grenoble)

UNIVERSITY OF GRENOBLE

Doctoral School of Physics

Development of nano-probe techniques for work function assessment and application to materials for microelectronics

PhD T H E S I S

Prepared at CEA - LETI - MINATEC

Defended at the University of Grenoble

to obtain the grade of

Doctor of the University of Grenoble

speciality: nano-physique

by

Khaled KAJA

on 18 June 2010 in front of the jury:

President :	**René-Louis Inglebert**	-	Polytech (Grenoble)
Reviewers :	**Thierry Melin**	-	CNRS - IEMN (Lille)
	Nick Barrett	-	CEA - IRAMIS (Saclay)
Thesis adviser :	**Guy Feuillet**	-	CEA - LETI (Grenoble)
Examiners:	**Brice Gautier**	-	INL - INSA (Lyon)
	Benjamin Grevin	-	CNRS - SPrAM (Grenoble)

To my parents.
To my family.

The test of all knowledge is experiment.
Experiment is the sole judge of scientific "truth".

Richard Feynmann

Acknowledgments

First, I want to thank my thesis advisor, Guy Feuillet for the freedom he gave me to explore my ideas. I thank him for his interest in my work and his availability when I needed his help.

I am also very grateful to my two supervisors, Nicolas Chevalier and Olivier Renault, for the interest they had in my work and for their investment. I thank them especially for the time they spent with me in the last part of my doctoral writing. It was a pleasure working with them. I learned a lot thanks to our very interesting discussions. I sincerely hope that we could have the opportunity to work together in the future.

I also thank François Bertin and Amal Chabli for their sincere support and guidance during difficult times I had to go through. I owe them a lot.

I would also like to thank Denis Mariolle for teaching me how to use the KFM. Thanks for all the discussions we had together. I hope we could cooperate in the future.

Many thanks to Aude Bailly and Maylis Lavayssière who were very patient with me while teaching me how to use the NanoESCA. I am deeply grateful to Maylis for the time she had spent to help me getting my XPEEM results and processing all data.

I would also like to express my appreciation and thanks to Philippe Brincard and Frédéric Laugier for welcoming me aboard when I started my PhD. I also thank Frédéric and Jean-Claude Royer for their help and support during the last period of my work.

I want to thank all my laboratory colleagues for the pleasant atmosphere they provided each day, especially during coffee (and cake) breaks. Thanks for Clément Gaumer (PBSDM) with whom I shared the office during the entire PhD period. Thanks to Louis Gorintin and all my wishes for the best in his work. Thanks to Christophe Licitra for all the guitar tricks. Thanks to Névine Rochat for being there to give me good advice when I needed it. Thanks to all my friends in Grenoble for all restaurants, games and activities that we had together. I also thank all my friends AITAP for all the good times spent together.

I deeply thank Pauline for being by my side at the end of my thesis. Without her support and presence, things would have been very difficult.

I want to thank Wiss, Houss, Bach, Abboud and Ssamir just for being the best part of my life. And Taha and Nada, the brother and the sister with whom

I grew up and I found my self a part of their new small family (with Douano!).

Finally, I want to thank my family, my brother and my sister for their support and true love. And last but not least, I present my gratefulness and my admiration for my mother and my father who supported me throughout my life. The words could not express how much I owe them. I am what I am now because they believed in me and gave me all their love and care.

Abstract

The reliable and spatially resolved work function measurement of materials and nanostructures is one of the most important problems in surface characterization for advanced technological applications. Among different methods for work function measurement, AFM-based Kelvin Force Microscopy (KFM) and X-ray Photo-Emission Electron spectro-Microscopy (XPEEM) are two of the most promising techniques.

In this thesis, we were interested in the investigation of local work function measurements using KFM under ambient conditions, and in the study of complementarities between measurements obtained by KFM and XPEEM. We first present an analysis of KFM measurement variations with the tip-sample distance on various metal samples. These variations can be explained by a simple model based on surface charge transfers associated with the non-homogeneity in local work function. The influence of the tip, environmental and experimental parameters on KFM measurements was also investigated.

We then show an increase in spatial resolution of KFM imaging in air through the implementation on the commercial microscope of an AFM-KFM combined mode, based on the simultaneous acquisition of KFM measurement with that of the surface topography.

Finally, we focus on the characterization of epitaxial graphene layers on SiC(0001) substrate, using both KFM and XPEEM techniques. KFM work function images in air reveal, qualitatively, the heterogeneity of these layers on the sample surface with high spatial resolution. Complementary measurements by XPEEM at the photoemission threshold show that this heterogeneity is related to the increase in work function due to a local variation of graphene layer thickness between 1 and 4-5 monolayers, as reported in literature. This is qualitatively correlated with local intensities from the corresponding Si2p and C1s XPEEM core-level images. Ways for understanding this atypical variation in work function of graphene layers are outlined according to the literature and to micro-spectroscopy results, in terms of electronic coupling with the SiC substrate.

Keywords: Work function, KFM, XPEEM, graphene on SiC(0001)

Résumé

La mesure fiable et spatialement résolue du travail de sortie de matériaux et nanostructures est l'un des problèmes les plus importants en caractérisation de surface avancée pour les applications technologiques. Parmi les méthodes de mesure du travail de sortie disponibles, la microscopie à sonde de Kelvin (KFM), basé sur l'AFM, et la spectromicroscopie de photoémission d'électrons par rayons X (XPEEM) apparaissent comme les méthodes les plus prometteuses.

Nous nous sommes intéressés dans cette thèse à l'investigation de la mesure locale du travail de sortie par KFM sous air ainsi qu'à l'étude de la complémentarité entre les mesures obtenues par KFM et XPEEM. Nous présentons tout d'abord une analyse des variations des mesures KFM avec la distance pointe-échantillon sur différents échantillons métalliques. Ces variations peuvent être expliquées par un modèle simple basé sur des transferts de charges de surfaces associés à l'inhomogénéité locale du travail de sortie. L'influence de la pointe, de l'environnement et des paramètres expérimentaux a été aussi étudié.

Nous avons ensuite mis en évidence une augmentation de la résolution spatiale de l'imagerie KFM sous air grâce à la mise en oeuvre, sur le microscope commercial, d'un mode combiné AFM-KFM basé sur l'acquisition simultanée des mesures KFM et de la topographie de surface.

Enfin, nous nous sommes focalisés sur la caractérisation croisée par KFM et XPEEM de couches de graphène épitaxiées sur un substrat SiC(0001). Les images du travail de sortie obtenues par KFM sous air permettent de révéler qualitativement, avec une grande résolution spatiale, l'hétérogénéité de ces couches en surface. La mesure complémentaire par XPEEM spectroscopique au seuil de photoémission montre que cette hétérogénéité est liée à l'augmentation du travail de sortie local dû à une épaisseur de graphène variant entre 1 et 4-5 monocouches d'après la littérature. Ceci est corrélé qualitativement avec les intensités locales Si2p et C1s extraites des images XPEEM correspondantes. Des voies pour la compréhension de cette évolution atypique du travail de sortie d'un matériau, sont esquissées d'après la littérature disponible et les résultats micro-spectroscopiques, en terme de couplage électronique avec le substrat SiC.

mots clés: Travail de sortie, KFM, XPEEM, graphène sur SiC(0001)

Contents

Chapter 1
Introduction

The work function, which is the minimum energy required to extract an electron from a crystal, is one of the most fundamental properties of materials' surfaces. It is extremely sensitive to very subtle changes in structure, composition and contamination or any alteration of surface properties of a physical or chemical nature. Therefore, the work function is an important property in many scientific disciplines. It governs the band alignment in semiconductors and forms a fundamental property in the quality of metal-semiconductor contacts, in the determination of residual contamination and the development of new carbon-based devices such as carbon-nanotubes gas nano-sensors or graphene-based transistors.

Nowadays developments in nanoscience and nanotechnology create a growing demand for characterization tools to determine the work function on a nanometer scale. The complexity of the systems studied often requires the use of several spectroscopic or structural surface analysis methods. The extreme sensitivity of the work function to the surface quality imposes the need to control the environmental conditions in which measurements are performed. This also requires a good understanding of the environmental effects on the quality of work function measurements. Furthermore, the smaller size of modern technology devices requires measurements with a high spatial resolution to characterize complex heterogeneities in new materials used in micro- and nano- electronics.

Therefore two principal requirements challenge the quality of the intended work function measurements: **reliability** and **high spatial resolution**. These nano-characterization requirements call for **suitable tools** and **appropriate experimental protocols** whose study and development form the basic core of this thesis.

Among the numerous characterization methods and techniques for determining the materials work functions, Kelvin Force Microscopy (KFM) and X-ray Photo Electron Emission Microscopy (XPEEM) emerge as two of the most powerful and promising tools for reliable and highly resolved work function measurements.

The main goal of our study is to investigate the characterization of the local work function using these two techniques. The objective of this investigation is threefold:

- The evaluation of the work function measurement with both techniques in terms of understandings, limitations, differences and quality.
- The improvement of KFM measurement capabilities in air for better reliability and spatial resolution.
- The complementarity between both methods in terms of coupled measurements and experimental protocols.

Therefore, this manuscript will be organized as follows:

In chapter 2, we define the work function of metals and semiconductors. We emphasize the property of the local work function and work function anisotropy. Finally we briefly review the experimental methods employed for work function measurements with a particular focus on the spatially resolved techniques used in our study.

In chapter 3, we describe in details the physical and working principles of KFM and XPEEM techniques. We discuss the nature of related image contrasts. We also provide a complete description of each equipment employed as well as the practical aspects of related experiments. We finally draw a first comparative panel between both techniques and point out their complementarity.

In chapter 4, we address the subject of analysis and improvement of KFM measurements in air. We first present a thorough study of the effects of experimental conditions and parameters on conventional KFM measurements. We then present a development of a new operational mode for the improvement of the spatial resolution of measurements.

In chapter 5, we present a complete study coupling both KFM and XPEEM techniques for the investigation of epitaxial few layer graphene grown on SiC(0001) substrate. Our main goal of this study is to characterize the thickness of graphene layers using two-dimensional work function maps obtained with KFM and XPEEM experiments.

Finally, in chapter 6, we draw our conclusions and perspectives.

Le travail sortie, défini comme étant l'énergie minimale nécessaire pour extraire un electron du volume d'un matériau, est l'une des proprietés les plus fondamentales des surfaces de matériaux. Grace à son extreme sensibilité à toute modification subtile des propriétés physiques ou chimiques de la surface, le travail de sortie intervient d'une manière fondamentale dans de nombreuses applications physiques.

Dans le cas des transistors MOS par exemple, les travaux de sortie du métal de grille ainsi que celui du semiconducteur utilisé dans ces composnants controlent la tension seuil de déclenchement et affectent d'une façon directe le fonctionnement des transistors. Dans les cellules photovoltaiques, le travail de sortie de l'électrode de contacte supérieur est directement liée à l'optimisation de la tension du circuit ouvert qui détermine l'efficacité de conversion en énergie de ces cellules. Le travail de sortie intervient aussi dans l'alignement des bandes dans les semiconducteurs et les contactes métal-semiconducteur. Il constitue une propriété importante pour le développement des nouveaux composants microélectroniques à base de carbone comme les nano-détecteurs de gaz à base de nanotube de carbone ou les transistors à base de graphène.

Avec les développements actuelles des nanosciences et nanotechnologies, la mesure du travail de sortie à l'échelle nanométrique est devenue l'un des problèmes les plus importants en caractérisation de surface avancée pour les applications technologiques. La compléxité des systèmes étudiés nécessite assez souvent l'utilisation de différentes méthodes spectroscopiques ou structurales pour la caractérisation et l'analyse des surfaces.

En plus, la sensibilité du travail de sortie à l'extreme surface ainsi que la réduction des dimensions composants utilisés dans les technologies modernes exigent d'une part le controle des conditions environmentales de la mesure et d'une autre part une résolution spatiale élevée pour la caractérisation des héterogeneités complexes dans les nouveaux matériaux utilisés en micro- et nano-technologies.

Ceci définit les besoins fondamentaux de la nano-caractérisation du travail de sortie : la fiabilité de la mesure et la haute résolution spatiale. Ces besoins font appels à des techniques de caractérisations adaptées et des protocoles de mesures appropriés dont l'étude et le développement consistuent le coeur de cette thèse.

Parmi les différentes méthodes disponibles pour la détermination du travail de sortie, la microscopie à sonde de Kelvin (ou Kelvin Force Microscopy (KFM)) et la spectromicroscopie de photoémission d'électrons par rayons X (XPEEM) apparaissent comme les méthodes les plus prometteuses pour une mesure fiable et spatialement résolue. L'objectif de cette thèse concerne l'investigation de la caractérisation du travail de sortie local en utilisant ces deux méthodes. Trois aspects sont ainsi développés :

- L'évaluation des limites et des différences de la mesure du travail de sortie par la technique KFM et la technique XPEEM.
- L'amélioration de la mesure sous air du travail de sortie par KFM pour l'augmentation de la résolution spatiale.
- L'étude la complémentarité entre les deux méthodes de mesure KFM et XPEEM.

Chapter 2

Local work function: concepts and experimental methods

Dans ce chapitre, nous adressons le sujet de la mesure du travail de sortie local. Nous introduisons, dans un premier temps, le concept du travail de sortie. Nous considérons ensuite les définitions du travail de sortie local et de l'anisotropie du travail de sortie. Finalement, nous passons en revue les différentes méthodes disponibles pour la détermination du travail de sortie en introduisant particulièrement les deux techniques utilisées dans cette thèse : la microscopie à force de Kelvin (KFM) et la spectromicroscopie de photoémission d'électrons par rayons X (XPEEM).

IN this chapter[1] we shall address the leading theme of this thesis: the local work function measurements. We introduce the concept of the work function. We consider properties such as the local work function and the work function anisotropy. An overview of the commonly used methods to measure the work function is presented. In particular, we introduce two techniques used in our studies for the local work function measurements: Kelvin Force Microscopy (KFM) and X-ray Photo Electron Emission Microscopy (XPEEM).

2.1 What is the "work function"?

The work function corresponds to the minimum energy required to extract one electron from a metal. More precisely, the work function is the energy difference between two states of the whole crystal. In the initial state, the neutral crystal containing N electron is assumed to be in its ground state with energy E_N. In the final state, one electron is removed outside the crystal, where it is assumed to be at rest and without interaction with its image.

[1] Historical photos were taken from different web sources, most notably from the Nobel prize web site (www.nobel.se).

J. Bardeen
1908–1991

Accordingly, it has only electrostatic potential energy described by the vacuum level, E_V. The crystal with the remaining $N-1$ electrons is assumed to be in its ground state with energy E_{N-1}. This definition calls for zero temperature and a perfect vacuum since the crystal is in its ground state, both before and after electron removal. The work function was first defined in this way by Wigner and Bardeen in 1935 [1].

Therefore, for zero temperature, the work function is given by:

$$\phi = (E_{N-1} + E_V) - E_N \cdot \tag{2.1}$$

For temperatures greater than zero, the removal of an electron from the metal is to be considered as a thermodynamic change of state. The difference $E_N - E_{N-1}$ has to be replaced by the derivative of the Helmholtz free energy F with respect to the electron number N, whereby the temperature T and the volume V are kept constant. This derivative is the chemical potential, μ, of the electrons:

$$(E_N - E_{N-1}) \rightarrow (\partial F/\partial N)_{T,V} = \mu, \tag{2.2}$$

Then, the general expression of the work function[2] for non-zero temperature can be written as:

$$\phi = E_V - \mu \cdot \tag{2.3}$$

For metals, the chemical potential (μ) remains equal to the Fermi level (E_F) to a high degree of precision. In fact the deviation of μ from E_F is of the order of T^2, which is typically only about 0.01 percent even at room temperature [2]. Therefore, the work function for metals can be written as:

$$\phi = E_V - \mu = E_V - E_F \cdot \tag{2.4}$$

In the definition of the work function, E_V represents the electrostatic potential energy of the removed electron at rest, in a region outside the crystal where it is has no interaction with its image. For an infinitely-extended homogeneous crystal, E_V is considered at an infinite distance from the crystal surface.

However for a finite non-homogeneous crystal, E_V is not considered at infinity because, in general, the work function is different for different crystallographic faces of the crystal. In this case, the distance between the removed electron and a crystal face should be sufficiently large such that the image force can be neglected (typically 10^{-4} cm) [3]. But, at the same time, this distance should be small compared to that between the electron and any other crystal face with

[2]The work function ϕ is expressed in eV.

a different work function. Otherwise it is not possible to discriminate between work functions of different crystal faces [4].

2.1.1 Energetic contributions to the work function

In the expression of the work function (equation 2.3) the absolute values of E_V and μ depend on the reference energy. If we consider the total average of the bulk electrostatic potential, E_{in}, as a reference energy level (E_{in} =0), the work function can be subdivided into two parts (see figure 2.1) [4]:

- a surface-dependent part: $W_s = E_V$ - E_{in}
- the chemical potential referred to E_{in}: $\bar{\mu} = \mu$ - E_{in}, which depends on bulk properties only.

The work function[3] is therefore given by:

$$\phi = W_s - \bar{\mu}. \tag{2.5}$$

Equation 2.5 shows the energetic contributions to the work function for a clean surface. However in the presence of surface adsorbate (adatoms or molecules that could be induced by physisorption or chemisorption), another surface contribution, $\pm|\psi|$, is added in equation 2.5 which induces changes in the work function (see section 2.1.1.2). Therefore we can generalize the expression of the work function by showing all energetic contributions:

$$\phi = W_s - \bar{\mu} \pm |\psi| \cdot \tag{2.6}$$

Figure 2.1 (b) shows an energy diagram explaining the different contributions to the work function of metals. It also shows the electrostatic potential energy V near the metal surface. Note that the in presence of adsorbates, their contribution (here considered as $+|\psi|$ in figure 2.1) displaces the position of the vacuum level (see section 2.1.1.2) and changes the electrostatic potential, V, near the surface (dashed line in figure 2.1 (b)).

In the following text we will make use of the terms: ***ideal surfaces*** and ***real surfaces***. We consider an ***ideal surface*** as infinitely-extended, homogeneous (single crystal) and rigorously flat. A ***real surface*** is considered as of finite-size, non-homogeneous (polycrystal) and mostly containing structural or chemical defects.

[3]It is important to note that the expression in eq.2.5 properly includes all many-body effects, in particular, the work done against the image force while removing electron from metal [5].

2.1.1.1 The surface dipole layer

For an clean ideal surface, the surface-dependent contribution W_s (equation 2.5) arises from the presence of a surface dipole layer. This dipole layer is due to the fact that a surface does not present an infinite potential barrier to the electrons within a solid. Although the electrons are bound in the solid, the electronic wave-functions themselves may have a non-zero amplitude 'just outside' (for practical purposes within 10 Å) of the surface [6], which gives rise to 'electron overspill'.

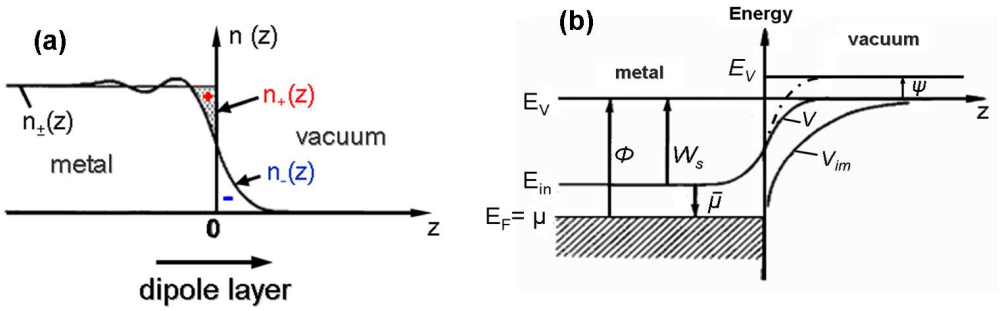

Figure 2.1: (a) the charge density $n_{\pm}(z)$ distribution perpendicular to a 'Jellium' surface and creation of the surface double layer. (b) the potential energy diagram explaining the components of the work function ϕ of metals. W_s is the surface dipole barrier. $\bar{\mu}$ the chemical potential referred to E_{in}, the total average of the bulk electrostatic potential. $|\psi|$ the barrier induced by surface adsorbates. V the electrostatic potential near the metal surface ad V_{im} the potential of the image interaction [7].

As shown in figure 2.1 (a) for the Jellium-model[4], the distribution of positive charges $n_+(z)$ (z, normal to the surface) abruptly falls to zero at the surface. However, the negative charge distribution $n_-(z)$ leaks beyond the geometrical surface plane ($z = 0$) thereby creating an excess of negative charge in front of the surface [7] [1].

To preserve overall electrical neutrality, the excess negative charge in front of the surface is balanced by a corresponding excess positive charge at the solid surface. Hence the surface dipole layer is formed.

Therefore this dipole layer induces an energy step W_s that the electron must overcome to leave the metal [7]. The moment of dipoles in this layer tends to confine electrons in the conduction band of the crystal and therefore increases the work function. A higher density of surface dipoles leads thus to a higher work function [8]. The value of W_s is determined by the manner

[4]In the Jellium model, the positive ions in the metal are replaced by a uniform positive background which exert an attractive electrostatic interaction on all the electrons of the system. The mathematical analysis of this model allows for the determination of the electronic density inside the metal and at the surface as well [5].

in which the charge distribution in the surface cells differs from that of the bulk [2].

The effect of W_s on the work function value has been pointed out by Smoluchowski in 1941 [8]. Smoluchowski determined the electron density for different crystallographic planes of the same crystal. He showed that the work function of a loosely packed crystal face is smaller than that of a closely packed face for face-centered cubic structure (fcc) metals. The density of surface dipoles is related to the atomic packing in the surface plane. Therefore, W_s increases with the packing density of a crystal plane, which explains the variation of the work function. This has been experimentally observed by XPEEM and KFM experiments for the different faces of Cu [9] [10].

This phenomenon introduces the concept of work function anisotropy for real surfaces, which will be discussed in section 2.2.4.

2.1.1.2 Work function changes induced by adsorbates

In ambient environment, samples are exposed to gaseous atoms and molecules which may adsorb on the surface. Adsorbates can either be induced by chemisorption or physisorption (see figure 2.2).

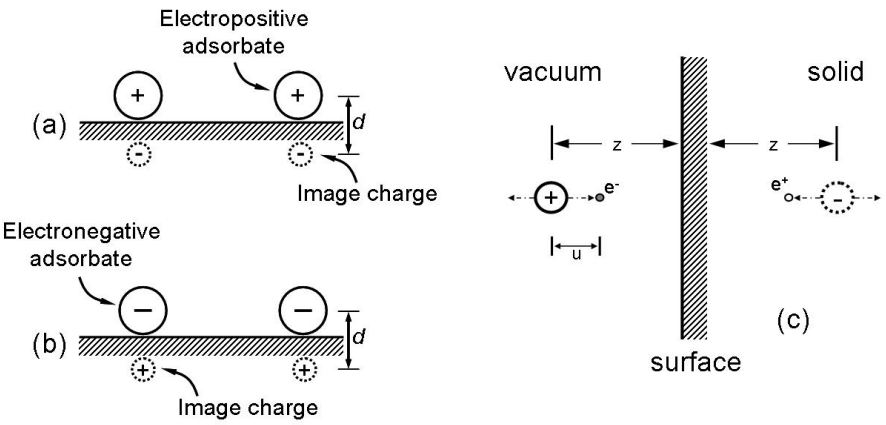

Figure 2.2: Surface dipole induced by the chemisorption of (a) electropositive adsorbates and (b) electronegative adsorbate on the metal surface. The transfer of charge between the adsorbate and the substrate, or vice versa, results in the formation of surface dipoles. (c) simple model of physisorbed atom consisting of a positive ion and a valence electron. The attractive interaction with the solid is due to screening (image charges) [3] [6].

In the case of chemisorption, a charge transfer occurs between the adsorbate and surface. Electropositive adsorbates (figure 2.2 (a)) tend to transfer electron charge from their outer valence shell to the substrate. As a result of this transfer, a net positive charge now resides on the adsorbate inducing an equal but opposite

image charge at an equivalent distance below the surface plane [6]. This results in the formation of a dipole moment, where the distance between the positive and negative charges is d, as illustrated on figure 2.2 (a). Electronegative adsorbates usually possess an unfilled affinity level and the charge transfer occurs in the opposite sense, i.e. from substrate to adsorbate (figure 2.2 (b)).

In physisorption of an atom for example, the valence electron and the nucleus of the adsorbed atom interact with their images below the surface plane (see figure 2.2 (c)). A resulting dipole moment is formed which depends on the distance z between atom and surface. For more details see [3].

The dipole moment induced by adsorbates gives rise to an additional electric field that acts on the electron leaving the surface. The direction of this field depends on the nature of the adsorbate as described above. This creates an energy barrier, $\pm|\psi|$, that is added to the one resulting from the surface dipole layer. The position of the vacuum level is therefore shifted (see figure 2.1(b)).

The presence of adsorbates on the surface induces changes in the work function as described in equation 2.5. The sign of this change depends on the nature of adsorbates ($-|\psi|$ for electropositive adsorbates and $+|\psi|$ for electronegative ones). Work function changes by adsorbates are used in monitoring the atomic coverage of species on metal surfaces (for example, alkali atoms on the surface of a single crystal Ni) [11].

2.2 The local work function

The local work function is an important property of real surfaces. It depends on the local quality of the surface which may vary due to the presence of local defects (structural or chemical), atomic steps or edges [7]. It may also vary with the local properties of the surface such as the presence of different crystallographic orientations [9] [10], locally embedded charges [12] or local changes in the doping level [13] in case of a semi-conducting surface (see section 2.3).

Here we discuss the local work function and we identify effects resulting from its variation over the surface, i.e. the work function anisotropy (see below).

2.2.1 Variations of the surface dipole layer

As previously discussed in section 2.1.1 the work function has two basic components: the electrochemical potential ($\bar{\mu}$) and the barrier from the surface dipole layer (W_s) (see equation 2.5). While $\bar{\mu}$ depends on bulk properties only [4], W_s is sensitively dependent on the surface conditions.

The value of W_s depends on the density of surface dipoles resulting from the electron "overspill" outside the surface. The density of dipoles itself is dependent on the atomistic structure at the surface. For a real (non-homogeneous) surface, lateral changes in the atomistic structure (caused by one of the reasons mentioned above) are therefore equivalent to a lateral modulation of the surface dipole density. Accordingly, W_s will vary parallel to the surface and its value will depend on its specific location ,i.e. $W_s^{(i)}(x_i, y_i)$.

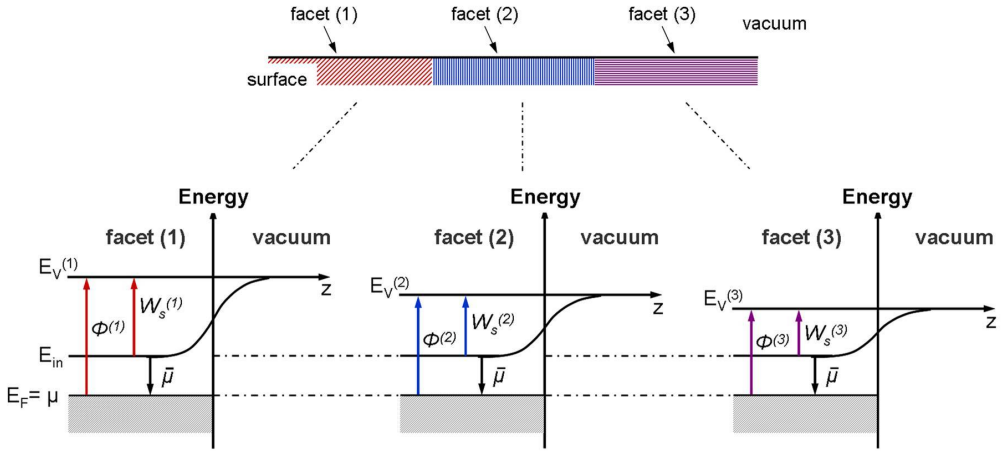

Figure 2.3: An example of a real surface of metal showing three facets with different crystallographic orientations (represented as hatched zones for illustration). The energy diagrams showing the components $\bar{\mu}$ and W_s for each facet.

Perhaps the case of a clean polycrystalline surface is the best example to illustrate this fact. We consider in figure 2.3 a clean (with no adsorbates) metal surface with three facets of different crystallographic orientations. We represent energy diagrams showing the energetic components of the work function for each facet.

At thermodynamic equilibrium the chemical potential, $\bar{\mu}$, and the total average electrostatic potential, E_{in}, inside the bulk are constant. Then, the change of the atomic structure (here related to the crystallographic orientation) is reflected in the variation of $W_s^{(i)}$ for each facet. Therefore the local work function of a specific facet (located at (x_i, y_i) on the surface) is given by:

$$\phi^{local} = \phi^{(i)}(x_i, y_i) = W_s^{(i)}(x_i, y_i) - \bar{\mu}\cdot \tag{2.7}$$

For a clean polycrystalline surface of Cu, KFM and XPEEM experiments have determined the local work function of grains with different orientations [9] [10]. Results showed that $\phi_{111} > \phi_{100} > \phi_{110}$, in agreement with theoretical predictions by Smoluchowski [8] for fcc metals.

Note that the example used for illustration can be generalized, i.e. a real metal surface could present inequivalent facets due to any of the reasons mentioned in the introduction of this section (structural defects, chemical defects or changes in the local geometry of the surface for example).

2.2.2 The local vacuum level

Local variations of $W_s^{(i)}$ at the surface of the same metal are equivalent to local variations of the vacuum energy level, $E_V^{(i)}$ (see figure 2.3). Hence $E_V^{(i)}$ acquires the character of local vacuum level [14].

Therefore, the variation in the local work function at different locations (x_i, y_i) and (x_j, y_j) on the surface with different local properties corresponds to:

$$\phi^{(i)} - \phi^{(j)} = E_V^{(i)} - E_V^{(j)}. \tag{2.8}$$

The local vacuum level, $E_V^{(i)}$, describes the energy in the final state of the electron removed from a specific location on the metal surface. Therefore, $E_V^{(i)}$ is defined in a region "just outside" the surface, i.e. a region where the electron in the final state is no longer in interaction with its image charge.

Accordingly, the local work function (ϕ^{local}) corresponds to the minimum energy required to extract an electron from the highest occupied state in the metal ($E_F = \mu$) to the local vacuum level ($E_V^{(i)}$) outside the surface.

2.2.3 Changes of local work function induced by adsorbates

The effect induced by adsorbates on an ideal surface's work function has been detailed in section 2.1.1.2. Here, for the case of a real (non-homogeneous) surface, the effect is the same. Therefore, if we consider adsorbates homogeneously distributed on the surface of the metal, the local work function could be written as:

$$\phi^{(i)} = W_s^{(i)} - \bar{\mu} \pm |\psi| \tag{2.9}$$

where the $\pm$ depends on the nature of the adsorbate (see section 2.1.1.2) .

2.2.4 Work function anisotropy

The work function anisotropy is the variation of the local work function at different regions on the surface of a crystal. Inequivalent regions on the surface with different work functions are called "patches" [15] [16]. "Patches" may be due to surface preparation, to the uneven distribution of adsorbates, to crystallographic orientations or to variations in surface local geometry [16]. Surfaces used in all technological applications may present

many of these aspects. Therefore it is interesting to address the work function anisotropy and show its effect on the measurement of the local work function.

In presence of inequivalent patches on the surface, macroscopic surface charges may develop on patches (in addition to the surface dipole layer), provided that the total charge of the whole crystal surface remains zero [2] [16] [17]. These macroscopic charges are called "patch charges".

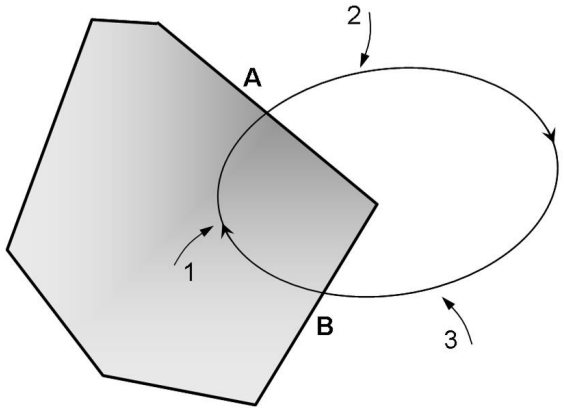

Figure 2.4: Zero total work is done in taking an electron from an interior level at the Fermi energy over the path shown, returning it at the end to an interior level at the Fermi energy. That work, however, is the sum of three contributions: ϕ_A/e (in going from 1 to 2), $1/e(\phi_A - \phi_B)$ (in going from 2 to 3, where ϕ_A/e and ϕ_B/e are the electrostatic potentials just outside faces A and B), and $-\phi_B/e$ (in going from 3 back to 1) [2].

Consider a crystal with two inequivalent faces (patches) A and B, as illustrated in figure 2.4. The work function of the two faces are different, i.e. $\phi_A \neq \phi_B$.

If one takes an electron (initially at E_F) out of the crystal through face A, the energy spent to do so is the work function $\phi_A = W_s^A - \bar{\mu}$. Now bringing it back in again to E_F through face B, the energy spent is: $-\phi_B = \bar{\mu} - W_s^B$.

The total work done in such a cycle mush vanish, if energy is to be conserved. However, this is not actually the case here. The total energy spent in extracting the electron from A and reintroducing it back through B is:

$$E_{total} = W_s^A - W_s^B = \phi_A - \phi_B, \tag{2.10}$$

which is not conserved since $\phi_A \neq \phi_B$.

There must therefore be an electric field outside the metal against which a compensating amount of work is done as the electron is carried from face A to face B. In other words, the two faces must be at two different electrostatic potentials V_A and V_B such that:

$$-e\,(V_A - V_B) = \phi_A - \phi_B\cdot \tag{2.11}$$

Since the surface dipole layer cannot yield macroscopic fields outside of the metal, the electric field outside the metal must arise from net macroscopic distributions of electric charges[5] on the surface (known as "patch charges") [2] [16]. Therefore the surface charge density must change from region to region. Note that the condition for the whole crystal to be neutral requires that the sum of the macroscopic surface charges over all regions (entire surface) must vanish [2].

This phenomenon is known as the "patch charge" effect [17]. It has long been known that patch charges affect electron trajectories in field emission microscopy [17] [18]. Electric fields induced by patch charges outside polycrystalline surfaces have been detected experimentally close to the surface by force microscopy techniques [17]. As we shall see later (see chapter 4), patch charge effect can explain variations observed in Kelvin force microscopy measurements [19].

2.3 Work function of semiconductors

Semiconductors are characterized by a band gap, E_g, between the valence band and the conduction band. In a non-degenerated semiconductor, the position of the Fermi level, E_F, is in the band gap. For an intrinsic semiconductor (no doping), E_F is close to the middle of the band gap at T = 0 K. For a doped semiconductor, the position of E_F within the band gap depends on the nature of doping.

For an N-type silicon semiconductor (for example, using phosphor atoms for doping), the position of E_F is closer to the minimum of the conduction band, E_{CB} (see figure 2.5). For a P-type silicon semiconductor (for example, using bore atoms for doping), E_F is closer to the maximum of the valence band, E_{VB}. For the definition of the work function of a semiconductor we first introduce two properties: the electron affinity, χ, and the ionization energy, IE.

χ at a semiconductor surface is defined as the energy required to excite an electron from the bottom of the conduction band (E_{CB}) at the surface to the local vacuum level (figure 2.5). Similarly, the ionization energy IE is defined as the energy needed to excite an electron from the top of the valence band (E_{VB}) at the surface to the local vacuum level [14].

Figure 2.5 shows an energy band diagram of a N-type semiconductor near its surface. eV_{BB} results from the band bending at the surface of the semiconductor. Regarding all these energies, the work function can therefore be defined by one

[5] Patch charge densities, compared to charge densities in the surface dipole layer, are very small. Patch charge densities are in the range of 10^{-9} electrons/Å^2, while the estimated order of magnitude for the surface dipole layer charge density is about 0.04 electrons/Å^2 [17].

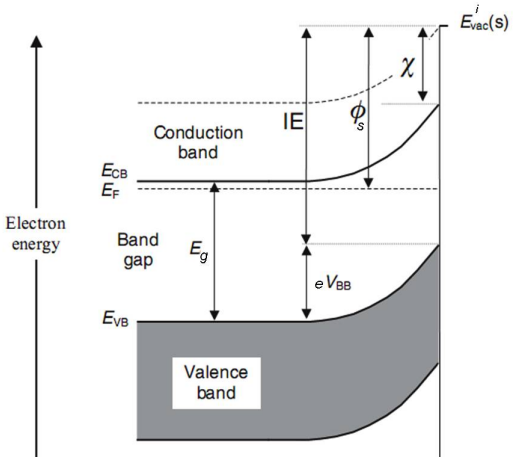

Figure 2.5: Energy band of a semiconductor near its surface showing the band bending eV_{BB}, the electron affinity χ, the ionization energy IE, the band gap E_g and the edges of the conduction and valence band, E_{CB} and E_{VB} respectively [14].

of the following expressions:

$$\begin{aligned} \phi_s &= \chi + eV_{BB} + (E_{CB} - E_F)_{bulk} \\ \phi_s &= IE + eV_{BB} + (E_F - E_{VB})_{bulk} \end{aligned} \tag{2.12}$$

Semiconductor's work function is relevant in all contact applications and Schottky barrier measurements which are widely employed for the characterization of the materials' resistivity and dopant profiling. Interested readers can find details about these subjects elsewhere [13] [3] [20] [21] [22].

2.4 Work function measurement: principles and experimental techniques

As discussed in section 2.2.4, real surfaces present a work function anisotropy resulting from the presence of surface patches. Experimental techniques should therefore measure the local work function of each patch on the surface, otherwise the work function anisotropy is lost. To do so, the final state in which the electron emitted from the surface is detected should correspond to the local vacuum level (see section 2.2.2).

In fact, this would not be possible if the detector was simply placed very far from the surface. Because in that case, the final state of the detected electron would be described by the vacuum level at infinity. It follows that for an anisotropic surface, a single work function will be measured as only an average. Its value is intermediate between the maximum and minimum work functions of the different patches on the surface.

Experimentally, detectors used to measure the work function are usually far from the sample surface. However to measure the local work function and characterize the surface anisotropy, external electric fields are applied in order to collect the electrons emitted from the surface.

If each electron reaching the detector can be associated with a particular emitting patch by observing its trajectory, then the work function of each patch can be inferred from its associated electron current. The electron current emitted from each patch is determined by the potential shape, and particularly by the maximum potential that the electrons must overcome. Even for small electric fields, this maximum is located close to the crystal surface and thus depends on the local work function of the patch [23].

In this way, the lateral work function anisotropy can be observed and the local work function is measured. The spatial resolution of measurements is determined by technical limitations of the experimental tool used to measure the work function.

2.4.1 Experimental techniques

The techniques for determining the work functions can be broadly classified into two groups. The first class of experiments aims at measuring the work function on an absolute scale and is based on electron emission processes. By stimulating a metallic surface in various ways, a current of electrons is produced, from which the work function is determined. The stimulus can consist of photons (photoelectric effect and UPS), be of a thermal nature (thermionic emission), consist of an applied electric field field emission or be a combination of these methods.

The second class of techniques concentrates on obtaining work function differences, either between various metals (Kelvin probe) or during surface modifications, such as adsorption processes. Work function measurements with these methods are relative and usually require a determination of a standard reference work function. Experimental protocols, combining techniques from both classes are often elaborated for reliable work function measurements.

In the following paragraphs, we shall briefly describe the common techniques available for work function determination. Technical details can be found in standard textbooks, to which interested readers are referred [15] [24] [3].

2.4.1.1 Electron emission-based techniques

Photoelectric measurements

When radiation, of frequency ν, is incident on a metal surface, photoelectrons are produced, provided that $h\nu \geq \phi$ (ϕ is the metal work function). The threshold

frequency, ν_0, at which electrons start leaving the metal is defined by $h\nu_0 = \phi$. Theoretical analysis, originally conducted by Fowler in 1931, shows that the quantum yield I (photoelectrons per light quantum absorbed) is related to ν - in the region which is not too close to the threshold frequency - by the equation:

$$I = bh^2(\nu - \nu_0)^2/2k^2, \tag{2.13}$$

where b is a material-dependent value related to the probability of absorbing a photon. k is the Boltzman constant and h the Planck constant. If $I^{1/2}$ is plotted against ν, then the extrapolation to zero would determine ν_0 and hence the work function ϕ. This zero-temperature approximation is the procedure commonly used to interpret experimental results. Corrections may be included to account for the collecting electric field, which lowers the surface barrier slightly [15].

The Ultraviolet Photoelectron Spectroscopy (UPS)

In UPS, a monochromatic ultraviolet light source of known frequency ν (Hg, D_2 or He discharging lamps) is used to illuminate the surface of a sample. Electrons in the valence band (of energy E_i with respect to the vacuum) are then excited into states above the vacuum level and may be emitted from the crystal if the $h\nu \geq \phi$ condition is satisfied. Emitted electrons are detected and counted by sweeping their kinetic energies.

The recorded spectrum consists of primary electrons as well as secondary electrons of lower kinetic energy. The secondary electrons result from inelastic scattering of the primary electrons during the emission process, and have kinetic energies down to zero. The total width of the spectrum of the emitted electrons is equal to $h\nu - \phi$, thus providing a measure of the work function ϕ.

The thermionic emission

When heating a metallic surface to high temperature T, in the range of 1000-1500 K, a fraction of the electrons acquire sufficient energy to leave the metal. Using thermodynamic theory, one can show that the saturation electron current density J can be approximated by the Richardson-Dushman formula [25]:

$$J(T) = A(1 - r)T^2 \exp(-\phi/k_B T) \tag{2.14}$$

where $A = emk_B^2/2\pi^2\hbar^3$ is a universal constant and r is the mean reflection probability for electrons incident on the metal surface in the equilibrium state. The determination of ϕ from measurements of the current J, as a function of the temperature T, is complicated by various factors. A collecting field E is applied to measure J, which lowers the work function slightly and induces a supplementary parameter which needs to be extrapolated to zero. The temperature dependence of work functions is usually around $\pm 10^{-3}$ - 10^{-4} eV/K [23].

2.4.1.2 Work function differences-based techniques

Contact potential difference: the Kelvin probe

The Contact Potential Difference (CPD) method provides a measure of a sample's work function relative to that of a reference metal [26]. It was first proposed by William Thomson (Lord Kelvin) in 1898, hence known as the Kelvin Probe (KP) technique. The KP technique relies on the existence of a potential difference outside the surface of two different metals electrically connected.

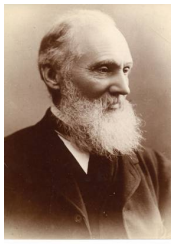

Lord Kelvin
1824- 1907

When metals are connected, the electrons start flowing from the metal with lower work function to the one with higher work function, until the electrochemical potential in both connected metals is the same, hence Fermi levels aligning (criterion of thermodynamic equilibrium). This movement of charges induces the appearance of a potential difference between the two metals, called the contact potential difference, V_{cpd}, which is equal to the initial work function difference existing before contact between the probe (ϕ_1) and the sample (ϕ_2) (see figure 2.6).

The establishment of the V_{cpd} can be easily observed by measuring the electric field $\vec{E}$ induced between the two metallic electrodes. In order to measure contact potential difference, this electric field can be then canceled out by the application of an external bias voltage V_{DC} between electrodes. Once $\vec{E}$ is null, then $V_{DC} = V_{cpd}$. Consequently, the work function of the sample electrode can be obtained by:

$$\phi_2 = \phi_1 - |e|\, V_{DC} \tag{2.15}$$

provided that the work function of the probe (ϕ_1), also known as the reference electrode, is identified[6].

The vibrating capacitor: Zissman method

In 1932, W.A. Zissman proposed an improved version of the Kelvin probe technique, in which the reference electrode (the probe), of several mm^2, was set to vibrate above a fixed sample electrode. Hence, a vibrating capacitor is formed when both electrodes are connected, where the distance between them varies as $d_0 + A\cos(\omega t)$. d_0 is the initial mean distance between electrodes before vibration, and A and ω are respectively the amplitude and the frequency of the reference electrode vibration.

The physical principle is the same as in the Kelvin probe method (see figure 2.6). However, the vibration of the present capacitor will induce an alternative

[6] e = -1.60219 $\times$ 10^{-19} C.

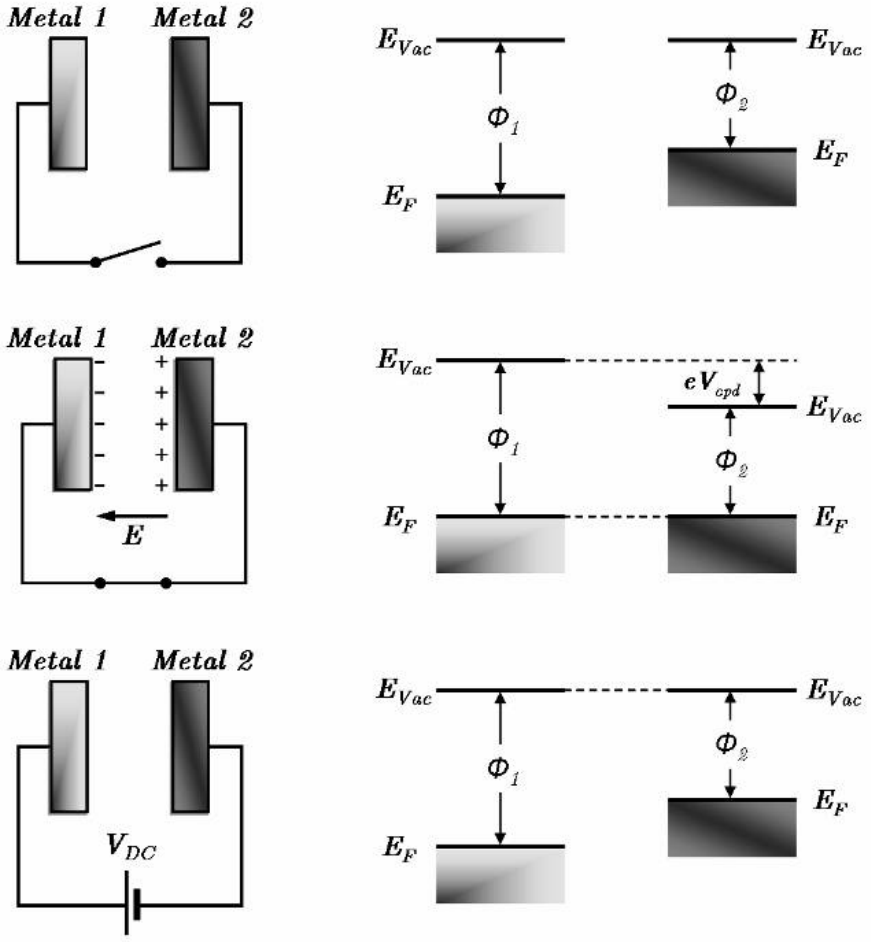

Figure 2.6: Principle of Kelvin Probe method and contact potential difference establishment.

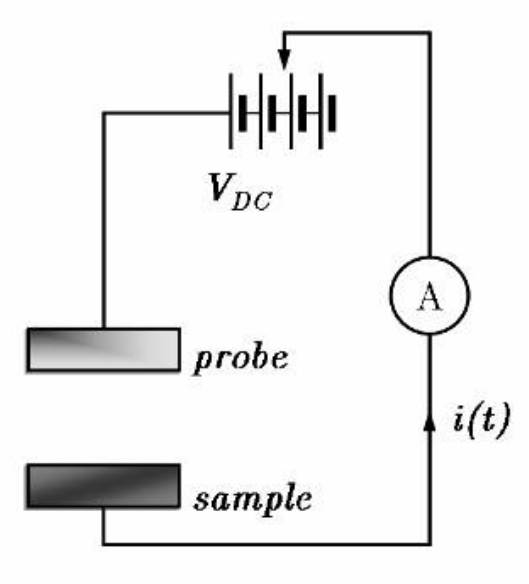

Figure 2.7: A simplified scheme of the Zissman method of the vibrating capacitor. The current $i(t)$ flowing between the probe and sample electrodes is nullified by adjusting V_{DC} which is therefore equal to V_{cpd}.

current $i(t)$ to flow between electrodes due to the movement of the capacitive charges on the capacitor plates (see figure 2.7):

$$i(t) = \frac{dC}{dt}V \approx C_0 \frac{A}{d_0}\omega \sin(\omega t)\,(V_{DC} - V_{cpd})\,\cdot \tag{2.16}$$

Hence, in Zissman's method, the V_{cpd} value is obtained by nullifying the current $i(t)$ which provides $V_{DC} = V_{cpd}$. The work function of the sample is then determined according to the expression 2.15. The accuracy of this method can reach $\sim$1 meV; however, the spatial resolution is limited by the size of the probe electrode (i.e. $\sim \mu$m). The obtained work function consists of an averaged value where the local information about its variation is lost.

The diode methods

An alternative method for measuring work function differences and variations was suggested by Anderson in 1935 [27]. Here, a slow beam of electrons is thermally emitted from a cathode source and is accelerated by an electric field onto the sample of interest that constitutes the anode. The beam size is large on the atomic scale but small compared with the crystal surface.

The resulting current I is measured as a function of the potential difference V applied between the electrodes. If the work function of the sample changes, the $I - V$ characteristic of the diode shifts horizontally. Usually a feedback mechanism fixes the current, which allows the work function change to be directly revealed from the difference in the applied potential. If the beam is produced by

an electron gun and slowed down near the sample, it can be scanned across the substrate, allowing work function maps to be produced [28]. This technique has been widely applied for *in situ* studies of gas adsorption on metallic surfaces [23].

2.4.1.3 Experimental data

Work function compilations for a large number of metals with various crystallographic orientations have been published in [29] [30] [31] [32] [33]. Some selected values are shown in table 2.1. Values were obtained using different techniques discussed in the previous paragraphs.

2.5 Fundamental characterization requirements

There are three major implications concerning measurement's quality and characterization tools for work function determination in view of modern technology.

High spatial resolution forms a major necessity for the characterization of work function changes at the deca-nanometer scale, imposed by the drastic scaling of devices in new-technology applications.

Reliable and absolute measurements are of crucial importance in most applications. Because the work function is extremely sensitive to the surface quality, contamination and environmental effects can lead to significant alterations. The need for appropriate characterization tools and experimental protocols is therefore of great importance.

In-line characterization The ability to characterize the work function at different stages during device fabrication is also a fundamental necessity in the field of micro- and nano- electronic applications. This point is not discussed in this work.

In this thesis, we used two complementary characterization techniques for work function measurements: Kelvin Force Microscopy (KFM) and X-ray Photo Electron Emission Microscopy (XPEEM).

2.5.1 KFM and XPEEM techniques for ultimate work function characterization

Kelvin Force Microscopy (KFM)

Also known as Kelvin Probe Force Microscopy (KPFM). This is an ultimate extension of the Kelvin probe method.

Element	W.F.(eV)	Technique	Reference
Au	4.25	Th.	[34]
	5.1	P.E.	[30]
	5.4	P.E.	[35]
	5.45	C.P.D.	[36]
	5.22	C.P.D.	[37]
	5.4	C.P.D.	[35]
Al	4.36	P.E.	[38]
	4.08	P.E.	[39]
	4.2	P.E.	[40]
	4.24	C.P.D.	[41]
	4.19	C.P.D.	[42]
	4.18	C.P.D.	[37]
Cu	4.5	Th. (1160 - 1280 K)	[34]
	4.6	Th. (∼1350 K)	[43]
	4.4	Th. (1100 - 1300 K)	[44]
	4.6	C.P.D.	[41]
	4.51	C.P.D.	[42]
	4.8 (111)	P.E.	[9]
	4.5 (100)	P.E.	[9]
	4.4 (110)	P.E.	[9]
	4.55 (poly)	P.E.	[9]
Pt	5.3 - 5.5	Th. (1600 - 1900 K)	[45]
	5.08	Th.	[31]
	5.65	P.E.	[29]
	5.2	P.E.	[46]
	4.52	C.P.D.	[31]
	5.36	C.P.D.	[31]
	4.82	C.P.D.	[47]
Ru	4.71	P.E.	[30]
	4.52	C.P.D.	[48]
W	4.52	Th. (1350 - 2200 K)	[49]
	4.5	Th. (1820 - 2940 K)	[50]
	4.6	P.E.	[51]
	4.49	P.E.	[52]
	4.55	C.P.D.	[42]
	4.38	C.P.D.	[43]

Table 2.1: Experimental work function values, in eV, of selected metals (acquired from [33]). Values were obtained using different techniques, Th.: Thermoionic emission, P.E.: Photo Electric threshold, C.P.D.: Contact Potential Difference.

G. Binning
1947

After the invention of the Atomic Force Microscopy (AFM) in 1986 by Binning *et al.*, the idea of adapting the Zissman's method to AFM was proposed in 1991 by Nonnenmacher *et al.* [53]. A conducting AFM tip and surface form a vibrating capacitor in which the very small dimension of the AFM tip plays a crucial role in improving the spatial resolution of the contact potential difference measurements. Differing from Zissman's method, the measurement of V_{cpd} with KFM is based on the detection and nullification of an electrical force arising between the two electrodes of the tip/sample capacitor instead of measuring a current[7].

Almost similar to Zissman's method, the feedback principle of KFM is based on adjusting an external bias voltage V_{DC} until the electrical force vanishes and hence $V_{DC} = V_{cpd}$, where:

$$V_{cpd} = \frac{\phi_{tip} - \phi_{sample}}{|e|} \tag{2.17}$$

allows to determine the value of ϕ_{sample} provided that ϕ_{tip} is identified[8]. In KFM measurements, the tip scans the sample surface and thus allows one to obtain two-dimensional maps of the V_{cpd} lateral variations. Moreover, it offers the interesting possibility of simultaneously measuring the variation of topography which provides important complementary information for most applications.

KFM provides high spatial resolution measurements due to the dimensions of the AFM tips (tip apex $\sim$ 10 nm). KFM can operate in ambient conditions and UHV environments. Its accuracy can reach 10 mV in air and is ten times higher under UHV thanks to the improved quality factor of the tip's oscillations (see chapter 3). Its working principle and installation make it a powerful candidate as an in-line characterization tool to monitor device fabrication process.

Figure 2.8 shows an example of typical KFM images (topography (a) and contact potential difference (b)) obtained under ambient conditions for a clean polycrystalline copper surface. The work function map of copper with the crystallographic grain orientations was recorded with a spatial resolution $\sim$ 50 nm.

However, the KFM technique suffers from the relative character of its contact potential difference measurements. Calibration protocols are therefore needed to allow quantitative or semi-quantitative results.

X-ray Photo Electron Emission Microscopy (XPEEM)

[7] Indeed, due to the small value of the capacitance, the current is too small to be measured
[8] e = -1.60219 $\times$ 10^{-19} C.

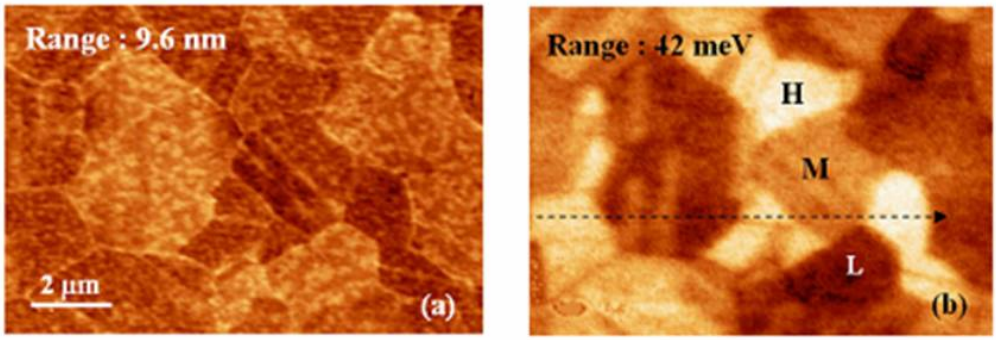

Figure 2.8: (a) Topography of a clean copper surface showing the boundaries of grains, (b) the work function map extracted from the V_{cpd} image obtained simultaneously in KFM experiments. The variation of the work function of copper with the grain orientations is emphasized and work function maps are recorded with a spatial resolution of $\sim$ 50 nm [10].

The photoelectron emission microscopy (PEEM) was invented by Brüche in the early 1930s [54]. Since then the improvement of PEEM benefited from several breakthroughs in related fields, such as the improvement in the quality of ultra-high vacuum (UHV), the invention and development of a variety of surface sensitive methods for structural and chemical analysis (in particular photoemission spectroscopy).

PEEM principle is based on the collection of the electrons emitted from a sample surface after irradiation with photons [55]. It uses electron lenses to directly image the distribution of the photoelectrons onto a screen. It is known as XPEEM when X-ray photons are used as an excitation source. XPEEM provides access to the electronic and chemical structure of surfaces with high spatial resolution that can reach several tens of nanometers. It forms a complete surface technique suitable for the study of materials and devices on the mesoscopic scale and beyond.

In our work we have employed a state of the art XPEEM spectromicroscope, the *NanoESCA* (from Omicron Nanotechnology), equipped with an aberration-corrected (double analysers) energy filtering system and multiple available laboratory photon sources: a monochromatic focused X-ray source (FXS) and three available UV and VUV photon sources (Hg, D_2 and He discharging lamps). A preparation chamber connected to the microscope is also available for surface treatments under UHV conditions (Ar^+ ion sputtering, resistive heating at high temperature)

NanoESCA allows different imaging modes providing microscopic, spectroscopic and spectromicroscopic measurements. Using XPEEM spectromicroscopy in the range of secondary electrons, the work function can be determined by measuring the emission threshold. Two dimensional maps of the work function

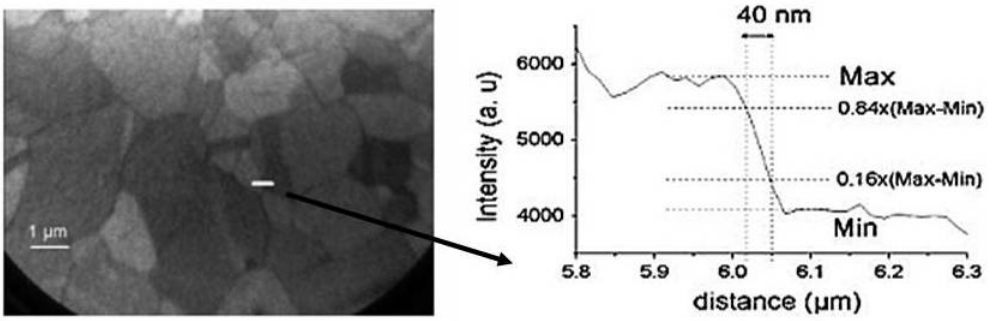

Figure 2.9: A PEEM image acquired using the *NanoESCA* spectromicroscope with an Hg (UV) photon source over a clean copper surface. The image of secondary electrons was taken at the energy of 4.4 eV, with a field of view of 15 μm. The spatial resolution of the secondary electron imaging was determined from the profile plot and evaluated at around 40 nm [9].

variations can be also obtained over the field of view (FoV) used in experiments (FoV between 20 to 600 μm are available with the *NanoESCA*). The study of the chemical and elemental composition of the surface is also possible with spectroscopic and spectromicrosopic measurements at core-level energies.

Figure 2.9 shows an example image acquired in XPEEM at the energy of secondary electrons of the same copper sample studied in KFM (see figure 2.8). The variation of the work function with the grains orientations is identified. The work function variations are measured with a 40 nm spatial resolution using an UV photon source.

complementarity of KFM and XPEEM...

It is our goal in this work to demonstrate the possibility of improving KFM measurements in air and to exploit the complementarity of KFM and XPEEM techniques as a way to attain high spatially resolved, reliable and reproducible measurements of the work function for newly developed technologies and materials.

In the next chapter, we will develop the working principles and used equipment of both KFM and XPEEM. In the last chapter, we will demonstrate an application of a coupled characterization protocol for the study of epitaxial graphene layers on SiC substrate.

Chapter 3

Spatially resolved work function mapping: principles and methods

Dans ce chapitre nous discutons en détail les principes physiques de la mesure du travail de sortie par les techniques de microscopie de force de Kelvin (KFM) et de spectromicroscopie de photoémission d'électrons par rayons X (XPEEM). Les propriétés, avantages et limitations des microscopes utilisés dans chaque technique seront aussi présentées. Finalement, une comparaison sera établie entre KFM et XPEEM en termes de fiabilité, résolution spatiale et complémentarité de la mesure du travail de sortie local.

In this chapter we shall provide a detailed overview of the two principal techniques of this thesis for the measurements of the local work function: the Kelvin Force Microscopy (KFM) and the X-ray Photo Electron Emission Microscopy (XPEEM). Key features addressed will include the principles of each technique as well as the properties, advantages and limitations of the equipment used in each measurement method. The KFM and XPEEM techniques will be compared in terms of reliability, spatial resolution, complementarity and direct measurement of the local work function.

3.1 Kelvin Force Microscopy (KFM)

From a technical point view, KFM is an adaptation of an Atomic Force Microscopy (AFM) method to produce electrical measurements of the Contact Potential Difference (CPD) as measured by a classical Kelvin Probe (KP) instrument. Therefore, the description of the KFM technique requires a certain level of understanding of the working principle of AFM technique. We shall thus provide a description of some basic concepts of the AFM followed by a detailed description of the KFM principle and the equipment used in our experiments.

3.1.1 Atomic Force Microscopy: a brief introduction

The invention of the Atomic Force Microscopy in 1986 by Binning and Quate [56] was intimately linked to the invention of the Scanning Tunneling Microscopy (STM) in 1982 by Binning and Rohrer for which they received the Nobel Prize in 1986. The core of Atomic Force Microscopy (AFM) is formed by a sharp tip mounted on a flexible cantilever. While scanning the sample, the tip 'sees' the surface as a field of interacting forces that disturb its equilibrium position. The detection of this disturbance and the regulation of the tip's position actually form the basic signal of the AFM.

3.1.1.1 General principle

Unlike the STM, the conducting nature of the sample is not important in AFM. AFM can thus be used to study insulator, molecular as well as conducting surfaces. The AFM explores the interacting forces between the tip and the sample. Its basic application is to measure the topography of a given surface. However, depending on the nature of the interaction between the tip and the sample, the AFM is also capable of mapping various properties of the sample surface (i.e. viscoelastic, ferroelectric, electrostatic, magnetic and chemical properties), which opens the doors to a wide range of applications in the field of material science and characterization.

The operating principle and experimental setup Figure 3.1 represents of the experimental setup of an AFM microscope. The AFM probe is formed by a micro-sharp tip mounted on the end of a cantilever. While the tip interacts with the surface, the cantilever moves depending on the nature of the interaction force (i.e. repulsive or attractive). These movements are transfered to a four segment photodiode by means of a reflected laser beam at the end of the cantilever. An electrical current proportional to the laser beam movement is therefore created in the photodiode. This current is then converted into a voltage signal which is compared to a setpoint value dictating the desired position of the cantilever.

The error signal resulting from this comparison is then used to move the tip vertically in order to maintain the cantilever position at the setpoint value. The vertical movement of the tip is provided by a piezo-electric ceramic tube moving in the Z direction. The feedback procedure is ensured by an automatic regulation of the proportional and integral gains of a PID controller. The lateral scan of the tip in the (X, Y) direction over the surface is provided by two additional piezo-electric ceramics. The height variations ΔZ, of the vertical piezo, forms the topography signal over the scanned surface $Z(X, Y)$.

The interacting forces between the tip and the sample Different types of interacting forces can be probed in AFM depending on the distance between

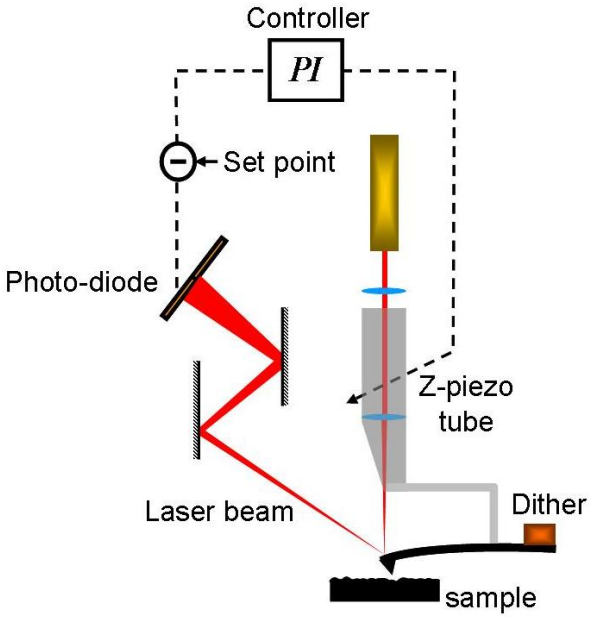

Figure 3.1: The general setup of a conventional AFM microscope.

the tip and the sample and their nature and composition. Forces have different intensities and ranges and can be classified into two main categories: attractive and repulsive forces.

Attractive forces Among the main attractive forces there are the van der Waals and Casimir forces resulting from the interaction of instantaneous dipoles. Capillarity forces caused by the formation of a water meniscus between the tip and sample in air resulting from a thin water layer on both surfaces (tip and sample). Electrostatic forces induced by the work function between a conducting tip and sample or from the presence of charges. For particular samples, magnetic or chemical forces can also be considered.

Repulsive forces Repulsive forces include the theories of elastic contact between solid bodies such as the Hertz theory and the Derjaguin-Muller-Toporov (DMT) theory. For interested readers, details can be found in [57].

The modes of operation In AFM techniques, two major modes can be distinguished: the contact mode and the oscillating or dynamic mode.

The contact mode The contact mode is the most intuitive mode which was demonstrated by Binning and Quate in 1986 [58]. The tip is brought into contact with the surface and changes of its deflection directly reflects the changes

of the surface topography. During an imaging procedure, the feedback loop maintains the deflection of the cantilever equal to a setpoint value by maintaining a *constant force* value along the scan.

The dynamic or oscillating mode In 1987, Martin, Williams and Wickramasinghe developed the use of the AFM with an oscillating tip at a very small distance above the surface [59]. They demonstrated a higher sensitivity when the cantilever oscillates at its resonance frequency. The amplitude, the resonance frequency and the phase shift of oscillations connect the dynamics of the vibrating tip to the tip-surface interactions. Any of them could be used as a feedback signal to track the surface's topography. Due to the absence of contact, this mode is rather damages-less for both the tip and the surface. In the case of KFM experiments, we are actually interested in one particular dynamic AFM mode known as the Tapping mode.

3.1.1.2 The Tapping mode

In this mode, the cantilever is mechanically driven by a piezo-electric actuator, very close to its resonance frequency with an oscillation amplitude of several nanometers. During an oscillation, the tip undergoes intermittent contacts with the surface of the sample, hence this mode is known as the intermittent contact mode or Tapping mode.

General principle Initially, the cantilever is driven to oscillate freely, at its resonance frequency, far from the surface of the sample in order to avoid any interaction with it. When the tip-sample distance decreases, the tip starts feeling the variation of the gradient of the interacting force with the surface. This induces variations of the oscillation resonance frequency depending on the nature of the interacting forces (i.e. attractive or repulsive).

This leads to the variation of the initial (free) amplitude of oscillation of the cantilever. It also induces the variation of the phase delay between the cantilever's stimulation signal and its actual oscillation. In Tapping mode, the amplitude of oscillations is often used as the feedback signal. The feedback loop keeps the amplitude constant (equal to a set point value) by maintaining constant the *gradient* of the interacting force.

An insight into the tip motion: amplitude and phase A thorough understanding of the Tapping mode operation requires solving the motion equation of the cantilever-tip ensemble under the influence of the tip-surface forces. A complete and rigorous approach involves the solution of the motion equation of a three dimensional vibrating cantilever. Although this approach is rather difficult, interested readers can find more details by following the works of Butt and Jaschke [60], Sader [61] and Stark and Heckl [62].

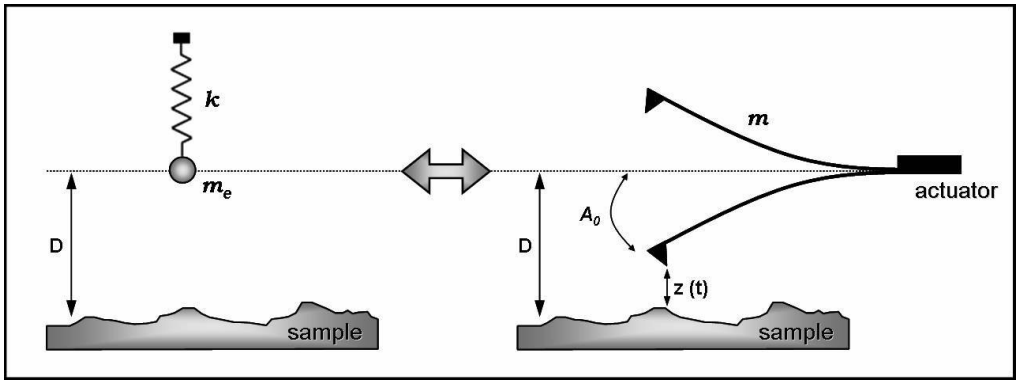

Figure 3.2: The probe formed by the cantilever with the tip mounted at its end is modeled by a point-mass spring system having the same cantilever stiffness k and an effective mass $m_e \approx 0.243{\cdot}m$ with m as the probe mass.

However, to gain some insight into the tip motion in Tapping mode, the cantilever-tip ensemble can be modeled as a point-mass spring system (see figure 3.2), acting as a simple harmonic oscillator. Here, we shall limit our study to the simplified linear (harmonic) case where the interacting forces between the tip and the sample are considered to be relatively weak during the tip oscillation. However, the non-linearity of these interactions has deep implications for the resulting tip motion which complicates finding analytical solutions. Details on non-linear treatments can be found in [63] [64].

The harmonic approximation

Far from the surface, no interacting forces act on the cantilever. Thus, according to the point-mass spring model, the motion equation of the mechanically-driven cantilever corresponds to that of a forced harmonic oscillator with damping caused by the viscous friction of the cantilever in the medium (generally air):

$$m_e\ddot{z} + c\dot{z} + kz = f_0\cos(\omega t), \tag{3.1}$$

where m_e is the effective mass of the point-mass [1], k is the stiffness of the spring (equal to that of the cantilever), c is the friction coefficient[2], z is the cantilever deflection, f_0 the amplitude of the driving sinusoidal force and ω its angular pulsation. Considering $\gamma = c/m_e$ and knowing the resonance angular pulsation $\omega_0 = \sqrt{k/m_e}$ implies:

$$\ddot{z} + \gamma\dot{z} + \omega_0^2 z = \frac{f_0}{m_e}\cos(\omega t)\cdot \tag{3.2}$$

[1] A rigorous estimation of the effective mass gives $m_e = 0.243\ m$, where m is the mass of the cantilever with the tip mounted at its extremity.

[2] In air c is about several nN.s.m^{-1}. It is a hundred times higher in a water environment.

In the harmonic interaction approximation where only the fundamental oscillation mode of the cantilever is considered, the solution of the above equation of motion (3.2) is given by:

$$z(t) = A(\omega)\cos(\omega t - \varphi(\omega)), \tag{3.3}$$

where A is the amplitude of the cantilever oscillation and φ is the phase delay of the oscillation with respect to the excitation signal. Thus using equations 3.2 and 3.3, the amplitude and the phase of the cantilever oscillation can be deduced:

$$A(\omega) = \frac{f_0}{m_e}\frac{1}{\sqrt{(\omega_0^2 - \omega^2)^2 + \gamma^2\omega^2}} \tag{3.4}$$

$$\varphi(\omega) = \arctan\left(\frac{\gamma\omega}{\omega_0^2 - \omega^2}\right) \tag{3.5}$$

The shapes of the oscillation amplitude $A(\omega)$ and phase $\varphi(\omega)$ are shown in figure 3.3. Note that the abscissa in the figure represents the frequency $f = 2\pi\omega$.

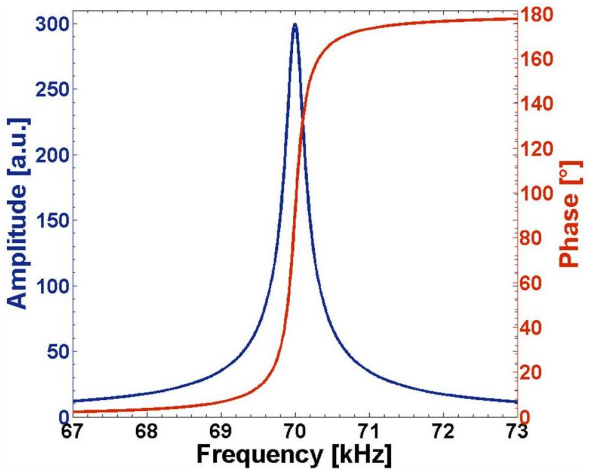

Figure 3.3: The amplitude $A(\omega)$ and the phase $\varphi(\omega)$ simulated for a oscillating cantilever with $Q = 300$ and a frequency of oscillations at ~ 70 kHz. The abscissa represents $f = 2\pi\omega$.

In the current linear treatment, the amplitude of the driving force, f_0, has no impact on the Lorentzian shape of the oscillation amplitude curve. However, this is not the case in the non-linear interaction considerations [63] [64] [65].

The quality factor The quality factor (or Q factor) is a dimensionless parameter that describes how damped the oscillator is. In other words, it characterizes the bandwidth of the resonance curve ($A(\omega)$) relative to its center frequency (the resonance frequency determined by ω_0). Higher Q indicates a lower rate of energy loss relative to the stored energy of the oscillator (the cantilever); the oscillations fade more slowly. In a harmonic potential, the Q factor is given, at the resonance frequency by:

$$Q = \frac{\omega_0}{\gamma}\cdot \tag{3.6}$$

The Q factors of the cantilevers oscillating in air can reach several hundreds. However their value can reach 10^4 in vacuum due to the decrease of viscous friction. The γ coefficient can be graphically estimated from the amplitude curve ($A(\omega)$) by measuring the width at the amplitude value $A_m/\sqrt{2}$, where A_m is the maximum amplitude of the curve. A_m can be rather determined from equation 3.4. For high Q factors $A_m \approx QA_0$, A_0 being the amplitude of oscillation at $\omega = 0$.

In the presence of linear interactions

However, when the cantilever-tip ensemble is brought closer to the surface, interacting forces ($F_{int}(z)$) with the sample arise. The cantilever motion equation cen be re-written as:

$$\ddot{z} + \gamma\dot{z} + \omega_0^2 z = \frac{f_0}{m_e}\cos(\omega t) + \frac{F_{int}(D+z)}{m_e}, \tag{3.7}$$

where D is the mean (equilibrium) position of the cantilever with respect to the sample (see figure 3.2). To solve this equation, one needs to know the expression of F_{int} as a function of z. However, in the linear approximation of small oscillations, it is rather possible to develop $F_{int}(z)$ into a Taylor expansion at the first order around the mean position D:

$$F_{int}(z) \approx F_{int}(D) + z\frac{\partial F_{int}}{\partial z}(D)\cdot \tag{3.8}$$

How does the interaction impacts the cantilever's movement? Thus by introducing the approximated expression of the interacting forces (3.8) in the cantilever motion equation:

$$\ddot{z} + \gamma\dot{z} + \left(\omega_0^2 - \frac{1}{m_e}\frac{\partial F_{int}}{\partial z}(D)\right) z = \frac{f_0}{m_e}\cos(\omega t) + \frac{F_{int}(D)}{m_e}\cdot \tag{3.9}$$

The term $F(D)$ at the mean position of the cantilever actually creates a simple static deflection of the cantilever, which does not actually affect the treatment. However, by comparing equation 3.9 with the initial form given by equation 3.2, one can see that the oscillating system (cantilever-tip) in interaction with the sample gets a new angular pulsation ω_1 instead of the initial ω_0:

$$\omega_1 = \sqrt{\omega_0^2 - \frac{1}{m_e}\frac{\partial F_{int}}{\partial z}(D)} \approx \omega_0\left(1 - \frac{1}{2k}\frac{\partial F_{int}}{\partial z}(D)\right)\cdot \tag{3.10}$$

So clearly, when the cantilever-tip ensemble interacts with the sample (i.e. when the distance tip-sample decreases), the initial resonance frequency (expressed in terms of ω_0) of the cantilever's free oscillations is actually shifted by the

gradient of the interacting forces. The new frequency (ω_1) could be lower or higher than the initial one (ω_0) depending on the sign of the gradient of the force: positive for attractive forces and negative for repulsive ones.

A softer or stiffer cantilever? Actually, one can express this fact with an interesting point of view according to the spring-mass model. Knowing that $\omega^2 = k/m_e$, the expression 3.10 can be written as:

$$k_1 = k - \frac{\partial F_{int}}{\partial z}(D)\cdot \tag{3.11}$$

Everything happens as if, in the presence of interacting forces with the sample, the stiffness of the cantilever decreases or increases depending on the nature of the forces. Attractive forces (positive gradient) soften the cantilever while repulsive forces (negative gradient) stiffen.

What happens to the amplitude? In fact, in Tapping mode the value of the amplitude of the cantilever oscillations is always measured at the frequency of the driving force (i.e. ω_{ext}). Let us first assume that the cantilever is driven with a signal having the frequency $\omega_{ext} = \omega_0$. Then, far from interacting forces, the resonance frequency of the cantilever's free oscillations will be equal to ω_0 and the amplitude of oscillations measured in Tapping mode will be equal to A_0 in this case.

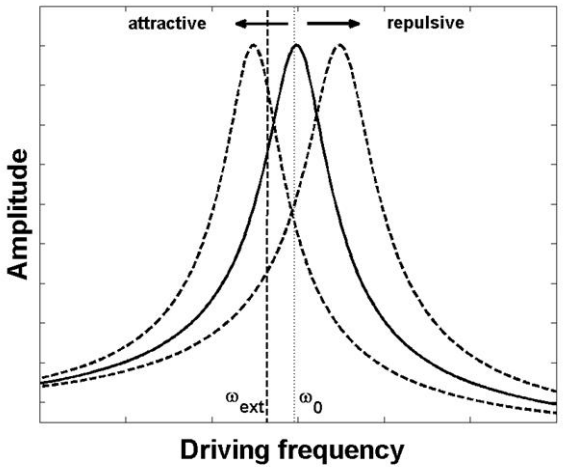

Figure 3.4: Resonance curve for a single harmonic oscillator (solid line) and under the influence of attractive and repulsive forces (dashed lines). The gradient of an external force produces a shift of the resonance curve without introducing any shape or size modifications (weakly disturbed harmonic oscillator model).

Now in the presence of interacting forces, the resonance frequency of oscillations shifts due to the gradient of forces (see equation 3.10) and consequently the resonance curve (i.e. amplitude curve $A(\omega)$) will also be displaced to the left or the right of the free resonance curve depending on the nature of the interacting force (left for attractive forces and right for repulsive ones). Therefore, the value

of the actual oscillation amplitude is obtained from the new resonance curve at the driving frequency ω_{ext}. As a consequence, the new oscillation amplitude (A_1) will be smaller than the free amplitude (i.e. A_0).

However, if the frequency of the driving signal was set slightly smaller than the value of the free resonance frequency ($\omega_{ext} < \omega_0$), then the actual oscillation amplitude, A_1 (in presence of interactions) could decrease or increase with respect to the initial A_0, depending on the position of the new resonance frequency ω_1 (i.e. depending on the nature of the interacting force). Figure 3.4 shows an example of this case.

What happens to the phase? The expression on the phase delay between the cantilever oscillations and the driving signal illustrated by the equation 3.4: $\varphi(\omega) = \arctan\left(\gamma\omega/(\omega_0^2 - \omega^2)\right)$. This equation establishes that the phase lag is exactly 90° at the resonance frequency.

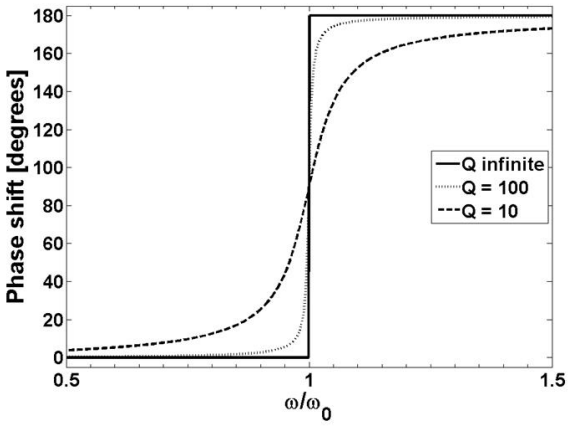

Figure 3.5: Phase shift behavior of a driven harmonic oscillator as a function of driving frequency. For ideal case (Q = infinite) there is a sharp transition from 0° to 180° at $\omega_{ext} = \omega_0$ The damping produces continuous changes of the phase shift.

Driving frequencies that are far below the free resonance produce zero phase shifts. Driving frequencies that are far above the resonance produce a phase shift of 180°. The dependence of the phase shift on the driving frequency is plotted in figure 3.5.

3.1.1.3 The sensitivity in Tapping mode

The amplitude As noted above, it is actually more interesting to drive the cantilever at a frequency (ω_{ext}) at a slightly different frequency than the free resonance frequency (ω_0) in order to probe attractive and repulsive forces. In other words, it is important to choose the driving frequency at a value where there is maximum sensitivity to the amplitude changes. The sensitivity is defined as the relative variation of the oscillation amplitude, dA, for a variation $d\omega$ of the cantilever resonance frequency driven at ω_{ext}:

$$s(\omega_{ext}) = \frac{1}{A_m}\frac{dA}{d\omega}. \tag{3.12}$$

The driving frequency values yielding maximum sensitivity should correspond to the solution of $d^2A/d\omega d\omega_0 = 0$. For high Q factors, two solutions can be found [65]:

$$\omega_{ext}^{\pm} = \omega_0\left(1 \pm \frac{1}{Q\sqrt{8}}\right). \tag{3.13}$$

Thus, the maximum sensitivity at these driving frequencies is given by:

$$s(\omega_{ext}^{\pm}) = \pm\frac{4Q}{3\sqrt{3}\omega_0}. \tag{3.14}$$

Consequently, the relative variation of the oscillation amplitude - when the cantilever is driven at $\omega_{ext}^{\pm}$ - can be deduced by using the expression of the resonance frequency shift (see equation 3.10):

$$\Delta A = A_m\frac{2Q}{3\sqrt{3}k}\frac{\partial F_{int}(D)}{\partial z}. \tag{3.15}$$

Clearly, the variation of the amplitude in Tapping mode is directly proportional to the gradient of the interacting forces between the tip and the sample.

The phase To determine the sensitivity of the phase, we re-write its expression given in equation 3.5 by introducing the term $\tilde{\omega} = \omega/\omega_0$:

$$\varphi(\tilde{\omega}) = \arctan\left[\frac{1}{Q}\frac{\tilde{\omega}}{(1-\tilde{\omega}^2)}\right]. \tag{3.16}$$

The value of the driving frequencies with maximum phase sensitivity is expressed by $d\varphi^2/d\omega^2 = 0$:

$$\frac{d\varphi(\tilde{\omega})}{d\tilde{\omega}} = Q\frac{\tilde{\omega}^2+1}{\tilde{\omega}^2}\sin^2\varphi(\tilde{\omega}). \tag{3.17}$$

Thus, by nullifying the second order derivative, the driving frequencies with maximum phase sensitivity are given by:

$$\omega_{ext} = \omega_0\left[1 - \frac{1}{8Q^2}\right]. \tag{3.18}$$

The second order power law of Q implies that in most cases (especially for high Q factors), these frequencies practically match the value of the free resonance frequency: $\omega_{ext} = \omega_0$ (therefore $\tilde{\omega} \approx 1$).

Consequently, the relative variation of the phase - when the cantilever is driven at ω_{ext} - can be deduced by using the expression of the resonance frequency shift (see equation 3.10):

$$\Delta\varphi(\tilde{\omega}) = \frac{Q}{k}\frac{\partial F_{int}(D)}{\partial z}. \tag{3.19}$$

Hence, in the dynamic Tapping mode, the phase variation is also directly proportional to the gradient of the interacting forces between the tip and the sample.

3.1.1.4 Lateral resolution

High spatial resolution topography measurements require ultra sharp tips. The typical tip radius is $\sim$ 10 nm. Tips used in Tapping mode are often made of silicon or silicon nitride. For different applications, however, specific types of tips could be required depending on the physical parameter being measured. In electric AFM applications, tips are usually coated with metallic materials.

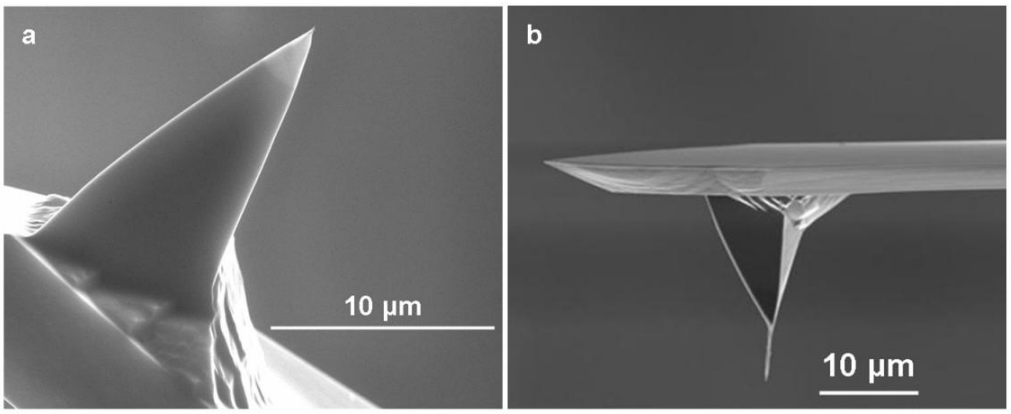

Figure 3.6: (a) SEM image of a silicon AFM tip (b) with a carbon nanotube grown on its apex for higher spatial resolution (image taken from *Xintek, Nanotechnology innovations*).

3.1.2 The double scan KFM technique: lift mode

3.1.2.1 The physical principle

As discussed in the first chapter, the physical principle behind the Kelvin Force Microscopy (KFM) technique is based on measuring the Contact Potential Difference (CPD) resulting from the difference in work function between an AFM tip and sample. Contrary to a classical Kelvin probe method, KFM is a force measurement tool that probes the electrical force arising between the tip and the sample due to the presence of CPD. The adaptation of this AFM-based technique to electrical measurement is mainly centered on the nature of the cantilever driving signal. While in AFM topography measurements the cantilever is mechanically driven by a piezo actuator, an electrical driving signal is used in electrical measurements such as in KFM.

Since its first demonstration by Nonnenmacher *et al.* in 1991, most KFM experiments measured the topography and the CPD by exciting the cantilever mechanically at its resonance frequency (ω_0) and adding an AC voltage to the cantilever at a second frequency (ω_e). Topography and CPD are detected simultaneously by locking the two frequencies ω_0 and ω_e respectively. With this method the detected topography is influenced by long-range electrostatic forces which can overcome short-range van der Waals forces. This results in faulting the actual topography of the surface.

The lift mode explained next, overcomes this problem by separating the two measurements of topography and CPD and thus minimizing the cross-talks between their signals.

3.1.2.2 The operating principle

The lift mode is a KFM method which consist of two distinct tracing steps. The first step involves measuring the sample topography, while the second step is measurement of the CPD between the tip and the sample.

First trace: topography In this step the topography of a single line on the surface is determined in standard Tapping mode. The cantilever is mechanically driven very close to its resonance frequency ($\omega_m \approx \omega_0$) and no additional voltage is applied to the tip. Thus, short-range van der Waals forces dominate long-range electrostatic ones.

Second trace: CPD In a next step, the tip is lifted up over the same line for a set 'lift height' (LH) distance from the sample surface (usually LH = 10-50 nm). The mechanical driving signal is turned off, so the cantilever is driven by an external bias voltage:

$$V_{bias} = V_{dc} + V_{ac}\sin(\omega_e t), \tag{3.20}$$

where V_{ac} is the amplitude of the sinusoidal voltage (usually V_{ac} = 2-5 V), V_{dc} an adjustable direct voltage and ω_e the frequency of the electric driving signal. In our experiments ω_e was set equal to ω_m, used to mechanically drive the cantilever in the first trace. Even though most of the KFM configurations in the lift mode follow this scheme, it is still possible to electrically drive the cantilever at different frequencies in the second trace. In particular we could set ω_e at higher cantilever vibration eigenmodes, possibly leading to an increase in measurements sensitivity. Figure 3.7 shows a sketch of this two step method.

The presence of the contact potential difference results in an additional potential drop (V_{cpd}) between the tip and the sample with different work functions. The total potential difference between the tip and the sample will therefore be expressed as:

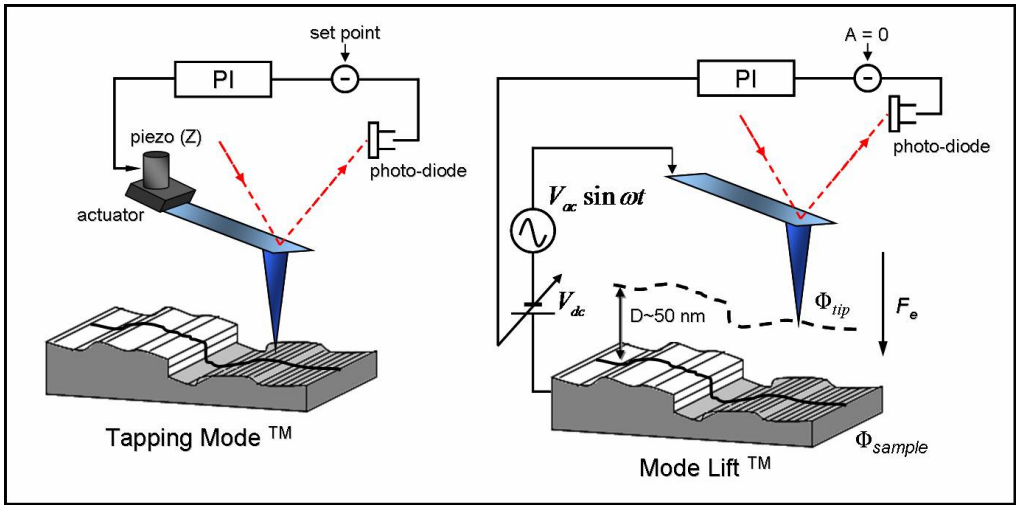

Figure 3.7: A representative scheme of the two trace principle of the KFM lift mode. In the first trace the topography is acquired over a given surface line in a Tapping mode operation where the cantilever is driven mechanically by a piezo actuator. In the second trace, the tip is lifted above the same surface line. The cantilever is electrically driven by an external modulated signal. The mechanical driving signal is turned off. The difference between the tip and the sample results in an electrical force inducing tip vibrations. The contact potential difference is measured between the tip and the sample.

$$V_{ts} = V_{cpd} \pm V_{dc} + V_{ac}\sin(\omega_e t)\cdot \tag{3.21}$$

However, the $\pm$ sign depends on the bias voltage (equation 3.20) applied to the sample or the tip. At a given lift height (LH), the Δz vertical displacements of the z piezo tube in the first Tapping mode trace are fed to the tip in the second trace. The tip thus retraces the topography of the surface line which keeps the tip-sample distance constant during the second trace.

The electrical force The potential difference (V_{ts}) generates an electrical force between the tip and the sample resulting in tip oscillations. The expression of this electrical force can be obtained by calculating the derivative of the electrostatic energy of the capacitor system formed by the tip and the sample as:

$$F_{el} = \frac{1}{2}\frac{\partial C_{ts}}{\partial z}V_{ts}^2 = \frac{1}{2}\frac{\partial C_{ts}}{\partial z}\left(V_{cpd} \pm V_{dc} + V_{ac}\sin(\omega_e t)\right)^2 \cdot \tag{3.22}$$

C_{ts} is the mutual capacitance between the tip and the sample, z is the distance between them. The derivation of the capacitor's electrostatic energy was obtained at constant voltage[3] [66] [67]. The electrostatic force as given by the equation 3.22 is always attractive and depends on the distance between the

[3]for more details readers can refer to the appendix section A.

tip and the sample.

The expansion of the electrostatic force expression gives rise to three different spectral components:

$$F_{dc} = \frac{1}{2}\frac{\partial C_{ts}}{\partial z}\left[(V_{cpd} \pm V_{dc})^2 + \frac{1}{2}V_{ac}^2\right] \tag{3.23}$$

$$F_{\omega_e} = \frac{\partial C_{ts}}{\partial z}(V_{cpd} \pm V_{dc})V_{ac}\sin(\omega_e t) \tag{3.24}$$

$$F_{2\omega_e} = -\frac{1}{4}\frac{\partial C_{ts}}{\partial z}V_{ac}^2\cos(2\omega_e t) \tag{3.25}$$

The first term, F_{dc} is a time-independent component of the electrical force. It causes a static bending of the cantilever depending on the value of the voltages involved and on the gradient of the tip-sample mutual capacitance. F_{ω_e} and $F_{2\omega_e}$ are both time-modulated components which induce cantilever oscillations at the same frequency as the driving signal and its second harmonic respectively.

By observing the expressions of the force components, one can see that the second harmonic component ($F_{2\omega_e}$) is always present whenever $V_{ac} \neq 0$, whereas the first harmonic component of the force is present only if $(V_{cpd} \pm V_{dc}) \neq 0$.

The electric feedback: measuring the CPD This latter observation is the core of the feedback principle in the KFM lift mode. In fact, the main goal is to minimize the electric force acting between the tip and the sample, possible if the term $(V_{cpd} \pm V_{dc})$ was zero.

To do so, in lift mode, the oscillations of the cantilever are detected by locking the signal at the ω_e frequency. Then, the feedback loop adjusts the value of the V_{dc} voltage in order to cancel out the cantilever oscillations at ω_e. Therefore the F_{ω_e} component of the force is nullified and the V_{dc} voltage will be equal to the value of the CPD:

$$F_{\omega_e} = 0 \quad \Longrightarrow \quad V_{dc} = \pm V_{cpd}. \tag{3.26}$$

Therefore in the second trace (or the lift step), the value of V_{dc} is continuously monitored. Hence, the CPD between the tip and the sample (V_{cpd}) can be continuously measured.

The work function difference from the CPD: the polarization sign However, to link the work function to the measured parameter in KFM (i.e. V_{dc}) we recall the relationship between the CPD and the work functions of the tip and the sample introduced in chapter 2:

$$V_{cpd} = \frac{\phi_{tip} - \phi_{sample}}{|e|}, \tag{3.27}$$

where e = -1.60219 $\times$ 10^{-19} C. By changing the polarization of the tip-sample system with an external bias voltage (V_{bias}) added either on the tip or the sample and grounding one of them, the sing of the V_{dc} voltage with respect to V_{cpd} will change (see equation 3.26). Therefore, we identify two different cases:

- When the external bias is applied to the tip

$$V_{dc} = V_{cpd} = \frac{\phi_{tip} - \phi_{sample}}{|e|}. \tag{3.28}$$

- When the external bias is applied to the sample

$$V_{dc} = -V_{cpd} = \frac{\phi_{sample} - \phi_{tip}}{|e|}. \tag{3.29}$$

These expressions show that the work function difference between the tip and the sample can be directly obtained from the measured value of the V_{cpd} depending on the polarization adopted in the actual setup. In our experiments, the external voltage was always applied to the tip while the sample was set to the ground, which is also the case in most KFM lift mode experiments.

KFM a relative measurement method However, it is worth noting that the KFM method is an inherently relative technique: in order to determine the sample work function (ϕ_{sample}), the tip work function (ϕ_{tip}) must be known and invariable, but this is not the case. As we shall soon see, the tip work function has a great influence on the KFM measurements. Wearing of the tip during the KFM imaging process can distort the measured value in KFM lift mode experiments.

The imaging procedure: two dimensional CPD mapping In order to record topography images and CPD maps of all the surface under study, the two tracing steps are thus repeated for each line of the surface along the slow-scan axis. The scan frequency is typically set to 1 Hz per line, which results in an acquisition time of about 4 minutes for a 256 $\times$ 256 pixel image, and thus 8 minutes for both the topography and CPD images.

Figure 3.8 shows an example from [68] of a copper sample surface. The images of topography (a) and V_{dc} map (b) show a changing intensity level at grains of different crystallographic orientations. On image (d), the data has been treated in order to monitor the ϕ_{sample} map derived from the V_{dc} image (b). Image (c) illustrates the crystallographic domains obtained by EBSD[4] measurements

[4]Electron Back-Scattered Diffraction

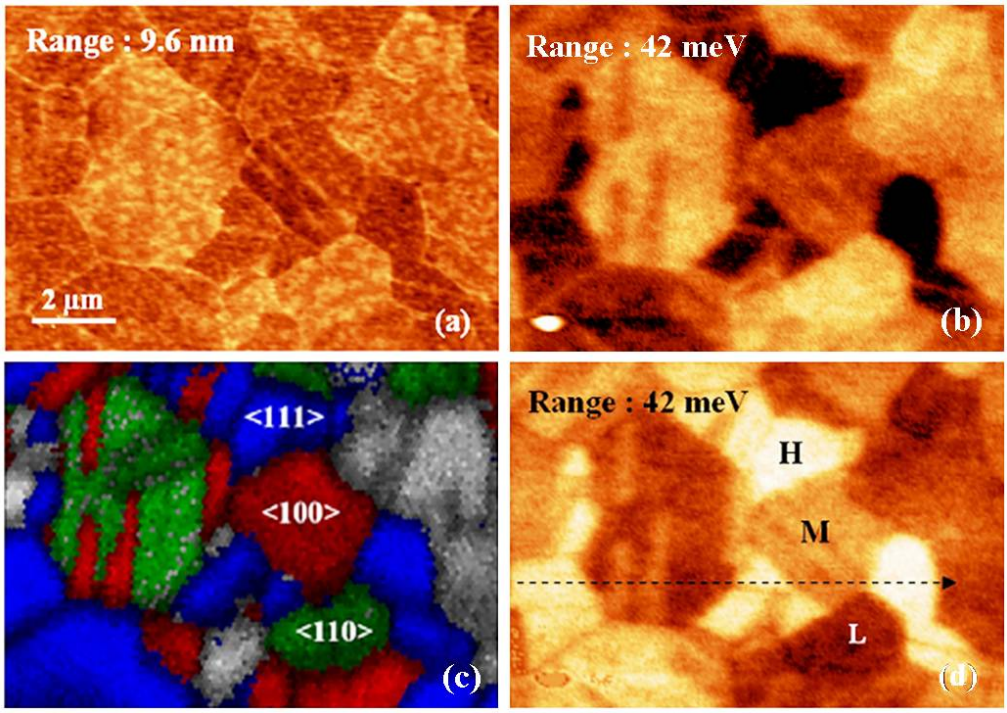

Figure 3.8: An example of KFM lift mode imaging of clean copper surface [10]. The topography image (a) shows the copper grains of different crystallographic orientations which exhibits a V_{dc} contrast (image b) measured in the second trace (lift). Data has been treated in order to derive a map of ϕ_{sample} (d) from the V_{dc} image. The same area has been imaged with EBSD technique and the crystallographic orientations were identified (c).

CPD contrast and work function variation In figure 3.8, the images were recorded in the KFM lift mode by applying the V_{bias} to the tip. According to equation 3.28, the relationship between the initially monitored V_{dc} value and the corresponding ϕ_{sample} is inversed. This can be observed by comparing the inversed contrast between images (b) and (c), where the V_{dc} and ϕ_{sample} were presented respectively.

Regions with lowest intensity level on the V_{dc} image (figure 3.8(b)), have high intensity level (H) on the derived ϕ_{sample} map (figure 3.8(d)), which is related to the highest atomic density of the crystallographic orientation of these zones. Results have been proved by correlating the ϕ_{sample} maps to EBSD images (d) recorded on the same zone of interest (for more details see [10]).

This example validates the established relationship between V_{dc} and V_{cpd} for the different polarizations and emphasizes the ability of the KFM technique to characterize local material properties by measuring the variations of their local work function. However, this technique does have some limitations, and

measurements can be considerably affected by experimental and instrumental conditions. This subject will be addressed in detail in chapter 4.

3.1.2.3 The instrument description

The microscope and electronics Our AFM microscope is a commercial model 'Dimension 3100' from Veeco Instruments (USA) equipped with the 'Nanoscope III a' and a 'Quadrex' control electronics.

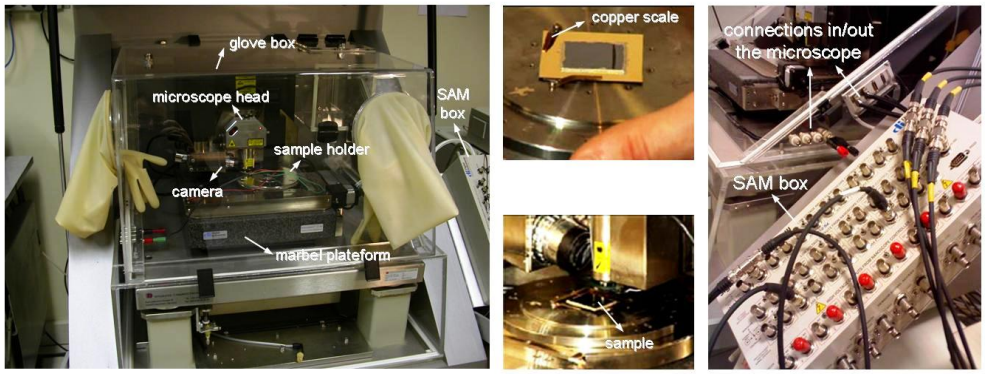

Figure 3.9: A photo of the microscope 'Nanoscope D3100' from Veeco instruments.

A Signal Access Module (SAM) box connected between the microscope output and the control electronics input, gives access to different signals such as the photodiode output, the cantilever mechanical driving signal and a direct connection to add polarization signals to the tip or sample, etc... In this model (figure 3.9), the piezo ceramics, responsible for the lateral (X, Y) displacements, are connected to the tip which moves in the three dimensional direction above a steady platinum sample holder.

The sample holder It is one of the advantages of this microscope. The configuration of the sample holder allows the characterization of large samples. It is formed by a platinum disc ($\sim$ 200 mm diameter) on which the sample can be placed either with a back air absorbing system or by using home made conducting copper scales. Even though the characteristics of the (X, Y) piezo ceramics allows a maximum scan zone of about 100 $\times$ 100 μm^2, the sample holder disc can be laterally moved with a motorized system, allowing to freely move the zone of interest under the tip.

The optical camera This free positioning is made possible thanks to an optical camera joined to the platinum sample holder. It allows to define the position on the sample surface with a precision of $\sim$1 μm and provides an important scale of magnification.

The tips In KFM experiments, conducting tips are required. In our experiments we used PtIr coated silicon tips from 'Nanosensors' manufacturer. The stiffness of tips was ∼3 $N.m^{-1}$ and their free resonance frequency ∼70 kHz. The tip holder used in the 'Dimension 3100' instrument provides an easily accessible tip installation. The tip can be fixed on the tip holder by a simple metallic scale attached to a small spring system providing a relatively steady position (see figure 3.10).

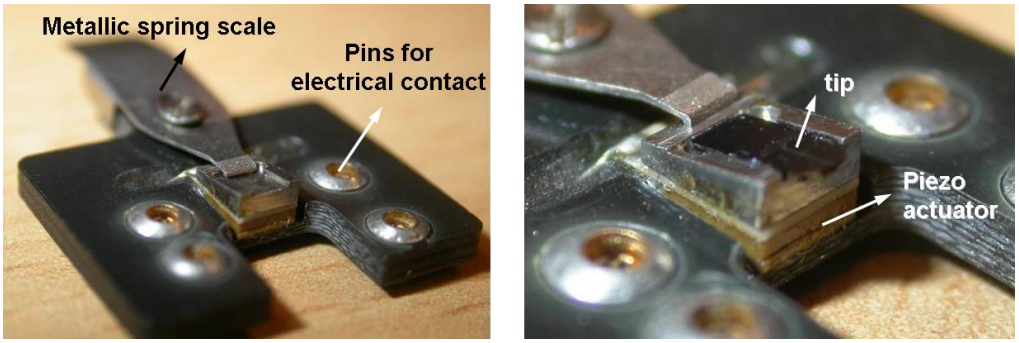

Figure 3.10: A closer photo of the tip holder used in the microscope. The photo shows the positioning system of the tip in addition to the piezo actuator responsible for the mechanical driving of the cantilever.

Parasitic perturbations External parasitic perturbations come from acoustic or terrestrial vibrations. Acoustic vibrations are considerably limited by the use of an overall acoustic-proof box in which the whole microscope is positioned. The terrestrial vibrations are minimized by a damping system formed by a marble platform positioned on top of a polymeric gel, supported by an air cushion steading the horizontal position of the platform.

Controlling the environment of measurements A home-made external glove box was specially designed to control the microscope experimental environment. Control of the relative humidity (RH) under the glove box is ensured by a continuous flow of nitrogen gas (N_2) which maintains the level of relative humidity at ∼2 %. RH is measured with a commercial 'test® 645 sensor' hygrometer providing a precision of 2 % of the humidity measurement.

The glove box is also equipped with a transfer chamber which allows the introduction of samples into the glove box without breaking its relative humidity level. Being also connected to the N_2 gas flow, the transfer chamber is often used as a transition cooling compartment for externally-heated samples before their installation on the platinum sample holder.

External electronics for instrumentation purposes In some case studies we had to change the KFM set-up configuration to explore the possibilities of spatial resolution improvements which will be addressed in detail in chapter 4. A set of external electronic instruments was available to easily connect to the commercial microscope.

A home made-parallel derivation card was developed to allow an external parallel acquisition of the photodiode raw signal before it goes through Veeco electronics. A commercial 'Signal Recovery 7280 DSP' lock in amplifier was available for detecting and locking signals of the cantilever vibrations at different frequencies. A 'SIM 960' analog PID controller from Stanford Research Systems was also available for an external feedback controlling loop. Finally, an 'HP' signal generator was used to provide external electric signal in the range of 10 mV to 10 V pp. Signals from and into the 'Dimension 3100' and external electronics were connected by the SAM box [69].

3.1.2.4 Physical characteristics: sensitivity and spatial resolution

Sensitivity of KFM lift mode measurements The sensitivity of KFM measurements is defined by the minimum V_{cpd} value that can be detected at a given set of instrument conditions. However, this minimum value is inherently dependent on the optical and thermal noise in the experimental environment.

The optical noise is caused by incident photons on the cantilever (in absence of any other source of light, i.e. the laser beam) and could be reflected and detected on the photodiode. This noise can be neglected since the force caused by incident photons is very small ($\sim$ 1 pN). However, the thermal noise is measurable and caused by the brownian motion of gas molecules of the medium where the cantilever is installed. The minimal measurable force is defined for a signal-to-noise ratio (SNR) equal to one:

$$SNR = \frac{f_{min}}{\sqrt{4ck_BTB_{[Hz]}}} = 1, \tag{3.30}$$

where k_B is the Botlzmann constant, T is the temperature and c is the friction coefficient ($c = k/\omega_0 Q$, with k the cantilever stiffness, ω_0 its resonance angular pulsation and Q its quality factor). Therefore, the minimum V_{cpd} value that could be measured in KFM experiments is expressed by an electrical force (F_{ω_e}) equal to the minimal measurable force (f_{min}):

$$V_{cpd}^{min} = \sqrt{4ck_BTB_{[Hz]}}\frac{1}{V_{ac}}\left(\frac{\partial C_{ts}(D)}{\partial z}\right)^{-1}, \tag{3.31}$$

where C_{ts} is the mutual capacitance between the tip and the sample. From this expression, one can see that the sensitivity of KFM measurements depends on the instrument parameters, the environmental conditions and the gradient of

the tip-sample capacitance (i.e. on the geometric form of the tip). One can approximate the tip-sample geometry as a sphere-plane system where [70] [71]:

$$V_{cpd}^{min} = \begin{cases} \sqrt{4ck_BTB_{[Hz]}}\frac{1}{V_{ac}}\frac{D^2}{2\pi\varepsilon_0 R^2} & D \gg R \\ \sqrt{4ck_BTB_{[Hz]}}\frac{1}{V_{ac}}\frac{D}{2\pi\varepsilon_0 R} & D \ll R \end{cases} \tag{3.32}$$

Considering a cantilever with $k = 2$ N.m^{-1}, a Q factor = 300 and a resonance frequency $f_0 = 80$ kHz, and setting $B_{[Hz]} = 1500$ Hz and $V_{ac} = 5$ V, then the V_{cpd}^{min} at $T = 300$ K can be theoretically evaluated between ∼0.8 mV ($D \ll R$) and ∼31 mV ($D \gg R$) for $R = 25$ nm and D varying from 10 nm to 100 nm respectively.

Experimentally, the sensitivity of the electric KFM measurements has been tested by measuring the KFM response to an external 10 mV peak to peak square-wave potential applied to the surface of a copper sample (see figure 2 in [10]). A sensitivity smaller than 5 mV could be measured.

Nevertheless, the parameters of the feedback loop can be adjusted in order to increase the sensitivity of measurements. It has been demonstrated [68] that increasing the amplitude of the electrical driving signal (V_{ac}) results in a reduced noise level as expected from the expression 3.31. A typical value of 5 V allows a noise level of 0.024 quadratic mean value. A minimal noise level of 0.022 quadratic mean value can be reached for a bandwidth $B_{[Hz]} = 1500$ Hz. And finally, when the proportional and integral gains of the PID controller are set to 1, a noise level of ∼0.1 could be reached. However, under UHV conditions, the electric sensitivity is ∼ 10 times higher than in air, since the Q factor increases by several hundred times.

Spatial resolution of KFM lift mode The spatial resolution in KFM measurements can be defined as the ability to resolve two adjacent regions, with different electrical properties in the zone of interest, laterally separated by a distance x. This can be represented by the lateral area (diameter d) under the tip where the lines of the electrostatic interaction are concentrated. The smaller the d, the better the the spatial resolution.

However, the spatial resolution is not only limited by the geometry of the tip but also by the separation distance z between the tip and the sample. These two factors are linked by the widening of the interaction zone under the tip covered by the electric field lines of the electric force (see figure 3.11). The higher the z, the wider the interaction zone on the sample. Moreover, different parts of the tip (i.e. the apex and the cone) become involved in the interaction. These facts result in a decrease of the spatial resolution of KFM measurements.

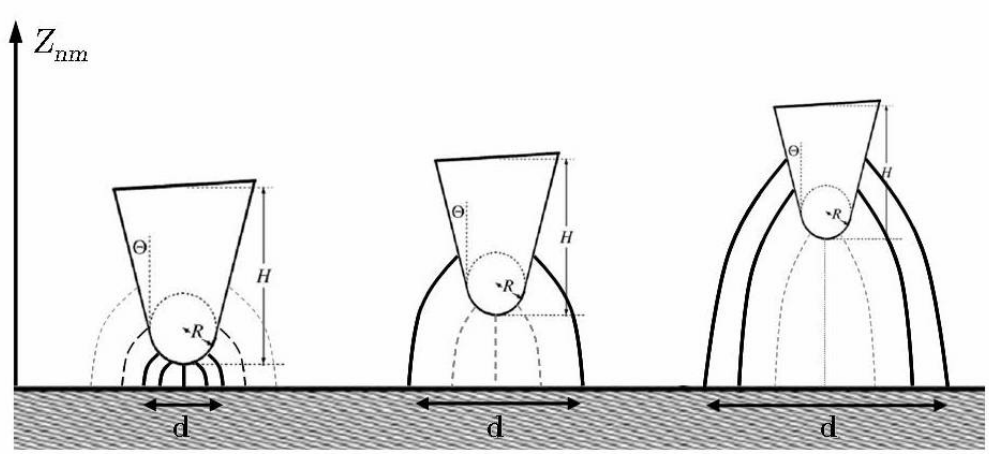

Figure 3.11: A schematic representation of the enlargement of the electrostatic interaction area under the tip when the distance z between the tip and the sample increases. The cone plays a bigger role for higher separation distances which results in a decrease of the spatial resolution. A better spatial resolution is obtained for small z and slighter tips with small opening angles (θ) and longer cones heights (H).

Cadet *et al*. demonstrated that the spatial resolution varies $\propto \sqrt{Rz}$ for $z < R$ (R being the radius of the tip apex (sphere)) and $\propto (R + D)$ for $z > D$. However, the evolution of the interacting force as a function of the distance between the tip and the sample has been studied intensively by modeling the geometry of the tip and analyzing the contribution of its different parts to the electric interaction [70] [71] [72], [73] [74]. We shall discuss this subject in more detail in chapter 4.

Therefore spatial resolution can be improved either by minimizing the distance between the tip and the sample (which helps concentrate the interaction between the tip's apex and small region on the surface), either by changing the tip shape in order to improve its sharpness and/or its aspect ratio. Carbon nanotubes, grafted on the tip's apex, form an important perspective for an improved spatial resolution of KFM electric measurements.

3.1.2.5 Advantages and drawbacks of the KFM lift mode measurements

KFM in the lift mode gives the advantage of monitoring the variation in the work function difference between the tip and sample surface with a high spatial resolution ($\sim$ 50 nm) practically with no cross-talks between topography and electric signals. It is an easily accessible tool providing facilities of large sample characterization, easy installation and control of the experimental environment (glove box). It can be also integrated in an in-line characterization procedure for micro- and nano-electronic device manufacturing.

However, this technique suffers from a certain number of limitations. Measurements under air conditions are always affected by the effects of surface adsorbents from environmental contamination or humidity. Studies show that the value of the measured work function can be considerably modified in presence of surface contamination either on the sample or on the tip [10].

KFM measurements are also very dependent on the tip's work function, which makes this technique inherently relative. So one should proceed with prudence before getting quantified work function results. Nevertheless, the spatial resolution of the KFM lift mode is somehow limited by distance between the tip and sample. We shall develop this further in chapter 4, focusing on the effects of experimental parameters on the quality of KFM measurements. We will then present an updated configuration to improve the spatial resolution of electric measurements in air.

3.2 X-ray photo electron emission spectromicroscopy (XPEEM)

In this section we address the photoelectron emission spectromicroscopy with X-rays (XPEEM). The photoelectron spectromicroscopy combines two surface analysis techniques: the photoelectron spectroscopy (PES) (also known as XPS for X-ray Photoelectron Spectroscopy) and the full field photoelectron emission microscopy (PEEM).

XPEEM provides access to the electronic and chemical structure of surfaces with spatial resolutions going from hundreds to tens of nanometers. It is then perfectly suited to the study of nano-objects or heterogeneous materials on the mesoscopic scale and smaller.

In the first part of this section, we introduce photoelectron spectroscopy and photoelectron emission microscopy techniques. Then we provide a description of the XPEEM spectromicroscope we used in this work, the *NanoESCA*. We describe as well the methods of work function measurements and mapping besides the practical aspects of sample preparation and handling.

3.2.1 Introduction

3.2.1.1 Photoelectron spectroscopy

Photoelectron spectroscopy exploits the photoelectric effect, discovered in 1885 by Hertz and explained by Einstein in 1905 [75]. When a photon of energy hν is incident on a sample, all electrons whose binding energy is less than hν can make a transition from their initial state. If this final state exists for the given

excitation energy, and the transition is allowed, the energy gained can remove the electron from the sample.

The surplus energy is transformed into kinetic energy of the photoelectron in the final state. In order to leave the material and to be detected, the work function ϕ_{sample} of the sample material should be considered. The kinetic energy of the photoelectron is then measured with respect to the vacuum level E_V. Another important energy level must also be considered: the Fermi level, E_F, which for metals is the highest occupied energy level in the solid. The photoemission principle in solids is schematically represented in figure 3.12.

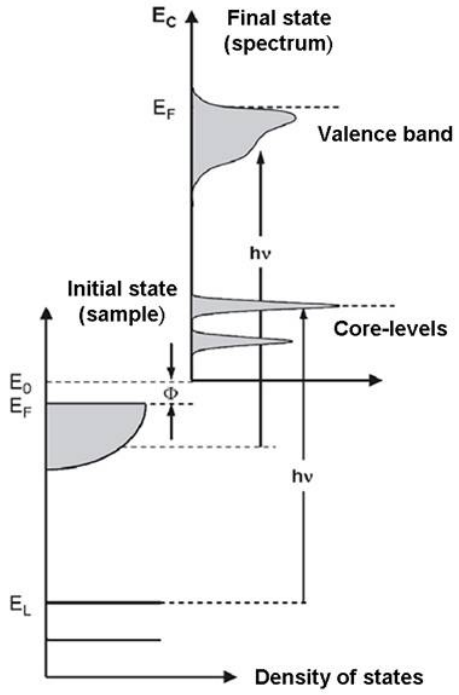

Figure 3.12: Schematic representation showing the principle of photoemission in solids. An electron in a bound state is excited by a photon of energy hν. The electron is detected in its final state outside the sample at a kinetic energy E_k (equation 3.34), allowing one to deduce its initial state and binding energy, E_b [76].

The kinetic energy of the resulting photoelectron is measured with the spectrometer (an electron analyser). The work function of analyser, $\phi_{analyser}$, should also be considered. There is a subtlety in the measurement process when considering the work function and Fermi and vacuum energy levels.

If the studied sample is in electrical contact with an instrument collecting the spectrum (i.e. the analyser), then the Fermi levels of sample and analyser align to the same energy by electron flow from higher energy states to available lower energy states. This causes a charge disparity between the surface of the sample and the surface of the analyser which results in a contact potential difference (noted $eV_s = \phi_{analyser} - \phi_{sample}$).

Consider an electron in a bound state (with a binding energy E_b) excited by a photon of energy hν. When this photoelectron leaves the sample surface it has kinetic energy, E_k, less the work function of the surface. Between the sample surface and analyser is eV_s which affects this kinetic energy. When detected by the analyser the kinetic energy of the photoelectron is hence:

$$E_k = h\nu - E_b - eV_s - \phi_{sample}. \tag{3.33}$$

The net result is that the kinetic energy of the photoelectron measured by the analyser is dependent on its work function ($\phi_{analyser}$) and is given by:

$$E_k = h\nu - E_b - \phi_{analyser}. \tag{3.34}$$

In solids, electrons occupy discrete energy levels, either localized levels (core-levels) or delocalized energy levels as bands (the valence band and for metals, the conduction band). The core-level binding energy (E_b) is characteristic of the emitting atom. It is sensitive to the chemical environment (nature of the first neighbor atoms) and the local atomic environment (length and angles of bonds) of this atom [77]. By measuring the kinetic energy of the photoelectron emitted from this atom, and knowing the work function of the analyser, the corresponding binding energy can be deduced from expression 3.34.

X-ray Photoelectron Spectroscopy (XPS) also known as the Electron Spectroscopy for Chemical Analysis (ESCA). It was developed as an analysis tool by Kai Siegbahn and co-workers 50 years ago [78]. Siegbahn received the Nobel Prize for this work in 1981. He demonstrated the possibility of producing spectra with discrete lines corresponding to energy levels in a material.

He also demonstrated that measuring the binding energy of electrons with XPS could reveal information about the chemical composition and the local chemical environment of the emitting atom. According to Koopmans theorem, the initial state of a photoelectron emitted from a given atom can be deduced by the measurement of its energy in the final state [79].

Therefore in a XPS-measured spectrum the binding energies of the peaks are characteristic of each element. The energy position and peak shapes are slightly altered by the chemical state of the emitting atoms, as illustrated in figure 3.13 for the C1s spectrum of a polymethylmethacrylate sample.

Owing to its important characteristics of chemical and surface sensitivity, XPS has emerged as an essential and powerful surface analysis tool in fundamental research as well as in industrial applications. An excellent introduction to XPS technique is provided by Briggs and Grant [81].

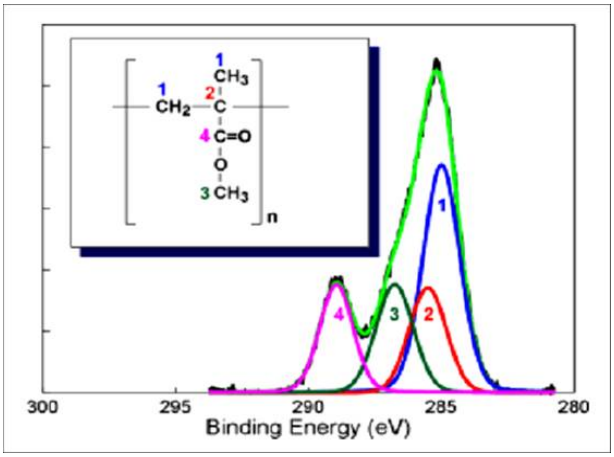

Figure 3.13: C1*s* photoelectron spectrum fitted to indicate the functional groups present in a polymethylmethacrylate sample [80].

3.2.1.2 Photo Electron Emission Microscopy (PEEM)

The photoelectron emission microscopy was invented by Brüche in the early 1930s [54]. Brüche used electrons emitted from a zinc sample target under UV irradiation in order to obtain an image of this target on a fluorescent screen. The magnification of Brüche's microscope was modest and allowed imaging of fields of view (FoV) in the millimeter range. It is possible to use a low-energy electron beam, as well, to illuminate the sample surface and to record images of the reflected electrons. This is called Low-Energy Electron Microscopy (LEEM).

After the pioneering work by Brüche and a theoretical work by Recknagel, the technique was refined and improved by Spivak *et al.*, Berthge *et al.* and Mollensted *et al.*. The first commercial version of PEEM was built already in the 1960's (Balzers 'Metioskop'). A major breakthrough was achieved by Telieps and Bauer who realized a LEEM image thanks to a sophisticated electron-optical system and the usage of ultrahigh vacuum (UHV). It was possible to observe the atomic terraces of a Mo(110) surface [82]. The imaging scale of Telipes and Bauer measurements was in the order of the micron.

Principle The principle of PEEM technique is illustrated in figure 3.14. A photon beam of energy hν is incident on the sample. A high voltage, typically between 10 and 20 kV, allows an extraction lens - located several millimeters from the sample - to collect the photoelectric emission on a wide range of emission angle. A system of lenses then focus and create a first intermediate image. Finally, a set of projection lenses allows the magnification of this first image.

The detector is typically formed by a multichannel plate coupled to a fluorescent screen which is finally imaged by a CCD camera. With a magnetic sector field it became possible, as well, to perform LEEM on the same sample surface.

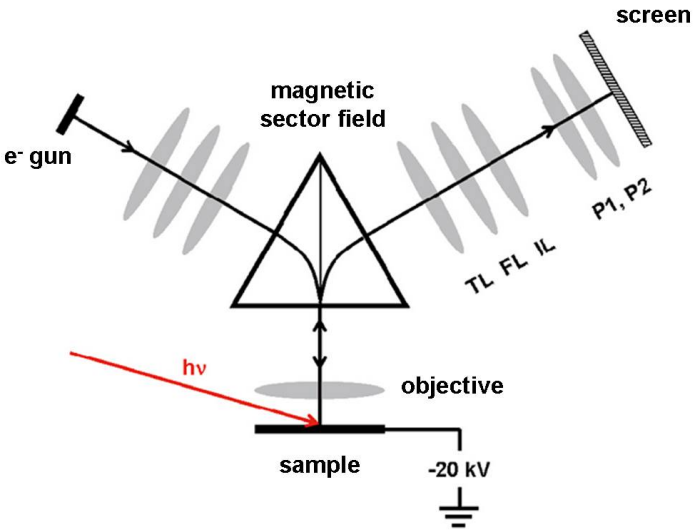

Figure 3.14: Schematic of an electron microscope in LEEM and PEEM modes. The magnetic sector field allows detection of the reflected and photoemitted electrons respectively [76].

A PEEM image is obtained by collecting all the energy distribution of electrons emitted from the sample after irradiation with photons. They are formed by photoelectrons from direct transitions (true core-level or valence photoelectrons) and by secondary electrons as well. Given that the intensity of secondary electrons (SE) is more important, the PEEM image is therefore dominated by the signal of SEs. Nevertheless, the PEEM optical system acts as low pass filter. Therefore, the combination of the electronic-optical system with a UV photon source (Hg (4.9 eV) discharging lamp, for example) allows for energy-selective imaging.

Electronic-optical system: technical conceptions There are two designs of electronic-optical systems currently used in PEEM: magnetic and electrostatic lens systems. They are optimized for different types of applications.

Magnetic lenses The first design is based on that developed by Telieps and Bauer from the emission microscopy techniques. The sample is polarized, typically at -20 kV, with respect to the system of objective lenses which are magnetic. This design is commercialized by Elmitec GmbH [83] and by SPECS GmbH [84] with a particular geometry (3.14).

Most of PEEMs installed in synchrotron beam lines are of this type. The high electrons energy in the PEEM column has two advantages. Firstly, the imaging conditions are made in the Gaussian optical approximation, i.e. the angle of electron trajectories with respect to the optical axis is small. This allows one to reach very small fields of view (typically 1 μm), and to provide aberration correction systems similar to those used in transmission electron microscopy (TEM). One advantage of magnetic lenses is the inclusion of a magnetic field sector that toggles between an electronic beam in LEEM mode and photoelectron detection in PEEM mode.

Electrostatic lenses The second design used in PEEM is characterized by a purely electrostatic lens system, as illustrated in figure 3.15. This design is the one used in this thesis. The sample is grounded at zero potential while a high positive voltage ($\sim$ 12 - 15 KV) is applied to the extraction lens. This design is commercialized by Focus GmbH [85], and the system is simpler than the one described above for two reasons.

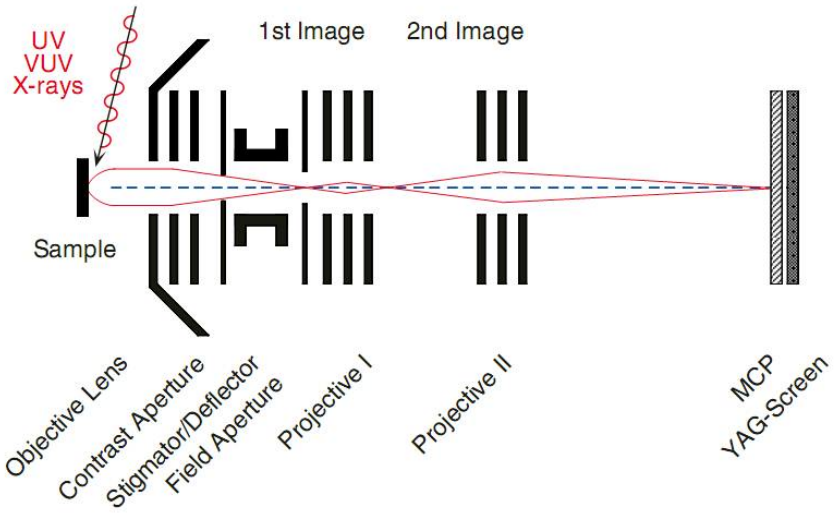

Figure 3.15: Schematic of a fully electrostatic PEEM column. Contrary to figure 3.14, the sample is close to ground and the extraction lens is at high voltage [86].

Firstly, it avoids intrinsic problems related to the polarization of the sample at high voltages. Secondly, because the optical system is electrostatic there is no image rotation when its magnification changes, unlike the magnetic lens system. Successive zooms of the zone or structures of interest on the surface thus became much more simple. One disadvantage of this type of PEEM is the difficulty to incorporate a LEEM due to the absence of a magnetic sector field. Most laboratory-based PEEMs are of this type.

Energy filtering In order to use the advantages of electron spectroscopy for chemical analysis (ESCA) (see above), however, the emitted photoelectrons have to be energetically filtered [86]. For this purpose band pass energy filters (such as an hemispherical energy analyser) can be used. An electron analyser with bandwidth ΔE allows for "spectroscopic" PEEM analysis (or PEEM spectromicroscopy), i.e. with a complete energy filtering.

With the PEEM column as an entrance lens to the analyser, it thus became possible to image the intensity of a given electronic level (a core-level, for example) with a lateral resolution of several tens of nanometers. The most common solution for energy filtering in PEEM is to add a hemispherical energy analyser (HSA) [87] similar to those classically used in XPS or UPS experiments.

However, a direct consequence of the high lateral resolution is a considerably reduced overall transmission of the analyser. The use of such systems (PEEM with an energy analyser) for laboratory experiments may be limited to low energy applications in the Ultra-violet photoelectron spectroscopy range. This disadvantage can be overcome when using high brilliance undulator beamlines at the synchrotron for imaging XPS experiments.

3.2.2 XPEEM spectromicroscopy: *NanoESCA*

A novel solution suggested for XPEEM spectromicroscopy consists of coupling an energy filtering analysis (using double hemispherical energy analyser) to a PEEM with full electrostatic lenses. Since electrons in electrostatic PEEM column have a low energy ($\sim$ 1 kV), the deceleration at the entrance of the analyser is then modest. This allows for transmission of a large phase space. This solution seems the most suitable method to guarantee a strong signal at high kinetic energies, far from the photoemission threshold (figure 3.17).

NanoESCA is a recently developed energy filtered imaging microscope (spectromicroscope) of this type, commercialized by Omicron Nanotechnology GmbH. The first commercially available *NanoESCA* was recently installed in our laboratory at the Nanocharacterization Platform of the CEA in Grenoble.

NanoESCA features a fully electrostatic PEEM column and an imaging double energy analyser (IDEA) formed by two hemispherical analysers instead of one (figure 3.16). The two hemispheres are coupled with an appropriate transfer lens. The symmetry of energy filtering through these two hemispherical analysers eliminates any aberration inherent in the use of a single hemispherical analyser [88] [89].

This enables the use of entrance and exit slits of millimetric size which provide a high transmission of this system [89]. Also, the pass energies (E_{pass}) are those commonly used in XPS and UPS experiments (i.e. E_{pass} = 100 eV and

less) which optimizes the isochromaticity of the image (i.e. the energy dispersion depending on the position in the dispersive plane).

Another strong feature of the *NanoESCA* instrument is the possibility to work with various complementary excitation sources. Besides synchrotron radiation, the instrument can be operated with three UV laboratory sources: Hg (4.9 eV), D_2 (6.4 eV) and He I (21.2 eV). It also operates with a monochromatic Al K_α radiation using a Focused X-ray Source (FXS). This makes the *NanoESCA* the first operational laboratory XPEEM instrument to date.

3.2.2.1 operation modes of the *NanoESCA*

Three operating modes are available: direct non-energy-filtered imaging; area selected spectroscopy; and energy-filtered imaging. The fully electrostatic PEEM column is either used for direct (secondary electron) PEEM-imaging or as an entrance lens for the analyser (figure 3.16).

The direct non-filtered PEEM mode In this mode, a magnified and unfiltered image is formed onto an image intensifier consisting of a multi-channel plate and a CCD camera. As the image is formed with the entire set of photo-electron energies, the contrast is dominated by the information carried by the secondary electrons and is therefore related to the entire photo-yield. Since the photo-threshold cannot be isolated, in this case, the work function is lost in the image obtained in this mode.

The small-area spectroscopy mode : μ-XPS In this mode, XPS is possible over small selected-areas of the surface thanks to a continuously variable field aperture located in the first intermediate image plane inside the PEEM column. Core-level photoelectrons are collected with a channeltron detector located behind the first hemispherical analyser of the IDEA system [88] (with the second analyser switched off).

The energy-filtered imaging mode In this mode the PEEM column is used as an entrance lens of the energy analyser. Photoelectrons are slowed down, at the entrance of the first hemispherical analyser, from the typical 1 keV drift energy inside the objective lens to the desired energy (typically 50-100) [89].

Image stacks are recorded by scanning the sample voltage with fixed analyser pass energy and automatic refocusing of the objective lens. The three dimensional data stack $I(x, y, E)$ thus contains at each image pixel microscopic and spectroscopic information; it can be analysed off-line by standard data reduction techniques [89].

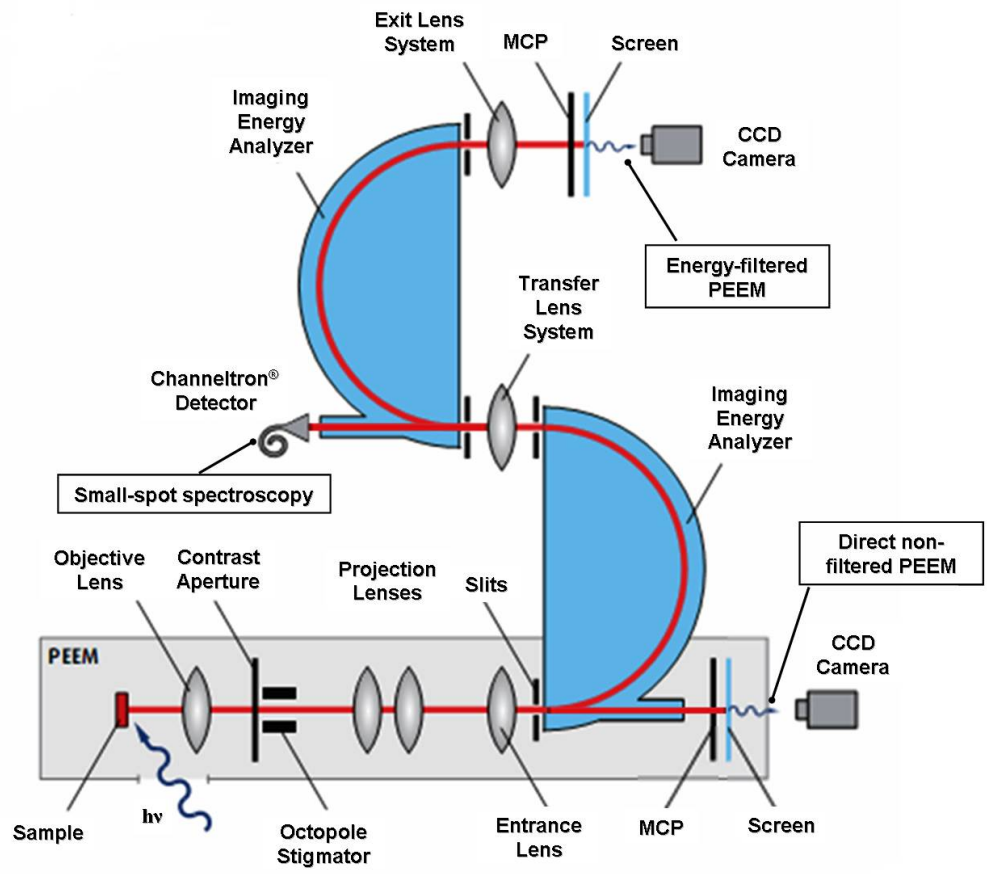

Figure 3.16: A schematic representation of the optical path of the three operation modes of the *NanoESCA*.

3.2.2.2 XPEEM spectromicroscopy: accessible information

When operating in the energy-filtered imaging mode, *NanoESCA* enables XPEEM spectromicroscopy measurements. XPEEM spectromicroscopy provides the possibility to choose the region of the photoelectron spectrum to image (i.e. selected energy windows, as illustrated in figure 3.17) [76]. This shows how the whole photoelectron spectrum can be studied with a XPEEM spectromicroscope.

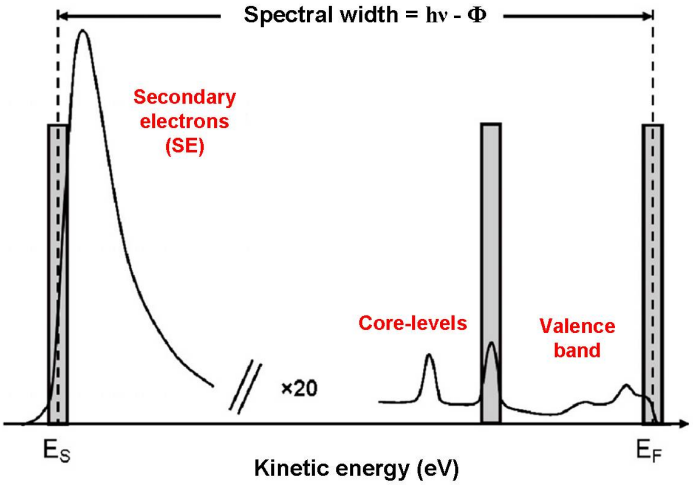

Figure 3.17: Schematic of a photoelectron spectrum showing the possibility of selecting a wide range of kinetic energies thanks to the optimized transmission of the *NanoESCA* [76].

Therefore we can image the region of photoemission threshold (using an energy window in the range of secondary electrons (figure 3.17). This gives direct access to lateral variations in the work function.

Or we can image a selected core-level by choosing an energy window in the range corresponding to this level. This gives access to the lateral distribution of the present elements and their chemical states.

We can also image the region of the valence band up to (and including) the Fermi level which allows us to map the lateral variations in the density of states.

However, two features of the photoelectron spectrum are of special interest in this thesis: the secondary electrons distribution (emission threshold region) and core-level electrons.

Work function measurement and mapping

This spectromicroscopy application with the *NanoESCA* is of primary interest in our work. Here we describe how the work function can be locally determined

when the surface is imaged using the energy-filtered mode in the range of secondary electrons (emission threshold range). In chapter 5, this method will be used to measure the work function of epitaxial graphene layers on SiC(0001).

Work function from the emission threshold energy In the *NanoESCA* the energy scale is referenced to the Fermi level (E_F) in the sample. The kinetic energy of photoelectrons is then noted as $E - E_F$ [9]. Therefore for a metal, the energy $E - E_F$ at which the photoemission threshold is observed is equivalent to the work function.

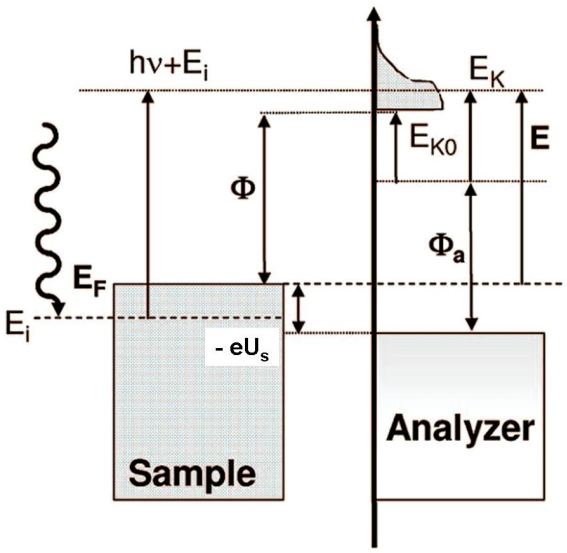

Figure 3.18: Energy level diagram illustrating the determination of the work function [90].

Figure 3.18 shows an energy level diagram illustrating the determination of the work function. The energy scale on the abscissa axis is referred to the Fermi level of the sample surface ($E_F = 0$). If E_k denotes the the kinetic energy of the photoelectrons measured at the entrance of the imaging analyser, and E denotes the final-state energy relative to E_F then:

$$E = E_k + eU_s + \phi_A \tag{3.35}$$

where, ϕ_A is the work function of the analyser and U_s the bias voltage applied to the sample surface. An electron having an initial state energy E_i (just below E_F) excited with photons of energy $h\nu$, will have a measured kinetic energy E_k given by:

$$E_k = (E_i + h\nu) - eU_s - \phi_A\cdot \tag{3.36}$$

Thus, the threshold kinetic energy E_k^0 is given by:

$$E_k^0 = \phi_s - eU_s - \phi_A\cdot \tag{3.37}$$

The work function of the sample (ϕ_s) is therefore obtained by the determination of the emission threshold energy, given the values of ϕ_A and U_s. Since ϕ_A is stable during measurements, the measured work function of the sample (ϕ_s) is then an *absolute* value.

Local SE emission spectra In order to determine the emission threshold, and therefore the work function, secondary electron emission spectra have to be extracted. The change of the sample polarisation changes the value of $E - E_F$. We can thus record a series of images in function of the energy of secondary electrons. It consists of a three-dimensional data set of photoemitted intensity $I(x, y, E - E_F)$. Local SE emission spectra can therefore be extracted at selected areas of interest (AOIs) by compiling the intensity level on each single energy image of the series (see figure 3.19).

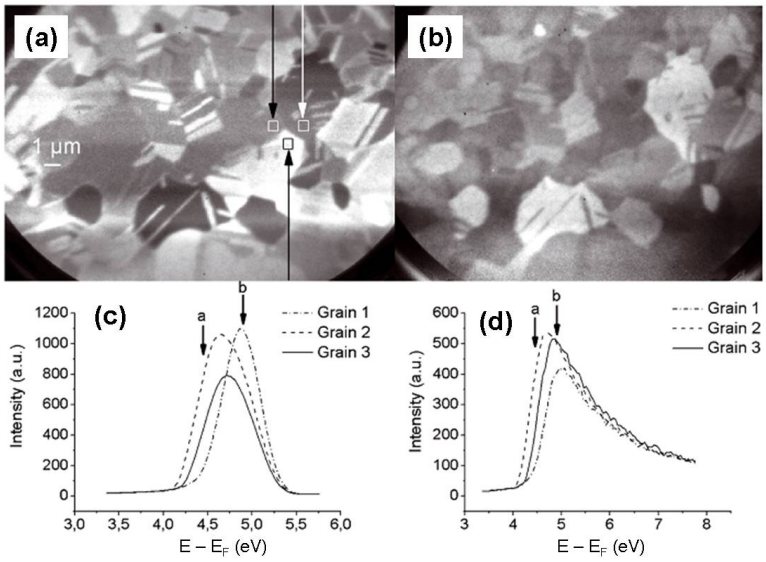

Figure 3.19: (a)Image of a polycristalline Cu surface using a Hg UV source (4.9 eV) at $E - E_F$ = 4.45 eV; (b) same surface imaged using a He I lamp (21.2 eV); (c) threshold spectra extracted from the three square areas of interest shown in (a); (d) the work function differences are clearly visible from the shifts of the photoemission threshold [9].

The electron energy is, however, lowered by the Schottky effect due to the high extractor field ($\delta E = 98$ meV for a 12 kV field). After the electron energy is corrected for this effect, the position of the emission threshold is determined by the best least-squares fit of corrected experimental spectra using a complementary error function [9] [91]. The position of the emission threshold thus corresponds to the work function.

Application example Figure 3.19 shows an example of the work function determination of grains in a polycrystalline copper film reported from [9]. Cu film was deposited on a Si substrate. The sample surface was treated by Ar^+ ion sputtering in UHV in order to eliminate the superficial oxide layer. The crystallographic orientation of grains was determined by the electron back-scattered diffraction technique (EBSD).

Two illumination sources have been used. A Hg discharging lamp ($h\nu$ = 4.9 eV) with a $\sim$ 0.2 eV bandwidth and a He I lamp ($h\nu$ = 21.2 eV) with a $\sim$ 50 meV bandwidth. Figures 3.19 (a) and (b) show images taken with these two sources respectively, over a FoV = 25 μm. The image contrast corresponds to the variation in the work function depending on the grains' crystallographic orientation. For a quantitative analysis of the work function, however, the He I photon source must be used.

In fact, at low photon-energy ($h\nu$ = 4.9 eV), the contribution of direct transitions from the valence band to the conduction band is important, whereas for the photon energy of 21.2 eV, the energy range ($E - E_F$) near the emission threshold consists mainly of true secondary electrons.

AOIs were chosen at specific positions corresponding to Cu grains with the crystallographic orientations (100), (110) and (111). SE emission spectra extracted from the image series at these positions are shown in figures 3.19 (c) and (d). The work function variations are clearly visible from the shifted positions of the emission threshold on each spectrum. Results showed a very good agreement with reported work function values obtained for Cu monocrystals [9] [76].

This way, the work function can be locally measured at a specific position on the sample surface. However, an extended data treatment enables the reproduction of a two dimensional map of the work function variations over the entire FoV, as explained below.

Mapping of the local work function variations over the FoV

The idea of work function mapping is to reproduce an image of local work function variations over the entire FoV. The method is rather simple and consists of the following steps:

- SE emission spectra are extracted at each pixel of the image as described above.
- The photoemission threshold (and therefore the work function) on each spectrum is determined by fitting the data with a complementary error function. The electron energy is corrected for the Schottky lowering effect as discussed above.

- The extraction of SE spectra and the fitting of the photoemission thresholds are automated with a Matlab code using a Levenberg-Marquardt algorithm.
- Finally, a two-dimensional work function map is reproduced from the values obtained at each image pixel.

Note that the opening angle of the energy analyser gives rise to a parabolic energy dispersion (non-isochromaticity) in the energy dispersive plane as a function of the position in the FoV [91]. The non-isochromaticity correction to the $E - E_F$ scale in the image series needs to be carried out. Details are provided in the appendix section.

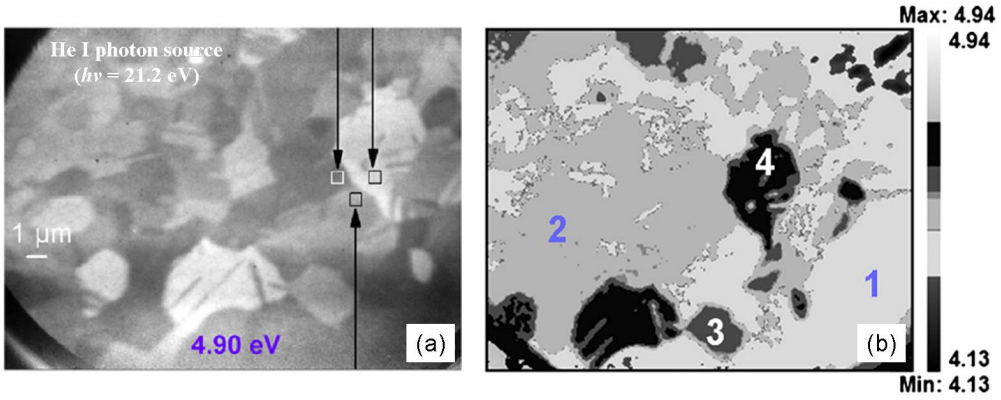

Figure 3.20: (a) a PEEM image acquired at $E - E_F = 4.9$ eV using a He I (VUV) photon source. Copper grains having different work functions (indicated by arrows) present different contrasts on the PEEM image. (b) a reconstructed work function map obtained using the method described in the text. Four different work functions can clearly be discerned [89].

Using this method, the work function map (figure 3.20 (b)) of the Cu polycrystalline surface has been reconstructed from the image series recorded in the SE emission range. Figure 3.20 shows an image (a) of the Cu surface taken at $E - E_F = 4.9$ eV with the He I) source and (b) the corresponding work function map [9].

Maps of present elements and chemical states

Another spectromicroscopy application of interest in this work is the mapping of elements and chemical states present on the sample surface. In this case, images are recorded in the region of the photoemission spectrum corresponding to a specific core-level. Thanks to the high transmission of the energy filtering system with double hemispherical analyser (IDEA), the use of a laboratory X-ray photon source (FXS) became possible. XPS imaging can be thus performed with high lateral and energy resolutions.

Here we present an example of spectromicroscopy experiments in the core-levels ranges reported from [92]. A sample of a polycrystalline CdTe substrate has been covered with a thin gold layer (5 nm). A cross-shaped pattern was engraved on the sample surface using focused ion beam milling technique (FIB). The ion beam was calibrated on a central square area (see figure 3.21).

Two image series have been recorded by tuning the instrument to the energies of interest, namely, around the gold (Au $4_{f_{7/2}}$, binding energy 84 eV) core-level peak and the Telluride (Cd-bounded Te $3_{d_{3/2}}$, binding energy 573 eV) core-level peak. A survey photoelectron spectrum allowed us to identify a contribution related to Te oxide chemical states at a binding energy of 576 eV. Therefore the set of images acquired across the Te peak were taken in the range of binding energies going from 571.2 eV to 578.7 eV. The energy step was 0.3 eV and the energy resolution 0.9 eV. The broad scan of binding energies then enabled a proper Shirley background subtraction in order to obtain the final image representative of each element's distribution.

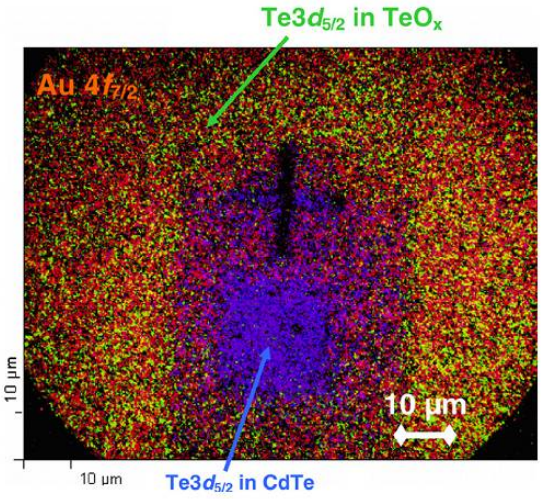

Figure 3.21: Laboratory XPEEM core-level bonding state image of a FIB-patterned layer deposited on CdTe, obtained by superimposing the following signals: Au $4_{f_{7/2}}$, Te $3_{d_{3/2}}$ bounded to Cd from the buried CdTe substrate (blue) and Te $3_{d_{5/2}}$ bounded to 0 (green) from the surface Te oxide directly below gold [90].

The core-level contributions represented in colors have been superimposed to obtain the image displayed in figure 3.21. Te is present in two distinct chemical states, Te-Cd (represented in blue) and Te-O_x of the surface oxide (represented in green). The gold contribution is represented in red. It can be seen from this image that gold is, as expected, homogeneously distributed at the surface except where the cross-shape and the square were patterned. In these specific areas, telluride happens to be bound exclusively to cadmium (blue color). This is consistent with the effect of the ion beam that eliminates the surface Te oxide. This oxide bonding state of telluride (green color) is obviously present everywhere else underneath the gold layer.

This example nicely illustrates that the *NanoESCA* with a laboratory source is capable of mapping both elemental and bonding states distribution over the sample surface. Furthermore, local core-level spectra can be extracted from the image series recorded in the range of core-level binding energies at specific areas of interest. This enables the possibility to study the local chemical composition of the surface.

3.2.3 *NanoESCA*: description of the instrument

Here we present the main elements of the *NanoESCA*. We also discuss its performance in terms of lateral resolution and energy resolution. The strength of the *NanoESCA* as a complete surface analysis tool is also discussed.

3.2.3.1 The elements of *NanoESCA*

The photon sources The instrument is supplied with four different excitation sources: mercury (Hg) and deuterium (D_2) discharging lamps providing photons at energies 4.9 eV and 6.2 eV respectively. An additional UV helium (He I) discharging lamp (photon energy of 21.2 eV) is also available for imaging with a true work function contrast (which is also possible with X-ray source). The important feature of the *NanoESCA* is the laboratory monochromatic X-ray source which delivers Al K_α radiation ($h\nu = 1486.6$ eV). Soft X-rays at synchrotron beam line can also be used thanks to a dedicated port.

The immersion objective lens The sample, positioned at ∼1.8 mm from the first electrode (extractor), forms the first lens of the PEEM column. While the sample is nearly grounded, high voltages (∼12 - 15 kV) are applied to the extractor lens resulting in an immersion field at the surface varying between 6.6 kV/mm and 8.3 kV/mm depending on the applied voltage. The electrons are then decelerated in the focusing field of the lens towards the low voltage column typically at 1000 eV drift energy. The objective lens is equipped with an exchangeable and adjustable contrast apertures (CAs) of different sizes (30 μm up to 1500 μm). It is also supplied by an octopole stigmator to compensate for axial astigmatism. A continuously adjustable iris acts as a field aperture for small spot spectroscopy.

The projection lenses Their role is to project and slow down the electrons into the analyser entrance, or to magnify the electrons onto the image intensifier for a non-energy filtered operation. A channeltron detector located behind the first hemisphere can be used to acquire fast small-spot overview spectra. A set of projection lenses after the second analyser is used to obtained the final magnification in an energy-filtered operation. The magnification can be adjusted over a large range between 5 μm and 650 μm field of view (FoV).

The IDEA energy filter It consists of two hemispherical analysers coupled by a transfer lens system (see figure 3.16) [89] [88]. The telescopic lens transfers electrons' positions and angles from the exit of the first hemispherical analyser into the entrance of the second one to ensure a complete Kepler orbit at the exit of the second hemisphere. In this way, geometric and chromatic aberration induced by the passage of electrons through the first analyser can thus be corrected [89].

Sample preparation chamber The *NanoESCA* is also equipped with an *in situ* sample preparation chamber (in UHV ($\sim 10^{-10}$ mbar)). A mechanical transition system transfers the sample from the preparation chamber into the analysis chamber of the microscope. Sample transfer is also done under UHV.

Several surface treatments are possible. An argon ion beam (Ar^+) is available for surface sputtering treatments. A resistive heating system is also available for sample heating at different temperatures. High temperature treatments are possible and requires a particular care for the pressure of the preparation chamber. The temperatures of the heated sample surface can be measured either with a thermo-couple system or with an external infrared pyrometer.

3.2.3.2 Performances the *NanoESCA*

When regarding the device performance, we have to consider the energy resolution as well as the lateral resolution.

Lateral resolution *NanoESCA* uses the PEEM column as an entrance lens to the double hemispherical energy analyser system (IDEA). Therefore, the lateral resolution of the spectromicroscope is determined by the electron-optical system. It is affected by the spherical and chromatic aberrations of the optical system and by the diffraction limit of the analyzed photoelectrons.

It has been demonstrated that the aberrations are mainly caused in the objective lens due to the strong extraction field. In the space between the sample and the first lens, electrons are subjected to the strongest acceleration. The strong electric field (extraction field) accelerates the electrons into the focusing part of the objective lens and simultaneously reduces the axial angle of the electrons inside the lens [89]. The aberrations are reduced by using a smaller angular spread of electrons. The larger angles are cut by the contrast aperture (CA) located in the back focal plane of the objective lens. The CA size can be reduced until diffraction at the aperture becomes dominant [89].

According to Escher *et al.* [cite Escher09] the total resolution of the entrance lens can be approximated by the diameter of the resolution disc as:

$$dr_{tot} = 2\sqrt{dr_c^2 + dr_s^2 + dr_d^2} \tag{3.38}$$

where, dr_c, dr_s, dr_d are the chromatic aberration, spherical aberration and diffraction disc radius respectively, with:

$$\begin{aligned} dr_c &\approx \left(l\frac{E_0}{E_a} + C_c \left(\frac{E_0}{E_a}\right)^{3/2} \right) \frac{\Delta E}{E_0}\alpha_0, \\ dr_s &\approx \frac{1}{4}\left(l\frac{E_0}{E_a} + C_s \left(\frac{E_0}{E_a}\right)^{3/2} \right) \alpha_0^3, \\ dr_d &\approx \frac{0.73nm}{\sqrt{E_0}\sin\alpha_0}, \end{aligned} \tag{3.39}$$

where E_a is the potential of the extractor cathode, l is the field length, E_0 the starting kinetic energy of electrons and α_0 the start angle at the sample surface. C_c and C_s are the chromatic and spherical aberration coefficients, respectively.

Figure 3.22 (a) represents the calculation of resolution diameters, dr_{tot}, for photoelectrons with kinetic energy of 100 eV for three different values of extraction voltage, E_a. The contribution of chromatic and spherical aberrations as a function of contrast aperture are shown in an energy-filtered PEEM. The contribution of electron diffraction is shown as well. Two experimental values (red stars) obtained with 12 kV extractor voltage were added [89].

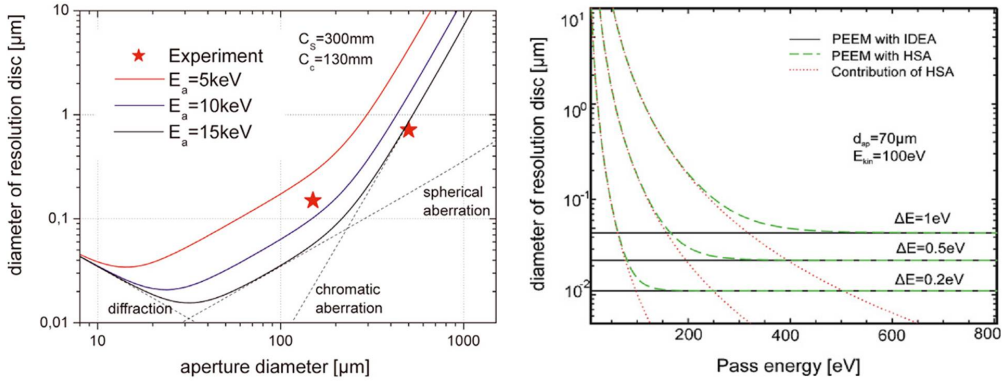

Figure 3.22: (a) Calculation of the contribution of chromatic and spherical aberrations and of electron diffraction in an energy-filtered PEEM as a function of the contrast aperture in the microscope focal plane and for three values of the extraction voltage. Electrons have a kinetic energy of 100 eV. Stars correspond to experimental values obtained with an extraction voltage of 12 kV. (b) Calculated ultimate resolution of the *NanoESCA* using the double hemispherical analyser, compared to a version with a single HSA [89].

The lateral resolution is also limited by the aberrations of the coupling lens in front of and behind the double hemispherical analyser (IDEA) (see figure 3.16).The analyser itself does not limit the lateral resolution since the second HSA always compensates for the dispersions of the first one (details can be found in [88] [89]). Comparative calculations of the ultimate resolution of the

NanoESCA are shown in figure 3.22. We can easily see that the resolution of the instrument is independent of the pass energy and it thus becomes attractive to work at low pass energies which is necessary for high general transmission and good energy resolution (as discussed below).

Energy resolution Slits are located at the entrance and exit of each HSA of the IDEA and their sizes are adjustable. The slits at the entrance and exit of the first hemispherical analyser (HSA), of the IDEA system (see figure 3.16), determine the energy resolution, ΔE of the *NanoESCA*, which is given by:

$$\Delta E = E_{pass} \cdot \left(\frac{w_1 + w_2}{2R} + \alpha^2 \right), \tag{3.40}$$

where E_{pass} is the pass energy of the first analyser, w_1 and w_2 are the widths of its entrance and exit slits. R is the mean path radius of the hemispherical analyser and α^2 is the spherical aberration of the analyser's dispersion.

One can easily understand from equation 3.40 that low pass energies and/or small slit widths lead to higher energy resolutions. In that case the α^2 term needs to be small enough for the best resolution. This is guaranteed thanks to the aberration compensation ensured by the unique configuration of the IDEA system with the presence of a second hemispherical analyser [89].

Applications with *NanoESCA*: complementarity The strength of *NanoESCA* lies in the combination of high energy resolution, enabling the separation of chemical core-level shifts (106 meV energy resolution was reported [88]) and high lateral resolution in both emission threshold and core-level imaging.

A spatial resolution of 500 nm has been shown for XPS imaging using an X-ray laboratory source [93]. A spatial resolution of 40 nm for work function measurements using VUV laboratory source [92] was also proved. Besides its high spatial resolution, *NanoESCA* provides an absolute and reliable quality for work function measurement under UHV conditions with a diversity of surface treatment possibilities.

The complementarity between its different imaging modes (threshold and core-level energies) makes it possible to correlate electronic and chemical properties, providing an entire and consistent picture of a well-defined area on the sample surface [90].

3.2.4 Practical aspects of XPEEM experiments: sample handling

In this section, we detail practical aspects related to sample handling in XPEEM experiments.

3.2.4.1 Dimensional constraints

The design of the sample holder of the *NanoESCA* imposes some constraints on the dimensions of the sample studied. The sample holder is formed by a Molybdenum square-shaped piece with a circular hole specially designed for positioning the sample (see figure 3.23).

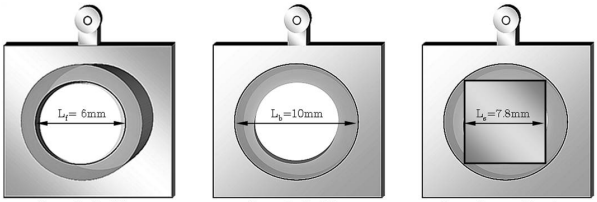

Figure 3.23: A schematic design of the *NanoESCA* sample holder showing the dimension of the circular hole where the sample is introduced. The front and back side openings of the positioning hole dictates the dimensions of the sample.

The dimensions of the circular hole are different on its front and back sides. The front side defines the part of the sample to be exposed to the photon beam in the analysis chamber, while the back side essentially dictates the dimension limitations of the sample. The sample must be square shaped with a 7.8 mm lateral dimension. A good control of these dimensions is required in order to damaging the sample while introducing it into the sample holder.

3.2.4.2 Sample positioning: flatness and focus

A circular metallic spring is used to maintain the sample fixed to the sample holder. The sample is sandwiched between the spring and the borders of the circular positioning hole on its front side.

However, after being fixed to the sample holder, the sample should not be tilted with respect to the horizontal plane of the circular positioning hole (see figure 3.24). In other words, the normal to the sample surface must be aligned with the optical axis of the PEEM column to ensure cylindrical symmetry of the accelerating field. Non-cylindrical symmetries will cause image distortions, i.e. the regulations of the focusing lens will not effect the whole image.

In order to ensure a flat horizontal positioning, the sample (fixed in the sample holder) is observed with an optical microscope and the focus is verified over the entire surface. The positions of the sample and the circular spring are still adjusted until the sample is horizontal. Afterwards, the sample holder-sample system is introduced, with care, into the *NanoESCA* so as to avoid any rough manipulation that may displace the position of the sample.

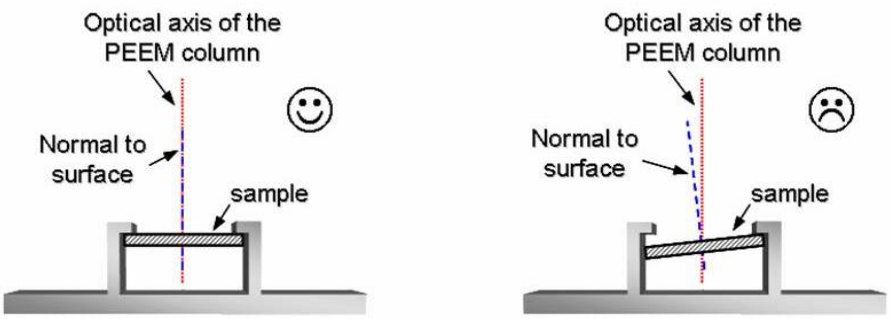

Figure 3.24: A representation of the sample positioning and flatness issues.

3.2.4.3 Sample-related effects in XPEEM imaging

It should be kept in mind that, in PEEM, the sample is part of the electron-optical system. However, a realistic surface always has a topography determined by micro- or nano- features, which leads to the formation of electrostatic microfields. This subsequently affects the trajectory of electrons as drawn in figure 3.25.

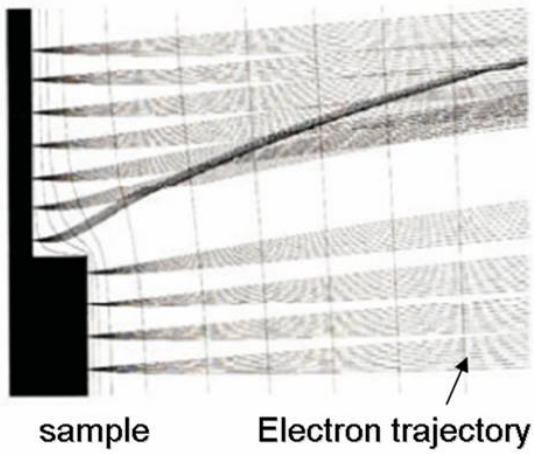

Figure 3.25: Resolution deterioration in the vicinity of a geometric step edge. The electron trajectory distribution is distorted by the effect of the formation of electrostatic microfields. Consequently, the spatial resolution of acquired images is deteriorated [86].

As a consequence, the image will be distorted and the contrast pattern will be smeared out. Therefore, it is very important to avoid topographical accidents on the surface in order to avoid such effects on the quality of the acquired images [86].

3.3 Lift mode KFM and XPEEM (*NanoESCA*): assessment and comparison

3.3.1 Advantages and constraints

Both KFM and XPEEM methods provide an access to the local work function value of a given sample. In the following table 4.2, we summarize and compare the properties of these methods for work function measurements and point out their complementarity.

3.3.2 Conclusion: further improvements

The comparison of the lift mode KFM and XPEEM techniques for work function measurements reveals some basic aspects that should be addressed either for each technique or for both combined or correlated. Regarding the summary table 4.2, we can classify these aspects as following.

Experimental effects on KFM measurements Since KFM is an inherently relative technique, different experimental parameters and elements (tip, LH, environment) can considerably alter the measurements. It is very important to understand the impact of these parameters on KFM measurements under ambient conditions. In addition, the tip's work function must be calibrated to evaluate the stability of the acquired measurements.

Improvement of the spatial resolution of CPD maps The flexibility of the KFM set-up makes it possible to perform some instrumental adjustments, either of the operational mode or the geometry and shape of KFM tips, which offers several possibilities for improving the CPD measurements. Such an improvement can enable further investigations of the sub-nanometric electric properties of interesting samples.

Coupling KFM and XPEEM The ultimate and most important aspect of our concern is to be able to define a characterization protocol coupling these two techniques for a study of the same sample and particularly the same zone of interest on its surface. The correlation and complementarity, offered by this kind of application, are fundamental for drawing a complete picture of sample properties (topography, work function and chemical composition).

All these points form the main axis of the following parts of this work. In chapter 4, we shall further develop the KFM-related aspects, and chapter 5 will be devoted to the application of a coupling protocol to investigate the properties of non-homogeneous few layer graphene epitaxially grown on SiC(0001) substrate.

KFM (air)	**XPEEM (NanoESCA)**
Provided information	
Direct mapping of the CPD variations over the whole scanned zone	No direct mapping - localized measurement of the work function at defined positions of the imaged zone (local spectra)
Reliability	
Not reliable (contact potential difference, relative to the WF of the tip)	Absolute and direct WF value (knowing the WF of the analyser)
Ambient conditions: surface adsorbents - contamination - humidity	UHV: non humidity, *in situ* surface treatments
Spatial resolution (work function)	
∼40 - 60 nm. Depends on the LH distance and environment conditions (RH%)	∼40 nm with VUV photon source. ∼ 150 - 200 nm with X-ray sources
Can be improved with different operation mode (gradient mode)	Depends on the intensity of X-ray photon source
Instrumental conditions	
Large sample dimensions (∼ 200 mm) - quasi free positioning over the sample (motorized sample holder)- maximum scan size ∼ 100 μm^2	Constraint on the size of the sample (∼ 7.8 mm square) - variable field of view (5 - 650 μm)
No easy surface treatments - heating with external tools - transfer in air conditions (re-contamination)	Preparation chamber: Ion sputtering (Ar+), resistive heating - surface treatment and transfer under UHV
Accessibility: installation and handling	
Relatively simple to control and install samples and tips	More complex and sophisticated protocol - control of multiple microscope parameters
Complementary information	
Acquisition of the surface topography map	Correlation with local chemical properties (spectromicroscopy and micro-XPS)

Table 3.1: A summary of the comparable properties of the KFM (lift mode) and XPEEM (NanoESCA) techniques for the measurement of the local work function.

Chapter 4

Analysis of experimental effects in KFM measurements

Dans ce chapitre nous abordons les différents aspects liés à la mesure du travail de sortie local par KFM et qui ont été listés dans la conclusion du chapitre 3. En effet, KFM opérant en mode lift permet d'imager les variations latérales de la différence de potentiel de contacte (CPD) d'une manière relativement simple. Par contre, les mesures réalisées sous atmosphère ambiente sont sujets à des effets de l'environnement et des conditions expérimentales de la mesure. Ceci peut altérer la mesure du travail de sortie local et compliquer l'analyse des résultats obtenus.

Pour cela nous élucidons dans un premier temps les effets des différents paramètres expérimentaux intervenants dans la mesure du CPD sous air et sous atmosphère controlée. Ensuite, nous discutons la possibilité d'amélioration de la résolution spatiale de la mesure KFM sous air grâce à la mise en oeuvre, sur le microscope commercial, d'un mode combiné AFM-KFM basé sur l'acquisition simultanée des mesures KFM et de la topographie de surface. Finallement, nous analysons la stabilité de la mesure KFM sous atmosphère controlée en étudiant différents échantillons de réference utilisés pour la calibration de cette mesure.

In this chapter the KFM-related aspects listed in the conclusion of chapter 3 will be addressed. In fact, lift-mode KFM has the capacity to illustrate CPD[1] variation over a sample's surface with a relatively simple protocol. Operating within an ambient environment, lift-mode KFM undergoes several experimental effects which can complicate measurements and make them dependent on environmental and instrumental conditions.

[1]CPD: Contact Potential Difference.

In order to get a thorough understanding of these effects we shall first elucidate the effect of experimental parameters on CPD measurements. In the second part we will investigate the possibility of improving the spatial resolution and sensitivity of the electrical measurements. Finally we will address the stability of the work function measurement by investigating several reference samples that could be used to calibrate the KFM measurements.

4.1 Effects of experimental parameters on the CPD measurements in lift mode

Even though KFM technique is based on the detection of the electrical force (F_{el}) between the tip and the sample as described by equation 3.22, it actually concerns a voltage measurement. As discussed in chapter 3, the nullification of the component force, F_{ω_e}, at the frequency of the electrical driving signal results in monitoring the V_{dc} value related to the CPD between the tip and the sample (equations 3.28 and 3.29). Here, the electrical signal was continuously applied to the tip, thus V_{dc} is given by[2]:

$$V_{dc} = V_{cdp} = \frac{\phi_{tip} - \phi_{sample}}{|e|}. \tag{4.1}$$

Therefore, from this starting point, the V_{dc} value is expected to be only dependent on the work function difference between the tip and the sample which emphasizes the role of surface quality in the intended KFM measurements. Dependency on the tip-sample distance does not seem to be a clear element, however, as shown by the above expression. Nevertheless, experimental results show reproducible tendencies which question this apparent relationship.

4.1.1 Experimental protocol

Instrumental conditions Measurements were carried out in the KFM lift mode. PtIr coated silicon tips (from Nanosensors) with a nominal resonance frequency $\sim$ 70 kHz and a stiffness $\sim$ 3 N.m^{-1} were used. The test samples are formed by metallic layers of different thicknesses (Al (650 nm), Pt (200 nm), Ru (100 nm), Au (200 nm), Cu(400 nm) and W (300 nm)) deposited by PVD on a 100 nm SiO_2 layer grown over a bulk silicon substrate. The control of the experimental environment was ensured by controlling the relative humidity level (RH%) in the home made glove box externally added to the microscope (see figure 3.9).

Sample and tip preparations We used FIB milling technique to make a cross mark on each sample which served as a referential point to define the coordinates of different positions of interest studied for each case (see figure 4.1).

[2] e = -1.60219 $\times$ 10^{-19} C.

No additional surface treatment protocols or cleaning methods were used. Tips and samples were continuously stocked in dry, reduced-humidity, conditions.

Measurement protocol In the following experiments, the KFM lift mode was used in a spectroscopic way. The tip was fixed over a defined position on the surface of the sample thanks to the referential cross mark and the scanning was disabled (see figure 4.1). The V_{dc} value was measured by systematically varying different experimental parameters: LH, RH% and V_{ac}.

Reproductibleness To evaluate the reproductibleness of the V_{dc} value measured in this spectroscopic method, measurements were reproduced at eight different positions defined for each sample with respect to the referential cross mark as represented on figure 4.1. The reproductibleness was found to be ~ 30 mV.

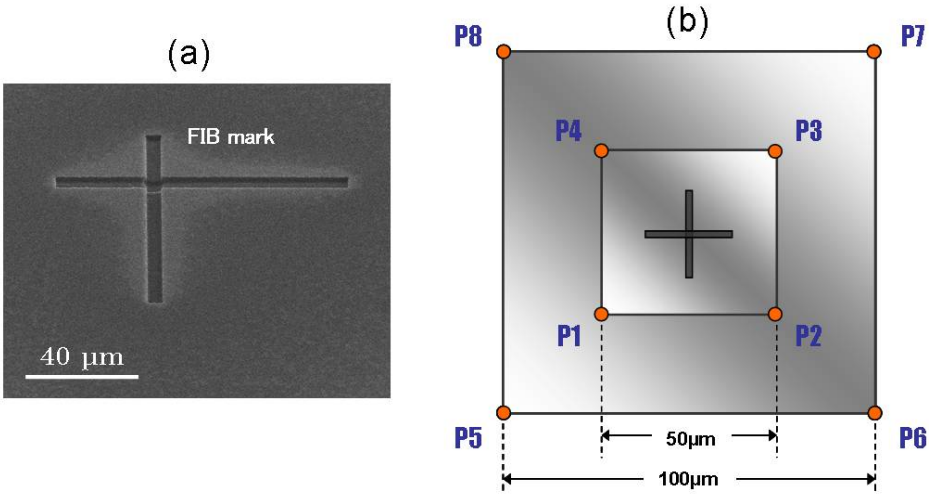

Figure 4.1: (a) SEM image of the FIB cross mark on the surface of the test samples. (b) A schematic representation of all positions of interest where spectroscopic measurements are done in each case.

4.1.2 Effect of the tip-sample separation: the lift Height

In KFM lift mode operation, the lift height (LH) distance is an adjustable parameter. However, according to the expression 3.26, the V_{dc} value measured in KFM for a given position on the surface of a homogeneous sample is supposed to be constant and dependent on the work function difference between the tip and the sample, and thus on the properties of the surface.

4.1.2.1 Experimental observations

The V_{dc} values, spectroscopically measured for different metallic samples by varying the lift height (LH) parameter between 10 and 900 nm, are presented in figure 4.2. The bias voltage was applied to the tip. The statistical deviations of each value for different samples were found to vary in the range of 20-25 mV. Although, the error bars at each point on the graph were omitted for clarity.

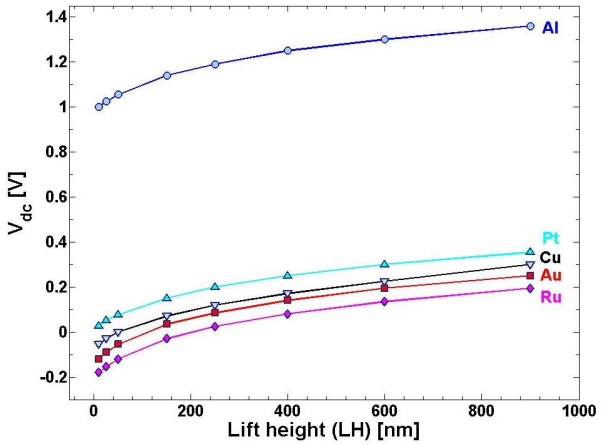

Figure 4.2: The V_{dc} value measured at different lift heights (10-900 nm) for all metallic layers samples. Similar trends of variation are observed for all cases. The difference between the curves matches well with the difference between the work functions of each material.

Measurements present similar variations of the V_{dc} value with respect to the tip-sample separation distance[3]. Contrary to what is expected from expression 4.1, the V_{dc} actually varies with the tip-sample distance even for measurement over one fixed position on the sample surface.

4.1.2.2 A recurrent behavior

These observations were previously reported for different samples such as semiconductors [94] [95] [96], organic structures [97] [98] and oxides with embedded charges [99] [100]. In all these cases, the presence of additional fixed charges or multipoles on the sample's surface are due to implemented charges [100] [101] [99] [12] [96], organic molecular dipoles [97] or accumulation charges in semiconductor samples [95]. This results in an additional Coulombic force that acts between the tip and the sample.

4.1.2.3 Metallic samples: a work function anisotropy effect?

Despite the fact that no additional charges are expected in our case (samples are formed by metallic layers with no organic structures grafted to their surfaces) the CPD value measured spectroscopically changes with the tip-sample distance.

[3]The separation distance in the lift mode is given by the lift height distance in the second lift trace added to the D position of the tip with respect to the sample in the first topography trace

Interestingly, a typical KFM experiment performed under UHV conditions with a symmetrical metallic configuration (where the tip and sample were coated with gold layers [102]) shows that the CPD value presents similar variations with tip-sample distance. This is despite that the CPD value is supposed to be null since, theoretically, no work function difference is expected between the tip and sample in this case.

In 1992, N. Burnham *et al.* questioned the origin of attractive forces observed between a diamond tip and a graphite surface without discrete charges, magnetic or capillarity forces. Authors first introduced the anisotropy of the local work function (see section 2.2.4) as a source of long-range attractive forces between the tip and sample. Local work function anisotropy can be induced by several perturbations of the sample surface such as changes in crystallographic orientations [10], the presence of surface steps or defects, uneven distribution of adsorbate or surface preparation defects. They demonstrated that the change in work function under the tip gives rise to a local 'patch charge' density thus responsible for the observed attractive forces. However, they assumed the effect of the 'patch charges' to be weak at large distances and that the neutrality of the total system must be maintained [17].

4.1.2.4 Modeling the interaction

The 'patch charges' density, as introduced by Burnham *et al.*, seems to provide an acceptable reason for our observations, especially since neither the presence of surface adsorbate nor the variation of the crystallographic orientation on the surface of our samples are excluded [68] [10].

Analytical approach Therefore, we have sought in our investigation a general analytical method to express the effect of the supposed additional contribution from the 'patch charge' density. We generalized the expression of the electrical force acting between the tip and the sample in KFM experiments:

$$F_{ele} = \frac{1}{2}\frac{\partial C_{ts}}{\partial z}V_{ts}^2 + Q_{tip}E_s \tag{4.2}$$

where V_{ts} is the total potential difference between the tip and the sample as expressed by equation 3.21 and C_{ts} is the tip-sample mutual capacitance. The additional term $Q_{tip}E_s$ expresses the Coulomb force acting on the tip, where E_s is the electrostatic field induced by the additional surface charge distribution (patch charges density) and Q_{tip} is the capacitive charge distribution on the tip:

$$Q_{tip} = C_{ts}V_{ts}. \tag{4.3}$$

By introducing the expressions of Q_{tip} and V_{ts} in equation 4.2, the ω_e component of the electrical force is given by:

$$F_{\omega_e} = \frac{1}{2}\frac{\partial C_{ts}}{\partial z}\left(V_{cpd} - V_{dc}\right)V_{ac} + C_{ts}V_{ac}E_s\cdot \tag{4.4}$$

Then, the application of the KFM measurement principle, $F_{\omega_e} = 0$ provides the expression of V_{dc}:

$$V_{dc} = V_{cpd} + \mathrm{g}_{ts}(z)E_s \tag{4.5}$$

where $\mathrm{g}_{ts}(z)$ is a geometric factor depending on the mutual capacitance and the separation distance between the tip and the sample:

$$\mathrm{g}_{ts}(z) = 2\frac{C_{ts}}{\partial C_{ts}/\partial z}\cdot \tag{4.6}$$

A geometric and distance dependency According to equation 4.5, the V_{dc} value measured in KFM is therefore dependent on:

- The variation of the mutual tip-sample capacitance, C_{ts}, defined by the geometric factor $\mathrm{g}_{ts}(z)$, with respect to the tip-sample, z, distance.
- The z dependency of the electric field, E_s, induced by the surface Coulomb contribution.

These two facts are actually linked by the variation of the effective area of the electrostatic interaction between the tip and the sample with respect to their separation distance.

This fact has been studied intensively by different groups who have developed several models providing analytical expressions for the mutual capacitance, C_{ts} between the tip and the sample [71] [103] [73] [70]. The contributions of the different geometric parts of the tip have been shown to change with respect to the distance between the tip and the sample. Jacobs *et al.* demonstrated that the observed potential in KFM measurements is a locally weighed average over all surrounding potentials present on the surface, where the capacitive coupling of tip parts (apex, cone, cantilever) with the sample vary as a function of the tip-sample distance [74].

Fitting experimental results We used the V_{dc} expression from equation 4.5 to fit the experimental measurements obtained for all samples. The expression of geometric factor $\mathrm{g}_{ts}(z)$ was derived from the expression of the electrical force determined by the analytical model of Hudlet *et al.*, where the tip was modeled by a spherical apex and a truncated cone [70].

The tip radius was set to $R = 30$ nm, the cone height $H = 25$ μm and the tip opening angle $\theta = 20°$. Figure 4.3 shows the fit curves of the model equation 4.5 (dashed curves) to experimental V_{dc} values (colored motives) for all samples. V_{cpd} and E_s were set as fit parameters. The model therefore corresponds well

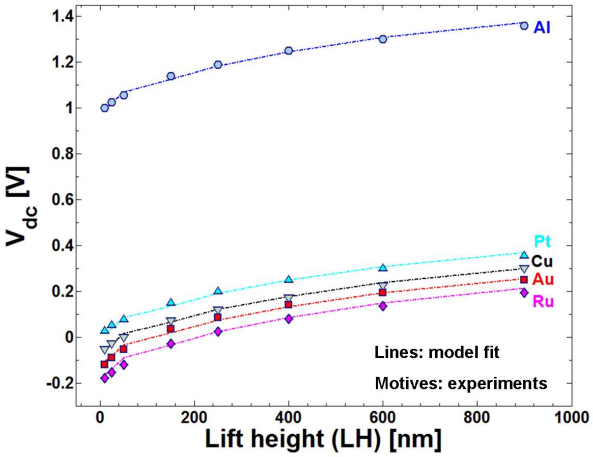

Figure 4.3: The fit (dashed line) of the equation 4.5 to the experimental V_{dc} values measured for the Al sample. The fit corresponds well with experimental results especially for high LH values.

with the experimental results.

Fit results are summarized in table 4.1. An electronic surface charge distribution $\sigma_s = \varepsilon_0 E_s$ was calculated for each sample as depicted in the following table. The surface electronic densities were found in the same order of magnitude as the 'patch charge' density previously reported by Burnham *et al.* for a graphite sample.

Table 4.1: The first (V_{cpd}) and second (E_s) fit parameters obtained from equation 4.5 applied to all samples. The electronic charge density σ_s is extracted from the values of electric field E_s found for each sample.

sample	V_{cpd} (V)	E_s (V.m^{-1})	σ_s (e^-.cm^{-2})
Al	1.0059 ± 0.015	1.4475 ± 0.21×10^5	8 ± 1.19×10^8
Pt	0.0316 ± 0.031	1.3153 ± 0.17×10^5	7.27 ± 0.96×10^8
Cu	- 0.0519 ± 0.010	1.3843 ± 0.15×10^5	7.65 ± 0.85×10^8
Au	- 0.1082 ± 0.018	1.4836 ± 0.26×10^5	8.2 ± 1.43×10^8
Ru	- 0.1722 ± 0.034	1.5098 ± 0.24×10^5	8.35 ± 1.36×10^8

The V_{cpd} values In order to test the validity of our fit results, we extracted the work function for each sample from the obtained V_{cpd} values by considering the work function of the PtIr tip as a reference value as given by [68]: $\phi_{tip} \approx 5.1$ eV and using equation 3.27. Then we compared our results to previously reported work function values obtained by different techniques (see table 2.1) as presented in figure 4.4. The large dispersion of reported values stem from the difference of measurement techniques and experimental conditions. However, actual results for Al, Pt and Au are in an acceptable range compared to previously reported

data, while the Cu and Ru work functions determined here present higher values. These differences can originate from either the quality of the sample surface (contamination, defects) or from the measurement conditions.

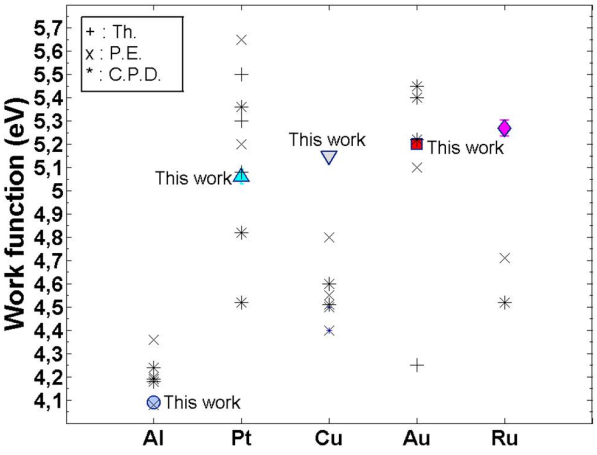

Figure 4.4: Work function values calculated from V_{cpd} obtained from the fit results in this work (colored motives). Results are compared to data reported from other studies as the work function has been measured by different techniques: Th. (thermoionic emission), P.E. (photo emission) and CPD (contact potential difference).

Comments Therefore, using this approach, the local work function anisotropy can provide an acceptable interpretation of the V_{dc} variations experimentally observed in absence of trapped charges, organic as well as molecular dipoles on the surface of the studied sample. However, the fit model (figure 4.3) presents less agreement for small tip-sample distances (LH<100 nm) than for higher distances. This likely due to the effect of the image charge interaction which arises at small distances. A good estimation of this effect requires a numerical treatment of an infinite number of charge images of both the tip and the sample [71], which has been neglected in our investigation.

However, it worth noting that the current approach that we described in this section is general. In other words, it can be applied to evaluate the surface charge density even in presence of organic structures or different sources of surface charges. The electric field (E_s), issued from a surface Coulombic contribution to the electrostatic interaction with the tip, can be generalized (see equation 4.2) and the expression of V_{dc} (equation 4.5) can be used to describe the variations of the CPD measurement in KFM experiments for different cases.

Besides analytical models and interpretations of KFM results, there are many numerical simulations of the electrostatic field between the tip and the sample based on the method of images and the solution of Laplace's equation. Even though these methods are rather difficult to handle, they provide a very important understanding of the tip-sample electrostatic interactions. Interested readers can follow the works of Shen, Barnett and Pinsky [104] [105] for numerical modelisation with boundary integral equations or the works by Belaidi [106],

Mesa, Moňivas and Saenz [107] [108] and Boer [109] for tip-sample modelisation using the image charge method.

4.1.3 Effect of the tip shape damages

PtIr-coated Si tips are often used in Kelvin Force Microscopy experiments. The work function difference between the tip and the sample provided by KFM measurements is directly dependent on the quality of the tip. In fact, the evolution of the tip properties is usually assumed to be very small during experiments. Thus electrical changes are conventionally considered as caused by the sample's changing properties, but this assumption is questioned here.

Experimental observations We systematically followed the evolution of the tip shape before and after a set of experiments using a scanning electronic microscope (SEM). As shown in figure 4.5, damaged tips induce radical and irreversible changes of the V_{dc} curves measured as a function of LH. The trends are inversed with respect to the starting behavior and measured V_{dc} values become altered. This phenomenon was systematically observed for various silicon tips with PtIr coating (two different tips in figure 4.5).

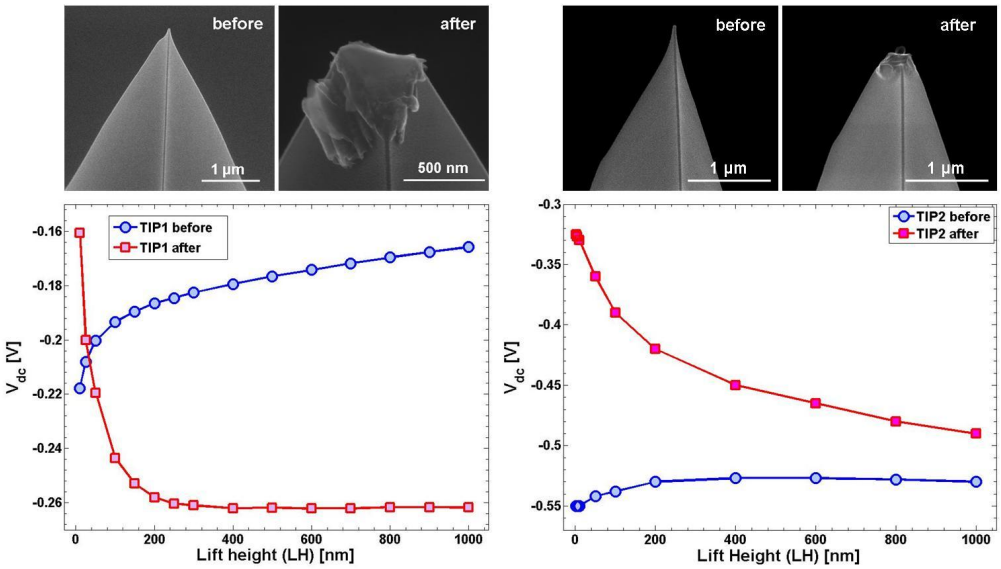

Figure 4.5: SEM images of two different tips (tip 1 on the left and tip 2 on the right) taken before and after damaging. Measurements were done over a ruthenium (Ru) sample in air environment. The plots of the V_{dc} versus the lift height show an inverted behavior when the tip is damaged, which can be used as indicator of the tip state evolution.

The wearing of tips is observed either after a large number of measurements, when high amplitude modulation signals ($V_{ac} > 5$ V) were used, when measurements were done at very small lift heights (LH $\sim$ 1-2 nm), or after contacts with

large topographic features on the sample surface. Even though our experiments were done by operating the KFM lift mode in a spectroscopic way, all these causes may be involved while acquiring CPD images by scanning sample surfaces and artifacts can seriously alter obtained results.

Interpretations According to the expression 4.5, the V_{dc} value monitored in the plots of figure 4.5 is closely dependent on both the changes of the work function either of the tip or the sample and on the changes in the geometry of the tip-sample capacitance (C_{ts}) which can be considerably modified with the tip shape damages.

Work function modifications When the tip is damaged, the PtIr coating covering its parts can be removed or altered which changes its work function and subsequently the CPD value measured in experiments. In addition, if the tip damages were induced by aggressive contacts with topographic features on the surface, this can result in a contamination of the sample surface under study and a modification of the CPD value. However, if the used tip has been initially calibrated to a known referential sample, it becomes possible to quantify and evaluate the changes of its work function after it has been damaged.

Tip-sample capacitive changes The modification of the damaged tip shape leads to a direct change in the geometry of the tip-sample capacitance, C_{ts}. If the surface under study is assumed to be a plane, the effects of the tip damages on the geometry of the tip are however arbitrary (see different tips on figure 4.5), which makes the interpretation of the C_{ts} changes very complicated. We can therefore not pretend to provide an exhaustive analysis of this phenomena. However, the changing of V_{dc} curves with the tip damages is real and has been recurrently observed.

A simple stability indicator Consequently, these observations could be used as a simple indicator that helps evaluate the stability of a used tip after scanning experiments. We therefore suggest that V_{dc} could be measured at different lift heights before and after any KFM scanning experiment at a defined position of a reference sample. If the measured curves (before and after) present similar trends , then one can conclude that no damages have affected the tip and no artifacts have been induced during the imaging process. This relatively simple protocol can provide fast information concerning the tip quality after scanning the surface, and better reliability of obtained results can be evaluated.

4.1.4 Effect of the environment: relative humidity

The adsorption of atoms and molecules on the sample surface in KFM measurements under ambient conditions results in significant modifications of its work function [110] [10]. In fact, chemical bonding between the adsorbed atoms and

the surface can induce several electronic rearrangements. Moreover, if adsorbed molecules have their own dipole moment (ex: water molecules), they contribute to an additional electric contribution effect at the sample surface [3]. Studies have showed that adsorbents can increase the CPD value measured in KFM between 20 meV and 50 meV [111] [10].

Protocol Thus in order to investigate the effect of the environment, measurements were performed on different samples by varying the relative humidity level. The whole system (tip and sample) was kept in the glove box under continuous nitrogen flow (N_2) for approximately 14 hours. Samples were externally heated under N_2 controlled environment, for ∼1 hour at 120°C in order to desorb residual water molecules. However, the tip used in these experiments was only stored in dry environment but no additional treatment was performed. Finally samples were transferred into the SAS compartment of the glove box and were cooled down under N_2 flow for about 10 minutes before starting measurements.

Experimental observations We have changed the RH% rate from 2% to 40%, with 2% uncertainity, by adjusting the N_2 flow introduced to the glove box. V_{dc} was acquired at different lift heights going from 10 nm to 900 nm. The electrical driving signal was applied to the tip with an amplitude $V_{ac} = 2.5$ V. Results obtained for different samples (Pt, Au and Al) are shown on figure 4.6 for different RH% values (0.5%, 10% and 40%).

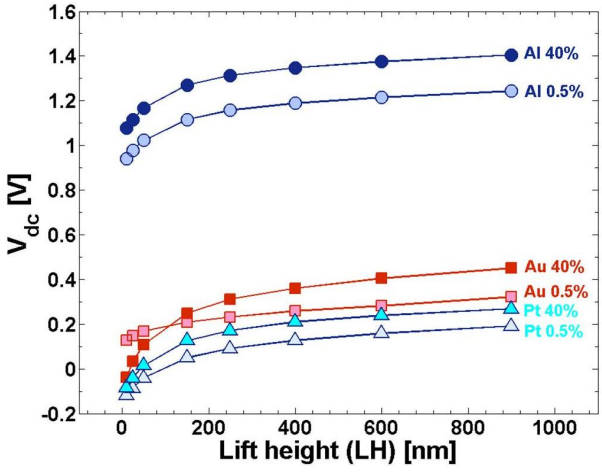

Figure 4.6: V_{dc} of Al, Pt, Au measured at different relative humidity (RH) levels. The variations with lift height distance are reproduced. Shifts toward higher V_{dc} values are induced by increasing RH%, especially at high LH distances where the Coulombic effects from the surface are rather weak.

Interpretation In order to understand the effect of the RH level, we first consider the variation of the V_{dc} measurements at high LH values. In fact, at a large separation distance (LH > 150 nm), the effect of the additional Coulombic surface contribution (described in section 4.1.2) becomes weak and hence could be neglected. Thus the dependency of the V_{dc} on the RH% variation may be

totally ascribed to the variation in the electronic properties of the water film adsorbed on the surface when RH% changes.

It is worth noting that the V_{dc} measurements are not absolute and actually depend on the work function of the tip. However, it has been showed recently by Liscio *et al.* that the impact of the relative humidity on the work function of the tip is assumed to be poor. This is due to the very small dimensions of the tip compared to the sample and the unchanged mechanical properties of the tip's vibration when changing the RH% rate [98].

Therefore, the variations of V_{dc} observed in figure 4.6 (at large LH distances) suggest a decrease of the work function of the sample (see equation 4.1). A simple, first approximated, model considering a regular arrangement of molecular dipoles in the adsorbed water layers can explain these observations [3]. The decreasing trend of the sample's work function suggests that the water dipole moments are pointing toward the sample surface. Positive charges are exposed on the interface with ambient air whereas the electron-rich oxygen atoms are close to the sample surface.

Nevertheless, when the tip-sample distance becomes smaller (LH $<$ 150 nm), the V_{dc} variations with RH% present different trends, depending on the nature of the sample. Despite the fact that the work function dependency on the RH% rate can be explained by the nature of the electronic density on the metal surface, it still is difficult to interpret actual results at small distances, since contamination layers prevent the samples surfaces from being considered as ideal pure metals [112].

4.1.5 Effect of the set-up parameters

We have also investigated the effects of experimental setup parameters on the measured V_{dc} values (the electric driving signal V_{ac} and, the bandwidth of the feedback loop $B_{[Hz]}$ and the 'drive phase' parameter).

4.1.5.1 The amplitude of the electrical driving signal: V_{ac}

V_{dc} was measured[4] for Ru, Au, Pt and Cu samples by systematically varying the V_{ac} value in the range of 250 mV to 10 V. The electrical signal was applied to the tip. The RH level was maintained at 0% under the glove box (with 2% uncertainity) for a reduced humidity effect. We also chose to measure V_{dc} at a large LH distance (1 μm) in order to reduce the polarization of adsorbed water due to the charged tip. Figure 4.7 shows that, under the current experimental

[4]The actual results were obtained in a measurement campaign different than the one for all previous results. Thus, the measured V_{cpd} values presented here differ from previous values in section 4.1.2.1

conditions, the CPD values of all investigated samples experience very slight changes when V_{ac} has been varied. Observed V_{dc} changes are in the range of 10-15 mV and thus can be neglected.

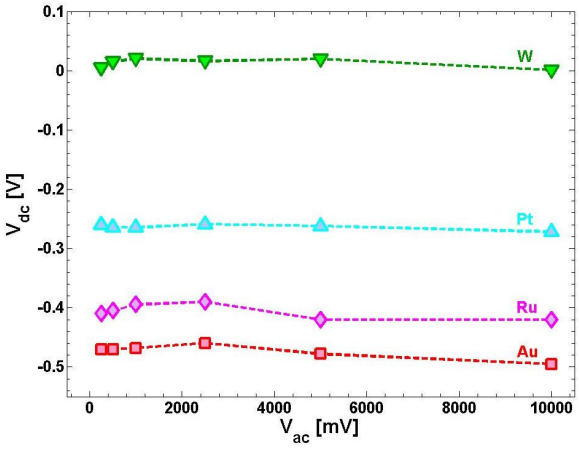

Figure 4.7: V_{dc} of Au, Ru, Pt and W measured for various V_{ac} values. Measurements are practically stable, small variations ($\sim$ 12 mV) were observed which is in the range of measurement sensitivity.

4.1.5.2 The feedback bandwidth: $B_{[Hz]}$

We measured the V_{dc} value for aluminum sample (Al) at different lift heights by changing the bandwidth of the KFM lift feedback loop $B_{[Hz]}$ between 50 Hz and 1500 Hz. Results are shown in figure 4.8. The V_{dc} - LH curves for different $B[Hz]$ values, show no changes and measurements remain practically constant. Actually no effect of changing the $B_{[}Hz]$ value is expected unless the feedback loop is turned on (i.e. the imaging mode is enabled). Since all measurements presented here were done spectroscopically (imaging mode disabled), then the present result is conform to expectations.

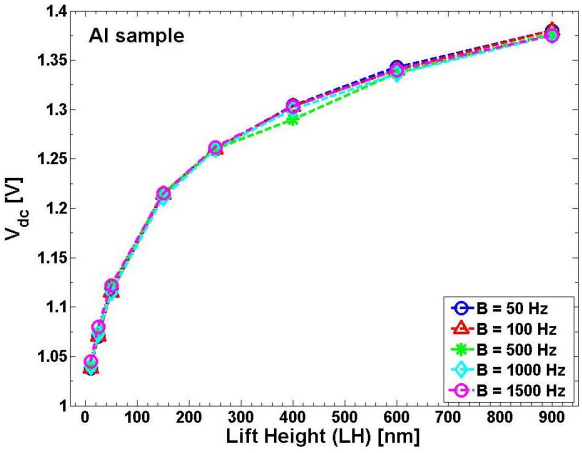

Figure 4.8: V_{dc} of Al sample for different values of the KFM feedback loop bandwidth $B_{[Hz]}$. No effect has been revealed in the V_{dc} value measured in KFM experiments.

4.1.5.3 The 'drive phase' parameter

In the present KFM lift mode setup, the so-called 'drive phase' is an additional parameter that has been integrated by Veeco instruments in the feedback loop. The role of this parameter is not clear, although it shows an important impact on the measurement procedure and results in considerable distortions of the V_{dc} values measured in this mode.

Previous studies [68] demonstrated that the work function of an aluminum sample estimated using the lift mode presents a change of about 0.7 eV when the value of the drive phase varied between -60° and +60°.In order to monitor the effect of this parameter on our measurements, the V_{cpd} value of a platinum sample was measured using PtIr coated tips while changing the 'drive phase' value between -90° and +90°. The amplitude of the cantilever oscillations at ω_e was simultaneously measured (see figure 4.9).

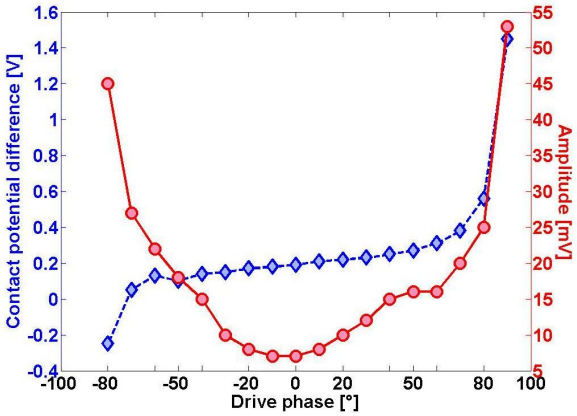

Figure 4.9: The amplitude of mechanical oscillations recorder for different 'drive phase' values while the KFM feedback loop is closed. Measurements performed with a PtIr tip over a platinum (Pt) surface. For large 'drive phase' values as discussed in the text, oscillations become no longer minimized. The CPD plotted for the same 'drive phase' values is rather stable for the range of minimized amplitude of oscillations.

The minimum value of the cantilever amplitude, measured for a drive phase ∼0°, indicates that the feedback loop is rather well adjusted and the cantilever oscillations are minimized. However, a large variation of the drive phase clearly affects the feedback behavior and the cantilever oscillations are no longer minimized. Therefore we found that for a drive phase changing between -15° and +15° the minimization of the amplitude of the cantilever oscillations is acceptable and the CPD value measured is relatively stable.

4.2 Improving the spatial resolution: a single scan method with multi-frequency excitation at higher eigenmodes

4.2.1 Introduction

In this section we shall address the second KFM-related aspect as discussed in the conclusion of chapter 3: the improvement of the spatial resolution of CPD maps. Despite its advantages of providing a direct imaging and semi-quantitative values of the work function difference between the tip and the sample, the KFM lift mode has several drawbacks. From a technical point of view, it is time consuming as two passes have to be performed for each image line. In addition, since the second lift trace is performed without topography feedback, drift or mechanical instabilities will change the tip-sample distance and may lead to different artifacts.

From a physical point of view, the lateral resolution of the lift mode is decreased as the lift height increases the effective tip-sample distance. Several developments and set-ups have been made in order to improve the spatial resolution of the KFM technique. However, it is worth noting that KFM measurements performed in UHV conditions using either the frequency modulation (FM) method or the amplitude modulation (AM) method inherently have a higher spatial resolution than KFM air measurements which are generally performed in the AM method [113] [114] [115].

Our goal here is to define a relatively simple and easy to install method capable of enhancing the spatial resolution of the CPD measurements under ambient conditions (air or N_2), using our available equipment.

4.2.1.1 Spatial resolution issues

In fact, all parts of the KFM probe, composed of the conducting cantilever, the conical shape and the tip apex, are involved in the electrical interaction with the sample. Each part of the probe is dominant for the total force in a particular range of tip-sample separation (figure 4.10). Only for very small distances, the force contribution from the end of the tip (apex) become relevant compared to the other two parts (cone, cantilever). However, a better spatial resolution is reached when the interaction is rather concentrated at the apex of the tip [116] [72] [73] [117] [118].

In conventional KFM lift mode operation, the tip cone, and not the apex, is rather responsible for the interaction with the sample since distances are relatively high (lift height effect). However, there are several ways to reduce the effects of the cone and the cantilever and consequently enhance the spatial resolution. One way consists of modifying the shape of the probe (cantilever

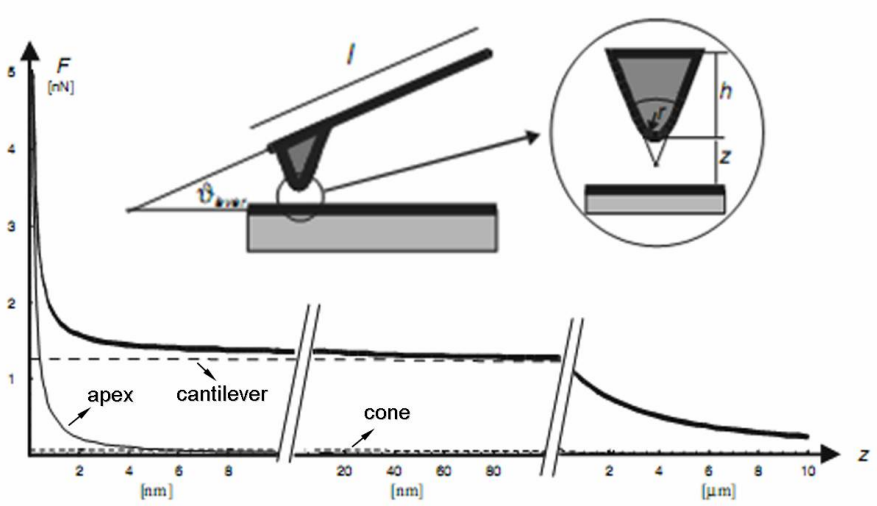

Figure 4.10: Electrostatic force versus tip-sample distance. The thick solid curve corresponds to the total electrostatic force, while the other three curves represent each of the contributions of the geometric parts of the tip. The force contribution from the tip apex become relevant only for very small distances ($\leq$ 5 nm) [72].

width, tip length, angle of tip cone and tip apex radius) [119]. In this context, Jacobs *et al.* demonstrated that the best are long and slender tips. Moreover, it has been suggested that the radius of the tip should be rather large [74]. Another study by Cockins *et al.* showed the interest of high-aspect ratio tip for electrostatic measurements [120].

Another way to reduce the effects of the cantilever and the cone is to study the electrostatic interaction by measuring the force gradient instead of the force. In the force gradient, both the cantilever and cone components are essentially 'derived away' leaving a predominant effect of the tip-apex in the electrostatic interaction with the surface. Higher spatial resolution could thus be reached [73] [72] [116].

4.2.1.2 Existing methods for enhanced spatial resolution in air environment

In 2002, Girard *et al.* [116] demonstrated a modified KFM lift mode scheme to measure the CPD using the force gradient signal. This method is based on a double scan step (similar to the lift mode). However, in the second step, the cantilever is driven with a double excitation scheme, mechanically at its fundamental resonance frequency (ω_0) and electrically at a smaller frequency ($\omega_e < \omega_0$). Being far from the surface, only long-range electrostatic forces are acting on the cantilever. The variation of the resonance frequency of the mechanical and electrical cantilever oscillations is therefore induced by the

time-varying electrostatic interaction at ω_e.

Thus the authors proposed two operational methods: the so-called Electric Force Gradient Microscopy (EFGM) and Kelvin Force Gradient Microscopy (KFGM). In EFGM, the phase of electrical oscillations (at ω_e) is simply monitored, and the phase contrast changes are induced by the variation of the force gradient. No quantification of the contact potential difference is possible in this case. However, in the KFGM method, besides being tracked, the variations of the phase of electrical oscillations (at ω_e) are nullified thanks to a feedback loop generating a V_{dc} signal equal to the contact potential difference (CPD). Thus in this case, the CPD variations are measurable and are proportional to the force gradient.

A similar principle was proposed by Colchero *et al.* [73]. However, this method still makes use of the lift height parameter, and small tip-sample distances are difficult to attempt since no topography feedback is operational in the lift trace. Moreover, tip collisions with the surface form a considerable risk which must be taken into account in this case. Since the frequency of the electrical driving signal is small, this method suffers from low sensitivity problems.

Very recently, Ding *et al.* [118] suggested a similar modification of the double scan lift mode but with increased sensitivity using higher eigenmode frequencies to electrically drive the cantilever in the second trace. In this method the variation of the electrical oscillation amplitude in the second trace is monitored instead of being nullified. These variations are dependent, however, on the gradient of the electrostatic interaction. Thus a better spatial resolution of 10-15 nm has been proved for imaging ZnS on Si substrate with this method compared to a 100-200 nm with conventional KFM lift mode measurements on the same area, as reported by the authors [118]. Although this method enhances spatial resolution, the double scan scheme results in slow time imaging, and direct CPD measurements are not yet possible with this method.

In order to achieve a fully parallel characterization of the surface topography and electrostatic properties (charge patterns, CPD), additional double excitation methods have been introduced in the past six years. The atomic force microscope operates in a conventional AM- tapping mode under air conditions for topography measurements while a second small electrical modulation signal is simultaneously applied to the cantilever. Different methods have been suggested in which the frequency of the additional electrical modulation is either set to a small value with respect to the resonance frequency [117] [72], or to a higher flexural eigenmode [121] [122]. Electrostatic imaging could be performed either in AM or FM operations.

It is worth noting that the simultaneous excitations scheme at higher flexural

eigenmodes has been used in different setups, especially for biological applications. Improved sensitivity and spatial resolutions have been demonstrated [123]. Interested readers can follow the works by Stark, Naujoks, Stemmer and Ziegler [124] [125] [121], by Lidon, Garcia and Colchero [122], by Martinez and Patil [126] and Proksch [123]. Theoretical studies can also be found by Lozano and Garcia [127].

4.2.2 Presentation of our method

4.2.2.1 The idea

The basic idea in our investigation is based on the resonant multifrequency electrostatic microscopy, as introduced by Stark *et al.* [128]. The microscope is set to a conventional tapping mode operation, where the cantilever is mechanically driven at its fundamental resonance mode (ω_0) as topographic feedback is performed. At the same time, an additional electrical modulation is applied to the cantilever at the second flexural eigenmode (ω_1), where electrical imaging is performed. We call this method the single scan Multi-Frequency EFM (MF-EFM).

4.2.2.2 The physical principle

By applying the modulated bias voltage $V_{bias} = V_{dc} + V_{ac}\sin(\omega_1 t)$ to the cantilever, the total electrostatic force between the tip and the sample is given by:

$$F_{el} = \frac{1}{2}\frac{\partial C_{ts}}{\partial z}\left(V_{cpd} - V_{dc} + V_{ac}\sin(\omega_1 t)\right)^2 \tag{4.7}$$

where, ω_1 corresponds to the frequency of the electrical excitation which is set to the second flexural eigenmode (i.e. $\omega_e = \omega_1$). Thus, the electrical force modulated at ω_1 is given by:

$$F_{\omega_1} = \frac{\partial C_{ts}}{\partial z}(V_{cpd} - V_{dc})V_{ac}\sin(\omega_1 t)\cdot \tag{4.8}$$

In contrast to the KFM principle previously described (see chapter 3), in the current single scan MF-EFM method the F_{ω_1} is not nullified. Instead, the value of the bias voltage V_{dc} in the above equation is set to zero (ground) and therefore:

$$F_{\omega_1} = \frac{\partial C_{ts}}{\partial z}(V_{cpd})V_{ac}\sin(\omega_1 t)\cdot \tag{4.9}$$

Thus in these conditions, the electrical force F_{ω_1}, and the cantilever oscillation amplitude at ω_1, are directly proportional to V_{cpd}.

The principle of the method consists of monitoring the variations of the amplitude/phase of the cantilever oscillations at the frequency of the electrical driving signal ($A(\omega_1); \phi(\omega_1)$) by using an additional lock-in amplifier locked to ω_1. The $A(\omega_1)$ (or $\phi(\omega_1)$) variations reflects the variations of V_{cpd} over the imaged

surface. The topography is simultaneously measured by locking the signal of the cantilever mechanical oscillations at the fundamental resonance mode ω_0.

4.2.2.3 The experimental set-up

The AFM topography measurements were carried out with our commercial Nanoscope D3100 from Veeco instrument (see description in chapter 2) operating in a conventional tapping mode. PtIr coated tips (from Nanosensors) with a stiffness $k \approx 3$ N.m^{-1} and a fundamental resonance frequency $f_0 \approx 65$ kHz were used.

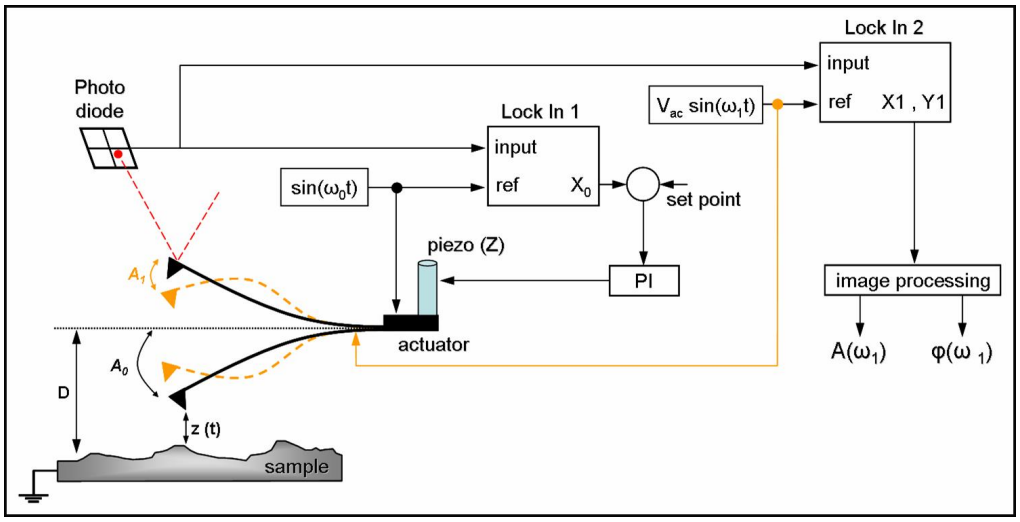

Figure 4.11: A schematic representation of the single scan MF-EFM set-up. The first feedback loop (Lock In 1 and PI) are actually integrated in the Veeco microscope system for the measurement of the topography at ω_0.

The experimental set-up is illustrated in figure 4.11. A modulated bias voltage is applied directly to the cantilever using an external signal generator. This is conducted at the same time as topographic imaging, where the cantilever is mechanically driven by the piezo actuator. Before engaging the tip in the imaging operation (far from the surface), the frequency of the electrical signal is set to the second eigenmode of the cantilever (ω_1). This is initially determined by using a frequency sweep protocol available on the commercial microscope.

set-up connections The connection of the external bias signal to the cantilever is ensured via the Signal Access Module (SAM) box connected to the microscope. An available entry (defined by ANA2) allows the connection of external signals directly to the cantilever.

Before starting the scanning procedure (tip withdrawn far from the surface), the precision of the second eigenmode frequency value is verified. To do so, the

mechanical excitation of the cantilever with Veeco system is shut off thanks to the SAM box, and the cantilever vibrates due to the electrical modulation signal applied to it.

Then the signal of the cantilever vibrations is fed into an external 'DSP 7280' lock-in amplifier from 'Signal Recovery', where its reference frequency is adjusted until the amplitude of electrical vibrations is maximum. Thus ω_1 is well defined.

Imaging at ω_0 and ω_1 During the scanning procedure, the topography is acquired at ω_0 from the internal feedback loop of the Veeco system. A home-made parallel derivation card, directly connected to the photodiode detector, allows a parallel acquisition of the cantilever deflection signal. This signal is fed into the external lock-in amplifier locked at the frequency ω_1. The lock-in amplifier is set to the fast demodulation mode (i.e. the fast output signals x and y are acquired).

Therefore the amplitude ($A(\omega_1)$) and the phase ($\phi(\omega_1)$) of the electrical signal are detected by the lock-in and calculated from the x_1 and y_1 signals in the image processing software (WSxM V4.0, Nanotec Electronica, spain):

$$A_1 = \sqrt{x_1^2 + y_1^2}, \tag{4.10}$$

$$\tan\phi_1 = \frac{x_1}{y_1}\cdot \tag{4.11}$$

4.2.2.4 Complex tip-sample dynamics: possible cross-talks

The simultaneous mechanical and electrical forces acting on the cantilever perhaps demands some clarification. First, the strong non-linearity of the intermittent contact regime induced by mechanical oscillations in this mode can give rise to very complex dynamics. Also, height artifacts induced by the electrostatic contribution can alter the topography of the scanned surface.

In fact, a steady deflection of the cantilever is always present due to the time-independent component F_{dc} of the electrical interaction force (see equation 3.23) which is given here by:

$$F_{dc} = \frac{1}{2}\frac{\partial C_{ts}}{\partial z}\left[(V_{cpd})^2 + \frac{1}{2}V_{ac}^2\right]\cdot \tag{4.12}$$

Besides its effect on changing the electrical resonance frequency, the gradient of the F_{dc} component also contributes to the shift of the cantilever mechanical resonance frequency, since it is a time-independent contribution. This component will thus affect the topography measurement (at ω_0) which can be detected either on the mechanical phase or amplitude signals.

According to the expression 4.12, the F_{dc} component in the current case, depends on two potential values: V_{ac} and V_{cpd}. It thus follows that the smaller the V_{ac}, the lesser the effect of the F_{dc} on the topography measurements [124]. As for the V_{cpd} potential, it is always present [102]. However, its value is usually of small magnitude which does not drastically contribute to the F_{dc} component.

Nevertheless, this latter assumption is not always true. For EFM measurements, where artificially injected charges to an oxide sample are studied, the V_{cpd} potential can reach high values depending on the amplitude of the embedded charges. Thus in such cases the effect of the F_{dc} component becomes relevant and the topography signal becomes distorted, depending on the sign of the embedded charges [129] [130].

Thus image data such as topography, mechanical phase and electrostatic information need to be verified, and possible interferences between them have to be identified. This can be also detected by observing possible spectral interferences between the mechanical and electrical interactions. To do so, we used an external oscilloscope to monitor the time-variation of the cantilever deflection when the two driving signals were applied and spectral data were acquired using a flexible resolution digitizer (Labview, National Instruments, Austin, TX).

4.2.3 Application: comparing single scan MF-EFM and KFM lift mode

In order to illustrate the capabilities in improving the spatial resolution of electrical measurements with the single scan MF-EFM method, we measured the same area of a test sample in both KFM lift mode and MF-EFM.

4.2.3.1 The test sample

The test sample used to perform the comparative experiment is formed by non-homogeneous graphene layers epitaxially grown on SiC(0001) substrate. It was chosen because of the high electrical properties of graphene layers which enable high electrical contrast to be measured. Moreover, the very small topographic features due to the thin graphene layers (one monolayer graphene $\approx$ 0.34 nm [131]) provide a typical system to be studied in tapping mode AFM, where uneven topographic incidents are ideally reduced.

4.2.3.2 The experimental protocol and parameters

Experiments were performed in reduced humidity conditions (RH $\sim$2% in the glove box). KFM lift mode measurements were first performed over a 3×1.5 μm^2 zone on the sample surface. Afterwards, the lift mode was disabled and the microscope was set to tapping mode. The external connection was then turned on, and the electrical modulation signal V_{ac} was

directly applied to the tip while a bias voltage $V_{dc} = 0$ was imposed on the sample.

The same area was scanned using the single scan MF-EFM method. The scan rate in both cases was set to 0.5 Hz resulting in an image acquisition time of ~ 8 minutes, for topography and CPD maps, in KFM lift mode and of ~ 4 minutes for topography and electrical signal ($A(\omega_e)$) and ($\phi(\omega_e)$) in MF -EFM.

of the KFM lift mode experiment In the first trace (topography trace), the cantilever was driven near its fundamental resonance frequency $\omega_0 \sim 61.5$ kHz. The amplitude of the free oscillations (far from the surface and before engaging the scanning procedure) was set to $A_0 \approx 2$ V. During the scan, the set point amplitude was $A_{sp} \approx 1.4$ V (the ratio $A_0/A_{sp} \approx 70\%$).

In the second trace (lift trace), the cantilever was electrically driven at the same frequency ω_0 as the first scan (no mechanical excitation was applied in this trace). The amplitude of the electrical excitation was set to $V_{ac} = 2$ V, the lift height to LH = 20 nm and the bandwidth of the feedback loop $B_{[Hz]} = 3000$ Hz.

of the single scan MF-EFM experiment We used the same parameters of the first trace KFM lift mode for the mechanical excitation of the cantilever. The simultaneous electrical driving signal applied to the cantilever was provided by an external signal generator with an excitation $V_{ac} = 2$ V. The calibration of the signal frequency and the cantilever electrical vibrations amplitude was conducted far from the surface. The frequency was set to the second flexural eigenmode $\omega_1 \approx 392$ kHz (see figure 4.12). The amplitude of the free electrical vibration of the cantilever was calibrated at $A_e = 0.73$ V. Therefore, the ratio of the amplitudes of the free electrical oscillations (A_e) to the free mechanical oscillations (A_0) of the cantilever was found to be $A_e/A_0 \approx 0.4$.

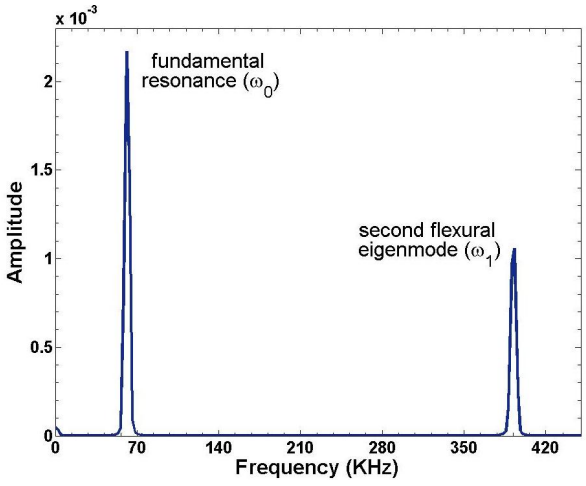

Figure 4.12: Power spectrum of the cantilever deflection (far from the surface) submitted to the double driving signals at ω_0 for topography measurements and ω_1 for electric measurements.

The external lock-in amplifier was locked at the frequency f_1. The bandwidth of its synchron detection was set to $\sim$ 159 Hz and the sensitivity of the output signal was tuned to 50 mV. The lock-in was set to the fast demodulation mode, where the output signals are x_1 and y_1 (see equation 4.10). The images of the x_1 and y_1 signals were recorded by using auxiliary entries in the commercial microscope software.

4.2.3.3 Imaging results

Figure 4.13 shows the KFM lift mode images of topography (a) and CPD map (b) and the topography image (c) obtained in the single scan MF-EFM method simultaneously with the x_1 (d) and y_1 (e) images of the variations of the electrical signal at ω_1.

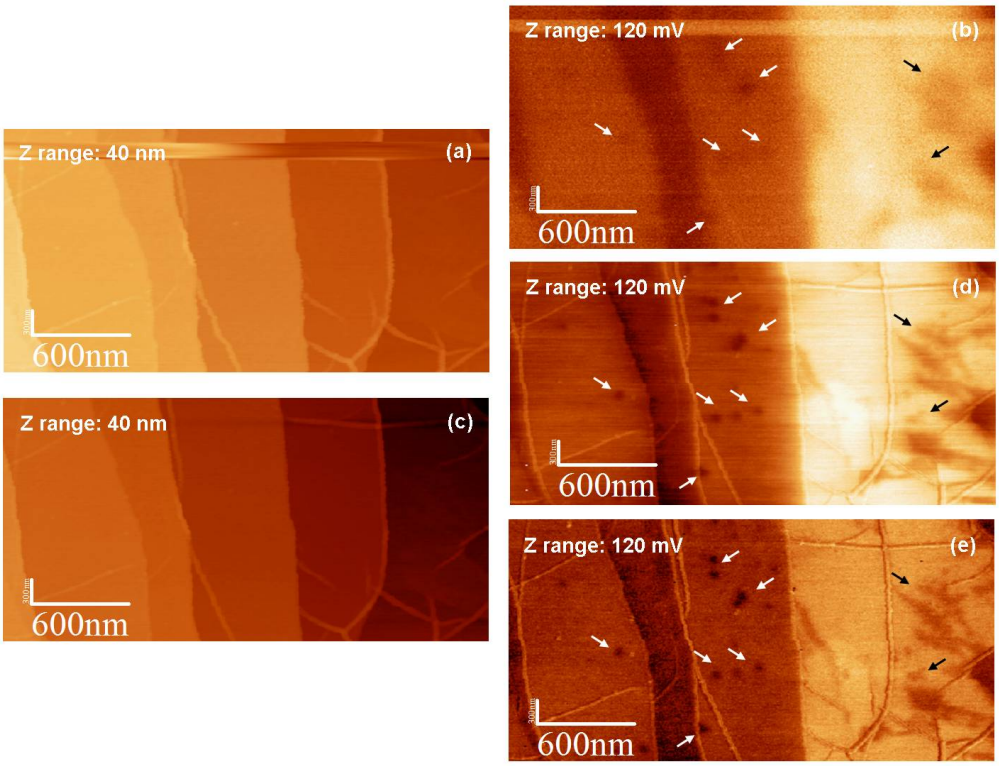

Figure 4.13: Topography (a) and CPD (b) maps acquired in the KFM lift mode (LH = 20 nm) compared to the topography (c) and electrical variations x_1 (d) and y_1 (e), simultaneously acquired in the single scan MF-EFM method. The topography images are rather similar. The contrast and the spatial resolution are drastically enhanced in the images (d) and (e) in the MF-EFM mode.

The x_1 and y_1 channels preserve the sign of electrical changes induced by the variation of the local contact potential difference, thus the contrast in the corresponding images (d) and (e) is similar to the contrast of the CPD map (b)

obtained in KFM lift mode measurements. However, according to equation 4.10, the sign of the electrical amplitude $A(\omega_1)$ is always positive and therefore could be different than the one in images (b), (d) and (e).

4.2.3.4 Improving the spatial resolution

The comparison of the KFM lift mode and MF-EFM images reveals an enhancement of the spatial resolution of electrical measurements. This can be attributed largely to the small tip-sample distance in MF-EFM measurements and to the increased sensitivity on the cantilever oscillations at the second flexural eigenmode.

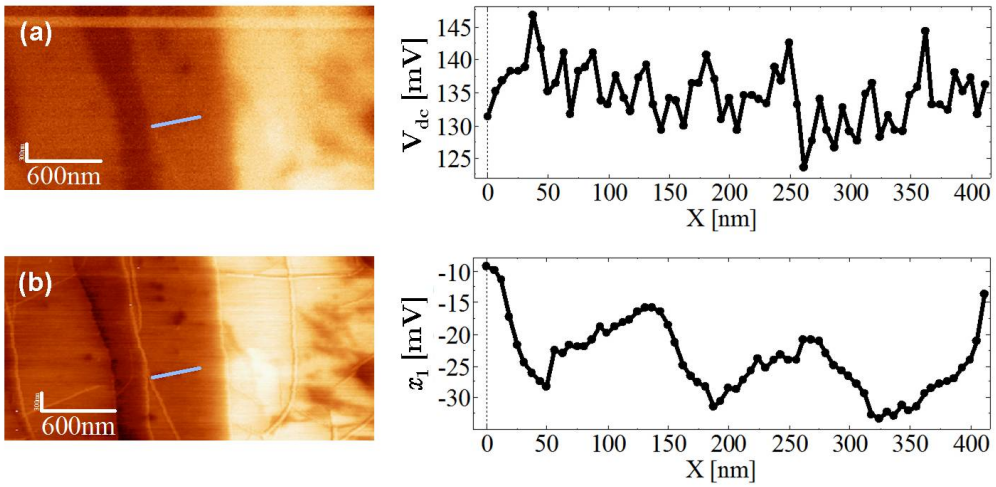

Figure 4.14: A cross section made among three distinguished holes in the x_1 image (b) obtained in MF-EFM and the CPD map obtained in KFM lift mode. It is practically impossible to distinguish these holes in the KFM image while the improvement of the spatial resolution in MF-EFM reveals their presence.

Several features (indicated with small arrows in figure 4.13) are hard to distinguish on the CPD map (b) acquired with KFM lift mode (LH = 20 nm). They are, however, perfectly clear in the x_1 and y_1 images of the MF-EFM mode (d) (e). The comparison of the cross section profiles (figure 4.14), drawn across three of these features, shows the enhancement of the spatial resolution where these features are perfectly resolved in the MF-EFM image, which is not the case on the CPD map in KFM lift mode.

Comparing the spatial resolutions To evaluate the improvement in spatial resolution with the MF-EFM method, a cross section line has been drawn along the same zone on the CPD map and the x_1 image (red line on figure 4.15). The spatial resolution is evaluated by measuring the lateral gap between the points

of 16% and 84% of the changing contrast step, which has been measured using 'ImageJ' software. Measurements show that the spatial resolution of electrical measurements in the single scan MF-EFM mode are approximately six times higher than the spatial resolution of KFM lift mode measurements.

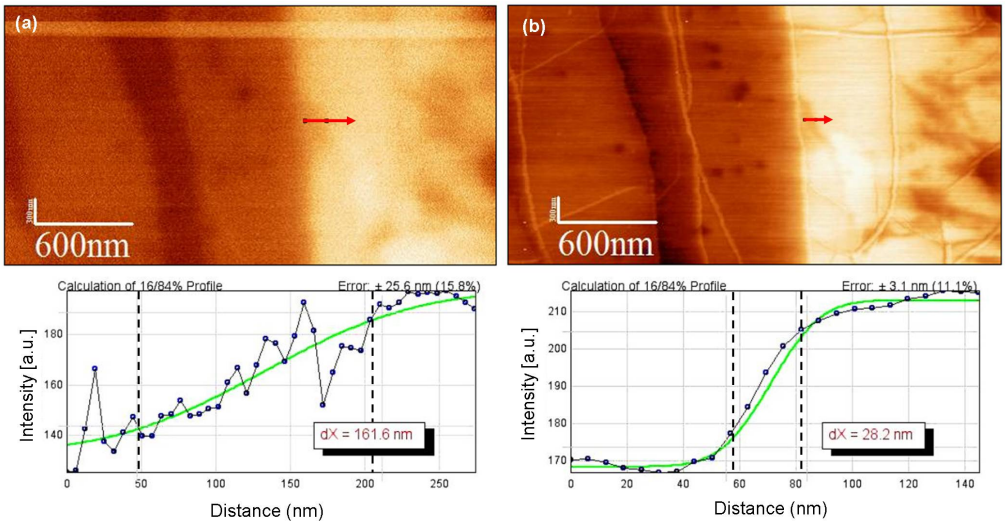

Figure 4.15: The spatial resolution across the red line on both the CPD map (a) in KFM lift mode and the image of the x_1 component of the electrical signal (b) in MF-EFM, was evaluated using ImageJ software (see plots). We found that the spatial resolution in MF-EFM is about six times higher than in KFM lift mode.

4.2.3.5 Effects on the topography

According to equation 4.12, the effect of the electrical interaction in MF-EFM on the topography is caused by the V_{cpd} and the V_{ac} potentials existing between the tip and the sample during the single scan operation. To evaluate the possible effect on the topography imaging channel in our case, we proceeded as following.

We considered a cross section over two zones (A) and (B) (see figure 4.16) presenting a contrasting step in the x_1 electrical image (a). The V_{cpd} over each zone was homogeneous. Then we compared the topography profiles, of the KFM lift mode image (b) and the MF-EFM image (c), over both zones (A) and (B).

We found that the topography profiles were noticeably similar at each stage (zone (A) and (B)). Since the V_{cpd} was homogeneous over each zone, then we conclude that the effect of the V_{ac} potential (V_{ac} = 2 V here) was practically small (see equation 4.12) and did not affect the topography scan during the MF-EFM measurements.

However, one can notice a slight lateral displacement between the KFM (red line) and MF-EFM (blue line) topography profiles in figure 4.16. This displacement is due to the lateral drift of the tip, or the sample, while performing KFM lift mode images in the two trace operation.

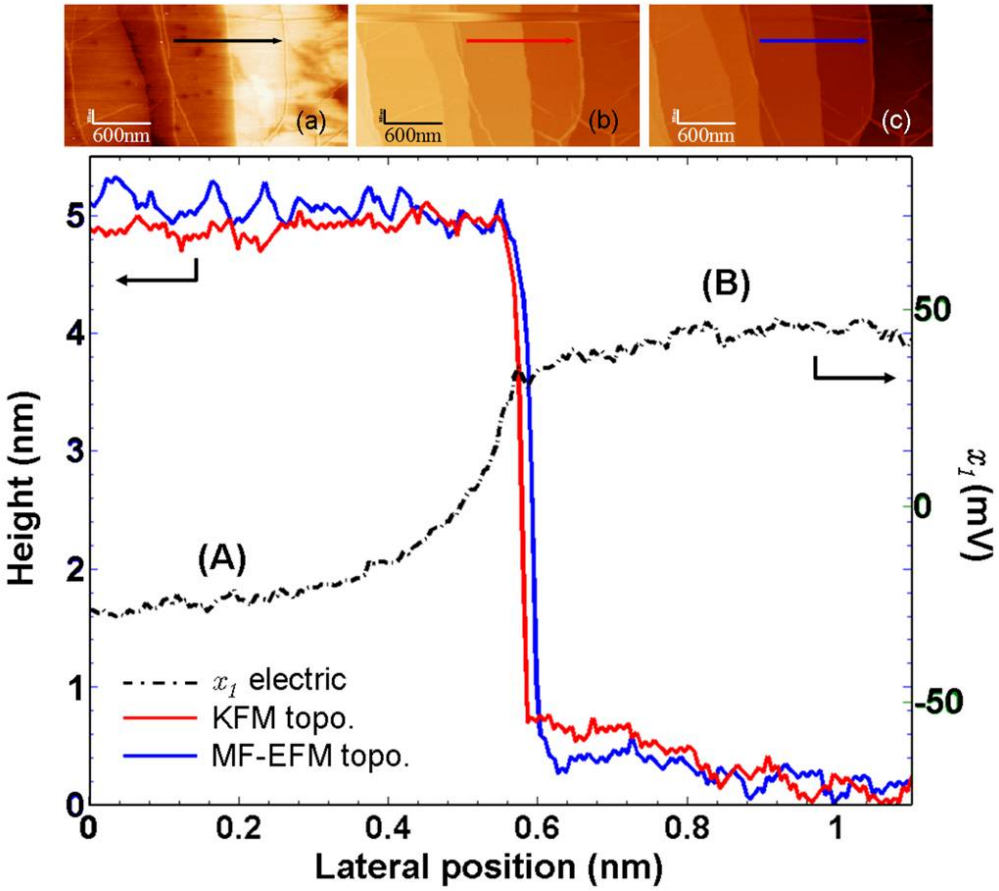

Figure 4.16: The cross section among a horizontal line over the x_1 electrical image (a) and the topography images from the KFM lift mode (b) and MF-EFM measurements (c). The electrical profile (dashed line) shows an electrical contrast step between two electrically homogeneous zones (A) and (B). The KFM (red line) and MF-EFM (blue line) topography profiles are practically similar over each zone indicating no important contribution of electrical excitations to the topography imaging.

4.2.3.6 Why is the spatial resolution higher in MF-EFM method?

In fact, the single scan MF-EFM method, as described above, actually benefits from three essential points for improving the spatial resolution of electrical measurements.

The tip-sample distance In KFM lift mode operation the effective tip-sample distance is given by $d_{eff} = d_{AFM} + LH$ (nm). d_{AFM} is the mean tip-sample distance determined by the set point value in the AFM topography trace, and LH is the lift height.

However, in the single scan MF-EFM, this effective distance is reduced to $d_{eff} = d_{AFM}$ and is determined by the parameters of the AFM tapping mode operation[5]. Thus, the reduced tip-sample distance helps increase the interaction between the tip apex and the sample which increases the spatial resolution.

Detecting the force gradient instead of the force An additional factor of spatial resolution enhancement is the nature of the detected signal in MF-EFM method compared to KFM lift mode. In fact, if we consider the cantilever under electrostatic interactions at ω_1 as a harmonic oscillator in a first approximation, then its behavior in response to the electrical interaction changes can be described in a similar way to the AFM behavior in chapter 3.

Thus the variation of the electrical oscillations amplitude and phase, when the cantilever is driven at the maximum sensitivity frequency (see equations 3.13 and 3.18) are given by:

$$\Delta A = A_m \frac{2Q}{3\sqrt{3}k} \frac{\partial F_e(D)}{\partial z} \quad ; \quad \Delta\varphi = \frac{Q}{k} \frac{\partial F_e(D)}{\partial z}. \tag{4.13}$$

Thus ,by monitoring the variations in the amplitude (ΔA) and the phase ($\Delta\varphi$) of the electrical signal at ω_1, the electrical information is directly proportional to the gradient of the electrostatic force. Hence, the spatial resolution is expected to be considerably improved [73] [72].

This is not the case for KFM lift mode operation. In fact, when the feedback principle of the KFM is applied, the electrical oscillation amplitude of the cantilever is canceled by adjusting the external V_{dc} value. In other words, ΔA from equation 4.13 is set to zero and consequently the force gradient is zero. Therefore in KFM lift mode, a constant force is measured, which is null regarding the feedback principle ($F_{\omega_e} = 0$). Consequently, the spatial resolution of KFM measurements is somewhat small due to the contributions of the cone and cantilever to the interaction force [73].

The capacitive contributions We can better understand the impact of the force gradient detection (rather than force) on the increase in spatial resolution if we consider the three components of the tip-sample capacitance (cantilever, cone and apex) as three parallel capacitor, then:

[5] In both methods one has to consider the deflection of the cantilever due to electrostatic interaction forces which in some cases (high voltages or charges) can lead to a considerable modification of d_{eff}

$$C_{ts} = C_{lever} + C_{cone} + C_{apex}. \tag{4.14}$$

The local CPD measurement is concentrated in the apex-sample interaction, while the interaction with the cone and the cantilever leads to an averaged global CPD measurement [74] [73]. Taking into account these considerations, we can rewrite the expression of electrical force in this way:

$$F_{\omega_e} = \left(C'_{lever} + C'_{cone}\right) V_{ac}(V_{cpd}^{global} - V_{dc}) + C'_{apex} V_{ac}(V_{cpd}^{local} - V_{dc}), \tag{4.15}$$

where C'_{ts} represents the derivative of the tip-sample capacitance with respect to the separation distance z ($C'_{ts} = \partial C_{ts}/\partial z$).

In fact, the capacitance derivatives C'_{lever} and C'_{cone} are much larger than C'_{apex} in a wide range of tip-sample distance (see figure 4.10). This first results in a reduction in the spatial resolution of electrical measurements as well as a considerable averaging of CPD value measured in KFM lift mode which detects the electrostatic force [73].

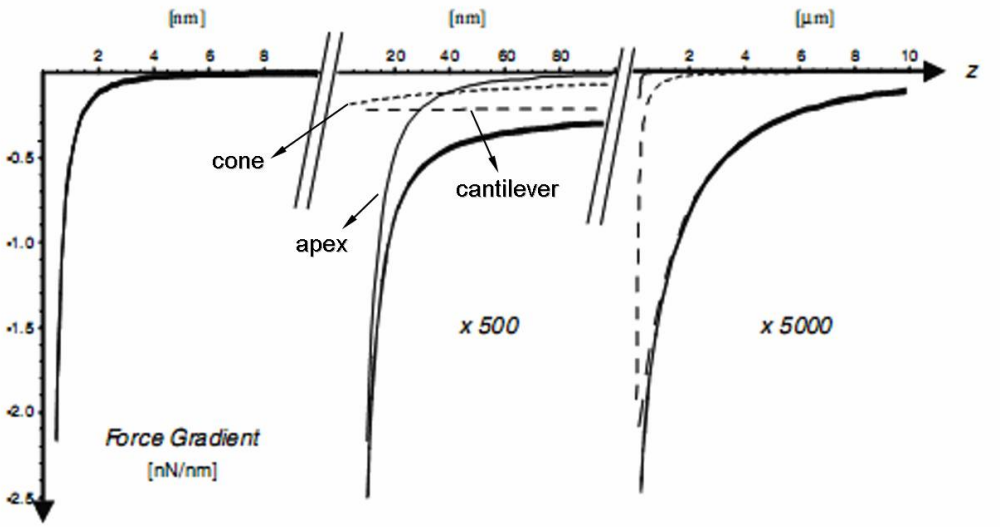

Figure 4.17: Calculated electrostatic force gradient versus tip-sample. The thick solid curve represents the total electrostatic force gradient, while the other three each represent of the contributions of the cantilever (dashed line), the tip cone (short dash) and the tip apex (solid line). These curves are obtained using the same parameters as in figure 4.10, and thus the comparison between the force and the force gradient could be made [73].

However, the gradient of the force is proportional to the second derivative of the tip-sample capacitances. It has been demonstrated by Colchero *et al.* that C''_{lever} and C''_{cone} are actually much smaller than C''_{apex}, and their effects can

be neglected especially for small tip-sample distances (figure 4.17). Thus the gradient of the force can be given by:

$$\frac{\partial F_{\omega_e}}{\partial z} \propto C''_{apex} V_{ac}(V_{cpd}^{local} - V_{dc}) \cdot \tag{4.16}$$

Consequently, in the MF-EFM method, the electric interaction with the sample is much more concentrated in the apex of the tip which explains the higher spatial resolution. A similar conclusion has been provided by Ding *et al.* by interpreting the shape of the cantilever during its oscillation at the second flexural mode.

4.2.4 Stability of the method: effects of of the external electrical excitation signal

The motion of the cantilever submitted to the double eigenmode excitation scheme of the single scan MF-EFM method undergoes very complex dynamics. This is still one of the most important subjects in study for such new imaging configurations [128]. However, in order to draw the experimental boundaries of our method, we investigated the impact of the electrostatic excitation parameters on the different imaging signals (i.e. the topography, mechanical and electrical oscillations).

4.2.4.1 Effect of the driving signal V_{ac} on cantilever dynamics

The amplitude (V_{ac}) of the external electrical driving signal impacts the cantilever motion during double (mechanical and electrical) excitations. To illustrate this, we used an external oscilloscope to monitor the deflection of the cantilever for difference V_{ac} values. The amplitude of the free mechanical oscillations was tuned to $A_0 = 1.5$ V.

The time series of the deflection signal show that for relatively small V_{ac} values, the actual motion of the cantilever is a superimposition of both mechanical and electrical vibrations. Whenever V_{ac} become larger than 1-2 V, the deflection of the cantilever is completely distorted and its dynamics are no longer approximated by the superposition of both mechanical and electrical vibrations.

4.2.4.2 Effect of electrical oscillations amplitude

Theoretical studies of cantilever motion dynamics subjected to multifrequency excitations have pointed out the importance of cantilever free oscillations (far from surface - with no interaction with the sample)induced by the different excitations [128] [127].

In our case, we compared the ratio of the free mechanical cantilever oscillation (A_0) at ω_0 to the free electrical oscillation (A_e) at ω_1. The free oscillation is measured when the cantilever is driven by one or the other excitation signal

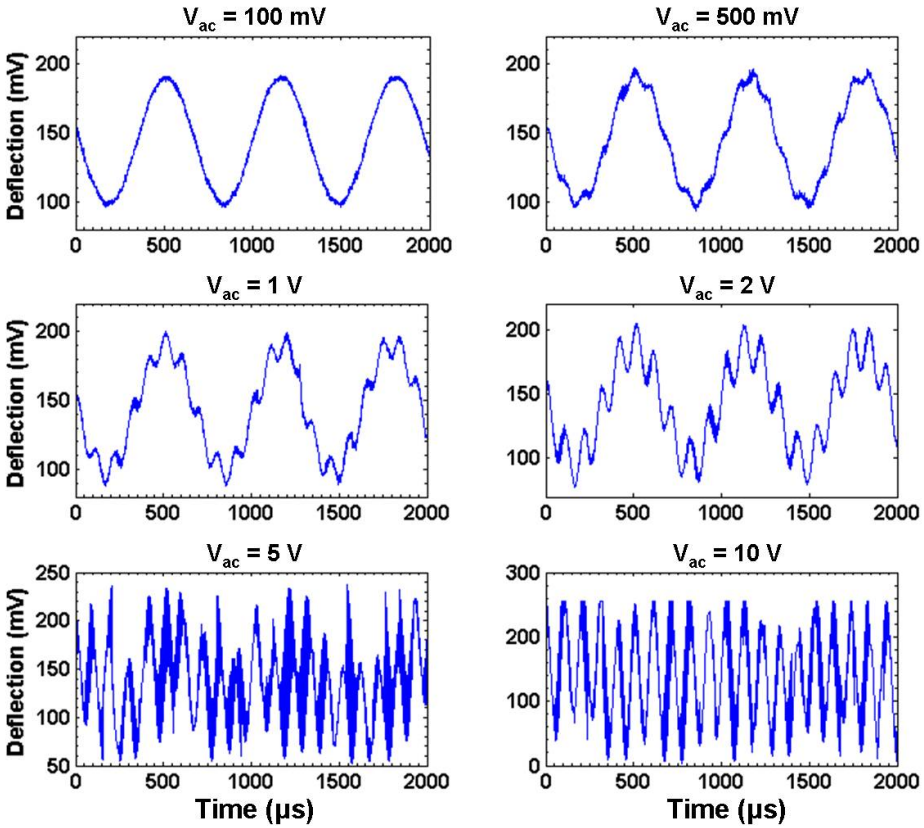

Figure 4.18: The cantilever deflection signal monitored (during the scan) for different values of the external electrical driving signal V_{ac}. The cantilever is simultaneously driven by mechanical and electrical exitations.

(not both) and in the absence of any interaction with the sample (far from the surface). Ratio A_e/A_0 is important because the energy stored in a higher eigenmode is the relevant quantity for the system dynamics [124].

The amplitude of free electrical oscillations was measured using the Veeco RMS amplitude indicator for each of the tested V_{ac} values. Figure 4.19 shows a calibration curve of the RMS amplitude of free electrical oscillations with respect to the external excitation amplitude V_{ac}.

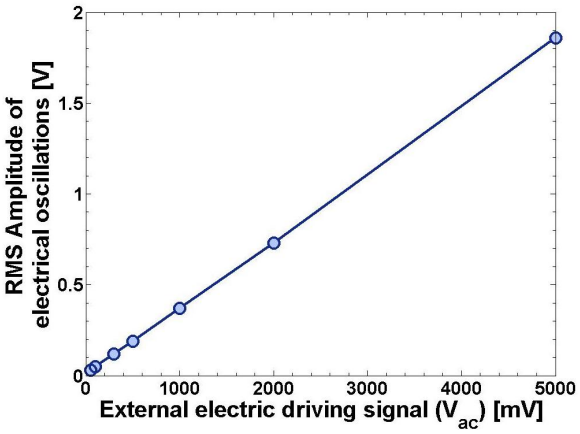

Figure 4.19: The calibration curve of the free cantilever oscillations (far from the surface) for different values of the external driving signal V_{ac}.

Therefore the ratio A_e/A_0 is linked to the dynamics of the cantilever motion by comparing it to the changes induced on the cantilever deflection, showed in figure 4.18 for each corresponding V_{ac} value.

We found that for A_e/A_0 ranging from 0.03 (V_{ac} = 100 mV) to 0.5 (V_{ac} = 2V), the cantilever deflection signal (figure 4.18) still shows a cantilever motion corresponding to a superimposition of both mechanical and electrical vibrations. Nonetheless, the effect of the electrical vibrations started to be considerably pronounced when A_e/A_0 exceeded 0.2 (for V_{ac} = 1 V).

However, when V_{ac} exceeded 5 V, the A_e/A_0 ratio became higher than 1. Thus, the amplitude of free electrical oscillations at the higher eigenmode are large and can no longer be considered as small perturbations of the free mechanical oscillations. Consequently, cantilever dynamics is completely distorted by high electrical oscillations compared to mechanical ones.

Theoretical studies of multifrequency excitation dynamics shows that this initial amplitude ratio, A_e/A_0, should be kept small ($\sim$ 0.1) in order to approximate the solution of the motion equation as the sum of the two motions induced by the double driving signals. Moreover, all reported set-ups using similar multi-excitation schemes emphasize this point [121] [124] [123].

4.2.4.3 Effects of V_{ac} on the different imaging channels

Finally, we illustrate the effect of changing the V_{ac} value on the different signals that could be recorded in our current configuration. Figure 4.20 shows the images of the electrical amplitude and phase (b-c) acquired simultaneously at the frequency of electrical excitation. The V_{ac} value was systematically changed during the scan.

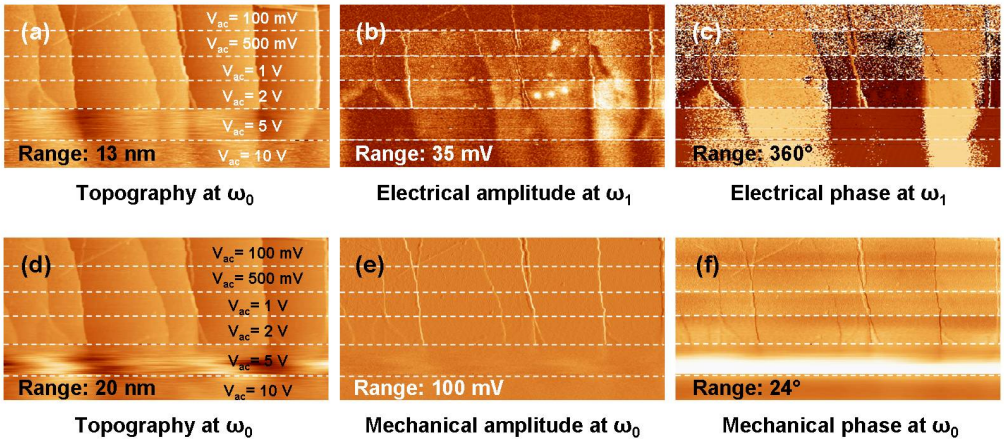

Figure 4.20: (a-c) the topography measured at ω_0, the electrical amplitude and phase signals measured at ω_1 with the MF-EFM method. The V_{ac} was systematically changed during the scan of the sample surface. (d-f) the topography, the mechanical amplitude and phase measured at ω_0. The variation of V_{ac} induces remarkable effects on the electrical signals at ω_1; while it is less evident on the mechanical amplitude and phase signals. For $V_{ac} \succ 5V$ both mechanical and electrical imaging are distorted.

We have also recorded the mechanical oscillation amplitude and phase of at ω_0, while the tip scans the surface following the MF-EFM method. The previously observed effects of V_{ac} on the cantilever's deflection (figure 4.18) are expressed by the changes in the different recorded signals.

However, it is worth noting that the topography imaging shows a relatively stable behavior for V_{ac} up to 2 V. Beyond this value the topography is completely distorted so that the feedback loop of the tapping mode is no longer closed. This happens when the energy stored in the second eigenmode (electrical oscillations) is initially higher than the energy stored in the fundamental resonance mode (mechanical oscillations. In other words, when A_e/A_0 become higher than 1, as previously discussed.

Nevertheless, the images of the electrical amplitude (b) and phase (c), at ω_1, are a demonstration of the arguments discussed in the previous section. When V_{ac} is very small (100 mV) the sensitivity to electrical interaction is low and so is the contrast on the images (b) and (c) (the upper part). For V_{ac} between

500 mV and 2V the contrast becomes relatively stable, best explained by the previous conclusion about the ratio A_e/A_0.

As discussed in section 4.2.2.4, the modification of the mechanical resonance frequency induced by the gradient of the electrical interactions is observed on the image of the mechanical phase (see equation 4.12). While the mechanical amplitude signal (figure 4.20(e)) is rather stable for $V_{ac} < 5$ V, a variation between 2° and 3° is observed in the mechanical phase signal (figure 4.20(f)) due to electrostatic contributions increasing with higher V_{ac} values.

4.2.5 Conclusion and further improvements

Conclusion We have demonstrated the possibility of improving the spatial resolution of electrical measurements under ambient (air, N_2) conditions. This is carried out with single scan double excitation scheme at higher flexural eigenmode frequencies.

The so called "single scan MF-EFM" method showed a particular improvement in spatial resolution about six times higher than KFM lift mode measurements. Its simple installation and set-up allow of reproducing measurements. Controlling the experimental parameters in this mode is delicate. It requires careful attention to avoid possible cross-talks between the different recorded signals.

Further improvements Contrary to the KFM lift mode, the MF-EFM method does not provide a direct measurement of the CPD over the surface. Instead, the variations in electrical amplitude (which are proportional to the CPD) are simply recorded. The proportionality factor depends on the first derivative of the tip-sample capacitance $\partial C_{ts}/\partial z$ (see equation 4.9). We could thus conduct an additional image treatment in order to extract the CPD map from the electrical amplitude images.

4.3 Calibration of KFM tips: defining reference sample using KFM and XPEEM

This section addresses the third KFM-related aspect: standard reference samples. In fact, KFM measurements of the sample's work function are inherently relative to the tip's work function. KFM measurements depend on its evolution in time. It then becomes very important to calibrate the tip's work function to a standard sample.

The tips used in KFM measurements (particularly in our study) are formed by silicon tips coated with PtIr conducting layer. Previous works [68] used the comparison with classical Kelvin Probe (KP) work function measurements of a

platinum (Pt) sample to evaluate the standard sample's work function in KFM experiments. Even thought this method has proved its efficiency, the standard sample's work function actually corresponds to a weighted value since it has been measured using the KP technique.

4.3.1 The goal of this study

In our study, the XPEEM and KFM techniques were used together to evaluate the stability of the tip's work function used during KFM measurements. For this goal, the stability of the contact potential difference (CPD) between the tip and a chosen standard sample was monitored under various conditions. We are therefore interested in defining a simple protocol enabling stable KFM measurements in the most common daily experimental conditions.

4.3.2 Using XPEEM to measure a standard work function value

Since the XPEEM technique offers the possibility of directly measuring an absolute work function value free from environmental effects (UHV), we chose it to evaluate of the work functions of a set of standard samples. Samples were formed by gold (Au), ruthenium (Ru), copper (Cu) and platinum (Pt) layers deposited on Si substrates. The evolution of the measured values was thus evaluated by repeating measurements within certain time periods.

4.3.2.1 Experimental protocol

A referential cross mark was made on the surface of each test sample to define the coordinates of a particular position, on which measurements would be reproduced both in XPEEM and KFM experiments. All samples (Au, Ru, Cu and Pt) were placed in the analysis chamber of the *NanoESCA* spectromicroscope and were kept under UHV conditions before experimenting. There were no surface preparation or cleaning protocol.

4.3.2.2 Monitoring the evolution of the work function

Each couple of samples was measured at two different runs. Figure 4.21 shows the work function values measured by XPEEM. For the first couple of samples (Au, Pt) repeated measurements were separated by a 14 day delay while for (Ru, Cu) measurements were repeated 36 days after the first run.

Meanwhile, samples were continuously stored in dry conditions to reduce the effect of water layers on their surfaces. All samples showed very small variations over time ($\Delta(WF) \leq 56mV$). This fact indicates that any one of these samples could be used as a standard sample for further investigations with KFM technique. However, Pt and Ru show the most stable work function values. Table 4.2 summarizes the initial work function values for each sample and the changes over time.

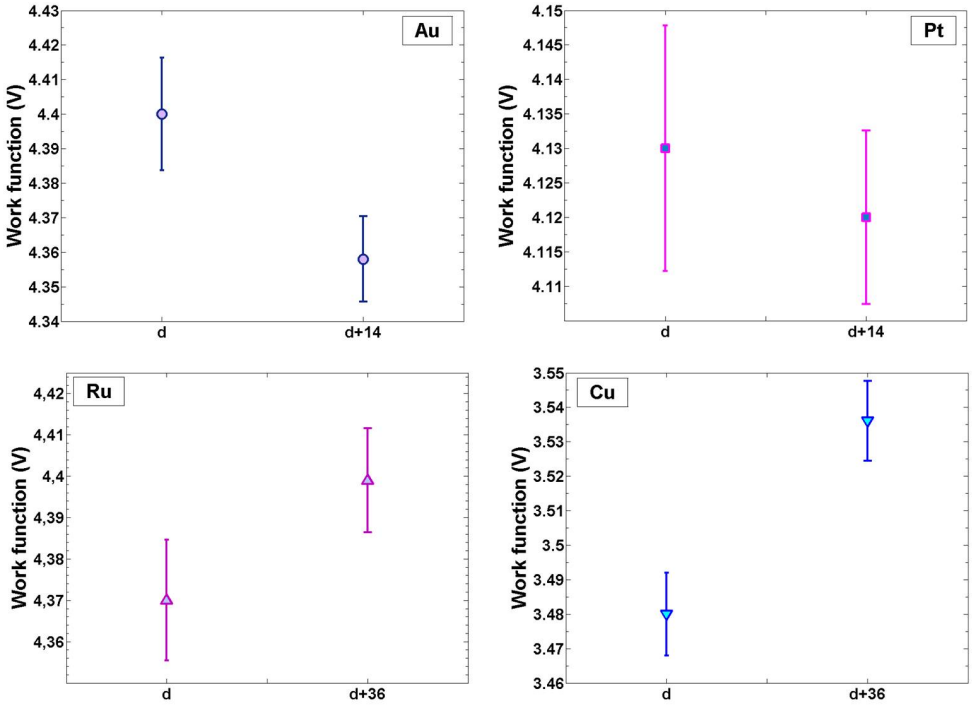

Figure 4.21: Work function of Au, Pt, Cu and Ru metallic layers measured twice for each case. The evolution of the work function over time is relatively small for all samples.

We thus chose the Ru sample to be investigated by KFM measurements by monitoring its time evolution for ambient air measurements.

4.3.3 Evolution of the CPD measurements with KFM: Ru as a standard sample

We will now address the stability of the KFM measurements. We measure and monitor the changes in CPD (corresponding to the tip-sample work function difference) values using the same tip during multiple experimental runs.

Table 4.2: Evolution of the work function measured with XPEEM for different time periods

sample	intial WF	Δ WF	time period
Au	4.4 V	- 42 mV	14 d.
Pt	4.13 V	- 10 mV	14 d.
Cu	3.48 V	+ 56 mV	36 d.
Ru	4.37 V	+ 29 mV	36 d.

4.3.3.1 Planning the experimental campaigns

Protocol A new PtIr tip (from Nanosensors) was identified and used during the entire measurements campaign. Each experimental run consists of measuring the CPD between this tip and the Ru sample. Each measurement is statically averaged over eight regular positions on the surface of the sample defined with respect to the referential cross mark.

Measurements The experiments will be divided into three categories (i) monitoring the evolution of the CPD under *air conditions* with several time periods, (ii) monitoring the CPD value under *dry conditions* (N_2) with several time periods and (iii) point out the effects of a simple surface treatment preparation on the stability of the CPD value.

Conditions Before and after each experimental run, the tip and the standard sample were stocked in a dry environment. Since we have seen that the CPD value is dependent on the LH between the tip and the sample, all following measurements were obtained spectroscopically at large LH values (LH = 1 μm) to avoid any polarization effects due to small tip-sample distances (see section 4.1.2.1).

4.3.3.2 Evolution of the CPD under air

Experiments under air conditions were performed in four consequent runs. The time period between each run is 7 days. Figure 4.22 shows the evolution of the CPD value measured between the PtIr tip and the Ru standard sample.

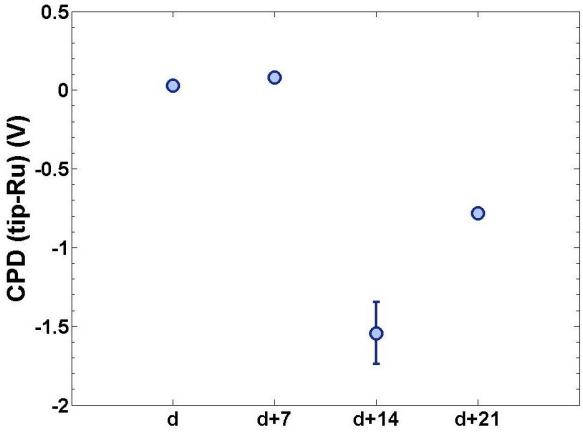

Figure 4.22: The evolution of the CPD value between the PtIr tip and the Ru standard sample under air conditions. Four experimental runs one every 7 days were performed. The evolution is rather large.

One can see that the evolution of the CPD measured under air conditions is not stable and presents large differences for experiments done at large time periods. Thus, in order to identify the source of this evolution we monitored the physical quality of the tip used among all experimental runs.

Evolution of the tip state SEM images of the tip, shown in figure 4.23, were taken at each experimental run. Images show that the tip state is physically unaltered neither by physical damage (see section 4.1.3) nor by the presence of uneven contamination or dust.

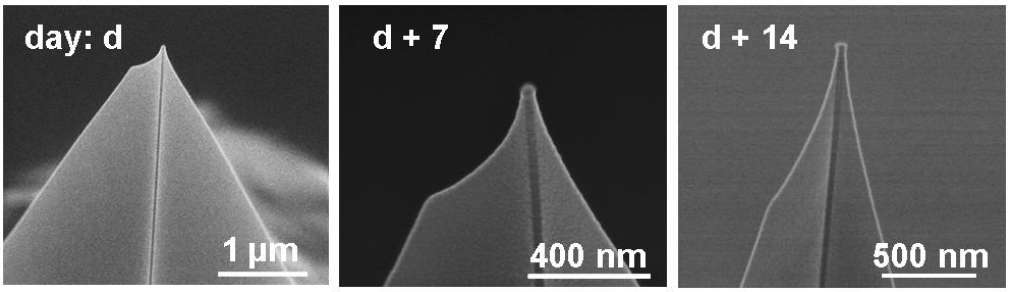

Figure 4.23: SEM images of tip used among the different experimental runs (figure 4.22). Images were taken at different angles and magnification conditions.

Evolution of the sample state Therefore, we safely deduce that the large variations of the CPD value measured under air at large time delays (figure 4.22) are practically induced by the change of the sample surface quality. This can reasonably result from the variation of the humidity level during each experimental run or from the different contamination that might occur when measurements are conducted at large time intervals.

Monitoring the CPD evolution on a smaller time scale Knowing the physical quality of the tip remains intact, we decided to follow the previous measurements by two experimental runs spaced one day apart. During this test, the tip and the sample were maintained under the same conditions (ambient air). Figure 4.24 shows that the CPD between the Ru sample and the tip presents a stable behavior. A very slight change ($\sim$ 16 mV) was identified between experiments, which is in the range of the KFM sensibility. Thus, the work function of the sample seems to be stable on such a short time scale. This fact helps in monitoring any alteration of the tip's work function during measurements.

4.3.3.3 Stability of the CPD after simple surface treatment

Even though a stable behavior has been monitored under air conditions for short-time experimental runs, the presence of humidity in such cases can have arbitrary effects if experimental conditions are not controlled. This is why we led additional experiments under controlled conditions in order to define a simple surface treatment protocol capable of providing stable and reproducible CPD measurements.

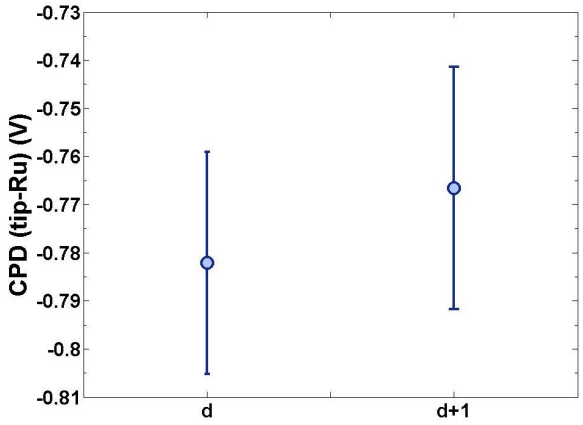

Figure 4.24: The evolution of the CPD value, between the PtIr tip and the Ru standard sample under ambient air conditions, determined between two experimental runs spaced one day apart. A stable behavior is reported, indicating that the sample's work function remains unchanged during the short time intervals.

Surface treatment The simplest surface treatment that could be done to the Ru sample in daily and routine KFM experiments was to heat the sample in an external heater where continuous N_2 flow ensures a reduced humidity level. The Ru sample was heated at 120°C for about 2 hours. It was then transfered into the glove box and cooled down in the dry environment of the glove box for about 10 minutes before starting experiments.

Unfortunately, it was not possible to heat the sample in the same glove box where the experiments were performed. The sample was thus exposed to air during the transfer from the external heater to the microscope. But the risks of recontamination are reduced if the sample's surface is sufficiently hot and the transfer is done quickly.

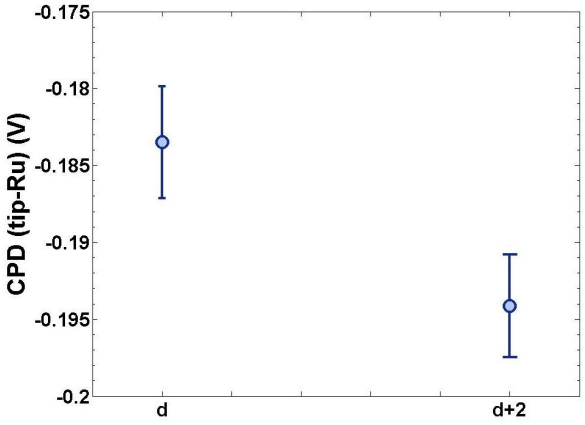

Figure 4.25: The evolution of the CPD value between the PtIr tip and the Ru standard sample under dry conditions (N2 flux) after the sample was first heated and kept for 2 days under dry environment. The measured CPD value was rather stable which emphasized the importance of the surface treatment for measurement calibration.

Measurement protocol After the sample was heated and the first experimental run was done (day d), the sample and the tip were kept under the glove

box for an entire two days. A second experimental run was then performed. Figure 4.25 shows that the CPD value measured between the two runs is rather stable. A very slight difference $\sim$ 10 mV was detected, which is in the range of the KFM sensitivity and thus negligible.

This experiment hence illustrates that when the Ru surface is initially heated (given that water molecules are desorbed and the sample is kept in dry conditions), one can use the same undamaged tip in short experimental runs to effectively measure the CPD.

4.3.4 Defining a daily KFM calibration routine

The latter result shown in figure 4.25 defines the most convenient calibration protocol for the identification of the tip evolution before and after any experiment using the Ru sample as a standard reference:

- The sample should be heated for a sufficiently long time ($\sim$ 2 hours), at a temperature $\sim$ 150 °C in order to desorb the adsorbed water molecules on its surface.
- The tip should be kept in the dry environment of the glove box before experiments under so as to reduce humidity effects. After a relatively quick transfer of the hot sample to the glove box, an initial set of spectroscopic measurement of the CPD between the tip and the sample should be done at a specific position on the surface.
- After the desired experiments are finished, the tip and the sample should be kept in the dry environment while a final spectroscopic set of CPD measurements is repeated at the same initial position on the surface.
- One can estimate the quality of the tip and the evolution of its work function from the difference observed between the initial and the final spectroscopic measurements.

4.4 General conclusion

In this chapter, we have investigated almost all aspects of the relative quality of KFM measurements in lift mode. We have established an analytical understanding of the CPD variation observed as a function of the tip-sample separation in lift mode experiments. Local work function anisotropy, leading to a local surface 'patch charge' density has been verified as the most likely reason for the current variations.

We have pointed out the effect of the tip shape quality on the CPD measurements in lift mode. Tip damages induce radical modifications in CPD variations with respect to the tip-sample separation when measured at a specific surface position. These observations were identified as a possible simple protocol to evaluate the quality of the tip shape before and after any scanning experiment in KFM lift mode.

We have also highlighted the effects of the measurement environment and the necessity of stable conditions to enable comparative studies so as to avoid additional measurement artifacts induced by environmental contributions. The parameters of the feedback loop involved in the KFM lift mode procedure $(V_{ac}; B_{[Hz]})$ have shown very small negligible effects.

In addition we have elucidated the possibility of improving the spatial resolution of the CPD measurements. A single scan method (MF-EFM) based on a multifrequency excitation scheme at higher flexural eigenmodes has been described and its capabilities and limitations in terms of CPD measurements were emphasized. We showed that the spatial resolution with MF-EFM mode is approximately six times higher compared to the KFM lift mode. However, a direct quantification of the contact potential difference with the MF-EFM mode is still not possible. Further treatments are required to enable this possibility.

Finally we have drawn experimental tests to evaluate the stability of the CPD measurement in KFM lift mode. We evaluated the evolution of the tip's work function during measurements with a Ru sample considered as a standard sample. We have thus defined an easily accessible and simple treatment protocol for a stable KFM measurement in a daily experiment.

Among the results described in this chapter, we can particularly emphasize the following conclusion: ***The nature of the KFM measurement is inherently relative. Experiments are capable of providing considerable qualitative characterizations, although a quantitative analysis should be assessed with a complementary characterization method capable of absolute determination of the local work function of studied materials, such as the case of XPEEM***.

The next chapter shall illustrate this fact by applying a complementary characterization protocol using both the KFM and XPEEM techniques for the study of a particular sample: graphene layers on SiC substrate.

Chapter 5

Characterization of epitaxial graphene on SiC (0001) using XPEEM and KFM experiments

Dans ce chapitre, nous utilisons les techniques XPEEM et KFM pour la caractérisation complémentaire d'un système formé par des couches de graphène épitaxiées thermiquement sur substrat SiC(0001). L'objectif de cette étude est de présenter une méthode d'estimation du nombres de couches de graphène à partir des cartographies du travail de sortie obtenues par XPEEM et KFM. La composition chimique de ces couches est étudiée par la spectroscopie des photoélectrons (XPS) en utilisant le NanoESCA. Des mesures spectromicroscopiques sont aussi menées pour une estimation locale de l'épaisseur des couches de graphène.

In this chapter, XPEEM and KFM are used together in the characterization of graphene layers thermally grown on SiC(0001) surface. The main goal of this chapter is to present a method for the estimation of graphene layer thickness using local work function measurements with both techniques. The chemical composition of graphene layers on SiC(0001) is also investigated using XPS measurements with the *NanoESCA*. Spectromicroscopy measurements are also used to estimate locally the thickness of graphene layers.

5.1 Introduction

5.1.1 What is graphene?

A single monolayer of graphite is called graphene. It is a two-dimensional sheet of sp^2-bonded carbon atoms arranged in a honeycomb lattice. It can be

considered as the building block of other carbon allotropes such as fullerenes [132], one-dimensional carbon nanotubes [133] and three-dimensional graphite [134]. Figure 5.1 shows examples of different carbon allotropes. Graphene, however, exhibits singular properties owing to its particular band structure.

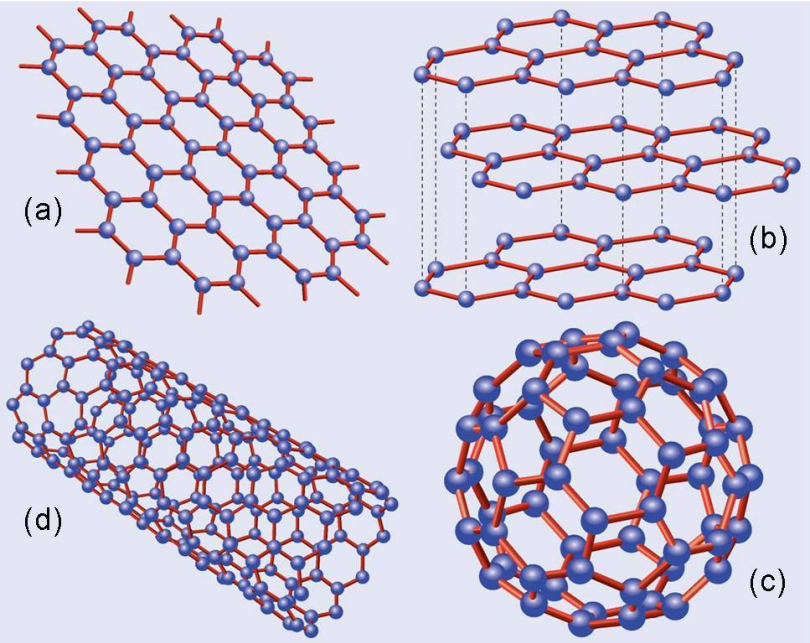

Figure 5.1: (a) Graphene is a honeycomb lattice of carbon atoms. (b) Graphite can be viewed as a stack of graphene layers. (c) Fullerenes C60 are molecules consisting of wrapped graphene by the introduction of pentagons on the hexagonal lattice. (d) Carbon nanotubes are rolled-up cylinders of graphene [135].

For an isolated single graphene sheet, the crucial aspect of the band structure occurs at the Fermi level (E_F) where the π and π^*-bands intersect at the K-$K^{'}$ points of the Brillouin zone [136]. The intersection points are known as Dirac points. Graphene is therefore considered as a semi-metal since the conduction and valence bands are in touch at the Dirac points. It is also considered as a semiconductor with a zero gap or a "gapless semiconductor".

Experimentally, stacks of a few monolayers of graphene are so-called few-layer graphene (FLG). It was shown that their electronic structure rapidly evolves with the number of layers, approaching the 3D limit of graphite at 10 layers [137]. This allows single-, double-, and few-(3 to <10) layer graphene to be distinguished as three different types of 2D crystals. For all intents and purposes, thicker structures should be considered as thin films of graphite [138].

5.1.1.1 Technological applications

Graphene was first synthesized between 2004 and 2005 by three different groups [139] [140] [141] [142]. Since then, it has attracted considerable interest due to its novel magneto-transport properties [140] [141] [143], high carrier mobility and ballistic transport up to room temperature [144].

It has the potential for technological applications as a successor of silicon in the post-Moore's law era [142] [145] [138], as a single-molecule gas sensor [146], in spintronics [147] [148] [149], in quantum computing [150] or as a terahertz oscillator [151]. Other promising applications for graphene include ultra-capacitors for energy storage purposes [152], or transparent conducting electrodes required for applications in touch screens, liquid crystal displays and organic photovoltaic cells [153]. For such applications, it is necessary to have uniform ordered growth of graphene on an insulating substrate [154].

5.1.1.2 Production methods

The successful development of graphene-based electronic devices depends on a large scale availability of the material [154]. Several methods for graphene production have been proposed [137]. Mechanical exfoliation of highly-oriented pyrolitic graphite [155] [140] [141] leads to isolated, high-quality crystals with dimensions only in the 10 μm range, which questions the practicality of this method [154]. Large, high-quality graphene islands were grown on the surface of transition metals such as Ru(0001) [156] [157]. Wafers of continuous few-layer graphene have also been grown on polycrystalline Ni films [158]. These techniques require however the transfer of graphene layers to an insulating substrate.

Another interesting method for graphene production is the thermal decomposition of silicon carbide (SiC) by annealing of SiC at temperatures above 1150°C which results in the graphitization of its surface. Graphene obtained by this method is so-called epitaxial graphene (EG). It has been proposed as a viable route for the synthesis of uniform, wafer-size graphene layers for technological applications [142] [145] [138]. A considerable advantage of this method is that the insulating SiC substrates can be used so that a transfer to another insulator is not required [154].

The growth of single- and few-layer graphene on both polar faces of the SiC substrate was demonstrated [159] [160] [161]. It was shown that graphene layers grown on the C-terminated face (noted as SiC$(000\bar{1})$) are of higher quality than those grown on the Si-terminated face (noted as SiC(0001)) [159] [162]. It was recently demonstrated that the growth of epitaxial graphene on SiC(0001) in an Ar atmosphere, close to atmospheric pressure, provides morphologically superior graphene layers in comparison with UHV graphitization [163] [154]. Figure 5.2 shows an example of epitaxial FLG on SiC(0001) obtained in UHV (a) and Ar

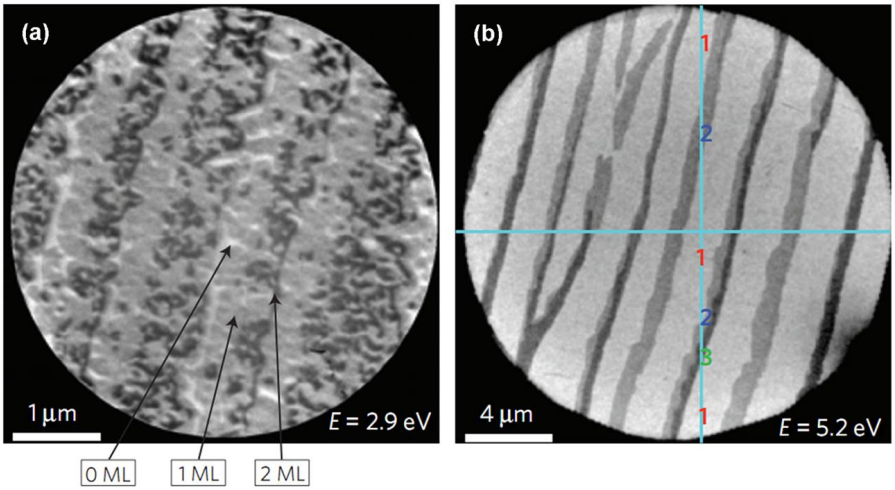

Figure 5.2: LEEM images of epitaxial FLG on SiC(0001) in different environmental conditions. Layers in (a) are obtained under UHV with annealing temperature at about 1280°C. The image contrast is due to locally different layer thickness. Light, medium and dark grey correspond to a local thickness of 0.1, 1 and 2ML respectively. (b) Layers obtained in Ar atmosphere with a pressure of ∼900 mbars. The layers morphology is of higher quality compared to layers in (a). Large continuous terraces (more than 50 μm) were found. Layers thicknesses are easily determined by reflectivity measurements and are indicated with numbers on the image [154].

(b) atmospheres. The improvement in morphological quality of graphene films is obvious for layers grown in Ar atmosphere.

5.1.2 Graphene layers: thickness measurements

As mentioned above, the viability of graphene-based electronic applications rests on the ability to make wafer-scale graphene films with controlled thickness. Homogeneous film thickness is particularly important because the electronic structure of the graphene film depends strongly on the number of layers [160] [164] [165]. However, for epitaxial graphene, the large-scale structural quality is presently limited by the lack of continuity and uniformity in the grown film [166] [163] [154] [167]. The decomposition of SiC is not a self-limiting process and, as a result, regions of different thickness levels coexist, as shown by low-energy electron microscopy (LEEM) [166] [164] [167] [163] [154].

5.1.2.1 Characterization issues

Growth conditions of epitaxial graphene are being continuously improved for better control of the film thickness and homogeneity [163] [154]. This improvement requires a continuous measurement of the graphene film thickness. This presumes the availability of suitable characterization tools and methods. With the possibility for different film thickness levels to coexist, high spatial resolution measurements became essentially required. Easily accessible (laboratory-based)

methods for measuring the graphene layers thickness with a high spatial resolution thus become important.

5.1.2.2 Methods and techniques

A number of surface analysis techniques have been employed so far to measure the thickness of graphene films. While some of which provide direct thickness measurements (namely LEEM [163] [154] [166], AFM-related methods [168] [169] [170] and Raman spectroscopy [171] [169]), others provide an estimation of film thickness by measuring graphene structural, electronic or chemical properties.

Among these technique, STM [172] [173] [174], SXRD [175] [176], ellipsometry and LEED [177] [163] [161] are used to probe the atomic structure of graphene. KRIPES [178] and ARPES [165] [161] [177] measure the electronic band structure. XPS [160] [161], PEEM [163] [164] and AES [142] [179] probe the local chemical properties. More details are provided in the appendix section (see appendix C). Table 5.1 summarizes the these techniques and there estimated spatial resolutions.

Technique	**Resol./limits**
AES	beam size ($>$ 5 nm)
SXRD	$\sim$ mm (beam size)
XPS	$>$ 10 μm (beam size)
Ellisometry	$\sim$ mm
LEEM	down to 10 nm
μ-RAMAN	1-2 μm (beam size)
ARUPS	No spatial resolution
LEED	$\sim\mu$m (beam size)
STM	$\sim$0.1 nm
AFM	$\sim$1 - 2 nm
KFM	$\sim$20 - 50 nm
XPEEM	40 nm

Table 5.1: Comparison of the different techniques used for the determination of the thickness of graphene layers.

5.1.2.3 This work: thickness determination using work function measurements

It has been recently shown [168] [166] that the work function of graphene films depends on the number of layers. Thinner graphene layers (1 LG) were found to have a lower work function ($\sim$ 0.3 eV) than that of thick graphitic layers ($\geq$

10 LG)) [166]. These are actually interesting but surprising findings since it is atypical that the work function of a material depends on its thickness.

However, based on these reported data, the work function can be used as a signature of graphene layers thickness. In this chapter we have exploited this idea by using the KFM and XPEEM techniques to measure and reproduce maps of the local work function. These methods provide high-resolution measurements with an easy accessibility due to the laboratory-based monochromatic X-ray (Al K_α) photon source.

5.1.3 The sample: epitaxial FLG on SiC(0001)

In this work we studied epitaxial graphene layers grown on 6H-SiC(0001) (Si-terminated). The SiC substrate, purchased from "Novasic", was n-doped (nitrogen) and the doping concentration was about $2.5 \pm 0.5 \times 10^{17}$ cm^{-3}. SiC(0001) substrate was annealed at 2000°C for 30 minutes in Ar atmosphere with a pressure of $\sim$ 600 mbars. The growth of graphene layers is therefore achieved by solid state graphitization where Si atoms desorb at high temperatures (above 1150°C) and excess C is left behind on the surface [161].

5.1.3.1 Basic elements of the epitaxial graphene on SiC(0001) system

The epitaxial growth of graphene layers has been demonstrated to be different depending on the polar face of SiC (i.e. SiC(0001) (Si-terminated) and SiC(000$\bar{1}$) (C-terminated) [161] [160] [180] [131]. Here we focus on graphene formation on the SiC(0001) surface. We provide the basic elements which define the structural and electronic nature of the interface between SiC(0001) and grown graphene layers.

Graphitization of SiC(0001)

The graphitization of the SiC surface generally occurs (for both polar faces) when SiC is annealed at a given temperature ($\sim$1100°C), above which Si atoms start to desorb from the substrate. When three Si atomic planes desorb, the remaining C atoms will be self organized and form a C graphitic plane on the SiC surface.

For SiC(0001), the first C-rich phase starts forming upon heating at $\sim$ 1150°C. This phase has a $6\sqrt{3} \times 6\sqrt{3} - R30$ (noted as $6\sqrt{3}$) pattern (with respect to SiC(0001) 1×1 surface cell) that appears on diffraction panels (see figure 5.3). Before the formation of this phase, the SiC(0001) surface goes through a number of surface reconstructions depending on the annealing temperature as observed by LEED experiments (see figure5.3).

Heating above 1050°C results in a well-defined $\sqrt{3} \times \sqrt{3} - R30$ phase (noted as $\sqrt{3}$), further heating above 1100°C causes a mixture of $6\sqrt{3}$ and $\sqrt{3}$ phases to develop. LEED panels of the surface heated above 1200°C show the diffraction spots corresponding to the $6\sqrt{3}$ only [162] [161].

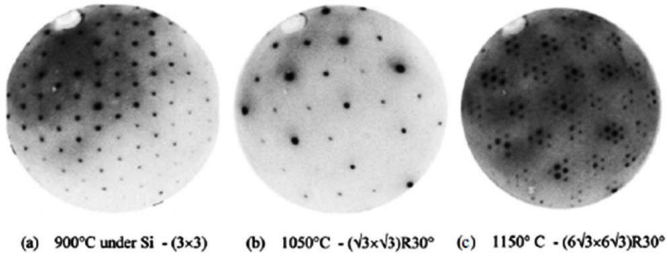

Figure 5.3: A sequence of LEED panels obtained on a 6H-SiC(0001) surface following the temperature-dependent surface reconstructions leading to the $6\sqrt{3} \times 6\sqrt{3} - R30$ phase [178].

Recent studies [160] [161] showed that the $6\sqrt{3}$ reconstruction compromises a single layer of C atoms with a graphene-like atomic arrangement. This has been demonstrated by the presence of σ-bands in the corresponding band structure from ARPES measurements (see figure 5.5 (a)). Consistent PES studies showed that this layer interacts with the underlying SiC(0001) surface by covalent bonds [160] [161]. As a result no signature of π-bands is observed in the electronic band structure of this layer (figure 5.5 (a)). Its electronic structure thus deviates from that of graphene [160], in accordance with *ab initio* calculations [131].

Growth of graphene layers

While increasing the annealing temperature upon 1350°C, the $6\sqrt{3}$ phase disappears from LEED diffraction panels and the surface become completely graphitic (signature 1×1 of graphite on LEED panels) (see figure 5.4) [178]. It is considered as a precursor phase to graphene/graphite formation.

By precisely controlling the annealing temperature, it is possible to grow epitaxial graphene on SiC(0001) in almost a layer-by-layer fashion. However, thermal gradients across a sample can produce lateral thickness distribution in the grown graphene layers. As cited above, environmental conditions (UHV or Ar atmosphere) seems to also have an important impact on the morphological quality of epitaxial graphene layers [154].

The interface between SiC(0001) and grown graphene layers

PES measurements [160] demonstrated that the same structural elements as in the $6\sqrt{3}$ reconstruction are present at the interface between FLG and SiC(0001) [160]. The interfacial layer is therefore formed by the first carbon plane grown

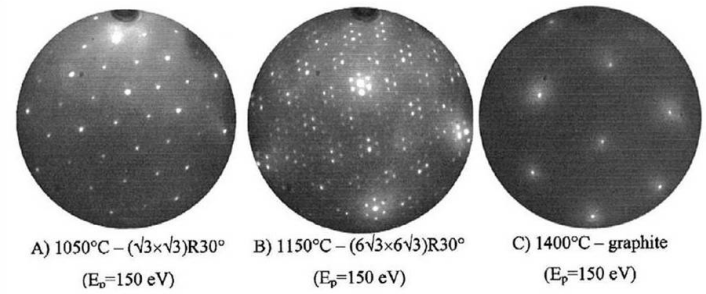

Figure 5.4: A sequence of LEED panels obtained on a 6H-SiC(0001) surface with an energy of 150 eV. One can distinguish the different surface reconstruction depending on the annealing temperature: A) $\sqrt{3} \times \sqrt{3} - R30$ at 1050°C; B) $6\sqrt{3} \times 6\sqrt{3} - R30$ at 1150°C and C) 1×1 of graphite formed at 1400°C [181].

above the SiC(0001) substrate. In agreement with density functional theory calculations [131], PES results [160] [161] showed that the interfacial layer consists of two inequivalent types of C-atoms. One part of these atoms are sp^2 hybridized and arranged in graphene-like (σ type bonds) honneycomb structure. Remaining C-atoms are covalently bonded to Si atoms from the underlying substrate.

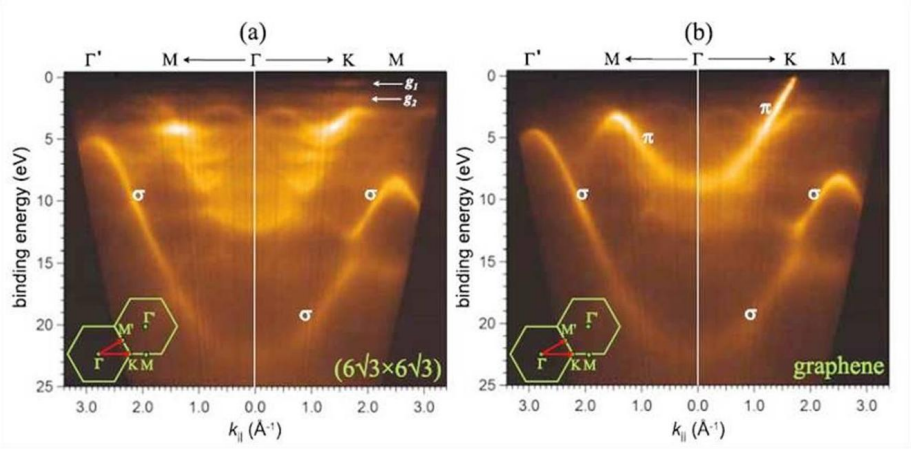

Figure 5.5: Photoelecton intensity map vs. binding energy and parallel electron momentum of (a) $6\sqrt{3}$ reconstructed buffer layer and (b) one monolayer graphene on top of the buffer layer. Photon energy was $h\nu$=50 eV. The insets show the direction of the direction of $k_{||}$ within the hexagonal Brillouin zone of graphene. σ-bands are clearly present in the $6\sqrt{3}$ buffer layer with a lack of π-bands. This shows that the buffer layer has no graphene-like electronic structure. Image (b) shows σ- and π-bands, the signature of the first graphene layer [161].

Due to its strong (covalent) interaction with the underlying substrate, the interfacial layer ($6\sqrt{3}$ reconstructed) has no graphitic electronic properties [131]. Its band structure deviates from that of graphene in the range of π-bands as demonstrated by ARPES measurements [160] [161] and *ab initio* calculations

[131]. It therefore acts as a buffer layer and decouples the subsequent graphene layers from the substrate. The interfacial layer is often referred to as "layer 0" or "0^{th} graphene layer". ARPES band structure measurements and *ab initio* calculation demonstrated that the next carbon plane grown on top of the buffer layer shows a "real" graphene-like Dirac band structure. It hence forms the first epitaxial graphene layer with π-bands signature (see figure 5.5 (b)).

The structure of epitaxial FLG on SiC(0001)

According to the structural model suggested by PES results in [160] and *ab initio* calculation in [131], we summarize the structure of FLG on SiC(0001) system as the following:

- The Bulk SiC with a Si-terminated surface (SiC(0001)).
- An interfacial layer formed by a single C-layer (with no graphene-like electronic character) on top of the bulk which bonds covalently to the underlying substrate. The surface of this layer has a $6\sqrt{3}$ reconstructed structure.
- Graphene layers grown on top of the buffer layer. These layers are decoupled from the substrate and have no interaction with it.

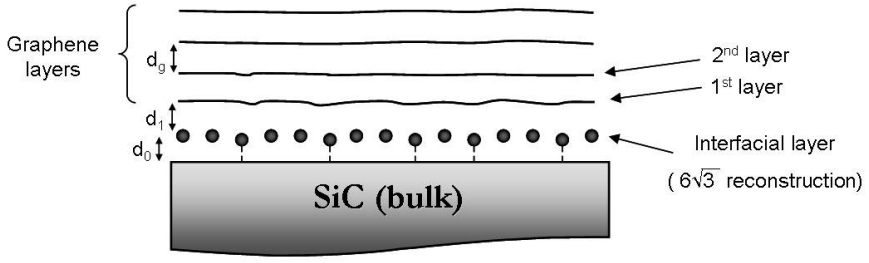

Figure 5.6: A schematic model of FLG on SiC(0001) system. The interface consists of the first C-rich plane which bonds covalently (covalent bonds represented by dashed lines) to the underlying SiC substrate. According to [131], $d_0 \sim 2.0$ Å is the distance of the interfacial layer with respect to the top outermost atoms of the last SiC bilayer. The 1^{st} layer graphene (second C plane) is at $d_1 \sim 3.8$ Å from the interfacial layer [131]. Subsequent graphene layers are spaced by $d_g \sim 3.9$ Å. Note that these distances were determined by *ab initio* calculations. Experimentally, the distance between two adjacent graphene layers is estimated ~ 3.35 Å.

Figure 5.6 shows a sketch representing the FLG on SiC(0001) system as described above. This model will be therefore helpful to understand further characterization results including XPS as well as local work function measurements detailed below.

5.2 Methodology of experiments

Multiple experiments (Raman, XPS, KFM and photo-electron spectromicroscopy) were performed in this study for the characterization of the FLG on SiC(0001) sample. Here we describe the methodology followed for the ensemble of experiments and sample treatments.

- First, Raman spectroscopy and micro-Raman (μ-Raman) experiments were done in order to identify the growth of FLG on the SiC(0001) surface.
- Second, micro-XPS (μ-XPS) measurements were performed over a selected area of the surface corresponding to a field of view (FoV) of 38.3 μm. Experiments were used to identify the chemical composition of FLG on SiC(0001).
- Third, XPEEM experiments were conducted at the emission threshold energy. Local work function of FLG was measured and work function maps were reproduced over the entire FoV. The dependence of FLG work function on the number of layers was investigated with these experiments.
- Fourth, KFM measurements were performed over the same area of the sample surface. CPD variations and work function variations were compared to XPEEM results. Highly resolved MF-EFM measurements were also carried out.
- Fifth, spectromicroscopy measurements at core-level energies were performed. Core-level spectra (C1s and Si2p) were extracted locally at precise regions of the FoV. The thickness of FLG was estimated using the simple attenuation model applied to the Si2p signal.

Sample preparation After being synthesized, the sample was resistively heated in UHV ($\sim 10^{-10}$ mbar) at $\sim$ 800 °C for 30 min. in order to eliminate surface contamination. As we will see later, μ-XPS and XPEEM (emission threshold) measurements were all performed before and after sample heating. Detailed practical aspects of sample orientation and handling are provided in the appendix section (see appendix D).

5.3 Experimental Results

5.3.1 Raman spectroscopy and μ-Raman imaging

5.3.1.1 Raman spectroscopy: identification of graphene

Raman spectroscopy is used to identify the growth of graphene on the SiC(0001) surface. For this aim, Raman spectra were measured for the SiC(0001) surface

before the thermal graphitization (annealing at 2000°C) was performed.

Figure 5.7 shows the characteristic second order peak of the initial SiC(0001) surface (blue line). Upon annealing at 2000°C for 30 min. in Ar atmosphere (∼ 600 mbars), the corresponding Raman spectrum (red line) shows the presence of two features characteristic of graphene formation on the substrate surface: the G peak (at $\sim$ 1600 cm^{-1}) and the $2D$ band (at $\sim$ 2710 cm^{-1}) [154].

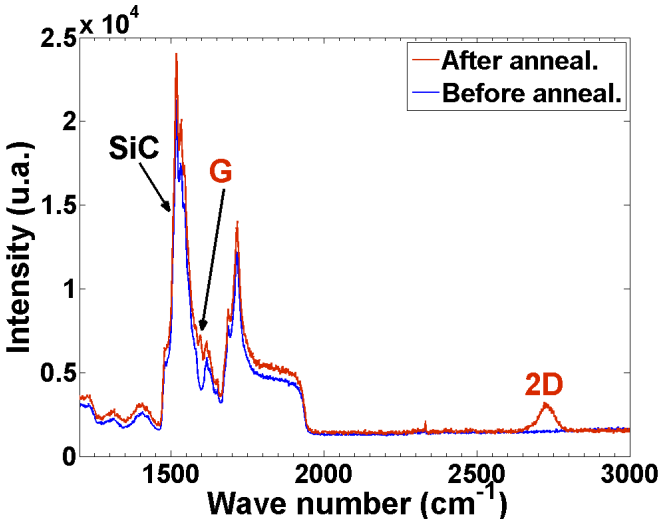

Figure 5.7: The Raman spectra acquired over the initial SiC(0001) substrate before graphitization (blue spectrum) and over the same substrate after the graphene started to grow (red spectrum). The G peak and the $2D$ band reflect the presence of graphene on the SiC(0001) surface.

5.3.1.2 μ-Raman imaging: heterogeneity of graphene layers

The coverage of graphene was identified by μ-Raman imaging experiments (see figure 5.8). Experiments were carried out on a Jobin Yvon T64000 Raman system. An Ar-Kr laser was used at the wavelength $\lambda = 514$ nm. The μ-Raman imaging was performed by scanning a 20 μm^2 area of the sample surface with a 1 μm step.

These measurements are based on the interpretation of the $2D$ band located around 2710 cm^{-1} in the Raman spectrum of graphene. In Raman experiments on graphene, the composition of the $2D$ band varies when the changing number of graphene layers [171]. Thus, $2D$ bands were extracted at each scanning step of the image and were deconvoluted as seen in figure 5.8 (b). Images (a) and (c) in figure 5.8 correspond to the lateral variation of the $2D$ band deconvolution components. The contrast in these images is the fingerprint of a lateral non-

homogeneity of graphene thickness over the sample surface. We thus know that FLG with different thicknesses coexist on the SiC(0001) surface. However, due to the scanning step of 1 μm, current μ-Raman experiments do not present a sufficient spatial resolution to accurately characterize the lateral FLG thickness distribution.

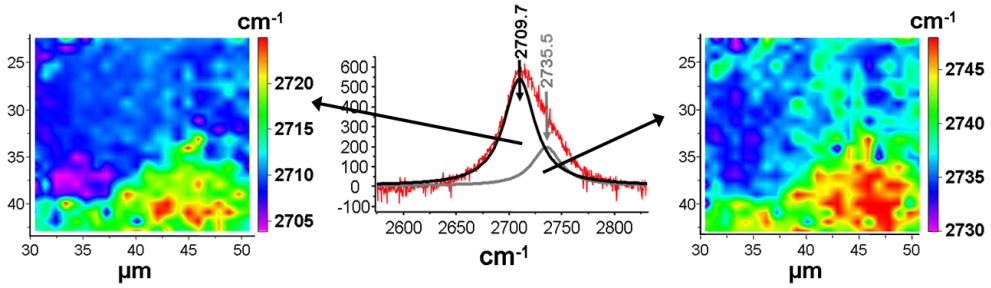

Figure 5.8: The Raman imaging of the two components of the asymmetric 2D band. The contrast of these images reflects a non-homogeneous graphene coverage over the surface. Thus graphene layers with different thicknesses coexist.

5.3.2 μ-XPS: chemical analysis over the entire FoV

Here we show results of μ-XPS measurements performed over the entire FoV (38.3 μm). The goal of these experiments is to investigate the average chemical structure of our sample. Measurements were systematically performed before and after surface treatment (heating in UHV at 800 °C for 30 min.). Effects of the sample heating on the chemical structure are also investigated.

5.3.2.1 Experimental parameters

Measurements were performed using the spectroscopy mode of the *NanoESCA*. The laboratory monochromatic focused X-ray source (FXS), Al K-α ($h\nu$=1486.6 eV) was used. The field of view was fixed to 38.3 μm. In all experiments, the size of the FXS beam spot was adjusted to 30μm for an improved flux of the photon source and a better yield of emitted photo-electrons. Table 5.2 summarizes the parameters of the PEEM column and the IDEA system. Parameters were adjusted for the best possible transmission of electrons within the microscope which impacts the overall counting statistics.

Table 5.2: The parameters applied to the *NanoESCA* in the present XPS experiments.

FXS spot size	CA	E_{pass}	EA_1	EA_2
30 μm	500 μm	100 eV	1 mm	4 mm

5.3.2.2 Survey spectra

The survey spectra were acquired by sweeping the kinetic energy of the photo-electrons between 850 eV and 1486 eV. The energy step is 0.5 eV and the time aquisition 1 sec/step. Unresolved spectra are obtained (figure 5.9) for the cases before (a) and after (b) sample heating in UHV at 800 °C for 30 min. Peaks of the carbon C1s ($\sim$ 285 eV), the silicon Si2s ($\sim$ 150 eV) and Si2p ($\sim$ 100 eV) are observed. Spectra show no trace of oxygen (O) (Binding energy $\sim$ 543 eV) on the sample surface. For the SiC(0001) surface, Johansson *et al* [182] demonstrated that the oxygen disappears from the surface before the $\sqrt{3}$ reconstruction develops upon annealing the SiC substrate.

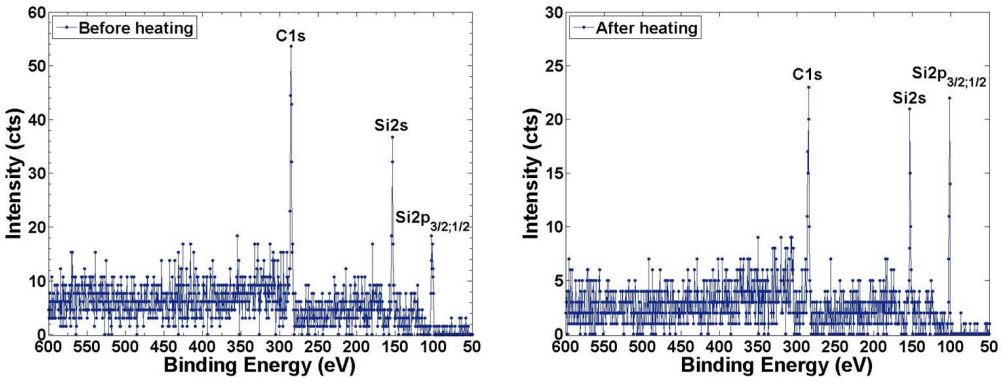

Figure 5.9: (a) The global spectrum at the initial state of the sample, before heating. (b) Spectrum obtained after heating. Spectra show no trace of oxygen on the sample surface.

Photoelectron spectrum in figure 5.9(b) shows the evolution of C1s and Si2p peaks after the sample heating in UHV. The intensity ratio of the C1s to Si2p peaks is observed to decrease after heating (see table 5.3). This indicates that a certain amount of carbon atoms desorb from the surface upon heating. It can be associated with carbon contamination, which is usually expected to desorb for heating temperatures above 600°C.

Although orbitals of the same element are expected to vary similarly, the intensity of the Si2s peak is observed to decrease after heating (contrary to that of the Si2p). This likely results from large uncertainties due to the very low energy resolution of survey spectra.

The investigation of the surface chemistry is thus further detailed by studying the high resolution spectra of the C1s and Si2p peaks, acquired before and after heating over the entire field of view (FoV = 38.3 μm).

Peak intensity (a.u.)	C1s	Si2s	Si2p	C1s/Si2p
Before heating	54	37	19	2.9
After heating	23	21	22	1.05

Table 5.3: The intensities of the carbon and silicon peaks as evaluated from the global spectra before and after heating.

5.3.2.3 High resolution spectra

Experimental procedure

The high resolution spectra were acquired at the C1s and the Si2p peaks before and after sample heating using the same microscope settings as presented in table 5.2.

The overall energy resolution ΔE can be written as the convolution of three Gaussian functions: the resolution of the spectrometer ΔE_{sp}, the width of the photon source ΔE_{ph} and the broadening due to the temperature ΔE_{KT}. It is given by the following expression:

$$\Delta E = \sqrt{\Delta E_{sp}^2 + \Delta E_{ph}^2 + \Delta E_{KT}^2}. \tag{5.1}$$

At ambient temperature 4 KT $\sim$ 0.1 eV. $\Delta E_{ph} \sim 0.26$ eV, and using a first slit of width EA1 = 1 mm with a pass energy E_{pass} = 100 eV, $\Delta E_{sp} \sim 0.4$ eV (here we consider only EA1 since it is the case of a spherical analyser with the IDEA system, and not an hemispherical analyser. Thus, EA2 do not get much importance in the determination of ΔE_{sp}). Based on these values, the overall energy resolution in the current experiments is $\Delta E = 0.63$ eV.

The C1s spectrum was acquired by sweeping the binding energy of the core level photo-electrons between 281.1 eV and 289.1 eV with a step of 0.025 eV. The Si2p spectrum was acquired by sweeping the binding energy of the core level photo-electrons from 97.6 eV to 105.6 eV with a step of 0.025 eV. The acquisition time was fixed to 10 sec. per step. Each spectrum was averaged over 50 sweeps.

The core-level spectra are shown in figures 5.10 and 5.11. The C1s and Si2p line shapes characterize the chemical states of the C and Si atoms in our sample, respectively. Given their shapes and widths, there are obviously several components to the C1s and Si2p lines. To deconvolute them, we fitted the spectra using the XPSPEAK program (developed by Raymond Kwok, from the Chemistry Dept. at CUHK, for analyzing core level spectra). The fit parameters (energy position, Lorentzian width, spin-orbital split (0.6 eV for Si2p)) were chosen close to those used in reported studies of similar graphene on SiC(0001) systems [160] [163] [183] [182] [184]. An integral background subtraction method was applied

to all spectra using the Shirley background model [81].

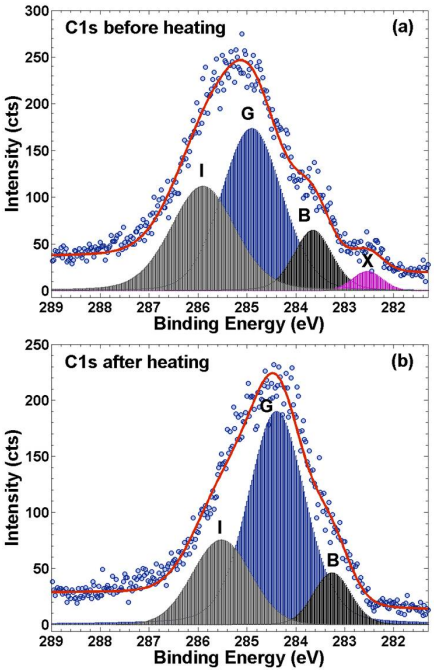

Figure 5.10: The fit model (red curve) to the data (blue circles) of the C1*s* spectra before (a) and after (b) heating.

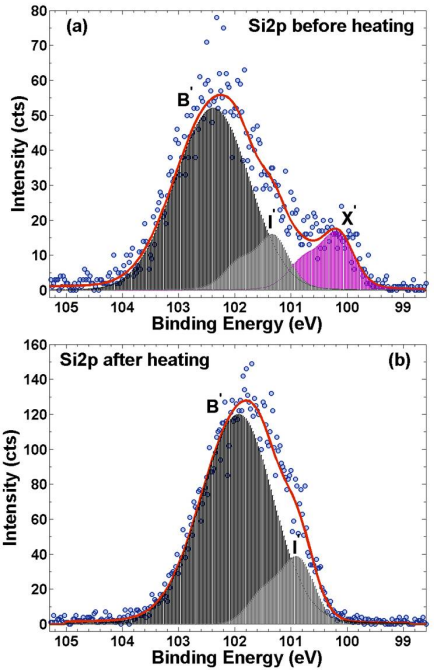

Figure 5.11: The fit model (red curve) to the data (blue circles) of the Si2*p* spectra before (a) and after (b) heating.

Chemical state components: assignments and interpretation

C1*s* spectra

The best fits (red curves) to the data (blue circles) of the C1*s* spectra before and after heating are represented in figure 5.10 (a) and (b), respectively. Four components, labeled B, G, I and X, were needed to fit the C1*s* spectrum before heating adequately. The energy position of peak B is found at 283.65 ± 0.1 eV and 283.25 ± 0.1 eV, before and after heating respectively. The peak G is found at 284.9 ± 0.1 eV (before heating) and 284.4 ± 0.1 eV (after heating). The peak I is found at 285.9 ± 0.1 eV and 285.5 ± 0.1 eV, before and after heating respectively. The peak X is located at 282.55 ± 0.1 eV before heating. It is missing from the C1*s* spectrum after heating.

Following recent studies on few layer graphene (FLG) thermally grown on SiC (0001) substrate [183] [160] [161] [163], peak B corresponds to C-atoms in the bulk SiC substrate. Peak G to C-atoms in the graphene/graphite layers and peak I to C-atoms in the interface ($6\sqrt{3}$ reconstructed) layer between the

C1s spectra

	Before heating		After heating		BE shift
Components	BE	FWHM	BE	FWHM	Δ_{BE}
B: bulk-SiC	283.65	0.93	283.25	0.90	0.4
G: graphene/graphite	284.9	1.45	284.4	1.35	0.5
I: interface	285.9	1.55	285.5	1.40	0.4
X: unclear	282.55	0.7	-	-	-
Carbon contamination signal is expected at 285 eV $\leq$ BE $\leq$ 285.5 eV, before heating.					

Table 5.4: The fit parameters for the C1s spectra before and after heating. The uncertainty on the BE and FWHM values is ± 0.1 eV.

substrate and graphene overlayers. The origin of peak X is, however, not clear and will be discussed later. Carbon contamination is expected before heating at the binding energy 285 eV $\leq$ BE $\leq$ 285.5 eV. It desorbs from the sample surface after heating, as suggested by the survey spectra (see section 5.3.2.2). The assignments and fit parameters of the C1s spectra are summarized in table 5.4.

Based on the value of the overall energy resolution $\Delta E = 0.63$ eV, the peak corresponding to the carbon contamination could not be resolved on the C1s spectrum before heating. The signal from the carbon contamination is thus expected to interfere with that of peaks I and G (given its position between both these peaks). This explains why the FWHMs of peaks I and G are higher on the C1s spectrum before heating (see figure 5.10).

However, the peaks I (interface) and G (graphene/graphite) remain relatively broad after heating (FWHM = 1.4 ± 0.1 eV and 1.35 ± 0.1 eV, respectively). This point deserves a comment, which we provide in the following section.

The interface-related peak I Recent PES experiments [160] [161] showed that the interfacial ($6\sqrt{3}$ reconstructed) layer consists of a single carbon plane with two inequivalent types of C-atoms. One-third of these atoms are covalently bonded to the underlying SiC substrate. The other two-thirds are sp^2-hybridized and bond to C-atoms within this layer in a hexagonal honeycomb structure with graphene-like σ type bonds (as seen from ARPES results in figure 5.5).

For this $6\sqrt{3}$ reconstructed layer, Emtsev *et al.* [160] reported three components for the C1s spectrum. One of which is related to bulk SiC, and the other two to the inequivalent types of C-atoms in this layer. The width of the signal including both these C-related components is $\sim$ 1.5 ± 0.1 eV [160], which is similar to that of peak I (FWHM $\sim$ 1.4 ± 0.1 eV) on our spectrum after heating. However, because of the low overall energy resolution, peak I could not be decomposed into subsequent components. Its signal thus includes that

issued from both types of C-atoms in the interfacial layer, which explains its large FWHM.

The graphene/graphite-related peak G In a recent study, Hibino *et al.* [164] measured C1*s* spectra for regions with different thicknesses using PEEM images of non-homogeneous FLG grown on SiC(0001). They showed that the position of the C1*s* spectra presents a down-shift of ~ 0.4 eV between 1LG and thick graphite layer (≥ 10 LG) regions. This shift was attributed to a transfer of negative charge from the substrate to graphene overlayers [164] [160]. The width of the envelope signal including all C1*s* spectra for different layer thickness is $\sim 1.3 \pm 0.1$ eV. This width is in accordance with the FWHM (1.35 ± 0.1 eV) of peak G in our C1*s* spectrum after heating.

This means that peak G should include the signal from regions on the surface with different graphene layer thicknesses. However, a high energy resolution is required in that case in order to distinguish these components. This is not possible in our case because of the low overall energy resolution. We could then explain the large FWHM by the non-homogeneity of the graphene layers over the present area under study. This is in accordance with the non-homogeneity of the results from Raman imaging experiments previously presented (see figure 5.8).

Now we will show that it is possible to learn more about the thickness of these layers by estimating the intensity ratios of the G and I peaks.

The intensity ratio of G/I peaks In another work, using LEEM, PEEM and conventional PES, Virojanadara *et al.* [163] measured the C1*s* spectra for areas of FLG with the thicknesses of 0.5, 1 and a mixture of 1-4 monolayers. They showed that the intensity ratio of the graphene-related component (G) and the interface-related component (I) provided a good estimate of the number of graphene layers.

For an area with a mixture of 1-4 ML graphene, authors found the intensity ratio G/I = 2.9. This value is very close to that measured from our C1*s* spectra after heating, G/I = 2.7. It indicates that the present area under study (entire FoV) may consist of graphene layers with thicknesses ranging from 1ML to 4 ML graphene. This is strongly supported by work function measurements at the emission threshold energy (presented later in section 5.3.3.4).

Si2*p* spectra

The best fits (red curves) to the data (blue circles) of the Si2*p* spectra before and after heating are represented in figure 5.11 (a) and (b), respectively. Three components, labeled B′, I′ and X′ were needed to fit the Si2*p* spectrum before heating. The energy position of peak B′ is found at 102.2 ± 0.1 eV (before

Si2p spectra

	Before heating		After heating		BE shift
Components	BE	FWHM	BE	FWHM	Δ_{BE}
$B^{'}$: bulk-SiC	102.2	1.35	101.8	1.31	0.4
$I^{'}$: interface C-Si *(covalent)*	101.3	0.65	100.9	0.68	0.4
$X^{'}$: interface Si-*dangling bonds*	100.2	0.68	-	-	-

Table 5.5: The fit parameters for the Si2p spectra before and after heating. The uncertainty of the BE and FWHM values is ± 0.1 eV.

heating) and 101.8 ± 0.1 eV (after heating). Peak I$^{'}$ is located at the binding energy 101.3 ± 0.1 eV (before heating) and 100.9 ± 0.1 eV after heating. Peak X$^{'}$ is located at 100.2 ± 0.1 eV before heating. It is missing from the Si2p spectrum after heating.

Following the study in [185] on graphite thermally grown on SiC(0001) substrate, the most tightly bound peak B$^{'}$ corresponds to Si atoms in the bulk SiC substrate. The less bound peaks I$^{'}$ and X$^{'}$ are ascribed to regular Si sites or specific defects in the C-rich interface layer between the SiC substrate and the grown graphene/graphite layers.

According to the structural model of the interfacial ($6\sqrt{3}$ reconstruted) layer in [160] and following a recent PES study by Virojanadara *et al.* [163] on FLG/SiC(0001), peak I$^{'}$ may be assigned to Si-atoms (in the topmost SiC bilayer) covalently bonded to C-atoms in the interface layer. Peak X$^{'}$ with the smallest binding energy can be assigned to Si-atoms, in the topmost SiC layer, bonded to fewer than four C-neighbor atoms [185]. These atoms are likely to form dangling bonds at the interface as predicted by *ab intio* calculations [131] [186]. They result from the near commensuration of the SiC(0001) surface and the graphene lattices [131] [160].

The disappearance of peak X$^{'}$ upon heating is further discussed in the next paragraph. The assignments and fit parameters of the Si2p spectra are summarized in table 5.5

Effects of sample heating: discussions

Heating the sample (in UHV at 800°C for 30 minutes) induces significant changes in the shape and energy position of the C1s and Si2p spectra. Firstly, all spectral components shift toward lower binding energies. Secondly, both the X and X$^{'}$ peaks disappear from the C1s and Si2p spectra, respectively. In the following part we will explain our attempt to interpret these changes.

The chemical shifts A down-shift $\Delta_{BE} = 0.4$ eV is observed for all bulk-related (B, B$'$) and interface-related (I, I$'$) components in the C1s and Si2p spectra after heating. However, the graphene/graphite-related component G in the C1s spectra shifts by $\Delta_{BE} = 0.5$ eV toward lower binding energies after heating. A similar shift (0.4 eV) of the bulk SiC component in the C1s spectrum was noted before [184]. It was attributed to a Fermi level (E_F) pinning effect associated with surface metalization.

The Fermi level pinning effect in semiconductors can be caused by the presence of electronic states, within the band-gap, that may fix the E_F position. For the epitaxial graphene on SiC(0001) system, density functional theory calculations [131] [186] and STM experiments [173] showed the presence of such electronic states close to E_F. They were interpreted to originate from the presence of Si-atoms, at the SiC(0001) - graphene interface, which exhibit dangling bonds that point toward the graphene layers [131]. PES measurements [185] also suggested the presence of Si-atoms bonded to fewer than four C neighbors, at the SiC(0001) - graphite interface. The peak X$'$ in our Si2p spectrum before heating shows the signature of such Si-atoms.

Since all energies (in our experiments) are referred to E_F, then the common shift of all (bulk and interface-related) peaks indicates a displacement of the Fermi level after heating. This supports the presence of electronic states before heating which initially fix the E_F position in our sample. It is then possible to suppose that sample heating induces an atomic re-arrangement at the interface resulting in the absence of these states. This seems likely since peak X$'$ disappears from the Si2p after heating, given that the electronic states were attributed to the presence of Si-dangling bonds at the interface represented by this peak (X$'$) in our measurements.

However, the larger shift ($\Delta_{BE} = 0.5$ eV) toward lower binding energies of the graphene/graphite-related component (G) deserves an additional comment. In fact, ARPES experiments and *ab initio* calculations have demonstrated that graphene layers, grown on SiC(0001) substrate, are n-doped. This doping is attributed to the transfer of a negative charge from the substrate to these layers [160] [131] [161] [165]. Simulations of ARPES band structures using tight binding calculations [165] showed that the total charge density in the as-grown few layer graphene remains roughly constant ($7.0\pm\ 1.0 \times 10^{-3}$ electrons/unit cell) [161]. About 85% of this charge resides in the layer closest to the substrate (the first graphene layer); most of the rest in the second layer [165] [161].

We suppose that this charge distribution may result in the formation of a dipole moment between the interfacial layer and graphene overlayers. The presence of such a dipole (under the graphene layers) can induce a change of the local vacuum level in graphene. Therefore, when the Fermi level shifts upon

heating (see above), the displacement of graphene-related binding energy would be higher than that of the bulk or interface-related one. This may explain the larger down-shift ($\Delta_{BE} = 0.5$ eV) of G compared to that of all bulk and interface-related peaks ($\Delta_{BE} = 0.4$ eV), as observed in our case. A similar interpretation was suggested recently by Hibino *et al.* [164] in order to explain the graphene work function dependence on the number of layers.

The chemical shifts of all spectral components in our experiments coincide with the disappearance of the low binding energy peaks X and X$'$ from the C1s and Si2p spectra respectively. However, the origin of peak X remains a subject for discussion.

The C1s low binding energy component X In an early PES study, Johansson *et al.* [182] investigated the chemical composition of the SiC(0001) surface at different stages of graphitization. For the complex surface reconstruction formed by a mixture of the $6\sqrt{3}$ and $\sqrt{3}$ structures, they reported a component located at $\sim$ 282.6 eV (same as the binding energy of peak X (282.55 $\pm$ 0.1 eV) in our measurements). This component (at 282.6 eV) was interpreted to originate from the second bilayer of the substrate surface affected by the arrangement of atoms in the $\sqrt{3}$ reconstruction [182].

The complex structure (mixture $6\sqrt{3} - \sqrt{3}$) was obtained after annealing the SiC(0001) substrate at 1150°C for 2 min. However, upon further heating at higher temperature ($\geq$ 1250°C) the surface was fully reconstructed in a $6\sqrt{3}$ structure and the component at 282.6 eV was no longer present in the corresponding C1s spectrum [182].

These reported observations raise an interesting question concerning the origin of peak X in our C1s spectrum before heating. Can the interfacial layer in our case be formed by a mixture of a $6\sqrt{3}$ and $\sqrt{3}$ reconstructions? Still this option is subjected to two different arguments.

On the one hand, the present sample was synthesized at 2000°C for 30 min. According to reported experimental data (see section 5.1.3.1), the interfacial layer would then be expected to be fully reconstructed in a $6\sqrt{3}$ structure when the substrate is annealed at such high temperatures.

If this argument is considered, then it becomes difficult to interpret the origin of X. In fact, no component at a binding energy close to X was previously reported from PES studies of graphene on SiC(0001) systems with the interfacial layer fully $6\sqrt{3}$ reconstructed [182] [161] [163] [183].

On the other hand, extended *ab initio* calculations [180] were performed in the actual $6\sqrt{3}$ cell with respect to SiC that correspond to the interface geometry on the SiC(0001) surface. Calculations, compared to STM measurements [186]

[180], showed that the actual interfacial layer is nanostructured due its strong interaction with the underlying substrate. This nanostructuration of the interface results in the presence of regions with an unexpected local $\sqrt{3}$ symmetry, beside the actual $6\sqrt{3}$ symmetry imposed by calculations.

If the argument of *ab initio* calculations is considered, then peak X may be interpreted to originate from C-atoms in the second SiC bilayer affected by surface rearrangements in the $\sqrt{3}$ structure, as suggested by Johansson *et al.* [182]. Given that the $\sqrt{3}$ geometry was demonstrated to cause the formation of dangling bonds at the interface (as described in [131]), peak X may be related the presence of electronic states before heating from the interfacial dangling bonds (see above). This is likely possible because peak X disappears after heating (as in the case of peak X' (see above)).

Nevertheless, several questions could be asked concerning what actually happens during the sample heating. Why does peak X disappear from the C1s spectrum after heating? Does the interfacial layer undergo structural reconstruction changes during heating?

Unfortunately from the present experiments no clear evidence concerning the structure of the interface in our sample could be provided. These questions thus remain unanswered and the origin of peak X not clearly identified. Additional LEED or XRD experiments may be envisaged to characterize the exact structure of the interface, before and after heating. This may show its evolution upon heating and help reveal some of the ambiguities presented in our present XPS results.

Summary

The chemical structure of the sample

The deconvolution of the C1s and Si2p spectra showed a structure of our sample consistent with the latest model proposed in the literature for the FLG on SiC(0001) systems, namely:

- The bulk SiC whose signature was represented by peaks B and B$'$ on the C1s and Si2p spectra respectively.
- The interfacial C-rich layer in which C-atoms exhibit two different chemical environments:
  - Some of these C-atoms are covalently bonded to Si-atoms from the underlying substrate surface. Their signature was represented by peak I$'$ on the Si2p spectra.

  - The other C-atoms are bonded to neighbor C-atoms within the interface layer (sp^2-hybridized). Peak I on the C1s spectra represented the signature of both these sp^2-hybridized C-atoms and those covalently bonded to the substrate.

- Graphene/graphite layers grown over the interfacial layer. Their signature was represented by peak G.

The sketch in figure 5.12 shows a simplified description of the chemical bonding configuration in our sample as deduced from the present spectra deconvolution and based on the literature reported data.

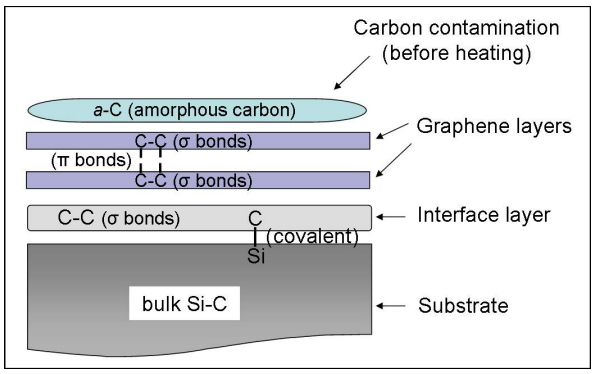

Figure 5.12: A sketch model describing the chemical structure of our sample, based of the data reported from literature and supported by the fit of both the C1s and Si2p spectra. The different chemical bonding configurations are represented.

Moreover, the analysis of graphene-related (G) and interface-related (I) showed two important pieces of information in agreement with other results in this work. Firstly, the width of peak G pointed out the non-homogeneity of graphene layers over the present area under study (in agreement with Raman imaging results). Secondly, the intensity ratio G/I provided an estimation of the thickness of these layers (in agreement with following measurements of the local work function).

Heating effects: Fermi level shift and dipole formation

The analysis of the sample heating effects on the C1s and Si2p spectra, supported by literature data, suggested the presence of electronic states before heating associated with the formation of Si-dangling bonds at the interface. The large down-shift of the graphene/graphite-related component G compared to all other components was explained by the formation of a dipole moment under the graphene layers. This dipole was interpreted to originate from the distribution of the charge that transfers from the SiC(0001) substrate to graphene layers through the interface.

5.3.3 Work function from threshold XPEEM measurements

In this section, we use XPEEM spctromicroscopy in the range of secondary electrons (SE), and we measure the local work function from the photoemission

threshold energy. Using SE PEEM images we also reproduce a two-dimensional work function map for FLG over the entire FoV.

5.3.3.1 Experimental protocol

Measurements of the photoemission threshold energy were performed using the energy-filtered imaging mode of the *NanoESCA*. The mercury UV photon source (Hg: $h\nu$= 4.9 eV) and the monochromatic focused X-ray source (FXS: $h\nu$= 1486.6 eV) were used. The parameters of the PEEM column and the IDEA system were adjusted for the best possible compromise between a good transmission and a good spatial resolution. These parameters are summarized in table 5.6 for the Hg and FXS sources.

CA	E_{pass}	EA1	EA2	Detector	time per image
150 μm	100 eV	1 mm	4 mm	950/4000 V(Hg)	5 sec (Hg)
500 μm	100 eV	1 mm	4 mm	1000/4000 V(FXS)	120 sec (FXS)

Table 5.6: Parameters of the NanoESCA and IDEA for the energy filtered ESCA imaging mode at threshold energy with FXS and Hg sources

First, the direct non-energy filtered mode was used with the Hg photon source for locating the zone of interest on the sample surface. This zone was determined with respect to a cross mark pattern made with focused ion beam (FIB) and used as a referential position (see appendixD). The zone was chosen sufficiently away (∼200 μm) from this cross mark to avoid probing any surface effects induced by the gallium ion beam used in the FIB milling procedure.

Second, the *NanoESCA* was switched to the energy-filtered mode. The surface was imaged at FoV = 38.3 μm. Image series were acquired in the range of secondary electrons between 2 eV and 8 eV range using both the Hg and FXS sources with a step of 0.025 eV. All energies are referred to the Fermi level and electron energy is noted as $(E - E_F)$.

5.3.3.2 The contrast of PEEM images

Figure 5.13 shows two SE PEEM images acquired at the threshold energy of $E - E_F$= 4.5 eV using the Hg (a) and the FXS (b) photon sources. The upper part of figure 5.13 shows images (a,b) taken before heating. The lower part shows images (c,d) taken at the same zone after sample heating. Intensity level changes on images are observed at different regions of the surface. The image contrast reflects a lateral non-homogeneous dependency of different surface regions on the energy of SE.

The Hg-acquired images (figure 5.13 (a), (c)) exhibit a higher intensity with respect to the FXS-acquired images (figure 5.13 (b), (d)). This is related to two aspects: (i) a much higher brightness of the Hg photon source, (ii) the narrower

energy distribution of UV photon sources at the threshold energy. This latter leads to a higher transmission through the microscope [86] and a better spatial resolution.

The choice of photon source It should be noted, however, that the signal acquired using low-energy UV (Hg) sources includes important contributions from direct transitions. This affects the intensity distribution on the Hg-acquired images near the photoemission threshold. These images are only used for locating the positions of interest in the FoV. However, they are not used for further work function investigations. At high-energy excitation (X-rays), the photoemission threshold represents a true SE signal, and direct transitions play no role in the intensity distribution near the photoemission threshold. Therefore, only the FXS-acquired images are used for the investigation of the local work function measurements presented below.

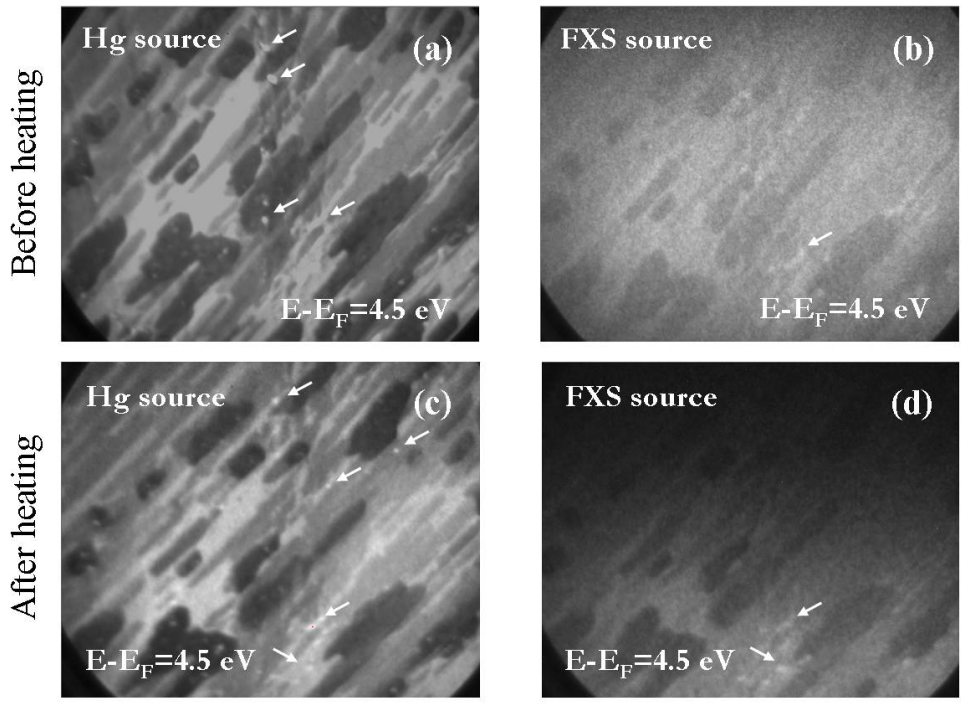

Figure 5.13: PEEM images taken at the SE threshold energy E-E$_F$ =4.5 eV with the Hg and FXS source: before heating (a)(b) and after heating (c)(d).

Surface dependent effects are more pronounced on the Hg-acquired images (a,c). Topography features (resulting from the presence of defects or dust) can induce notable changes in the intensity level observed on images. Such features were observed on the Hg-acquired images and are indicated in figure 5.13 with

white arrows. Most of them are not observed on the FXS-acquired image. The small remaining ones are probably caused by high local topographical features.

After heating, the contrast in images (c) and (d) remains similar to that before heating (images (a) and (b)). No morphological changes of the surface were observed. Bright features (white arrows) also remain visible on images after heating. A vertical displacement is noted for images (c) and (d) after heating with respect to images (a) and (b). It results from the repositioning of the sample in the analysis chamber or the microscope, after heating.

Imaging artifact After heating, a dark stripe is observed on the upper part of the FXS-acquired image (figure 5.13 (d)). We verified that this stripe remains visible for all SE images taken at different energies. It results from a bad regulation of the first entrance slit (EA_1) of the first electron analyser. This eclipses the electron signal in the upper part of the acquired images.

The intensity level over this part of the image is thus artificially low. It could not be used for further measurements of the local work function. For that, this artificially dark (upper) part was removed from all images acquired after heating. Image dimensions are therefore modified compared to those acquired before heating (see figures 5.14 and 5.15).

Image series Image series were recorded around the photoemission threshold energy in the 2-8 eV range with a 0.025 eV step. Figures 5.14 and 5.15 show single energy images taken between 3.5 eV and 6 eV, before and after heating respectively.

The features' positions and shapes are quite similar on all images at different electron energies. Before heating, the contrast fades at the SE energy $E - E_F$ = 5 eV. It re-appears at around 5.5 eV similarly to images at smaller energies. For electron energy $E - E_F = 6$ eV no contrast is observed. After heating, the contrast starts to be visible around $E - E_F = 4$ eV. It remains similar for all images at higher energies. For electron energy $E - E_F = 6$ eV, the intensity of the image becomes very low. To understand the energy dependence of the XPEEM images, SE emission spectra were extracted from the image series between 2-8 eV at different positions shown in figures 5.14 (c) and 5.15 (b).

5.3.3.3 Secondary electron emission spectra

Each SE spectrum was extracted from a 500 × 500 nm^2 region. The photoelectron energy was corrected for the Schottky effect ($\Delta E_{Schottky}$=98 meV) and for the non-isochromaticity at the exit of the IDEA system (parabolic energy dispersion) while extracting the spectra (see appendix B).

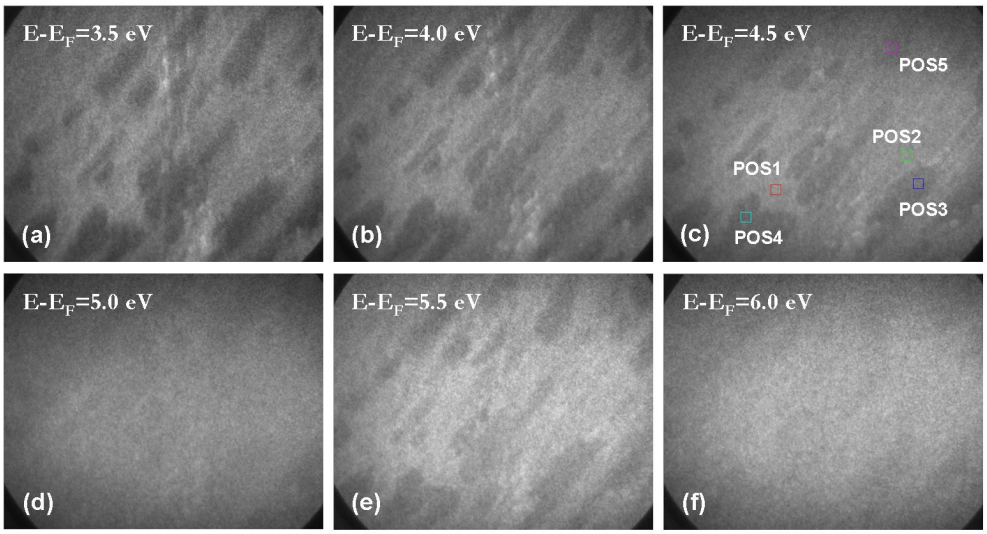

Figure 5.14: XPEEM images at the photoemission threshold (before heating) recorded at different photoelectron energies, $E - E_F$. FoV = 38.3 μm, CA = 500 μm and acquisition time = 120 sec. Areas of interest (500 $\times$ 500 nm^2) indicated with colored squares (c).

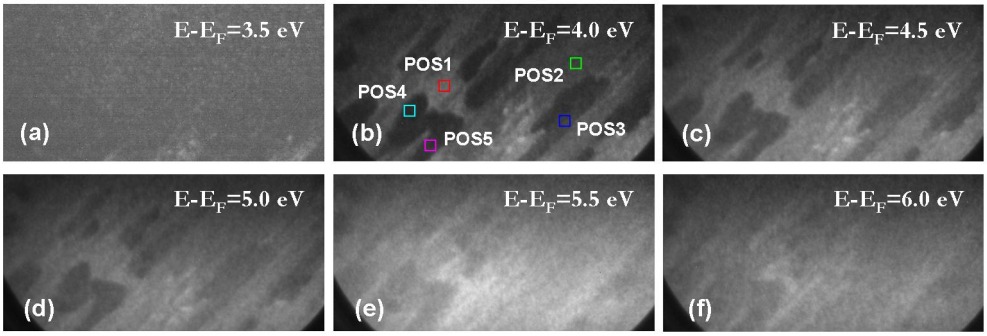

Figure 5.15: XPEEM images at the photoemission threshold (after heating) recorded at different photoelectron energies, $E - E_F$. FoV = 38.3 μm, CA = 500 μm and acquisition time = 120 sec. Unlike the image (a) in fig. 5.14, no contrast is observed at $E - E_F = 3.5$ eV, which indicates that the emission threshold has shifted. Areas of interest (500 $\times$ 500 nm^2) indicated with colored squares in (b).

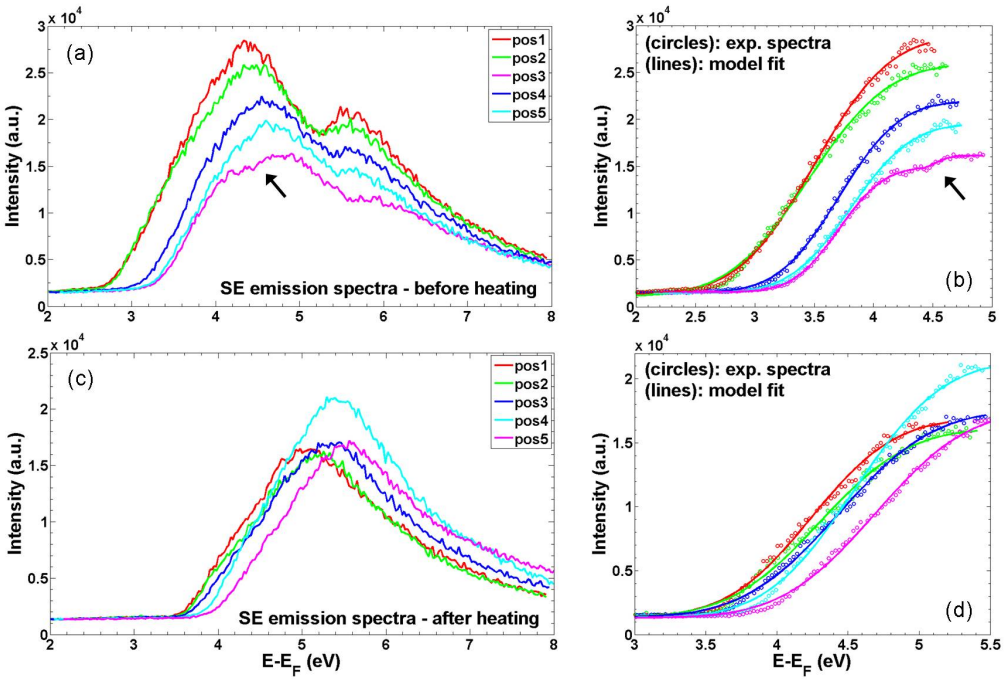

Figure 5.16: (a) SE emission spectra, before heating, extracted from image series recorded in the SE energy range 2-8 eV.(b) Zoom on the threshold region. Spectra are characterized by a single emission threshold except for the spectrum at position 5 (magenta) where two emission thresholds are observed (indicated with black arrow). Solid lines represent the best fit of experimental spectra using equation 5.2. (c) SE emission spectra, after heating, extracted from image series recorded in the SE energy range 2-8 eV. (d) zoom on the threshold region. All spectra show a single emission threshold. Solid lines represent the best fit of experimental spectra using equation 5.2.

SE emission spectra are represented in figure 5.16. Upper plots (a) and (b) show spectra obtained from SE PEEM images before heating. Lower plots (c) and (d) show spectra obtained from SE PEEM images after heating. These spectra are shown to depend on the position over the sample surface in two aspects: the SE emission threshold energy and the spectrum shape. These aspects will be investigated in the following part.

Emission threshold energy: local work function

The emission thresholds from SE emission spectra before and after heating are emphasized in figures 5.16 (b) and 5.16 (d), respectively. The variation of the emission threshold energy for SE spectra obtained at different positions reflects changes of the local work function over the sample surface.

All spectra are characterized by a single emission threshold except for the one extracted at position 5 (magenta) before heating (indicated by a black arrow in figures 5.16 (a) (b)). Two convoluted secondary electron distributions are observed on this spectrum. Therefore there are two emission thresholds which indicate two work function values in the 500 nm^2 selected area at position 5 before heating. This will be discussed below.

Work function determination For the work function extraction from SE emission spectra, the emission threshold can be fitted using a complementary error function [9]. However, for the case of the two deconvoluted secondary electron distributions, the second threshold should be taken into account. We thus extended the error function model in order to fit the double emission thresholds as in the particular case of the spectrum at position 5 before heating. The secondary electron distribution can be written as $S_{1,2}(E_k) = S_1(E_k) + S_2(E_k)$, with:

$$S_i(E_k) = \begin{cases} \frac{A_i}{2} \cdot \mathrm{erfc}\left(\frac{\phi_i - E_k}{B_i}\right) + C_i & \text{for} \quad E_k^{(i+1)} \geq E_k \geq E_k^{(i)} \\ 0 & \text{for} \quad E_k \leq E_k^{(i)}. \end{cases} \tag{5.2}$$

Where, $A_{1,2}$ are scaling factors, $B_{1,2}$, $C_{1,2}$ and $\phi_{1,2}$ are the fit parameters, $\phi_{1,2}$ are the work functions of the first and second emission threshold respectively. $E_k^{(1,2)}$ are the initial kinetic energies of the corresponding SE distribution for a single emission threshold.

Figures 5.16 (b) and (d) show the fit of all SE spectra (before and after heating, respectively) using equation 5.2 in the region of the emission threshold. Solid lines represent the best accord between the fit model and experimental spectra. The uncertainty in the work function value determined by the fit varies between 4 and 15 meV.

Figures 5.17 (a) and (c) represent the work function values measured at different positions on the sample surface before and after heating respectively. These values were statistically obtained as explained below.

We have located domains of similar intensity level, observed on XPEEM images. Then we extracted four local SE spectra in each domain (each local spectrum was taken from a 500 × 500 nm^2 area). They are shown in figures 5.16 (b) and (d) for XPEEM images before and after heating respectively. Each point in figures 5.16 (a) and (c) represents an average value of work functions determined from the four local SE spectra in each domain. Error bars plotted around each point correspond to the standard deviation of the work function values added to the uncertainty from the fit of the emission threshold.

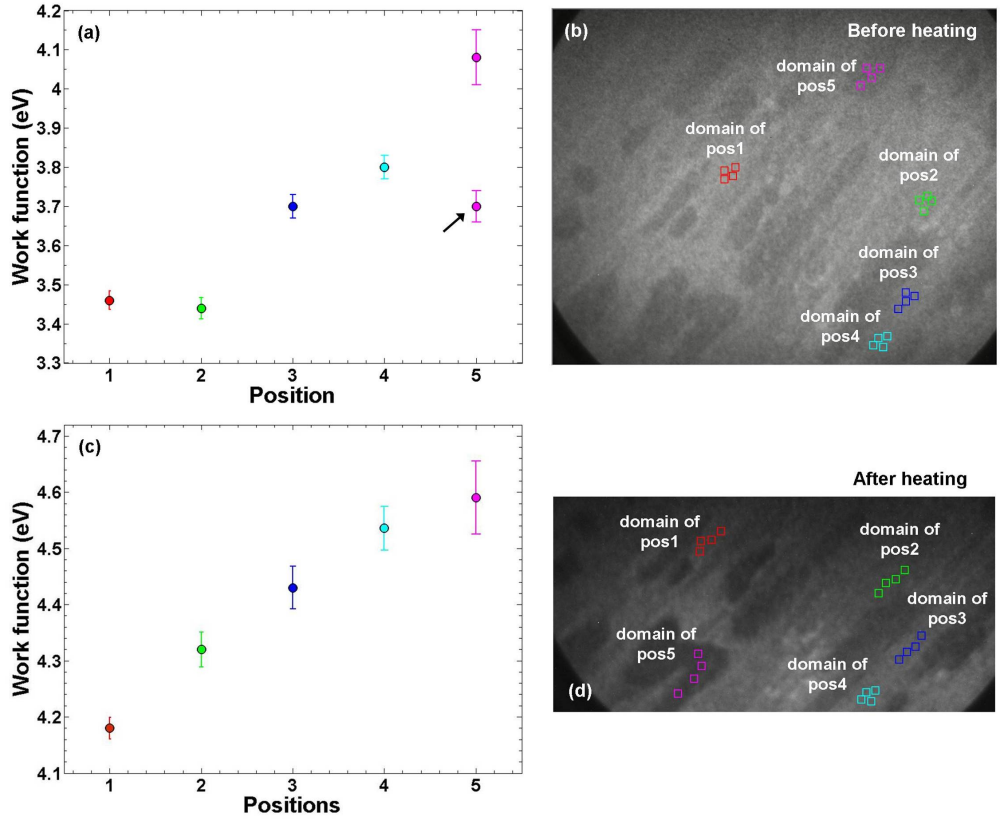

Figure 5.17: Work function values obtained from the fit of the SE emission spectra using equation 5.2 in the emission threshold range, (a) before heating and (c) after heating. The black arrow in (a) indicates the work function value obtained from the double emission threshold on the spectra of position 5 (figure 5.16). (b) and (d) XPEEM images (before and after heating) show the domains corresponding to the positions of interest.

The dependence of the FLG work function on the changing intensity level of SE PEEM images was recently investigated by Hibino *et al.* [164]. They measured the local work function of FLG on SiC(0001) at regions with various

intensity levels using PEEM experiments with a synchrotron radiation photon source (hν = 400 eV). Using LEEM measurements, authors showed that these regions correspond to FLG of different thicknesses. They hence demonstrated that thinner graphene layers have a lower work function ($\sim$ 0.3 eV between 1LG and thick graphitic layers ($\geq$ 10 LG)). In the following, we detail our experimental results compared to those reported by Hibino *et al*. [164] and other experimental and theoretical works [168] [187].

Before heating The work functions measured before heating increase depending on the position over the sample surface. According to Hibino *et al*., this variation would reflect a changing of FLG thickness at each position. Values vary between 3.46 eV and 4.08 eV going from position 1 to 5. However, these values are those smaller than reported for the thinnest graphene layer (i.e. $\sim$ 4.3 eV for 1 LG) [164]. This is explained by a screening effect due to the surface contamination before heating, which lowers the measured work functions.

At position 5, two work function values were extracted from the fit of the double emission thresholds as discussed above. One of which is found $\sim$ 4.08 eV and the other (indicated with black arrow (figure 5.17)) is $\sim$ 3.7 eV. The latter is actually similar to the work function measured at position 3. This means that the corresponding selected area (500 nm^2) at position 5 may present FLG with different thicknesses. This is strongly supported by highly resolved MF-EFM measurements presented later (see section 5.3.4.6) where the growth of FLG is found to be inhomogeneous over a selected area of 1 μm^2.

After heating The absence of contamination after heating enables reliable work functions to be measured. Our results (figure 5.16 (c)) show an obvious increasing trend depending on the local position over the sample surface. The work function increases for regions of high intensity level on XPEEM images after heating (figure 5.16 (d)).

This trend presents a perfect similarity with results reported by Hibino *et al*. [164]. The comparison of our measurements to these results thus helps in the determination of FLG thicknesses at different surface regions.

Thick graphite-like layers The work function of bulk graphite, measured on HOPG, was reported at 4.6 eV [164]. This value matches very well the work function measured at position 5 (4.59 $\pm$ 0.07 eV). All surface domains represented by this position can be thus attributed to thick graphite-like, regions.

One monolayer graphene (1LG) Hibino *et al* [164] found the work function of 1 LG between 4.3 eV and 4.34 eV. This result is in good agreement with the work function measured at position 2 in our experiments. The work

function at this position is found $\sim 4.32 \pm 0.03$ eV. All domains represented by position 2 are therefore attributed to 1 LG. We note that theoretical work function of 1LG was also determined at 4.3 eV by first-principles calculation [187] for FLG on SiC(0001). This represents an additional point of agreement with our measurements.

The C-rich buffer layer Hibino *et al.* [164] have indicated that the work function corresponding to the C-rich buffer layer is lower than that of 1 LG. Filleter *et al.* [168] showed that the work function of this layer is ~ 140 meV lower than that of 1 LG. Authors used KFM experiments in UHV to measure the CPD of FLG on SiC(0001).

Our measurements show that the work function at position 1 is about 4.18 $\pm$ 0.02 eV. It is ~ 0.12 eV lower than that measured at position 2. Given that position 2 has been attributed to 1 LG, we can therefore attribute position 1 to the buffer layer, according to the reported results above.

However, this result differs from the work function value of the buffer layer determined by first-principles calculation (~ 3.75 eV) [187]. This may be attributed to contributions of the charge distribution at the interface between SiC(0001) and the buffer layer that may not be accounted in calculations.

The work function of 2-3 LG Hibino *et al.* [164] found the work function of 2 LG to be ~ 0.1 eV higher than that of 1LG. A similar increasing step was found between 2 LG - 3 LG and 3 LG - thick graphite-like films [164].

Our measurements are in perfect accordance with these results. The work function measured at position 3 ($\sim 4.43 \pm 0.04$ eV) is found higher than that measured at position 2 by 0.11 ± 0.04 eV. Given that position 2 was attributed to 1 LG, then position 3 can be attributed to 2 LG thickness.

We also found a similar difference ($\sim 0.106 \pm 0.04$ eV) between the work function measured at position 4 (4.53 ± 0.04 eV) and the one at position 3 (4.43 $\pm$ 0.04 eV). This is also in accordance with reported data [164]. Thus position 4 can be attributed to 3 LG thickness.

In addition our results are in good agreement with the data reported by Filleter *et al.* [168]. Authors found the work function difference between 1 LG and 2 LG to be ~ 135 meV. This value is comparable to that measured in our case (i.e. $\sim 0.11 \pm 0.04$ eV). Tables 5.7 and 5.8 summarize all results obtained in this work compared to data reported from literature. Assignments of all positions (1 to 5) on the surface to FLG of different thicknesses are also represented.

Dependence of FLG work function on the number of layers

In accordance with reported data [164], our results show that the work function of thinner graphene layer (1 LG) is ~ 0.32 eV smaller than that

Table 5.7: Comparison between the work function values measured in this work and values reported in the literature.

Positions	Number layers	Exp. WF (this work)	Exp. WF Ref. [164]	WF theory Ref. [187]
1	buffer	4.18 ± 0.02 eV	–	3.75 eV
2	1LG	4.32 ± 0.03 eV	4.3-4.34 eV	4.3 eV
3	2LG	4.43 ± 0.04 eV	4.38-4.4 eV	–
4	3LG	4.53 ± 0.04 eV	4.5-4.55 eV	–
5	Thick graphite-like	4.59 ± 0.07 eV	4.57-4.58 eV	–

Table 5.8: Comparison between the work function difference, between layers, measured in this work and values reported in the literature.

Layers	Exp. WF diff. (this work)	WF diff. Ref. [164]	WF diff. Ref. [168]
buffer - 1LG	0.14 ± 0.02 eV	–	0.14 eV
1LG - 2LG	0.11 ± 0.04 eV	0.1 eV	0.135 eV

of thick graphite-like layers. Here we will discuss the understanding of this number-of-layer dependence of FLG work function. However, complete understanding clearly requires further investigation.

In fact, the variation of the work function with the number of graphene layers reflects a change of the local vacuum level. It was demonstrated that a transfer of negative charge from the substrate to FLG results in a doping of these layers [165]. This charge transfer causes a shift of the C1s core-level binding energy (BE) measured for different FLG thicknesses [160]. Hibino *et al*. have found the C1s BE shift about 0.4 eV toward lower values between 1 LG and thick graphite-like layers. This shift was found similar to the displacement of the Dirac point below the Fermi level depending on FLG thickness as determined by ARPES measurements [165]. Authors showed that the work function and C1s binding energy change rather similarly with the number of graphene layers. Therefore they assumed that the vacuum level, as well as the C1s core-level, shift rigidly with the Dirac point.

However, the shift in the work function is smaller than that of C1s BE. Thus there is a difference between the shift of the vacuum level and that of the C1s core-level, depending on the thickness of graphene layers. In fact, while the C1s PES technique senses the graphene layers within the inelastic mean-free-path, only the topmost layer would be relevant to the vacuum level. The vacuum level

does not always shift by the same value as the C1s core-level.

The on-site Coulomb energy at the topmost layer would determine the work function. In fact, simulations of ARPES measurements using tight binding calculations [165] showed that, for thick graphene layers (4 LG), the on-site Coulomb energy of the 1st layer is lower than that of the topmost (4st) layer. This difference is due to the decrease in the carrier concentration when the number of graphene layers increase [165]. The first layer (close to the interface with SiC(0001)) is more doped with electrons than the topmost layer [165] [161].

ARPES simulations also showed that the shift of the on-site Coulomb energy of the topmost layer in 3LG and 2LG, with respect to that of thick graphitic layers (4LG) are $\sim$ 0.09 eV and $\sim$ 0.19 eV, respectively. These shifts are very close to those of the work function of 3 LG and 2 LG with respect to thick graphite-like layers in our measurements. Moreover, the difference of the on-site Coulomb energy of the topmost layer in 2 LG is $\sim$ 0.1 eV lower than that in 3LG. This difference is similar to that between the work functions of 2 LG and 3 LG (see table 5.7). This may be evidence of the screening of carrier in FLG.

However, the shift of the on-site Coulomb energy of 1 LG with respect to thick layers is actually different from that of the work function between 1 LG and thick graphite-like layers. This suggests that other effects (such work function changes due to the surface/interface dipoles) also contribute to the number-of-layer dependence of the work function.

This suggestion holds up well when looking to results reported by first-principles calculation [187] for FLG on SiC(0001). Calculation showed that the work function of the buffer layer, 1LG and isolated graphene were 3.75, 4.33 and 5.11 eV respectively. The calculation demonstrated the tendency for the thicker graphene to have higher work functions. It also reproduced the measured Dirac point shift of monolayer graphene.

However, it showed that the difference between 1 LG and isolated graphene is much larger than the experimental value between 1 LG and thick graphene. This calculation result suggests that the work function does not move in the same way as the Dirac point, which would mean the charge distribution (dipole moments) at the surface/interface greatly influences the work function of FLG.

We note, however, that Hibino *et al.* assumed that all the electronic structures of FLG are shifted rigidly by the charge transfer. This assumption explains well the number-layer-dependence of the C1s binding energy but roughly explains that of the vacuum level. It is in contradiction with first-principles calculation results cited above.

The shape of SE spectra

In this part, we discuss the number-of-layers dependence of the shape of SE emission spectra presented in figure 5.16. Before heating, all SE spectra show small peaks at a higher SE energy with respect to the main SE emission peaks. Main SE emission peaks are centered around $\sim$ 4.4 - 4.8 eV. Additional small peaks are found between 5.6 eV and 6.9 eV. After heating, these additional peaks become very attenuated and are barely observed on the SE emission spectra.

Here below we explain our attempt to interpret these observations. In a recent study, Hibino *et el.* [164] investigated the SE photoemission from FLG domains of different thicknesses epitaxially grown on SiC(0001) surface. Authors found that thick graphitic layers ($\geq$ 10 LG) produce a weak peak on the high energy tail of the SE emission spectra at about 2.8 eV higher than the main peak [164].

The origin of this peak was interpreted similarly to that observed in SE emission spectra of graphite at about 7.5 eV above E_F (3 eV above the main SE emission peak). Authors explained that under photon irradiation some of the excited electrons are relaxed to the unoccupied states and are emitted into vacuum as secondary electrons [164] [188]. This peak was therefore attributed to the unoccupied states in the band structure. This interpretation could explain the observation of the second peaks on our SE emission spectra. However, our results differ from those reported by Hibino *et al.* on many aspects:

- SE peaks, above the main peaks, are observed for all SE emission spectra, i.e. for the buffer layer as well as for FLG with different thicknesses (1-,2-,3- and thick-graphite like layers). Reported results showed no additional peak on SE emission spectra of thin graphene layers [164].

- Positions of these peaks are found at about $\sim$ 1.2 eV higher than the main SE peaks. These positions are lower than those found in reported results.

- Interestingly, these peaks become very attenuated (almost undetectable) after heating on all SE spectra.

These differences with respect to reported results raise additional questions concerning the exact origin of the observed peaks above main SE emission ones.

We suggest that the presence of these SE peaks could be related to electronic states in the band gap previously observed in μ-XPS measurements (see section 5.3.2). We recall that μ-XPS results indicated a pinning of the Fermi level before heating, due to electronic states related to Si-dangling bonds at the graphene-SiC(0001) interface. The sample heating was shown to induce a shift in the E_F position accompanied by the absence of the chemical states attributed

to Si-dangling bonds.

We think that, before sample heating, some of the excited electrons could also be relaxed to these electronic states (related to Si-dangling bonds) in the band gap. They could be emitted into vacuum as secondary electrons. This could therefore result in the presence of additional SE peaks observed on our spectra. This seems likely since all SE peaks (above the main peaks) are strongly attenuated on all SE emission spectra after heating. This hypothesis seems to be in accordance with the effects of sample heating on the core-level spectra observed in μ-XPS experiments.

All of this indicates that the origin of the second emission peaks observed on the SE emission spectra is related to unoccupied states in the FLG band structures.

5.3.3.4 Work function map from threshold XPEEM measurements

In this section, we represent a two-dimensional map of the lateral variation of the FLG work function. The work function map was reconstructed from the image series recorded in the range of secondary electrons (2-8 eV) after heating. Following the method described in chapter 3, the work function was determined from SE emission spectra extracted at each pixel of the image. Each pixel-related spectrum was automatically extracted, and the emission threshold was fitted using the complementary error function in the emission threshold region.

Figure 5.18 shows the work function map. Due to an imaging artifact discussed above, the upper part of XPEEM images acquired after heating has been removed. Therefore, the dimensions of the work function map are 312×640 pixel^2 which corresponds to 16×32 μm^2. The colormap was adjusted to match the color indexation given for the position of interests as shown in figure 5.17 (c).

According to work function results summarized in table 5.7, the work function contrast on the 2D map (figure 5.18) reflects a direct image of the FLG thickness distribution over the area of study. The histogram of the work function map is shown in figure 5.19. It shows the coverage of graphene layers over the present surface. One can see from figure 5.19 that the surface is mostly covered with 1LG (green) and 2LG (blue).

5.3.3.5 Summary

In this section, we investigated the work function variation of FLG on SiC(0001) using XPEEM spectromicroscopy in the SE energy range with the laboratory FXS (Al K_α) photon source.

Results showed a number-of-layer dependence of the FLG work function. We demonstrated that thick graphene layers tend to have a higher work function.

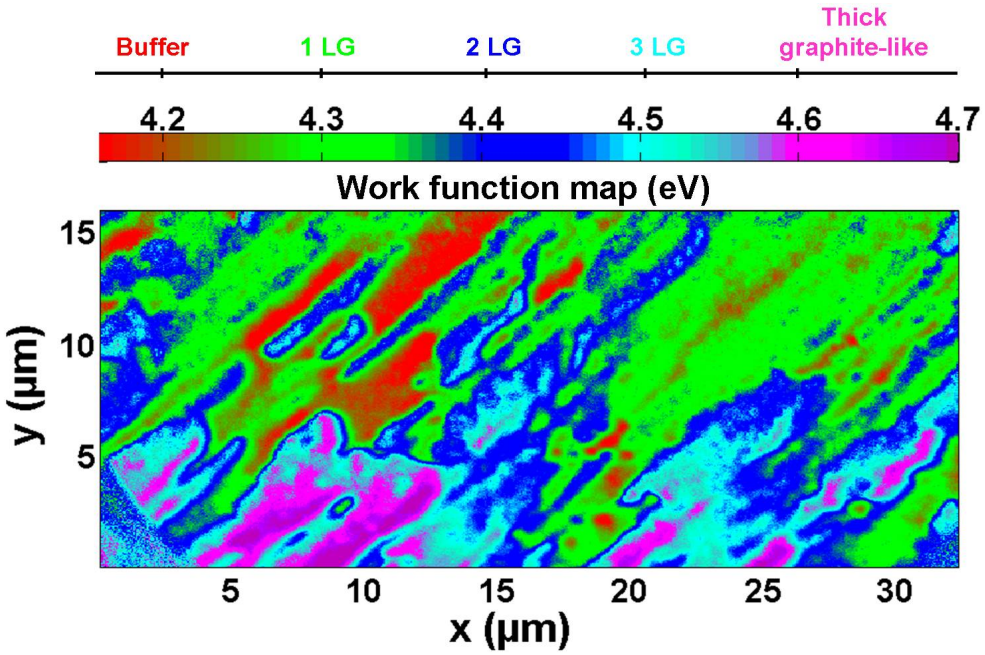

Figure 5.18: Two-dimensional map of the lateral variation of the FLG work function, reconstructed from XPEEM images after heating. Map dimensions, 16×32 μm^2. The number-of-layer dependence of the FLG work function is shown on the scale.

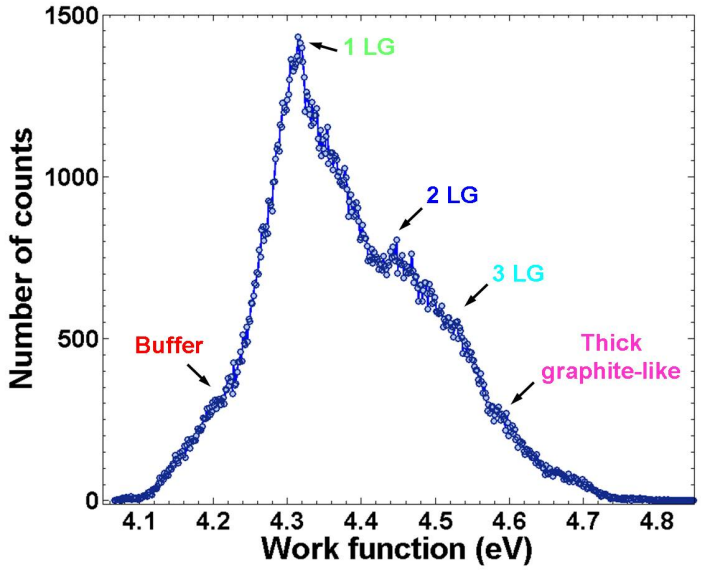

Figure 5.19: The histogram of the work function map shows the distribution of the work function values over the entire FoV.

Our results were in good accordance with data reported from literature.

We also discussed the dependence of FLG work function on the number of layers. At the present understanding, it seems that this dependence can be evidence of screening of carriers in FLG, but a contribution of surface/interface dipoles seems to have an important impact on the work function of FLG on SiC(0001). However, a rigid-band model of FLG (suggesting the shift of all electronic structures of FLG with the charge transfer from SiC(0001) to graphene layers) is not excluded.

A better understanding requires further investigation. Calculations properly including the interface structure ($6\sqrt{3} \times 6\sqrt{3}$) are essential for the understanding of this number-of-layers dependence.

A two-dimensional work function map was also reproduced from XPEEM images. It provides a direct image of the distribution of FLG with different thicknesses over the area of study. This method, using the laboratory FXS source, is an important technique for an easily accessible characterization of FLG thickness.

5.3.4 Evidence of topographic changes from KFM measurements

The number-of-layer dependence of the FLG work function was demonstrated by XPEEM measurements in accordance with literature data. Proving a real height variation over the different regions characterized in the previous section adds further physical support to the demonstrated results. KFM experiments were used to this aim.

5.3.4.1 The common zone of interest in XPEEM and KFM experiments

To enable comparison of KFM measurements to previous XPEEM results, we used the FIB cross mark pattern on the surface (see appendix D) as a reference to locate the same zone of interest imaged in XPEEM experiments.

Unfortunately, due to misalignments while positioning the sample on the KFM sample holder, we fell short of a perfect match between the zone of interest studied in KFM and the one imaged in XPEEM experiments. Figure 5.20 shows a schematic representation of the zones of interest characterized in XPEEM and KFM, with respect to the referential cross mark. However, we were able to define an overlapping zone between the areas of both studied zones (hatched area (23.5 μm $\times$ 5.4 μm)in figure 5.20).

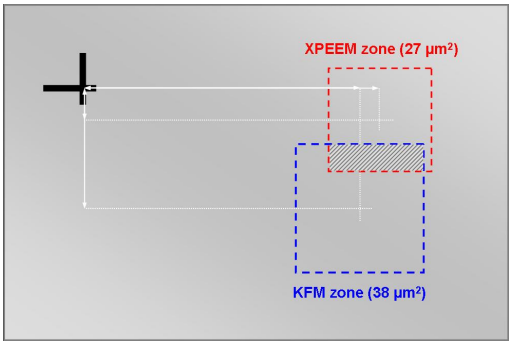

Figure 5.20: A schematic representation of the zones of interest, in KFM and XPEEM experiments, as determined with respect to the FIB cross mark. The hatched gray area indicates the common overlapping zones where measurements of both experiments are compared. The scale on the image is only representative.

5.3.4.2 KFM: experimental parameters

KFM experiments were performed in the lift mode. The tip and the sample were kept in the dry environment of the microscope's glove box. Nitrogen gas (N_2) was continuously fed into the glove box. The relative humidity level (%RH) was maintained at $\sim 0.2 \pm 0.2$ %RH. We used PtIr coated tips, with a stiffness $K \sim 3$ N/m and a fundamental vibration eigenmode frequency $f_0 \sim 62$ KHz.

No *in situ* heating of the sample was possible. Surface contamination is expected in these experiments. However, measurements were conducted in a dry environment (glove box). This reduced effects induced by thin water layers on the sample and tip surfaces. The tip was kept in dry conditions, and no particular cleaning preparation was made.

5.3.4.3 Imaging the CPD and topography variations

The scan size of the entire zone of study in KFM is 38 μm^2. Topography and contact potential difference (CPD) measurements were done at the first (fundamental) eigenmode vibration frequency of the cantilever. The lift height (L.H.) was chosen at 10 nm from the sample for a better spatial resolution of electrical measurements.

Figure 5.21 shows images of topography (a) and V_{dc} map (b) obtained over the entire scan size. The polarization was applied to the tip. The work function map was then extracted from the V_{dc} map based on the following expression:

$$V_{dc} = V_{cpd} = \frac{\phi_{tip} - \phi_{sample}}{|e|}. \tag{5.3}$$

The work function of the sample was 'estimated' by referring to that of the PtIr tip as reported [68] by $\phi_{tip} \approx 5.1$ eV. The contrast of the work function map (c) is thus inversed with respect to that of the V_{dc} map (b) (see section

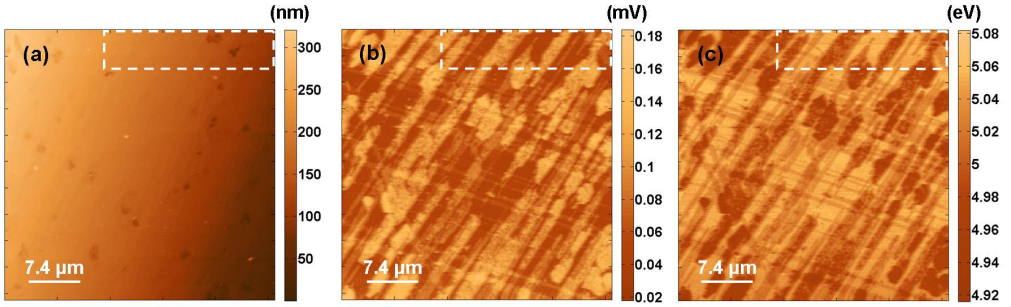

Figure 5.21: The topography (a), V_{dc} (b) and work function (c) maps obtained over the 38 μm^2 scanned zone in the lift mode (tip polarization). The L.H. was chosen at 10 nm for higher spatial resolution of V_{dc} measurements.

3.1.2.2). Images dimensions (figure 5.21) are defined by 512 × 512 pixels. A flatten and a plane fit procedures were applied to the topography image only, in order to visualize the slope of the real height variations. This resulted in the overall intensity gradient observed on image 5.21 (a). The overlapping zone between the XPEEM and KFM zones of interest is indicated by white dashed rectangles on the images in figure 5.21.

5.3.4.4 Contrast of the topography and work function maps

Interestingly, the contrast of the 'estimated' work function map (figure 5.21 (c)) appears to be different from that of the topography. The pseudo-regular terrace-like pattern observed on the topography image is not clearly reproduced on the work function map. Instead, the surface shows elongated streaks in an unregular pattern and with different intensity levels (presenting some similarities with the contrast of the SE XPEEM images (see figure 5.13)). These observations where investigated over the overlapping zone (dashed rectangle).

5.3.4.5 The overlapping zone

Figure 5.22 shows magnified images (topography (a) and work function map (b)) of the overlapping zone. The slope of real height variations, resulting from a local plane fit procedure, was kept for the topography image. This explains the intensity gradient observed on this image (figure 5.22 (a)).

Analyzing the contrast on the work function map

Three intensity levels can be clearly identified from the contrast of the 'estimated' work function map (figure 5.22(b)), which we identified as: (L) for low, (M) for medium and (H) for high work function values. Figure 5.23 shows the histogram extracted from the work function map. It shows the distributions of work function values present on this map (figure 5.23 (b))

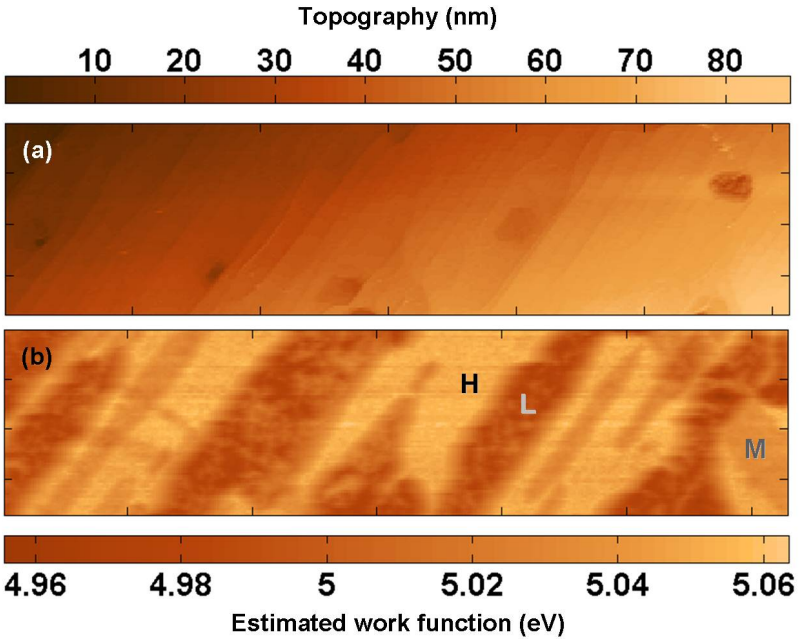

Figure 5.22: (a) Topography and (b) 'estimated' work function map of the overlapping zone. A local plane fit procedure was applied to the topography image (a) which results in the overall intensity gradient. The contrast of the work function map (b) exhibits three different intensity levels (L), (M) and (H).

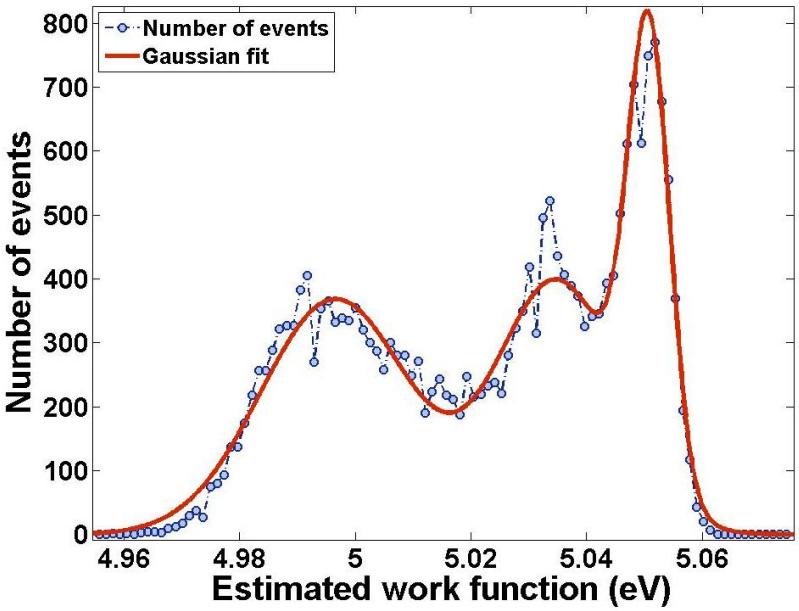

Figure 5.23: Histogram of the work function map of the overlapping zone. The histogram (blue circles) was fitted to three Gaussian functions (red curve) which describes three different distributions of work function values. These distributions represent the indexation showed in figure 5.22 (b) for Low, Medium and High work function values.

The histogram data (blue circles) were fitted to a sum of three Gaussian functions (red curve). The high (H) work function values, centered around 5.05 eV, present the highest and narrowest distribution with the smallest dispersion ∼12 meV. The medium (M) and low (L) values present much broader distributions centered around 5.03 eV and 5 eV with dispersions of 34 meV and 43 meV, respectively. These values were calculated from the results of the Gaussian fit to the histogram data.

The trend of variation Figure 5.24 shows the variation of the work function[1] with respect to the positions on the surface where the intensity level is variable (L, M and H). The error bars drawn around each point correspond to the FWHM calculated from the σ values obtained from the Gaussian fit for each distribution.

An obviously increasing trend is in accordance with the number-of layer dependence of the work function of FLG determined in XPEEM measurements (see table 5.7). Therefore, figure 5.24 indicates that the contrast on the work function map (figure 5.22 (b)) results from the inhomogeneous distribution of the FLG thickness over the zone of study.

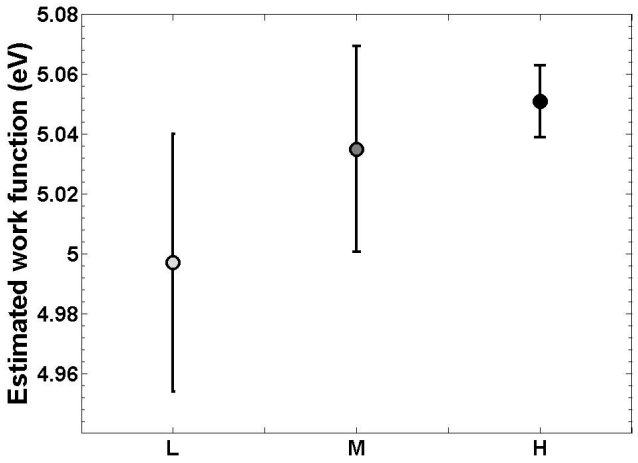

Figure 5.24: The evolution of the estimated work function with respect to the positions on the surface. Error bars are calculated from the results of the Gaussian fit to the histogram of the work function map.

Figure 5.24 shows the presence of at least three different graphene film thicknesses. Error bars indicate a large distribution of the 'estimated' work function values, especially for the (M) (L) regions. The work function differences between (L) - (M) and (M) - (H) regions are ~ 0.03 eV and ~ 0.05 eV, respectively.

[1] We recall that the work function is always estimated with respect to the work function of the PtIr tip considered as a reference ($\phi_{tip} \approx 5.1$ eV)

These differences are much lower than those reported in previous studies (see table 5.7) [168] for FLG with different thicknesses. This results from the influence of the surface contamination and environmental effects in ambient KFM measurements [98].

Comparing the work function maps from KFM and XPEEM measurements Figure 5.25 shows the work function maps over the intended overlapping area between the zones of interest in KFM and XPEEM measurements.

A similarity between the contrasts of both images can be identified. This observation suggests that the contrast of the present work function map (in KFM lift mode in ambient environment) is directly related to the variation of the FLG thickness over the scanned zone.

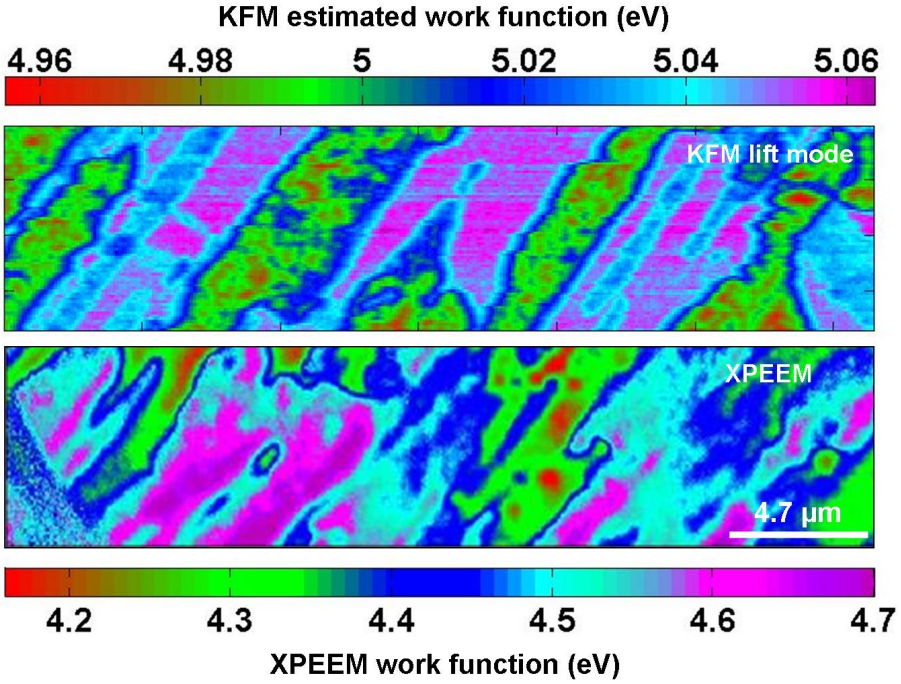

Figure 5.25: Work function maps of the overlapping area between (a) KFM and (b) XPEEM measurements. Contrasts are far from being the same due to several factors resulting from KFM misalignments and environmental effects.

An estimation of the graphene coverage from the XPEEM work function map was discussed in section 5.3.3.4. Comparing the contrasts between KFM and XPEEM work function maps from figure 5.25, however, does not enable us to estimate the FLG thickness for two reasons:

- The work function values, represented on both maps, are largely different.

This is due to the difference between the experimental and environmental conditions of both techniques.

- Even though the imaged zone is expected to be the same in both measurements, it was difficult to obtain a perfect match between the contrasts of both images

Thanks to XPEEM threshold measurements, however, we could analyze the origin of the contrast observed on the KFM lift mode images as related to changes in FLG thickness.

However, the important question is whether it is possible to directly measure the thickness of graphene layers from the topography maps obtained in KFM lift mode experiments in ambient conditions.

Topography variations: the problem of SiC substrates

Several studies have demonstrated the correlation between thickness measurements from topography changes and the electronic properties of graphene layers [168] [170] [172] [169]. However, all these works were performed in different conditions than our experiments (in terms of environmental conditions, spatial resolution or operating modes). The question is whether it works to determine the graphene layer thickness using topography measurements in ambient conditions.

The contrast of the topography image The topography image shown in figure 5.22 exhibits a regular terraces-like pattern, which reflects the surface topography of the SiC(0001) substrate [183] [163]. We found the width of these terraces to vary between $\sim$0.14 μm and $\sim$0.4 μm, in agreement with measurements reported by Virojanadara *et al.* for clean SiC surface ($\sim$0.17 μm) and by Penuelas *et al.* for SiC (0001) surface annealed at 1200°C ($\sim$0.37 μm) where graphene layers start growing.

We also found the step height between terraces to vary between 1.5 nm and 5 nm. Virojanadara *et al.* found a $\sim$1 nm step height for the clean SiC surface, while Penuelas *et al.* found $\sim$1.5 nm at 1100°C and $\sim$1.2 nm at 1300°C for the surface with homogeneous graphene growth [183]. The variation of the measured steps could reflect the height variation between zones of different layer thicknesses [170] [168].

The SiC terraces and the graphene coverage In order to understand the change in topography with respect to the variation in graphene layer thickness, magnified images were taken over zones with different intensity levels in figure 5.22.

Homogeneous graphene coverage A homogeneous distribution of low work function values (zone (L) in figure 5.22) was chosen as a first example. Figure 5.26 shows the cross section profiles taken among the lines drawn on the topography image (left) and work function map (right).

The work function image presents a homogeneous contrast whereas the topography exhibits a continuous increase following the step height of SiC terraces. An averaged value of ∼1.5 nm can be measured from the cross section profile on the topography image. Assuming a step height between terraces of clean SiC given by ∼0.75 nm (for three SiC bilayers) and ∼1 nm as reported in [163], we can identify an additional layer homogeneously covering these terraces with a thickness between ∼0.5 nm and ∼0.75 nm. Regarding the theoretical thickness of one monolayer graphene (∼0.34 nm), the graphene thickness over these zones can be approximated by 2LG coverage.

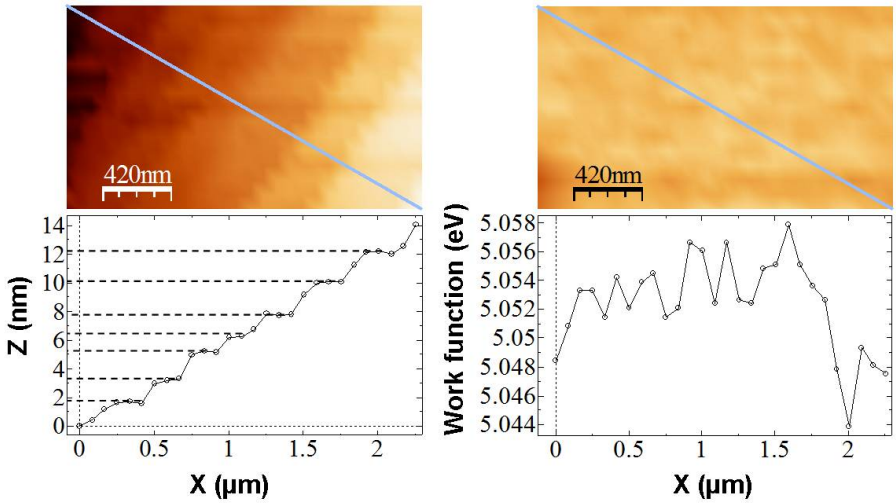

Figure 5.26: The topography(left) and work function (right) images magnified over the low work function values regions indicated by zone L in figure 5.22. Cross sections across the line drawn on the images clearly indicate a continuous increase of the topography following the terrace-like pattern of the SiC substrate.

However, these findings clearly show that *even with an homogeneous coverage of thin graphene layers, the topography still increases following the terrace-like pattern of the SiC substrate.* This fact has been argued and discussed in highly resolved STM measurements, and graphene layers were shown to adopt the same topographic variation of the underlying substrate [172].

Non-homogeneous graphene coverage The question becomes more complicated when the thickness of graphene layers varies. To emphasize this point we present in figure 5.27 magnified images taken for the region where the

zones L, M and H coexist (see figure 5.27).

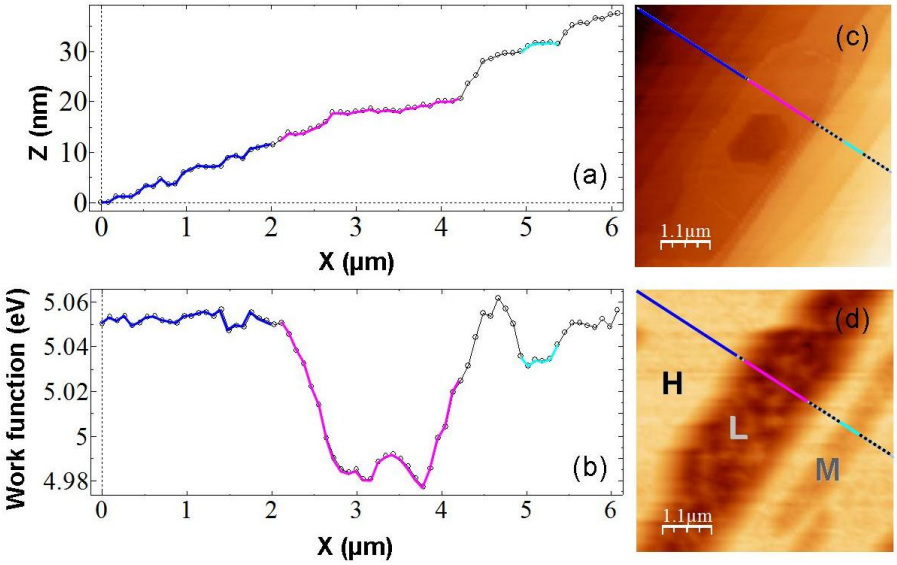

Figure 5.27: The topography (c) and the work function (d) images were magnified over the region where H, M and L zones coexist. The profiles (a)-(b) along the lines drawn on the images show the variation of the topography and the work function over the different zones.

According to the number-of-layers dependency of the FLG work function (see table 5.7), the number of graphene layers over the zone of low values (L) (magenta curve) is expected to be smaller than the number of layers over the (H) zone of high work function values (blue curve). The cross section profiles in figure 5.27 (a) (b) show that the topography over the (L) zone is higher than that over the (H) zone. This is due to the continuous increase of the step induced height of the underlying SiC substrate.

The effect of the SiC terrace-like topography This fact makes the quantification of FLG thickness inaccessible using topography maps in the present experimental conditions (KFM lift mode in ambient environment). This is the reason why most reported works using topography measurements to evaluate the FLG thickness were performed in different conditions. They have used either better experimental conditions (UHV) and higher spatial resolution modes [168] [172] or used a completely different type of substrate such as SiO_2 where exfoliated graphene flakes are studied and substrate-induced topography is no longer a concern.

5.3.4.6 High-resolution imaging in the MF-EFM mode

To study graphene coverage over the SiC terraces, high-resolution measurements were performed using MF-EFM experiments, as described in chapter 4 section

4.2.

Experimental parameters Experiments were performed in a dry environment. Experimental details described in 4.2 were used here. Conventional KFM experiments in the lift mode were also performed on the same zone for comparison. The lift height was set to LH = 10 nm, and the electrical driving signal (in the second trace) was applied to the tip.

High resolution images: comparison to KFM lift mode

Figure 5.28 shows the topography (a) and V_{dc} (b) images obtained with the KFM lift mode and the images of the topography (c) and the electrical amplitude $A(\omega_1)$ (d) obtained with the MF-EFM mode.

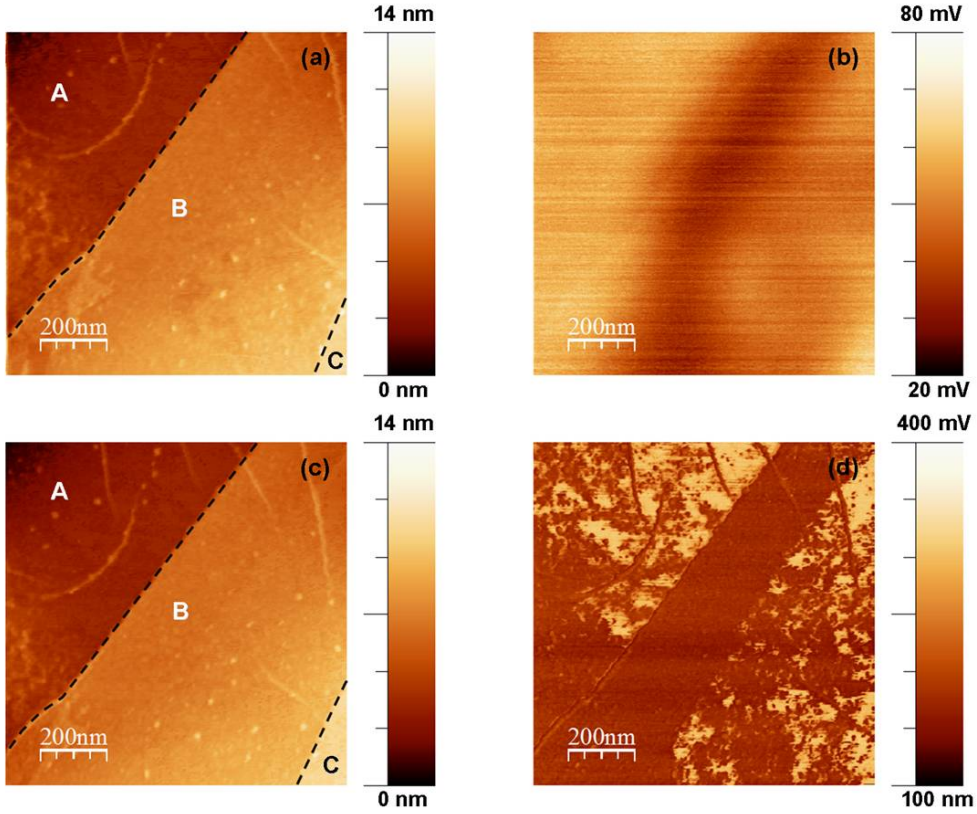

Figure 5.28: (a) topography and (b) V_{dc} images obtained with KFM lift mode with a lift height LH = 10 nm. (c) topography and (d) electrical amplitude $A(\omega_1)$ obtained with the MF-EFM mode. The scan size of each image is 1 μm^2.

Topography images from both methods are similar, showing mainly three

terraces A, B and C (marked by dashed lines on images (a) and (c)). However, a slight lateral shift of the KFM image (b) can be observed with respect to the MF-EFM image (d). This fact results from the movement of the tip (or sample) during the passage from the first to the second trace in lift mode operation.

Nevertheless, the comparison of the V_{dc} image (b) and the image (d) of the electrical amplitude $A(\omega_1)$ highlights the important improvement in spatial resolution with MF-EFM mode. Both images show a central, vertical, dark streak (low intensity level). Clear flake-like features (high intensity level) are observed on the $A(\omega_1)$ image, whereas it is strictly impossible to identify them on the V_{dc} image. Instead, a blurry contrast, with clear (high intensity level) regions is observed on both sides of the central dark streak.

Analyzing the contrast: coverage of graphene layers

In fact, $A(\omega_1)$ is directly proportional to the value of V_{cpd} (see section 4.2). The contrast of both images (b) and (d) therefore stems from the variation in CPD over the scanned zone. Accordingly, the presence of the flake-like features, observed on image (d), indicates a changing CPD with respect to the regions of dark contrast which dominates the central part of the image.

Topography and electrical amplitude distributions Figure 5.29 shows histograms extracted from the topography and the electrical amplitude images (figure 5.28 (c),(d) respectively) obtained in MF-EFM. The topography histogram (figure 5.29 (a)) shows three principal distributions corresponding to the terraces (A, B and C) of the SiC(0001) substrate observed on the images of figure 5.28. The step heights between terraces are respectively 3 nm and 4 nm. Given that the terrace step height of a clean SiC(0001) surface reported at about 1 nm [163], the terraces A, B and C are therefore probably recovered by graphene layers.

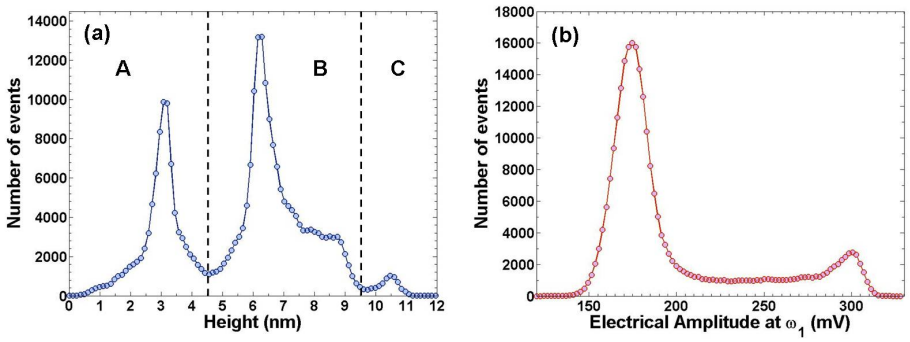

Figure 5.29: (a) histogram extracted from the topography image (figure 5.28 (c)) and (b) histogram extracted from the image of the electrical amplitude $A(\omega_1)$ (figure 5.28 (d).

Nevertheless, the histogram (5.29 (b)) extracted from the image of the

electrical amplitude $A(\omega_1)$ (figure 5.28 (d)) shows only two principal distributions. The strongest distribution (centered around 175 mV) actually corresponds to the dark regions on the image. The smallest distribution (centered around 300 mV) represents the clear flake-like features.

Interestingly, the blurry contrast of the V_{dc} image (figure 5.28 (b)) varies similarly as the contrast of the $A(\omega_1)$ image (figure 5.28 (d)) (i.e. the vertical central streak is dark, and regions on the left and right sides are clear on both images). This means that the flake-like features actually present a higher CPD. This may suggest their attribution to thinner graphene layers according to the number-of-layers dependence of the FLG work function (see equation 5.3).

However, the thickness of the underlying coverage (i.e. the dark zones) cannot be identified from the present experiments. As far as we can tell, these observations indicate that FLG in our sample seem to epitaxially grow over the terraces in an non-homogeneous pattern.

This non-homogeneity is observed over an area as small as 1 μm^2. Graphene layers thus seem to present an non-homogeneous growth on SiC terraces. This result is in accordance with XPEEM measurements done in the photoemission threshold range (see section 5.3.3). We recall that XPEEM results (see figure 5.16) showed the presence of double emission thresholds on the secondary electron emission spectra, extracted from small areas of 500 nm^2. The double emission thresholds indicate two work function values in this area.

We estimate that measurements under UHV conditions can, however, provide the possibility to identify real graphene coverage in a similar way to what was reported in [168].

Alternative approach to estimate the layers thickness In the following section, we shall demonstrate the ability of the *NanoESCA* to provide an estimate of the thickness of FLG using spectromicroscopy measurements in the range of core-level energies. As detailed further, this method - if optimized - allows one to efficiently overcome most of the difficulties that arise from the SiC underlying-induced effects.

5.3.5 Measuring the layer thickness with local spectromicroscopy experiments

The method for FLG thickness estimation using spectromicroscopy experiments, presented here, is mainly based on the investigation of local C1s and Si2p core-level spectra measured at different locations on the sample surface. Local spectra are extracted from an XPEEM image series through the C1s and Si2p core-levels (see chapter 3).

5.3.5.1 Spectromicroscopy: estimating the thickness from local core-level spectra

Here we recall the principle of spectromicroscopy measurements which consist of two principal steps. Figure 5.30 shows the C1*s* full-field spectrum plus 8 sample images recorded at different core-level energies.

Imaging the chemical bonding states This step is possible once the chemical states present on the studied surface are identified. This is done by the deconvolution of the core-level C1*s* and Si2*p* spectra to the chemical state components (see section 5.3.2). Then XPEEM image series are recorded at different core-level energies around the C1*s* and Si2*p* binding energies, as illustrated in figure 5.30.

Extracting local micro/nano core-level spectra Local core-level spectra are then extracted from the XPEEM image series at specified positions of interest over the FoV, where the change in graphene film thickness is investigated.

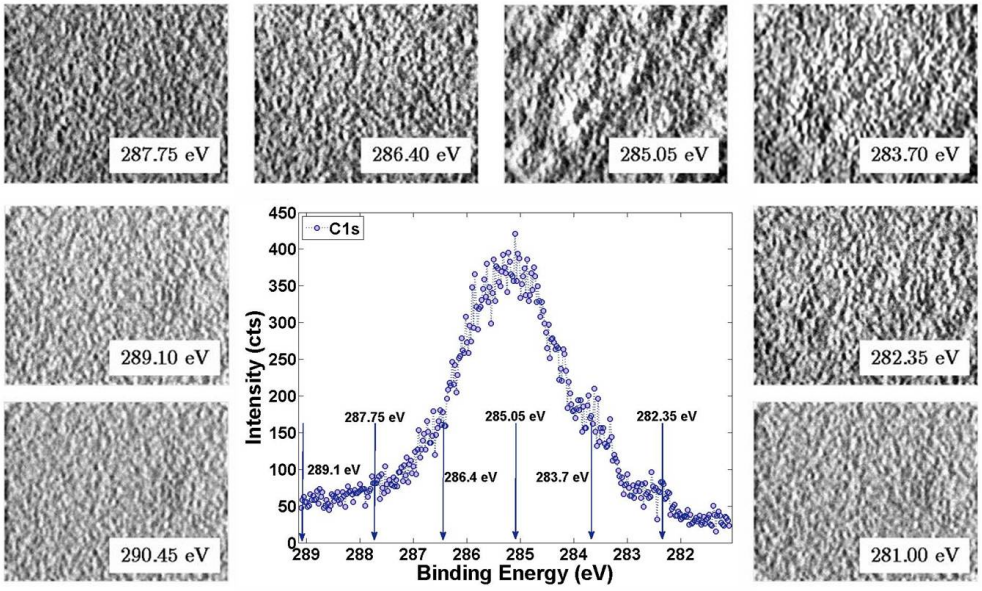

Figure 5.30: In spectromicroscopy experiments images are recorded around a specific chemical peak. In this example XPEEM images were recorded around the C^{1s} peak. By stacking these images, one can extract local core-level spectra defining the chemical state at a specific position of interest on the image.

5.3.5.2 Experimental parameters

Measurements were performed using the energy-filtered imaging mode of the *NanoESCA*. Image series at the core-level photoelectron energies were acquired using the FXS monochromatic photon source ($h\nu$=1486.6 eV). The field of view was set to FoV = 38.3 μm. The beam spot size was adjusted to 30 μm for an increased photon flux, and the contrast aperture was set to 500 μm in order to enhance the photoemitted electron intensity. Table 5.9 summarizes the parameters of the PEEM column and the IDEA analyzers that were used in the current experiments.

Table 5.9: The settings parameters applied to the *NanoESCA* in present spectromicroscopy experiments.

FXS spot size	CA	E_{pass}	EA_1	EA_2
30 μm	500 μm	100 eV	1 mm	4 mm

5.3.5.3 Imaging the surface at the core-level electron energy

XPEEM image series were recorded at different core-level energies around the the C1*s* and the Si2*p* peaks.

Before heating Eleven single-energy XPEEM images were recorded by sweeping the photoelectron core-level binding energy from 278.3 eV to 291.8 eV with a step of 1.35 eV. While for the Si2*p* spectrum, ten single-energy XPEEM images were recorded in the range between 96.55 eV and 106.9 eV with a step of 1.15 eV. The acquisition time for each image is 15 minutes.

After heating After the sample was heated, eight single-energy XPEEM images were recorded among the C1*s* spectrum at core-level binding energies ranging between 280.3 eV and 289.75 eV with a step of 1.35 eV. For the Si2*p* spectrum, nine XPEEM images were recorded between 98.8 eV and 105.2 eV.with a step of 1.15 eV. The acquisition time for each image is 15 minutes.

Improving the intensity of a single energy image

The intensity of the XPEEM image recorded at a core-level photoelectron energy (using the present experimental conditions with the laboratory FXS source) is very low compared to that recorded at an energy of secondary emission photoelectrons. In order to improve it in the present case we proceeded as following:

- The acquisition time for each image was set to the maximum amount available (900 seconds).

- The potential of the channeltron detection system was set to 1050/4000 V.
- The acquisition of each image of a series was repeated 16 times in the same conditions.
- The 16 images were added together, which resulted in a single-energy image with an acquisition time of 4 hours. We called it the 'super image'.

Consequently, we obtained a new image series, where the acquisition time of each single-energy image was 4 hours.

Noise treatment Setting up the detection parameters to their maximum values leads to an increase of the 'Dark noise' (expressed by the presence of 'hot pixels'). 'Dark noise' is the noise detected in absence of any source of photons or electrons hitting the channeltron. 'Hot pixels' correspond to the points of highest 'Dark noise' intensity level. In order to eliminate the 'Dark noise' from the 'super images', the following treatment was performed:

- A set of eleven 'Dark noise' images (900 sec./image) were acquired while the FXS photon source was turned off.
- All these 11 'Dark images' were averaged in order to get an acceptable statistic of the 'Dark noise' resulting from the detection system. This resulted in a single 'super Dark image'.
- Finally, the 'super Dark image' was subtracted from each single energy image of the new image series which results in 'Dark noise' free 'super images'.

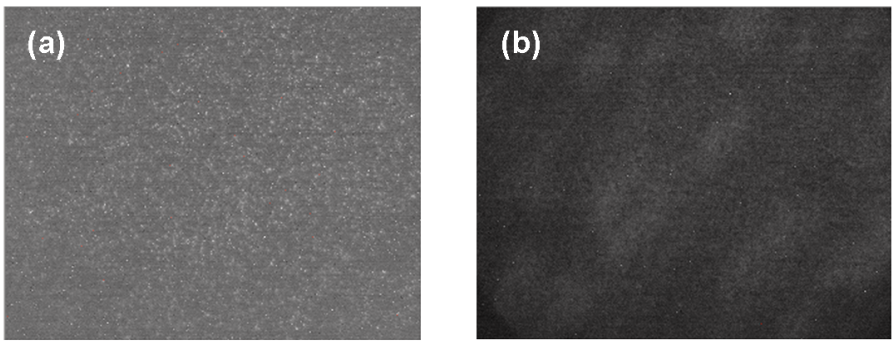

Figure 5.31: (a) a single energy image acquired for 900 sec. at the core-level energy of 285.05 eV before heating. (b) the 'super image' obtained by adding together 16 'super images' recorded in the same conditions, the 'Dark noise' being subtracted from each image. The contrast on the 'super image' is obviously more enhanced than image (a).

Figure 5.31 shows a single energy XPEEM image acquired at the core-level energy of 285.05 eV for (a) 900 sec. and (b) the corresponding 'super image'

of 4 hours artificial acquisition time. The contrast of the 'super image' (b) was obviously increased by this procedure even though the intensity of the image remained relatively low.

Limitations The Nexus software, used for the acquisition of the core-level images, imposes a limit of 52 compartments for each acquisition file. This limitation prevented us from extending the number of acquisitions of each single-energy image to more than 16 times. However, for a same number of image duplications, the intensity could be improved by an eventual increase in sensitivity for the CCD camera of the detection system.

Contrast of core-level images among the C1s and Si2p spectra

Figure 5.32 shows the 'super images' taken at different core-level binding energies among the C1s and Si2p spectra acquired before heating. A false color scale has been added to images to emphasize the variation of the contrast.

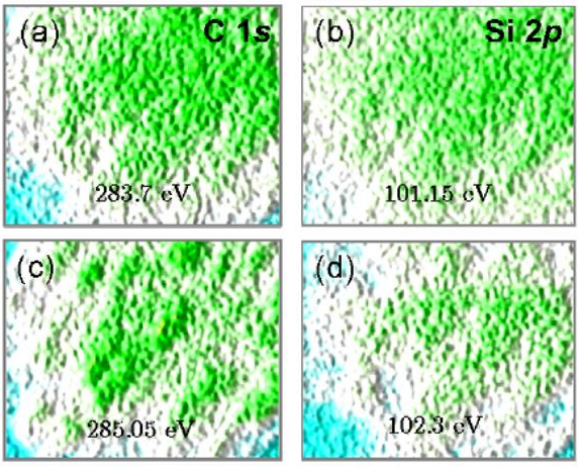

Figure 5.32: High resolution C1s (a) (c) and Si2p (b) (d) images acquired before heating over the entire field of view (FoV = = 38.3 μm). False colour scale has been added where intensity increases from the blue to the white and finally green color.

The contrast observed on both C1s and Si2p images of figure 5.32 depends on the considered binding energy in each case meaning a chemical state contrast. More important is the complementary information of the observed contrasts: in images (a) and (b) where the SiC substrate components are imaged, the Si2p and C1s contrast is similar as expected. However, in images (c) and (d) where the graphene/graphite-related components are imaged, the contrast is inverted between the Si2p and the C1s image. This is due to the stronger attenuation of the XPS signal from the SiC substrate in the area where a graphene/graphite overlayer is present.

According to the observed complementarity between the chemical contrast on the C1s and Si2p core-level images, the goal of the following investigation is

thus twofold:

- to estimate the thickness of graphene layers by extracting local core-level spectra from these images at different regions (with a changing intensity level)
- to compare the evolution of their local intensities.

5.3.5.4 Extracting the local spectra from core-level image series

In order to investigate the evolution in the local intensity of the C1s and Si2p spectra, local spectra have to be extracted at different locations where the contrast on the 'super images' is variable. Several procedures had to be carried out in order to reach this goal:

1. Locating the positions of interest on the core-level 'super images'
2. Extracting and handling the local core-level spectra
3. Exploring the properties of the local spectra

The experimental operations and results of each step are detailed in the following paragraphs.

Locating the positions of local spectra on the core-level images

The high contrast in the secondary electron XPEEM images (see figure 5.33 (a)) helps to easily define the positions of interest (i.e. where the thickness of FLG changes). However, the low intensity and poor contrast on the core-level images make this task much more difficult.

Contrast-related difficulties Figure 5.33 shows three images of the same FoV acquired: (a) at the emission threshold energy (E-E$_F$ = 4.5 eV); (b) at the core-level energy of 285.05 eV before heating; and (c) at the core-level energy of 284.35 eV after heating.

A certain similarity can be observed between the contrasts of the threshold image (a) and the core-level image (b) before heating. This facilitates locating the positions of changing graphene thickness on the core-level image (b).

A reliable investigation of the surface properties, however, requires the local spectra to be extracted from the image series recorded after heating. Unfortunately because of the complete blurring of contrast on these images (after heating), it becomes very difficult to locate the positions of interest(see figure 5.33 (c)). Yet, we do not know why the contrast exhibits such a change between the core-level images before and after heating.

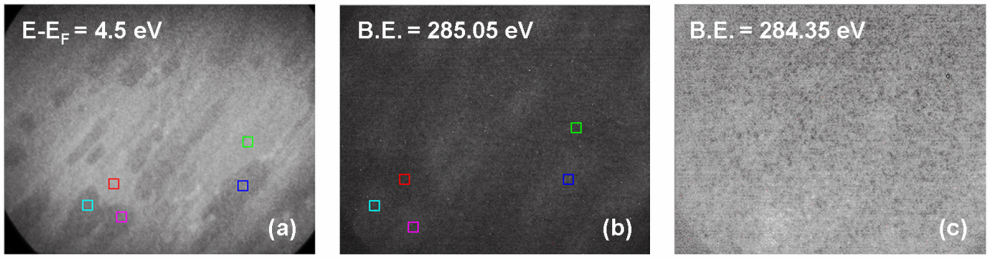

Figure 5.33: (a) SE XPEEM image recorded at the emission threshold energy $E - E_F = 4.5$ eV using the FXS photon source. (b) a single energy 'super image' at the core-level energy of 285.05 eV before heating. (b) a single energy 'super image' at the core-level energy of 284.35 eV after heating. The colored squares indicate the positions where the graphene layer thickness is variable, as found in the XPEEM threshold images.

How did we locate the positions on the images after heating? Firstly, we considered the positions located on the core-level images recorded before heating (see figure 5.33(b)) thanks to the contrast similarity with XPEEM threshold images. We note that, according to XPEEM work function measurements (see table 5.7), these positions were well assigned to FLG with different thicknesses: position 1 to the buffer layer (0 LG) - position 2 to 1LG - position 3 to 2 LG - position 4 to 3 LG and position 5 to thick graphite-like layers.

A trial and error method Therefore, we followed a 'trial and error' method to find the suitable positions on the blurry contrasted core-level images after heating. We defined suitable positions as being a set of five locations on the core-level images, after heating. The C1s and Si2p local spectra extracted at these suitable positions should present changes corresponding to an increase in FLG thickness in the same order of positions as determined from XPEEM work function measurements.

- We started by testing the coordinates of the positions that had been visually located on the core-level images before heating.
- Then several attempts were made to adjust the coordinates of these positions on the images after heating.
- For each attempt, five local spectra were extracted from the set of the five trial positions.
- The relative variations of all these trial spectra were continuously compared to the expected behavior for an ideal set of local spectra (where the graphene film thickness is expected to increase).
- From each attempt, the coordinates of the positions whose local spectra exhibited a coherent variation were kept, while the coordinates of positions with a divergent variation were adjusted in new consecutive attempts.

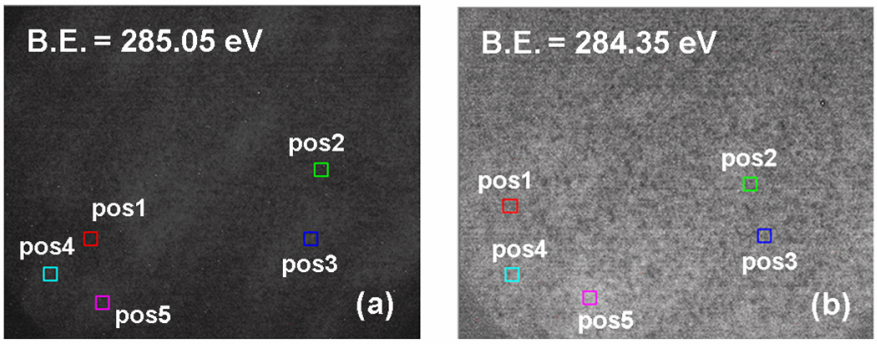

Figure 5.34: Single energy 'super images' taken at the core-level energy of (a) 285.05 eV before heating and (b) of 284.35 eV after heating. The positions on the image (a) were visually located by comparison to the contrast of the SE PEEM images. The positions represented on the image (b) were defined after a certain number of trials and errors before finding the suitable positions.

It took four trials before we could find a set of positions with an acceptable and suitable variation of the corresponding local spectra. These positions are presented in figure 5.34(b). Images correspond to the graphene/graphite chemical bonding state, and were taken at the binding energies of 285.05 eV (before heating (a)) and 284.35 eV (after heating (b)).

Image intensity and graphene thickness Core-level images indicate that regions with a different number of graphene layers are seen at different intensity levels. Since the positions on the core-level images were defined by comparison to those on the SE XPEEM images, then the number of layers is expected to increase going from position 1 to position 5.

Extracting and handling the local spectra

Spectra extraction Local spectra were extracted, from the C1s and Si2p 'super images' series, at the five positions defined in figure 5.34(b). Each spectrum was extracted from a 1 μm^2 square zone, which corresponds to $\sim 21 \times 21$ pixels. Regarding the number of super images of each sequence (section 5.3.5.3), the obtained local spectra consist of a small number of experimental (or raw) points. Local C1s spectra were formed by 8 experimental points and Si2p spectra were formed by 9 experimental points (see figure 5.35).

Energy corrections The corrections for the Schottky lowering effect and the energy dispersion (non-isochromaticity) effect were applied before extracting the core-level spectra at the defined positions (see appendix B).

Removal of the Shirley background signal We used the XPSPEAK software to remove the Shirley background from the raw local C1s and Si2p

spectra. Therefore normalized raw spectra were obtained.

Fitting the raw spectra with a Gaussian envelopes To estimate the local intensity from the C1s and Si2p local spectra, a Gaussian model was used to fit the distribution of experimental points for each spectrum. Regarding the very small number of raw points, this model forms an approximation of the present spectra leading to an approximate estimation of the local intensities.

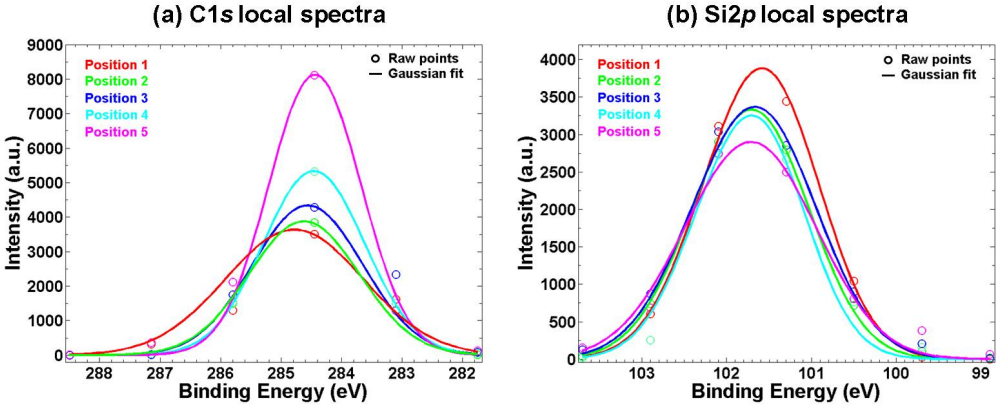

Figure 5.35: (a) C1s normalized local spectra extracted at the defined position in figure 5.34(b). Empty circles represent the raw points and dashed lines correspond to the Gaussian fit. (b) Si2p normalized local spectra. The evolution of the shape, intensity and peak area of all spectra is coherent with the expected evolution of graphene layer thickness at the present positions.

Figure 5.35 shows all the C1s and Si2p spectra as extracted (circles) from the set of positions after heating. The Gaussian fit (solid lines) of each spectrum are also presented. The color of each spectrum corresponds to the color index of the positions on the surface, as initially attributed in the XPEEM threshold measurements (see figure 5.17 for an example).

The initial conditions on the fit parameters A constraint was introduced to the initial values of the binding energy at the maximum intensity of each spectrum. We assumed that the binding energy of the C1s spectra refers to the reported value of graphite ($\sim$ 284.4 eV) for the spectrum extracted at position 5, where thicker graphene layers are expected [164]. A margin of 1 eV was kept for each initial condition.

Exploring the properties of the local spectra

In order to understand the relative variations of the C1s and Si2p local spectra (depending on the position on the surface), the data of each Gaussian envelope were fed to the XPSPEAK software, where the characteristics (binding energy,

FWHM and peak area) were determined. The evolution of these characteristics with respect to the position on the surface reflects the variation of the graphene layer thickness and helps confirm the good choice of these positions on the core-level images after heating.

Approximations We must clarify that the experimental procedure described above involved important approximations. The first approximation was made for the determination of the positions of interest. It was due to the poor contrast and intensity level of images after heating. The second one was made by fitting a very small number of experimental points for the C1s and Si2p spectra.

Therefore, the determination of characteristics of the local spectra using the Gaussian envelope fit result (figure 5.35) will yield values with a great approximation. Error bars are therefore large.

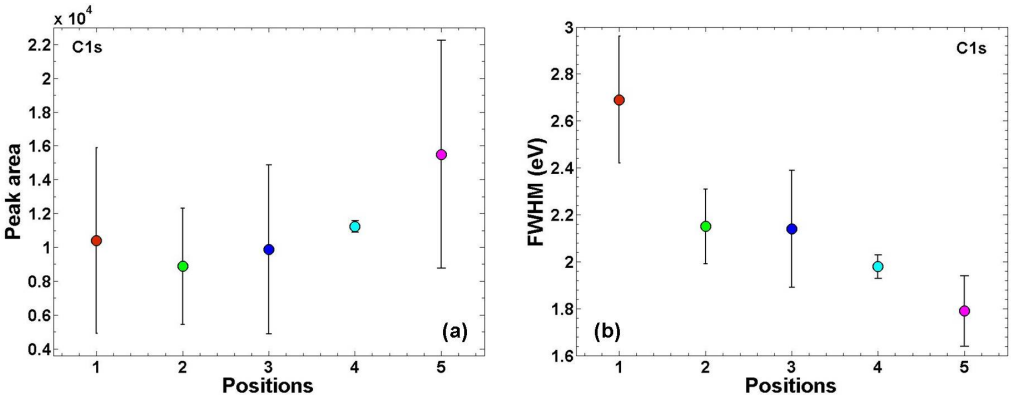

Figure 5.36: (a) The normalized peak area of the C1s local spectra as a function of the position on the surface. (b) FHWM of the C1s local spectra as a function of the position on the surface. Error bars were obtained from the confidence bounds of the Gaussian fit. Large error bars are due to multiple approximations (see text).

The evolution of the graphene coverage and the parameters of the C1s spectra Figure 5.36(a) shows the evolution of the normalized peak area of the C1s local spectra presented in figure 5.35(a). The confidence bounds of the Gaussian envelope approximation were used to determine the error bars on the normalized peak area. The large error bars can thus be explained by this accumulation of approximations.

Thick graphite-like zones The highest peak area value corresponding to position 5 (figure 5.36(a)) indicates the presence of more graphene layers compared to other positions. Moreover, the narrower shape of the local spectra at this position is reflected by the smallest value of the FWHM in figure 5.36(b). This indicates a predominance of the graphene/graphite component to the present spectrum. Therefore, thick graphite-like zones can be assigned to position 5,

which was initially expected from the choice of its coordinates on the core-level images after heating.

Buffer layer zones A monotonic increasing trend of the peak area is identified between the position 2 to 5, with the exception of position 1 where the peak area is found slightly higher. Moreover, the large FWHM value at the position 1 with respect to other positions (figure 5.36(b)) reflects the widening of the corresponding local spectra (figure 5.35).

This fact indicates that the contributions of the interface and the bulk chemical states to this local spectra (position 1) are more pronounced [164]. Therefore, this helps assigning position 1 to zones with a buffer layer coverage, which is in agreement with the choice of its coordinates.

1LG, 2LG and 3LG coverage While the local spectra at positions 1 and 5 were shown to be representative of the buffer layer and thick graphite-like layer coverage respectively, the relative variation of the peak areas between the positions 2, 3 and 4 may be respectively assigned to regions with 1LG, 2LG and 3 LG. This assumption will be quantitatively verified later by the estimation of the layer thickness from these local spectra.

These observations are consistent with recent PES results on the evolution of the C1s spectrum upon graphene growth of up to ∼4 layers [161] [189]. Wide spectrum was yielded over the buffer layer where the components of the bulk SiC and the reconstructed layer are most present. These components appear as small shoulders around a narrower peak, centered at a binding energy close to graphite with a higher intensity.

The evolution of the C1s binding energy with graphene thickness Figure 5.37 shows the evolution of the binding energy of the local C1s spectra at different positions on the surface. Error bars were determined from the parameters of the approximated Gaussian model, used to fit the experimental points of the C1s local spectra. We found the binding energy of the C1s local spectrum to shift toward smaller values when the number of graphene layers increases.

The binding energy at position 5 is ∼0.34 eV lower than that at position 1. This behavior is in accordance with recent results where the binding energy of thick-graphite layers was found lower than one monolayer graphene by about ∼0.4 eV [164].

The shift of the binding energy of the C1s spectra as a function of the number of layers results from the transfer of negative charge from the substrate to graphene layers. Simulation of ARPES measurements [165] demonstrated that the closer the layer is to the substrate, the more it is doped with electrons

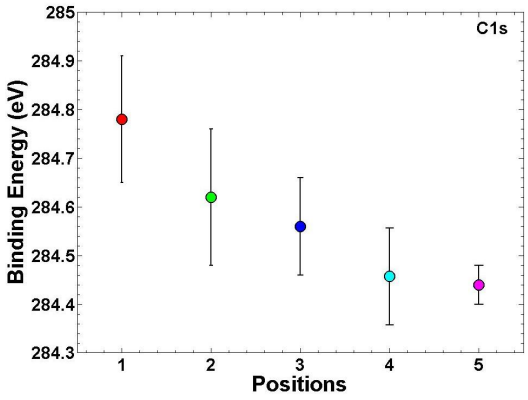

Figure 5.37: The binding energy of the maximum intensity of the C1*s* local spectrum, as determined from the characteristics of the Gaussian envelope of raw local spectrum at different positions on the surface. The binding energy of thicker layers (position 5) was initially assumed to tend toward the value corresponding to the bulk graphite (∼284.4 eV).

[161]. The change in doping level as a function of the number of graphene layers causes the Dirac point in FLG to shift further below the Fermi level [131] [165].

The displacement of the Dirac point with respect to the Fermi level is found close to the shift in C1*s* binding energy as a function of the thickness of layers [164]. Therefore it can be assumed that the C1*s* core-level shifts rigidly in FLG with the Dirac point [164]. However, as we discussed in section 5.3.3.3, this assumption explains rather well the shift in C1*s* core-level; but it roughly explains the shift of the work function with the number of FLG (section 5.3.3.3).

The evolution of the parameters of Si2*p* spectra with graphene coverage Figure 5.38 (a) shows the evolution of the normalized peak area of the Si2*p* local spectra depending on the position on the surface. Error bars were determined from the confidence bounds of the approximated Gaussian model (used to fit the small number of experimental points forming the local spectra). The large spread of these bars is a result of a series of approximations that were made during the experiment (as described above). However, we shall consider the values estimated from the fit (represented with colored circles).

The peak area presents a decreasing trend when the thickness of graphene layers at the different positions increases from position 1 to 5. However, the intensities at positions 3 and 5 are slightly higher than expected, compared to positions 2 and 4, respectively. This divergent behavior can be explained by the low intensities of Si2*p* core-level images.

Several attempts were made to adjust the coordinates of these two positions (3 and 5) to reconcile their behavior relative to other positions, but all efforts were unsuccessful.

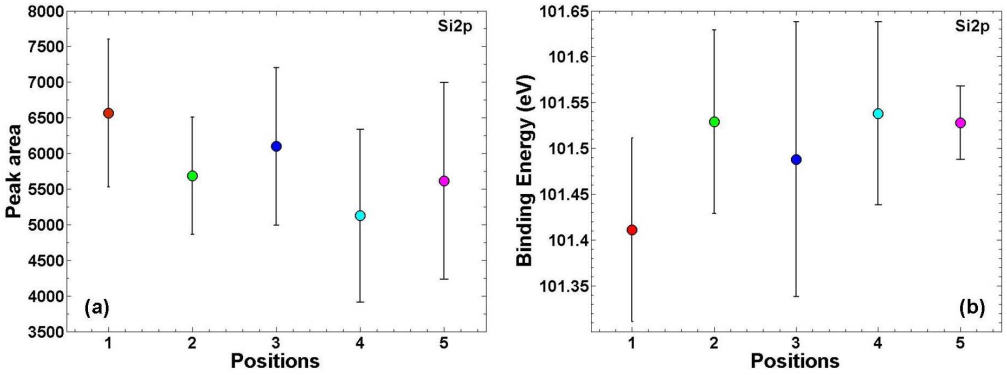

Figure 5.38: (a) The normalized peak area of the S2p local spectra as a function of the position on the surface. (b) binding energy at the maximum intensity of each Si2p local spectrum as a function of the position on the surface. Error bars were obtained from the confidence bounds of the Gaussian fit. Large error bars are due to multiple approximations (see text).

The binding energy of the Si2p spectra A shift of ∼0.1 eV toward higher binding energy values was found between the local spectrum at position 1 and the one at position 2 (figure 5.38(b)), which may explain the attribution of position 1 to a buffer layer coverage.

The core-level electrons are emitted from the bulk SiC and the reconstructed surface. When the number of graphene layers starts increasing, these core-level electrons can experience an additional scattering within these layers. This can explain the shift in binding energy of the core-level spectra to higher values.

However, the variation in binding energy of Si2p spectra between positions 2 and 5 with the thickness of graphene layers was barely noticeable. Nevertheless, the increase in layer thickness is mostly reflected by the decrease in peak area of the Si2p local spectra.

5.3.5.5 How to measure the thickness from local core-level spectra?

Principle The graphene thickness estimation is based on the usage of the simple attenuation model, i.e. the simulation of exponential decay of the bulk SiC component when the graphene films become thicker (emphasized by the complementarity between the C1s and the Si2p peak areas).

Using the Si2p spectra Because the bulk SiC signal is the principal component that contributes to Si2p spectra, they were used to estimate the thickness from the attenuation of their normalized peak area.

The reference position We chose the peak area of the local spectrum extracted at position 1 (where no graphene coverage is expected) as the reference

point. At this point, the peak area includes the signal from the bulk and the interfacial layer. Therefore, the comparison of all other local spectra directly reflects the evolution of graphene layer thickness. In addition, choosing this point as a reference helps overcome the question of topography variations of the underlying SiC substrate that was highlighted in KFM measurements.

What about the impact of the SiC underlying topography? Theoretical calculations and STM measurements have proved that the interface layer adopts the topographic variations of the underlying SiC substrate [186] [172]. Thus, by choosing position 1 (buffer layer coverage) as the referential point, we actually ensure two facts:

- First, the thickness of the buffer layer is not altered by the topography of the underlying substrate.
- Second, this thickness does not actually contribute to the value estimated from the local spectra since it is considered as a reference.

The law of exponential decay The expression of the exponential decay law used to estimate the layer thickness from the Si2p spectra is given by:

$$I_{Si2p}^{position} = I_{Si2p}^{reference} \exp\left(\frac{-t_G}{\lambda}\right) \tag{5.4}$$

where $I_{Si2p}^{reference}$ is the normalized peak area of the local Si2p peak extracted at reference position 1 (buffer layer coverage); $I_{Si2p}^{position}$ is the normalized peak area of the local Si2p peak extracted at any other position with different graphene thickness; t_G is the graphene layer thickness in nanometers; and λ is the electron escape depth in graphene layers estimated at 3.5 nm [131].

Measuring the graphene thickness from the Si2p peak areas

Therefore, the law of exponential decay was applied to the Si2p normalized peak areas presented in figure 5.38(a). Considering the peak area measured at position 1 as the referential value, we calculated the theoretical values of peak areas for an increased number of graphene layers (1 LG at a time) by using the exponential law from equation 5.4 with a theoretical thickness of 1 LG considered as 0.34 nm.

In figure 5.39 (a) we show the comparison between the measured peak areas (red circles) of the Si2p local spectra and the calculated values (blue squares). The peak areas measured from the local spectra at positions 2 and 4 present the best coherence with the calculated values. This confirms the fact that positions 3 and 5 present a divergent behavior that could not be corrected due to low intensity problems (as previously discussed).

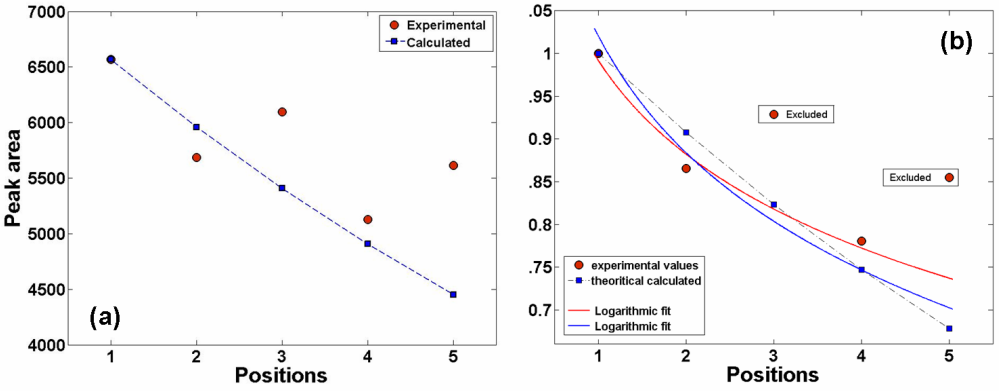

Figure 5.39: (a) The experimental values of the Si2p peak areas (red circles) and the calculated areas (blue squares) for an increasing number of graphene layers (1LG per point). (b) The normalized peak area with respect to referential position 1. The solid lines show the logarithmic fits of the experimental and calculated areas following equation 5.5

Normalization and direct thickness estimation To obtain the value of thickness from the measured Si2p peak areas, these values were normalized with respect to referential position 1. Therefore the graphene layer thickness can be estimated using:

$$t_G = \lambda \mathrm{Ln}\left(\frac{I_{Si2p}^{position}}{I_{Si2p}^{reference}}\right). \tag{5.5}$$

The logarithmic law from equation 5.5 was used to fit the experimental and calculated peak areas represented in figure 5.39 (a). However, since the points corresponding to positions 3 and 5 were shown to present a divergent behavior, they have been excluded from the current fit.

Thus figure 5.39(b) shows normalized peak areas with the logarithmic fit (solid lines) of the measured (red circles) and the calculated (blue squares) values. Both red and blue curves are in good accordance, which indicates the coherence of positions 2 and 4 with the theoretically calculated peak areas for 1LG and 3LG thickness.

The layer thickness at positions 2 and 4 Using equation 5.5 we found the graphene layer thickness at position 2 equal to 0.504 $\pm$ 0.315 nm and at position 4 equal to 0.866 $\pm$ 0.413 nm. The error on each calculated value was determined by considering the relative error in electron escape depth $\delta\lambda/\lambda = 30\%$ and by evaluating the difference between the measured peak areas and the theoretically calculated areas as seen in figure 5.39.

Validity of the estimated thicknesses On one hand, a 1 LG thickness is expected at position 2. However, the calculated value (0.504 nm) is slightly higher than the expected one (0.34 nm), which comes from the Si2p peak area of the spectrum extracted at this position. As we have seen, the low intensity of core-level images and the noise contribution to the local spectra are the principal reasons for the uncertainty encountered during our measurements. Similarly, the thickness calculated at position 4 (0.866 nm) is lower than the value expected for 3 LG thickness (1.2 nm).

5.3.5.6 Summary

A real increasing thickness Even though the thicknesses estimated at positions 2 and 4 present certain uncertainties with respect to the expected values, the increasing value between these two positions is an obvious demonstration that the graphene layer thickness becomes higher at position 4 where the contrast on the core-level images was variable.

If we thus revert back to when positions on core-level images were determined, we can ascertain a correlation between real thickness variations (estimated from local core-level spectra) and the work function variations (from XPEEM SE emission spectra).

Shifts of the C^{1s} binding energy Our spectromicroscopy measurements showed that the C1s binding energy shifts by $\sim$ 0.34 eV between FLG and thick graphite layers (see figure 5.37), which is quite close to the shifts of the Dirac point below the Fermi level (as reported by Ohta *et al.* and Zhou *et al.*). This can explain the interpretation that the C1s core-level in FLG is shifted due to charge transfer from the SiC substrate [164].

Present limitations and further improvements The low intensity of core-level images has been emphasized as the primary and principal source of limitations in our study. This has led to serious difficulties and time-consuming problems in determining the positions on the surface where the variation of contrast on the core-level images is purchased.

In addition, important alterations from the noise on these images caused the extraction of the local spectra to undergo several approximations. These approximations were extended to the estimation of local graphene layer thicknesses.

The improvement in detection conditions of core-level images is thus important for reliability and reproducibility of spectromicroscopy measurements. In fact, an increased sensitivity of the channeltron and camera systems can lead to a serious decrease in the acquisition time of a single core-level image. The approximations

of the local spectra could hence be reduced, which would improve the thickness estimation from these spectra.

5.4 General conclusion

The main goal of this chapter was to characterize the epitaxial graphene layers on SiC(0001) substrate by coupling the XPEEM experiments, using the different modes of the *NanoESCA* spectromicroscope,and KFM experiments.

We have demonstrated that the work function, measured by XPEEM threshold experiments, shows a directly increasing relationship with the number of graphene layers (in accordance with previous studies). At the present understanding, the number-of-layer dependence of the FLG work function seems to be evidence for screening carriers in FLG. A shift of the FLG electronic structures with the 'Dirac point' (i.e., due to the charge transfer from the substrate to FLG) is suggested.

However, charge distribution at the surface/interface, has an important effect on the work function and greatly contributes to the number-of-layer dependence. We also showed that reliable measurements require an effective elimination of carbon contamination at the surface of graphene layers (which was performed thanks to *in situ* heating treatments in the *NanoESCA*).

From SE PEEM measurements, we were able to automatically reproduce a real work function map on the surface under study. Thanks to the relationship established between the graphene work function and the number of layers, the work function map forms a direct image of the thickness distribution of graphene layers.

The increasing tendency of graphene's work function with the thickness of layers has been confirmed by KFM measurements in the lift mode. The contrast comparison of work function maps from KFM and XPEEM threshold measurements showed similarities. This indicated that the contrast of the V_{dc} images was related to the change in graphene layer thickness over the scanned zone. However, the environmental effects lead to a significant decrease in CPD values measured in the KFM lift mode in air. We thus believe that future KFM measurements in UHV conditions would facilitates comparison of reliable KFM and XPEEM measurements.

However, KFM Lift mode measurements have highlighted the problem of the terrace-like pattern topography of the underlying SiC substrate. This was found to continuously increase even on areas with homogeneous graphene coverage. Using topography maps in the current ambient conditions to determine layer thickness would thus be impossible. This could rather be done in UHV conditions, similar to results reported by Filleter *et al.* [168].

Nevertheless, thanks to spatial resolution enhancement with the MF-EFM mode in air conditions, we were able to identify a non-homogeneous growth of epitaxial graphene on the SiC terraces (not possible with KFM lift mode measurements). However, it is still not possible in current conditions to determine the graphene layer thickness using this technique.

Using XPEEM spectromicroscopy experiments, we identified a real increase in graphene layer thickness. We were able to estimate the graphene layer thickness from the local core-level spectra extracted at different positions on the sample surface. We found a thickness of ~ 0.504 nm for an expected 1LG coverage, and ~ 0.866 nm for an expected 3LG coverage. However, our estimations were very approximated and different from expected thickness values. All the approximations that were made for these estimations were due to the poor quality of core-level images in terms of intensity and contrast. Further advances in detection system sensitivity would help improve the quality of our estimations and thus increase the accuracy of layer thickness measurements.

The chemical composition of graphene layers on the SiC substrate was investigated with μ-XPS measurement over the entire FoV. The deconvolution of the C1s and Si2p spectra showed a structure of our sample consistent with the latest model proposed in literature for epitaxial FLG on SiC(0001).

The effects of the sample treatment by heating to 800°C in UHV for 30 min. revealed a Fermi level pinning effect present before heating. All bulk-related and interface-related chemical state components were shifted towards lower binding energy upon heating by $\Delta_{BE} = 0.4$ eV. A larger shift of the graphene/graphite peak suggested the presence of a dipole moment between the buffer layer and graphene overlayers. The formation of this dipole was assumend to originate from the distribution of the negative charge transferred from the substrate into graphene layers, which mostly resides in the first graphene layer.

Chapter 6
Conclusions

In this thesis we have focused on the characterization of the local work function using KFM in ambient conditions and laboratory-XPEEM with the *NanoESCA* spectromicroscope. The complementarity between both techniques has been evaluated in a complete investigation of the properties of epitaxial few layer graphene (FLG) thermally grown on SiC(0001) substrate.

By virtue of their particularly interesting electronic properties, FLG on SiC(0001) have recently sparked interest in new nanotechnology applications, especially in nanoelectronics development. The thermal growth of graphene layers on SiC(0001) results in a non-homogeneous distribution of the film thickness. The characterization of these layers (with high spatial resolution and easily accessible protocol) forms an important technological challenge. In this work, the coupling of KFM and laboratory-XPEEM measurements has been showed to offer important solutions to the problem of FLG characterization.

Evaluation of the work function measurement with KFM experiments In the first part of our study we investigated the quality of measurements performed in conventional KFM lift mode in ambient environment.

Effects of experimental parameters Spectroscopic measurements of the contact potential difference (CPD) on a set of metallic test samples showed a recurrent variation of the CPD as a function of the tip sample separation distance. We explained this variation by the presence of a local surface 'patch charge' density, induced by the local anisotropy of the work function. A 'patch charge' density of about $\sim 10^8$ $e^-.\mathrm{cm}^{-2}$ was determined from the fit of experimental results to the analytical model based on the current interpretation.

We showed that ***tip damages*** induce radical modifications in the CPD variation measured at a defined position on the sample surface. We identified these observations as an indicator of the evolution of tip quality before and after any scanning KFM experiment. We monitored the effect of the ***relative humidity*** level, of the measurement environment. Shifts in CPD towards higher

values were explained by the contribution of the electric dipoles of water molecules present on the sample surface when the RH% level increases. Finally, we showed that the amplitude of the ***electrical excitation*** of the cantilever (V_{ac}) and the ***bandwidth*** $B_{[Hz]}$ of the feedback loop have negligible effects on the spectroscopic measurements of CPD.

Improvement in spatial resolution A single scan method (MF-EFM) based on a multi-frequency double excitation scheme at higher flexural eigenmodes (in ambient conditions) was developed and described. We demonstrated that the spatial resolution of electrical measurements could be improved up to six times higher with the MF-EFM mode compared to conventional KFM lift mode measurements. However, we showed that a direct determination of the CPD is still not yet possible with MF-EFM, and further treatment and development are required to improve the capabilities of this method.

Stability of CPD measurements We investigated the stability of CPD measurements by studying the evolution of the tip work function during measurements using a standard sample (Ru), and by monitoring the tip's status from SEM images. We were thus able to define a simple treatment protocol for a routinely stable KFM measurement in a daily experiment operation.

Characterization of the FLG on SiC(0001) system In the second part of our study we investigated the properties of the epitaxial graphene layers thermally grown on SiC(0001) substrate. We were mainly interested in the characterization of the layer thickness using work function two-dimensional maps from KFM and laboratory-XPEEM experiments. We also investigated their chemical composition using XPS and spectromicroscopy modes of the *NanoESCA*.

Work function and graphene layer thickness The work function was measured at different positions on the sample using XPEEM threshold measurements. Values were found in a perfect accordance with experimental and theoretical work functions reported for graphene layers of different thicknesses. XPEEM threshold measurements have thus demonstrated an increasing trend of the FLG work function consistent with the increase in number of graphene layers. Thicknesses up to 3LG could be identified. This increasing tendency was confirmed by ambient KFM measurements in the lift mode performed on the same zone of the sample.

Work function, two-dimensional, maps have been reconstructed from XPEEM threshold images. The sample was found to be mainly covered by 1LG and 2LG, as expected from the present elaboration conditions. Similarities were identified between the contrast of KFM and XPEEM work function maps, indicating that

the CPD contrast of KFM images is consistent with the change in FLG thickness over the scanned zone.

Number-of-layer dependence of FLG work function This dependence can be evidence of screening of carriers in FLG, but a contribution of surface/interface dipoles seems to have an important impact on the work function of FLG on SiC(0001). A rigid-band model of FLG suggesting the shift of all electronic structures with the charge transfer from SiC(0001) to graphene layers provides a first order explanation. A better understanding requires further investigation. Calculations properly including the interface structure $(6\sqrt{3} \times 6\sqrt{3})$ are essential for the understanding of this number-of-layers dependence.

Determination of layer thickness To experimentally measure graphene layer thickness, KFM, MF-EFM and XPEEM spectromicroscopy measurements were used. KFM lift mode measurements showed that the topography of the surface increases continuously, even on zones with homogeneous graphene coverage (following the terrace-like pattern of the underlying SiC substrate). It was thus impossible to determine the graphene layer thickness in the current conditions. We estimate that KFM measurements in UHV should enable such a possibility.

Using MF-EFM mode with an improved spatial resolution, in air conditions, we observed that the formation of epitaxial graphene layers seems to occur in an non-homogeneous pattern over the terraces of SiC(0001). However, we are still unable of identifying the real coverage of SiC(0001) terraces observed on the MF-EFM images.

Using XPEEM spectromicroscopy measurements, a real increase of graphene layer thickness was observed from the evolution in local core-level spectra intensity. This thickness increase was found consistent with the increase in work function measured in XPEEM threshold experiments at the same positions on the sample surface. However, the layer thickness, as determined from our measurements, is only a result of a sequence of approximations induced by the poor intensity of core-level images and the determination of the local core-level spectra intensities.

We estimate that improving the quality of core-level images (by using synchrotron radiation or by using an advanced detection system sensitivity) would improve the accuracy of the procedure and provide a better estimation of graphene layer thickness deduced from local core-level spectra.

Chemical composition and number of layers We investigated the chemical composition of graphene layers on SiC(0001) by studying the C1s and the Si2p spectra on two levels: over the entire field of view using μ-XPS measurements and; locally at different positions using spectromicroscopy measurements.

Buffer layer and interfacial states We identified, from μ-XPS experiments, the continuous presence of the buffer reconstructed layer remaining at the interface with the SiC substrate, even after the growth of graphene layers. The analysis of the sample heating effects (at 800°C in UHV for 30 min.) on the shape and position of C1s and Si2p spectra (supported by literature data) suggested the presence of electronic states before heating associated with the formation of Si-dangling bonds at the interface. The large down-shift after heating of the graphene/graphite related component G compared to all other components was explained by the change in the dipole moment under the graphene layers. This dipole was interpreted to originate from the distribution of the charge that transfers from the SiC(0001) substrate to graphene layers through the interface.

Shift of the local C1s spectra with the number of layers Spectromicroscopy measurements showed that the binding energy of the local C1s spectra, extracted at different positions on the sample surface, decreases by $\sim$ 0.34 eV between FLG and thick graphite-like layers. This shift was reported in accordance with the displacement of the Dirac point below the Fermi level of graphene layers, due to negative charge transfer. The shift in C1s core-level is therefore interpreted to be caused by the negative charge transfer from SiC(0001) substrate to FLG.

All measurements that we have performed during this thesis emphasized the ability of ambient KFM and laboratory-XPEEM experiments to provide an interesting and complementary set of information for the understanding of FLG on SiC(0001) systems. They pointed out the possibility to characterize these systems with entirely laboratory-based protocol. We believe that the current protocol could be improved by a further coupling between KFM and XPEEM experiments, both performed in UHV conditions. This would help increase the accuracy of measurements in terms of spatial resolution, as well as reliability of work function measurements and determination of the FLG thickness.

Notre travail portait sur la caractérisation du travail de sortie local par les techniques de microscopie de force de Kelvin (KFM) sous air et de spectromicroscopie des photoélectrons excités par rayonnement X (XPEEM). Nous avons évalué la complémentarité entre ces deux techniques dans le cadre d'un cas d'étude d'un système model formé par des couches de graphène épitaxiées sur un substrat SiC(0001).

Grâce à leurs propriétés électroniques singulières, les couches de graphène sur SiC ont suscité récemment, un vif intêret pour différentes applications technologiques avancées, notamment en nanoelectronique. L'épitaxie par voie thermique du graphene sur SiC résulte dans la formation de couches d'épaisseurs inhomogènes à la surface. La caractérisation de ces couches (avec une résolution spatiale élevée et au moyen d'un protocol expérimental simple et accessible) forme une clé technologique importante. Dans ce travail, nous avons montré que la caractérisation couplée du travail de sortie par KFM et XPEEM offre des solutions importantes à cette problématique technologique.

Evaluation de la mesure du travail de sortie par KFM sous air Dans la première partie de notre travail, nous avons investigué les différentes aspects expérimentaux de la mesure du travail de sortie par la technique KFM en mode lift sous conditions ambiantes.

Effets des paramètres expérimentaux Des mesures spectroscopiques de la différence du potentiel de contacte (CPD) sur un ensemble d'échantillons métalliques ont montré une variation récurrente du CPD en fonction de la distance entre la pointe et l'échantillon. Nous avons expliqué cette variation par la présence de charge de surface associées à l'inhomogéneité locale du travail de sortie. Nous avons défini un modèle analytique qui nous a permis de déterminer la densité de ces charges surfaciques dans l'ordre de $\sim 10^8$ $e^-.\mathrm{cm}^{-2}$ en très bon accord avec les données de la littérature.

Nous avons montré la forte dépendence de la mesure du CPD sur la qualité de la pointe. Une modification radicale et reproductible de la variation du CPD en fonction de la distance est observée quand l'état de la pointe est détériorée. Ceci été identifié comme un indicateur de l'évolution de l'état de la pointe avant et après toute mesure KFM par balayage. Nous avons aussi étudié l'effet de l'humidité relative de l'environnement expérimental sur la mesure KFM. Les mesures effectuées sur les échantillons métalliques étudiés, montrent une diminution du travail de sortie quand le taux d'humidité relative augmente. Ceci été expliqué par la formation de dipôles moléculaires H_2O à la surface des échantillons, dont la densité augmente avec l'augmentation du taux d'humidité relative. Et finallement, nous avons montré que l'amplitude du signal de l'excitation électrique du levier (V_{ac}) ainsi que la bande passante ($B_{[Hz]}$) du la boucle de retroaction, présentent des effets négligeables sur la mesure spectroscopique du CPD.

Amélioration de la résolution spatiale Dans le cadre de l'étude des différents aspects liés à la mesure du travail de sortie par la technique KFM, nous étions intéressé par le développement de la mesure sous air pour améliorer sa résolution spatiale. Nous avons réussi à mettre au point une nouvelle méthode de mesure basée sur l'excitation simultanée du levier à différentes fréquences propres de vibration. Cette méthode dite MF-EFM[1] consiste à mesurer simultanément la topographie de surface et l'amplitude de vibration électrique du levier qui est proportionnelle à la valeur du CPD. Nous avons montré que la résolution spatiale de la mesure par MF-EFM est approximativement six fois plus élevée que celle de la mesure par KFM en mode lift. Néamoins, plusieurs développements restent à accomplir pour pouvoir accéder à une mesure directe du CPD avec la méthode MF-EFM.

La stabilité de la mesure du CPD par KFM Nous avons étudié la stabilité de la mesure du CPD par KFM en analysant l'évolution du travail de sortie de la pointe. Pour cela nous avons effectué des séries de mesures dans des conditions différentes sur un échantillon de réference formé par des couches de Ruténium (Ru) déposées sur substrat Si. Nous avons aussi suivi l'évolution de l'état de la pointe utilisée dans ces mesures par imagerie MEB[2]. Nous avons ainsi définit un protocol expérimental qui permet de réaliser des mesures KFM routinière et stable dans le temps.

Caractérisation des couches de graphène épitaxiées sur SiC(0001) Dans la seconde partie de notre travail nous étions intéressé par la caractérisation du travail de sortie des couches de graphène sur SiC(0001) par les techniques KFM et XPEEM. Nous avons aussi étudié leur composition chimique en utilisant les techniques de spectroscopie (XPS) et de spectromicroscopie des photoelectrons avec le *NanoESCA*.

Le travail de sortie des couches de graphène et la relation avec leur épaisseur Nous avons déterminé le travail de sortie par XPEEM à différentes positions sur la surface de notre échantillon. Les résultats expérimentaux sont en très bon accord avec les données fournies dans la littérature. Les valeurs du travail de sortie mesurées par XPEEM présentent une tendance d'augmentation selon la position à la surface, ce qui est liée - d'après la littérature - à la variation du nombre des couches de graphène. Cette tendance d'augmentation du travail de sortie été aussi confirmée par les mesures KFM effectuées sur la même zone à la surface de l'échantillon.

Une cartographie 2D du travail de sortie été reconstruite à partir des séries d'images XPEEM filtrées en énergie au niveau des électrons secondaires. Nous

[1] MF-EFM : Multi Frequency - Electric Force Microscopy
[2] MEB : Microscopie Electronique à Balayage

avons constaté que la surface de notre échantillon est recouvert principalement de 1 MC et de 2 MC de graphène. Ceci est en bon accord avec les résultats obtenus dans la littérature pour des conditions d'élaboration similaires à notre échantillon. Nous avons observé que les contrastes des images de cartographies du travail de sortie obtenues par XPEEM et par KFM sont similaires. Ceci indique que le contraste des images KFM est lié aux variations de l'épaisseur des couches de graphène sur SiC(0001).

La dépendence du travail de sortie sur le nombre des couches Nous avons trouvé que le travail de sortie des couches de graphène sur SiC(0001) augmente avec leur épaisseur. Selon la littérature, cette tendance met en évidence un effet d'écrantage de charge négative transférée du substrat SiC vers les couches de graphène. Une contribution supplémentaire dûe à la présence de dipôles à l'interface entre le substrat SiC et les couches de graphène, semble avoir une forte influence sur la variation du travail de sortie de ces couches.

Un modèle de bandes rigides proposé dans la littérature, suggère un déplacement de toutes les structures électroniques des couches de graphène avec le transfert de charges à partir du sustrat SiC. Néanmoins, une meilleure compréhension de cette variation observée du travail de sortie nécessite des investigations plus approfondies. Des calcules théoriques tenant compte de la structure $6\sqrt{3} \times 6\sqrt{3}$ de l'interface sont essentielles pour comprendre la dépendance du travail de sortie du graphène sur l'épaisseur des couches.

La détermination de l'épaisseur des couches Nous avons cherché à mesurer expérimentallement l'épaisseur des couches de graphène en utilisant les techniques KFM et MF-EFM ainsi que la technique XPEEM spectroscopique. Les résultas KFM en mode lift (sous air) ont montré que la topographie de la surface présente une augmentation monotone suivant les terraces du substrat SiC. Ceci nous empêche de determiner correctement l'épaisseur des couches de graphène à la surface de l'échantillon. Par contre, les données de la littérature ont montré qu'il est possible d'estimer l'épaisseur des couches par KFM en opérant sous ultra-vide (UHV).

En effectuant des mesures avec la méthode MF-EFM, mise en oeuvre dans ce travail, nous avons réussi à observer - avec une grande résolution spatiale ($\sim$ 10 nm) - la formation de domaines inhomogènes de graphène sur les terraces du substrat SiC(0001). Néanmois, les résultats restent qualitatifs, et nous sommes incapables de determiner la vraie épaisseur des couches de graphène par MF-EFM sous air.

Pour déterminer quantitativement l'épaisseur des couches de graphène, nous avons estimé l'intensité des spectres locaux obtenus au niveau des électrons de coeur C1s et Si2p par XPEEM spectroscopique. Les résultats montrent

une augmentation locale de l'épaisseur des couches de graphène en accord avec l'augmentation du travail de sortie. Par contre, la méthode que nous avons adoptée pour estimer l'épaisseur des couches comportait plusieurs sources d'incertitude dûes essentiellement à la faible statistique en imagerie des électrons de coeur. Nous pensons qu'une amélioration de la qualité des images obtenues avec les électrons de coeur permettra d'améliorer la précision de cette méthode. Ceci peut être envisagé par une augmentation du flux de photons (rayonnement synchrotron) ou par l'augmentation de la sensibilité du système de détection, par exemple.

La composition chimique des couches de graphène sur SiC(0001) Nous avons étudié la composition chimique des couches de graphène épitaxiées sur le substrat SiC(0001) en analysant les spectres des électrons de coeur C1s et Si2p sur deux niveaux : globalement sur tout le champ de vue (FoV = 38 μm) en utilisant les mesures de micro-spectroscopie (μ-XPS) et locallement à des positions d'intêret bien définies sur la surface en utilisant les mesures XPEEM spectroscopiques.

La couche tampon et les états d'interface Les mesures μ-XPS effectuées sur l'ensemble du champ de vue nous ont permi d'indentifier la présence de la couche tampon entre le substrat SiC(0001) et le graphène. Ceci est en très bon accord avec les données de la littérature. Nous avons analysé les effets d'un traitement de surface par chauffage *in-situ* de l'échantillon (à 800°C pendant 30 min.) sur les spectres C1s et Si2p. Les résultats expérimentaux, appuyés par les données de la littérature, suggèrent la présence d'états électroniques (avant chauffage) liés à la formation de liaisons pendante Si à l'interface. En plus, nous avons observé un déplacement de 0.4 eV après chauffage de toutes les composantes chimiques liées au substrat SiC et à la couche interfaciale. Ceci été expliqué par un phénomène d'ancrage du niveau de Fermi lié à la présence des liaisons pendantes avant chauffage. La composante chimique liée au graphène présentait un déplacement plus élevée (0.5 eV) par rapport aux autres composantes. Ceci été expliqué par la présence d'un dipôle sous les couches de graphène. L'origine de ce dipôle été interprété comme étant dû au transfert de charges négatives du substrat vers les couches de graphène.

Le déplacement des spectres locaux C1s avec le nombre de couches Nous avons extraits des spectres locaux à différentes positions sur la surface de l'échantillon, à partir des mesures XPEEM spectroscopique effectuées au niveaux des électrons de coeur C1s. Les résultats montrent que l'énergie de liaison des spectres C1s diminue de l'ordre de 0.34 eV lorsque le nombre des couches de graphène tend vers les couches graphitiques (+ 5 MC). Cette observation est en très bon accord avec les résultats rapportés dans la littérature. Ce déplacement de l'énergie de liaison C1s été expliqué par le transfert de charges négatives entre le susbstrat SiC(0001) et les couches de graphène.

Appendix A

The general expression of the electrostatic energy in EFM

The determination of the electrostatic force acting between the tip and the sample in electric force microscopy (EFM/KFM) is obtained by the derivation of the electrostatic energy of the entire system. So far, from general electrostatics, the electrostatic energy involves either fixed charges, or fixed potentials on the conductors forming the studied system. Therefore, deriving the expression of the force should take into account the one or the other of these cases, or even both, depending on the description of the actual electrostatic situation.

Actually, some confusions frequently occur in EFM published studies, where the expression of the electrostatic force describing the interaction between the tip and the sample, is sometimes badly written, which results in an inversion of signs. Therefore, in this appendix, we shall provide a clear and general method to determine the electrostatic energy of an arbitrary system of conductors, and then focus on its application in, where a corrected expression of the force is provided in order to overcome confusing situations.

A.1 Electrostatic energy of an arbitrary system

The system We consider, in a first place, a system formed by a set of finite metallic conductors of arbitrary shapes brought together in proximity. We assume that the conductors (designated by the index m) are kept at some fixed potentials by the mean of external voltage sources. In a general manner, we also consider an arbitrary distribution of point charges q_i at the positions $\mathbf{r}_i$ anywhere in the free space outside the conductors.

Electrostatic energy It is known from standard textbooks how to calculate the energy accumulated in the electrostatic field $\mathbf{E}$ created by point charges and metals [190]. Using the total energy of the field:

$$U = \frac{\varepsilon_0}{2} \int_V \mathbf{E}^2 dV \tag{A.1}$$

the integral is taken over the volume (V) outside the metals since inside them the field $\mathbf{E} = 0$. By applying the Poisson equation for the field, one gets:

$$U = \frac{1}{2} \sum q_i \phi(\mathbf{r}_i) + \frac{1}{2} \sum Q_m \phi_m \tag{A.2}$$

where ϕ_m is the fixed potential on the m^{th} conductor, Q_m is the total charge distributed on the surface of the conductor. $\phi(\mathbf{r}_i)$ is the electrostatic potential "felt" by the fixed charge q_i at the position $\mathbf{r}_i$. $\phi(\mathbf{r}_i)$ is formed by different contributions, associating the potential created by the Q_m charges on conductors and the potential created by all $q_j(\mathbf{r}_j)$ charges ($i \neq j$).

The effective energy: work of external sources In order to express the force imposed on any of these conductors, one have to consider the fact that the potential on conductors is kept constant by external voltage sources. The method of the "virtual work" is the tool to describe the way these external sources should be accounted.

As detailed in [67] [129], if some conductors were moved by an infinitesimal displacement $\delta\mathbf{r}$ with respect to their initial positions, then a certain work, δA, have to be rendered against the electrical force F acting on these conductors. When the displacement occurs, the potentials on the conductors, in their new positions, will be modified by an amount $\delta\phi_m$. Also is the case for the potential felt by the fixed charges (q_i) which will be changed by $\delta\phi(\mathbf{r}_i)$.

However, since the potential on the conductors is not allowed to vary because of the external voltage sources, then the $\delta\phi_m$ change will be rather expressed by some charge flow, δQ_m, between the connected conductors to maintain the potential on them. Therefore, some work will be spent in changing the potential energy of the field by the amount:

$$\delta U = \frac{1}{2} \sum q_i \delta\phi(\mathbf{r}_i) + \frac{1}{2} \sum \delta Q_m \phi_m \cdot \tag{A.3}$$

Moreover, some work $\delta A_{sources}$ is done in transferring charges between the conductors. This work is done by the external voltage sources and so should be taken with a minus sign:

$$\delta A_{sources} = -\sum \delta Q_m \phi_m \cdot \tag{A.4}$$

So, the total work δA done against the force F imposed on the conductors is given by:

$$\delta A = -F\delta\mathbf{r} = \delta A_{sources} + \delta U \cdot \tag{A.5}$$

Therefore, using the expression of $\delta A_{sources}$ the force can be deduced by:

$$-F\delta\mathbf{r} = -\frac{1}{2}\sum \delta Q_m \phi_m + \frac{1}{2}\sum q_i \delta\phi(\mathbf{r}_i)\cdot \tag{A.6}$$

One can see that the displacement of the conductors is energetically expressed by two type of variations. The first term, on the right side of the above equation, expresses the work done at constant potentials, while the second term expresses the work done at constant charges. Knowing that $F = -\partial U/\partial\mathbf{r}$, than the *"effective electrostatic energy"* is given by:

$$U^{eff} = \frac{1}{2}\sum q_i \phi(\mathbf{r}_i) - \frac{1}{2}\sum Q_m \phi_m\cdot \tag{A.7}$$

The difference between equation A.7 and equation A.2 is the minus sign before the term of the energy of the conductors m.

A.2 Application to KFM experiments

The expression of U^{eff} is therefore used to derive the electrostatic force acting on the tip in KFM experiments. The electrostatic system, in this case, is formed by two conductors: the tip and the sample. The displacement discussed above is applied, in this case to the tip. Then, the force acting on the tip can be deduced from the equation A.7 by calculating the first derivative of the *"effective electrostatic energy"*, which gives:

$$F_{ele} = -\frac{\partial U^{eff}}{\partial z} \tag{A.8}$$

where z is the vertical direction for positive displacements. Therefore, in absence of fixed charges (which could be caused by trapped charges), the correct expression of the force is given by:

$$F_{ele} = +\frac{1}{2}\frac{\partial Q_t}{\partial z}V_{ts} \tag{A.9}$$

where V_{ts} is the potential difference between the tip and the sample. Q_{tip} is given by the mutual tip-sample mutual capacitance: $Q_{tip} = C_{ts}V_{ts}$. Thus the electrostatic force is:

$$F_{ele} = +\frac{1}{2}\frac{\partial C_{ts}}{\partial z}V_{ts}^2\cdot \tag{A.10}$$

It is worth noting that, in presence of trapped or fixed charges in KFM or EFM experiments, the expression of the force should be extracted from the equation A.7 by taking into account the constant charge-related term.

Appendix B

Corrections of instrumentally induced artifacts

B.1 The correction of the Schottky effect

As detailed in the PEEM column description, the electrons emitted from the surface are accelerated by the mean of a strong electric field applied between the sample and the extractor within a distance of 1.8 mm. While the sample is grounded, the extractor is set to the potential $U_{ext} \approx 12$ kV. Thus the electric field can be estimated $E_{ext} = 6.66{\times}10^3$ kV.m^{-1}.

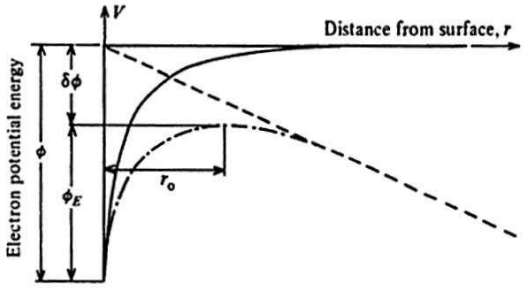

Figure B.1: A representation of the electrostatic electron energy. The full line shows the image potential, the dashed line shows the potential due to the E_{ext} and the chain line represents the total potential energy of electrons outside the metal. r_0 is the distance outside the crystal were the work function is defined.

The application of such a strong electric field causes the electrostatic potential energy of an electron to be lowered, and thus induces the lowering of the electronic work function. This effect is known as "the Schottky effect" [191] [192]. The decrease of the work function of electrons (figure B.1) is given by :

$$\delta\phi = \left(\frac{eE_{ext}}{4\pi\varepsilon_0}\right)^{1/2} \tag{B.1}$$

where e is the elementary charge ($e = 1.6{\times}10^{-19}$ C).For more details on the Schottky effect calculations one can refer to the reference [15]. As a result of this effect, kinetic energy of the photoemitted electron will be shifted by :

$$\Delta E_{Schottky} = -e\left(\frac{eE_{ext}}{4\pi\varepsilon_0}\right)^{1/2}. \tag{B.2}$$

For the present experimental settings, acceleration field $E_{ext} = 6.66\times10^3$ kV.m^{-1}, the energy shift due to the Schottky effect lowering is $\Delta E_{Schottky} = 98$ meV. Consequently, this "Schottky effect" correction term should be subtracted from the kinetic photoelectron energy in all further experiments.

B.2 The narrowing of the field of view

One of the experimental effects that should be specified in the case of imaging microscopy modes is the narrowing of the field of view depending on the kinetic energy of the photoelectrons. This effect results in a slight reduction of the dimensions of the field of view of the core-level images compared to secondary electron images. More details can be found in the review article by Schneider *et al*. [86]]. Theoretical aspects can also be found in the developed parts in the 'Electron spectroscopy' section of the reference [15]. The care for the arrowing effect gets a great importance in the particular case of the comparison between electronic and chemical properties of the surface using SE images and core-level images respectively.

The experimental procedure, for the determination of this effect, consists on imaging a well defined structure (here a FIB milled mark on a gold layer sample) using both threshold emission and core level electrons. The ratio of the measured dimensions on acquired images gives the narrowing factor of the FoV for the core level emitted electron images as shown on figure B.2.

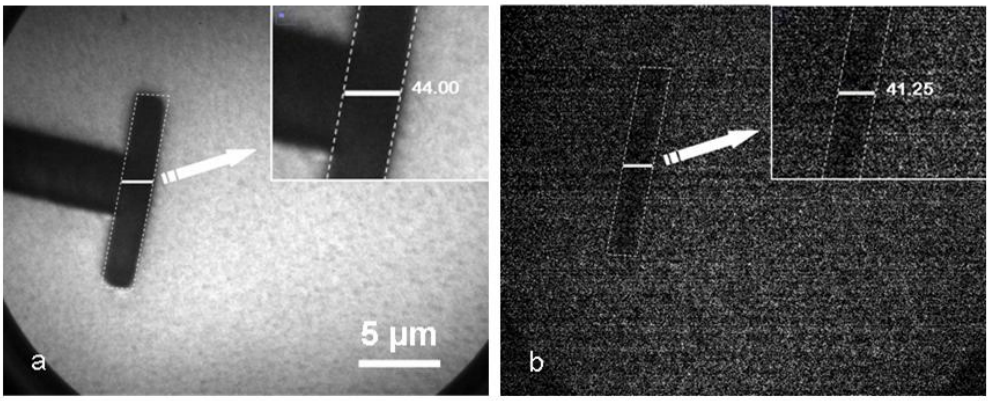

Figure B.2: Images of, a FIB made, cross- mark acquired using (a) Hg source ($h\nu = 4.9$ eV) at threshold emission energy of 5 eV and (b) FXS Al-K$_\alpha$ source ($h\nu = 1486.6$ eV) at the $4f_7/2$ core level energy of gold. The width of the FIB mark is narrower on the core level image by a factor $R = 0.94$.

The upper image (a) has been acquired at the threshold emission energy of 5 eV using the Hg photon source ($h\nu = 4.9$ eV). The field of view was set to FoV = 38 μm. The lateral width of the FIB mark structure has been found equal to 44 pixels. The lower image (b) has been obtained using the X-rays photon source (h$h\nu = 1486.6$ eV). The image was acquired at the binding energy (88.1 eV) of the gold $4f_{7/2}$. Experimental conditions and adjustments were kept the same as the previous image case. The lateral width of the FIB structure has been found equal to 41.25 pixels on the core level acquired image.

Consequently the ratio of the latter measured width to the one measured on image (a) is $R = 0.94$. Consequently, the narrowed dimension of the FoV of the core level images can be given by : $FoV_{core} = R \cdot FoV_{threshold}$. Therefore, the narrowing factor, R should be accounted for while leading a locally defined comparative study of electronic (work function from threshold emission images) and chemical properties (chemical bonding from core level images). However, practical examples show a disymmetric changes of the dimensions of the FoV which should be carefully considered, which make this issue much more complicated.

B.3 The non-isochromaticity of a energy-filtered image

This effect is due to energy shift within a single energy image, depending on the position inside this image). In fact, the take-off angle of the photoelectrons, coming from a given off-axis point at the sample surface, defines the initial divergence of the resulting electronic beam. This angular divergence changes after photoelectrons cross the retarding field in the PEEM column, in order to adjust their kinetic energy to the pass energy of the double analyzer entrance slit. This effect is expressed by the Helmholtz-Lagrange equation for any electron optical system which in this case may be written as:

$$\alpha_0^2 E_k^i = \alpha_1^2 E_{pass} M_1^2 \tag{B.3}$$

where,α_0 is the divergence when a photoelectron had the original kinetic energy E_k^i after being extracted from the sample. α_1 is the divergence after retardation to the energy E_{pass} and M_1 is the first lateral magnification of the microscope in the image plane at the coupling lens entrance. It is obvious that the divergence of the electronic beam after retardation, thus at the entrance of the first analyzer of the IDEA system, is directly proportional to the pass energy at the first entrance slit.

When the off-axis photoelectrons enter the IDEA system they fall shorter inside the hemispherical field and are cut by the exit slit. This effect occurs symmetrically to the optical axis and is directly proportional to the analyzer pass

energy. For a point on the sample, at a distance x_0 from the optical axis in the dispersive direction, the corresponding energy shift can be deduced by:

$$\Delta E = E_{pass} \left(\frac{M_1 x_0}{f} \right)^2 . \tag{B.4}$$

Therefore, this energy shift should be corrected for all images acquired in the energy-filtered mode. From an experimental point of view, the energy dispersion correction consists, first, on the determination of the optical axis position in the field of view of the acquired image, and second, on the calculation of the x_0 with respect to the optical axis, for each position in the image plane. Knowing the microscope experimental parameters (M_1, f and E_{pass}), the ΔE shift can be determined for any position in the FoV of the image.

Application of the experimental procedure Actually, a photoelectron emitted from a position x_0, on the sample surface, with respect to the optical axis of the microscope, will not have the same distance with respect to the optical axis in the dispersive direction on the acquired image. This is a direct result of the energy dispersion effect.

In order to correct this effect, the correct x_0 value of the electron position with respect to the optical axis should be found on the image in the dispersive direction. To do so, we draw a cross section of a vertical line on the energy-filtered image using a Matlab code developed for this purpose.

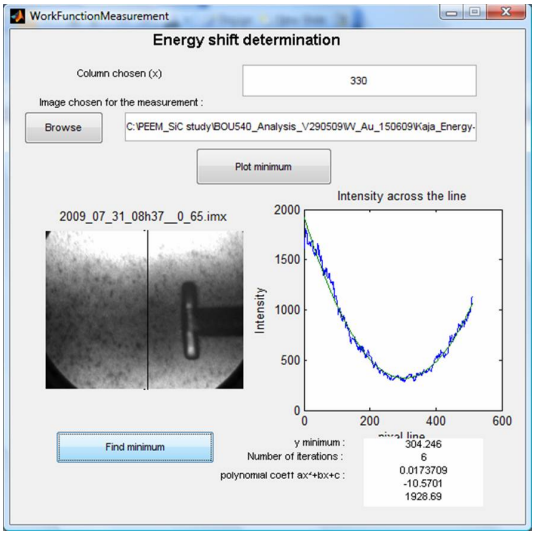

Figure B.3: The application of the Matlab code used for the determination of the center of the parabolic energy dispersion curve obtained from a cross section profile in the dispersive direction of the image.

The parabolic profile of the energy dispersion, as shown on figure B.3, is actually not centered on the actual center of the FoV on the acquired image. This displacement, due to ΔE can be corrected by determinating the value of

the center of the parabolic profile and adjust it to the actual center of the FoV.

Consequently, the ΔE can be ultimately calculated for each position on the image and the energy of photoemitted electrons should be corrected.

Appendix C

An overview of existing methods for the characterization of FLG thickness

Different surface analysis techniques have been employed together in order to make conclusions about the morphology of graphene films. While each of these techniques provide pieces of the puzzle, it is crucial to understand what is being measured, the particular accuracy of measurements and the conditions in which these techniques are used. In this section we will overview these existing methods and will point out their advantages and their limitations.

C.1 Auger Electron Spectroscopy (AES)

An early method that is still used to determine graphene thickness is AES [162]. The carbon (KLL) AES spectrum shows a distinct change from C in SiC to C in graphene. The ratio of the Si(LVV)/C(KLL) peak area can be tracked as the films develop and used as an estimate of the number of graphene layers. Actually, AES measurements can overestimate the graphene film thickness by $\sim$1 layer because the C(KLL) intensity includes a contribution from the dense non-graphitic interface carbon layer. AES estimation is very uncertain for graphene films exceeding more than four layers because the electron penetration depth of the Si(LVV) electron is short.

C.2 Surface X-ray Diffraction (SXRD)

The SXRD methods measures the graphene layer thickness in two ways: (i) by measuring the specular reflectivity and (ii) by measuring the crystal truncation rods of graphene [162]. The first method (i) gives the density gradient vertical to

the surface (including the interface layer) and allows for a weighted average of film thickness over the beam size. The second method (ii) is only sensitive to the number of crystallographic graphene layers. But because of the grazing incidence geometry, the results represent an average over millimeter dimensions.

C.3 X-ray Photo Emission Spectroscopy (XPS)

The C1*s* photoemission spectrum shows a binding energy shift from C in SiC to C in graphitic structures. The relative intensities of the graphitic peak and the bulk SiC peak of the C1*s* spectrum can be used to estimate graphene thickness. A similar estimate can be made by comparing the relative intensities of the Si2*p* and C1*s* peaks. The spatial resolution of conventional XPS measurements is limited by the beam size (down to 10 μm) and results represent an averaged estimate of the layers thickness. Conventional XPS experiments are unable to provide spatially resolved measurements of the graphene non-homogeneous lateral thickness distribution.

C.4 Ellipsometry

This technique probes the surface on a millimeter scale. The beam size is typically 200 μm but is elongated due to the incidence angle. In principle the technique can measure film thicknesses from less than 1 layer up to 10^3 layers [162]. Its accuracy, as applied to epitaxial graphene, primilarly depends on the reliability of the optical constants of graphene, which vary significantly in the literature. Like AES, ellipsometry predicts an average of 1-2 extras graphene layers compared to SXRD estimates. The advantages of ellipsometry over AES are that surface segregated Si has less than an effect on the graphene thickness estimate and is not limited to measurements of films less than 4-5 layers.

C.5 Low Energy Electron Microscopy (LEEM)

LEEM is a surface imaging technique that has a typical spatial resolution smaller than 10 nm. The number of graphene layers is actually determined by using quantized oscillations in the low energy electron reflectivity [166]. Hibino *et al.* measured graphene thickness variation on UHV grown SiC(0001) graphene that range from one to seven layers (see figure C.1). Another work by Virojanadara *et al.* showed more spatially resolved measurements with the same reflectivity technique on a spectroscopic photoemission and low energy electron microscope with a synchrotron radiation. A thickness range from 1 to 4 layers has been probed by these experiments.

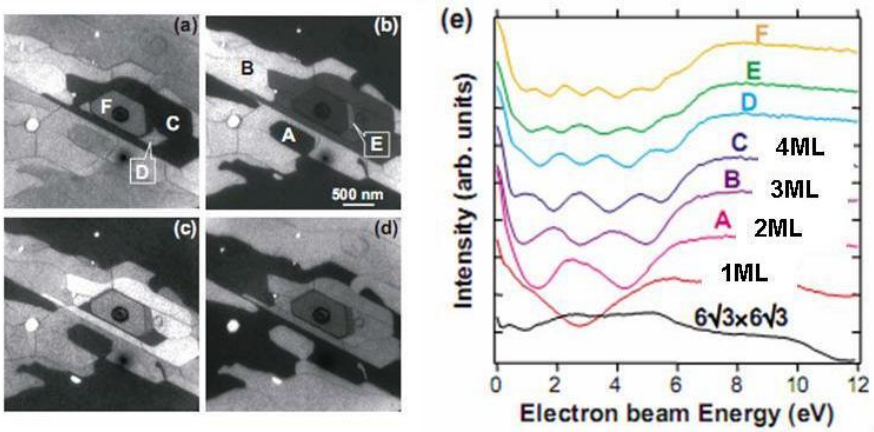

Figure C.1: (a)-(d) LEEM images of a 6H-SiC(0001) surface graphtized at 1460°C. (e) The electron reflectivity from the regions indicated on images indicating the increase of the number of layers. The $6R30$ and 1ML data were obtained from different samples. From ref [166]

C.6 Micro-Raman spectroscopy

Raman spectroscopy techniques is used to study vibrational, rotational and other low-frequency modes in a system [171]. The most pronounced informative Raman features of graphene, excited by visible lasers, are a distinctive peak in the vicinity of 1580 cm^{-1} (the G peak) and a band around 2700 cm^{-1} (the $2D$ band) [171]. The ratio of the G and $2D$ intensities is used for the identification of the number of graphene layers from 1 to 7 layers thickness. The deconvolution of the $2D$ band to elemental peaks also helps in determining the number of layers on the basis of the double resonance model. A recent study by Calizo *et al*. shows the evolution of these spectral features as the number of graphene layers increases (see figure C.2). The typical lateral and in-depth resolutions of micro-Raman spectroscopy are 1 and 2 μm, respectively. Thus results are expected to provide averaged measurements for non homogeneous graphene thickness distribution.

C.7 Angle Resolved Ultra-violet Spectroscopy (ARUPS)

This technique has been widely used to experimentally determine the band structure of ordered systems and therefore naturally applies to graphene layers. The band structure evolves with the increasing number of graphene layers. While a linear dispersion of the π bands at the Dirac point is observed for a monolayer graphene, the number of these π bands increases for thicker graphene films and a gap between these bands appears around the Dirac point. By counting the number of π bands, Riedl *et al*. measured one, two and three epitaxial graphene layers using ARUPS experiments (figure C.3). While ARPES experiments are based on a complex usage of synchrotron radiation facilities, ARUPS measurements

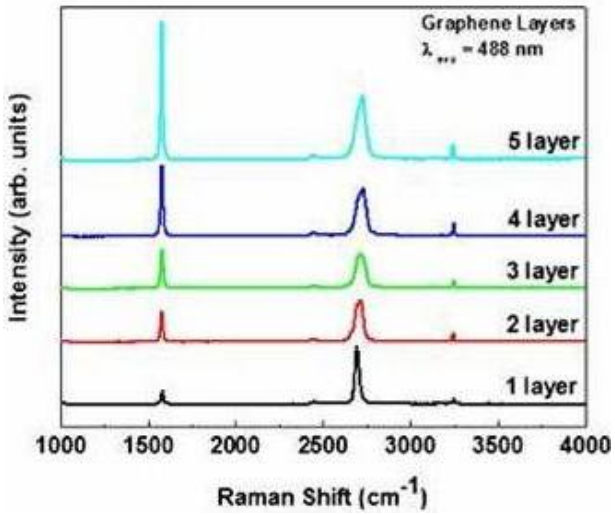

Figure C.2: Evolution of Raman spectrum of graphene under visible laser excitation λ=488 nm as the number of atomic planes increases from $n = 1$ to $n = 5$. From [171].

are much easily and directly performed using a laboratory UV photon source. However, the spatial resolution of this technique still roughly dependent on the beam size and the $E(k)$ dispersion curves are obtained indirectly from an important number of angle dependent experiments, where a precise control of the sample rotation is crucial.

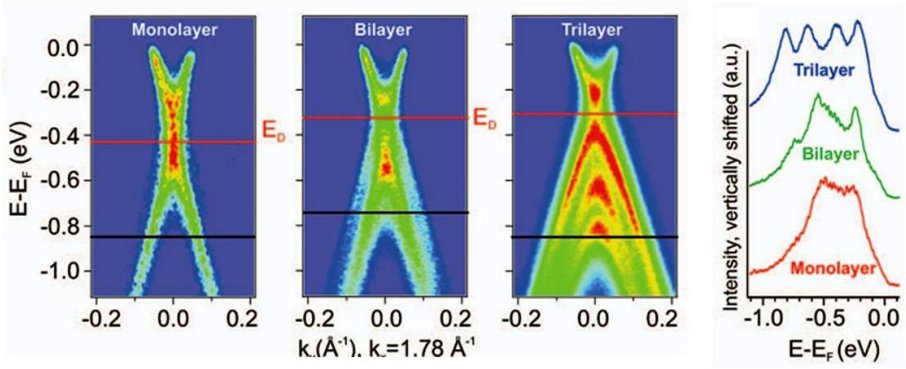

Figure C.3: Photoemission images measured inthe ky-direction revealing the different branches ofthe π bands for different number of layers and energy distribution curves extracted at k_y=0 and integrated over $0.01\mathring{A}^{-1}$. From ref [177]

C.8 Low Energy Electron Diffraction (LEED)

LEED is a electron diffraction technique which allows the determination of the surface structure in the reciprocal space. Actually, LEED experiments, alone,

are not suitable to measure the thickness of graphene layers. But different studies have demonstrated the possibility of coupling LEED measurement to other characterization methods which allows to calibrate the LEED diffraction patterns and subsequently to approximate the thickness of graphene layers. The previously mentioned work by Riedl *et al*. showed that the calibration of LEED patterns with ARUPS data allows an unambiguous assignment of the LEED intensities to the number of graphene layers. A similar calibration procedure of LEED measurements has been employed by Virojanadara *et al*. by comparing the patterns to electron reflectivity measurements using LEEM experiments as previously described.

C.9 Scanning Tunneling Microscopy (STM)

STM has been intensively used to image the atomic arrangement of carbon atoms in honeycomb lattices form of graphene layers thanks to its high spatial resolution that can reach values as small as 0.1 nm. A stable imaging with STM is a very hard task, and even harder is the interpretation of the acquired images. Mallet *et al*. showed that monolayer and bilayer graphene on SiC(0001) can be distinguished by STM by interpreting the changes of the images contrast and atomic arrangement due to the layer stacking[173]. Lauffer *et al*. demonstrated that an 'interface-induced roughness' in few layer graphene films on SiC(0001) can be used to quantitatively diagnotize the layer thickness. This 'interface-induced roughness' decreases monotically with layer thickness as seen on figure C.4. Authors demonstrated that the thickness estimation based only on the interpretation of the images contrast can lead to errors due to possible underlying changes in the layer stacking symmetry. Similar observations have been reported by several groups [172]. However, STM is still a hardly accessible and non straightforward way to estimate the thickness of graphene layers.

C.10 Atomic Force Microscopy (AFM)

AFM measures the topography of a sample with a spatial resolution that can varies from several tens of nanometers to several nanometers depending on the experimental conditions and operational modes. For the estimation of the graphene layer thickness, AFM topography measurements have been frequently compared to other measurements using either different characterization tools (RAMAN spectroscopy [169]) or another AFM-related techniques such as EFM or KFM. Obraztsova *et al*. used a statistical analysis of AFM topographic measurements coupled to Raman measurements in order to determine the thickness of exfoliated graphene layers. Layers thickness was found to vary from 0.7 nm to 1.4 nm for one-, two- and three layers respectively with a precision of $\pm$ 0.2 nm. Results show an over-estimation of the layers thickness due to contamination related effects in ambient environment.

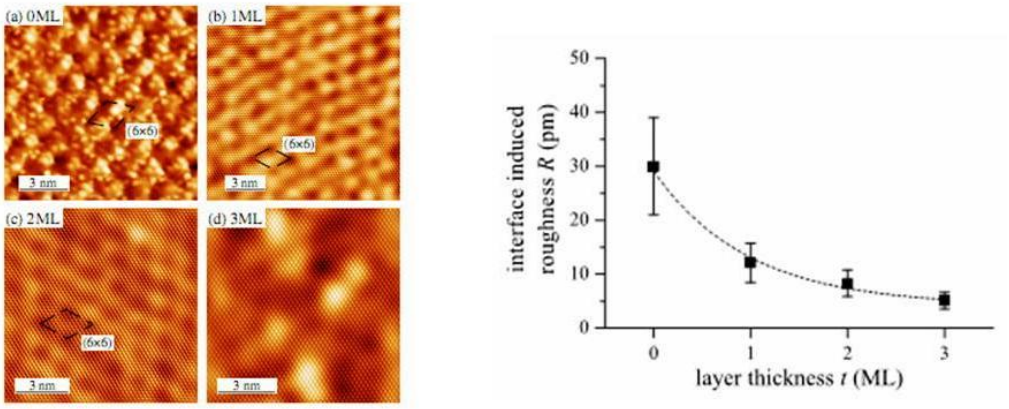

Figure C.4: (a)-(d) STM images of FLG films with well defined thickness. The curve on the right side shows the decrease of the interface reduced roughness R with the number of graphene layers. From [172].

C.11 Kelvin Force Microscopy (KFM)

More accurate results have been reported by Filleter *et al.* using Kelvin Force Microscopy (KFM) under UHV condition in non-contact operational mode. Authors were able to distinguish graphene zones with different thicknesses grown on SiC substrate based on the interpretation of the highly resolved topography images that can be acquired in the actual conditions as it can be seen on figure C.5. A 135 meV variation of the surface potential between mono- and bilayer graphene has been reported, which is found to be in a good agreement with reported doping-induced shift of the Fermi level as measured by ARPES experiments. Similar results have been reported by Datta *et al.* for exfoliated graphene flakes with thickness ranging from 1 to 5 layers using the surface potential measurements with Electric Force Microscopy.

C.12 X-ray Photo Electron Emission Microscopy (XPEEM)

In fact, the limitations imposed by instrumental conditions and measurements artifacts (aberrations, energy shifts) on conventional PEEM microscopes have prevented the usage of this tool to determine the thickness of graphene layers. Instead, recent studies have assessed the graphene layers thickness measurements, particularly performed by LEEM experiments, by XPEEM measurements. Virojanadara *et al.* have measured PEEM images of epitaxial FLG grown on SiC using Si2p core-level electrons and have showed that zones of 1 - 4 layers thickness can be distinguished on these images. Hibino *et al.* have adopted XPEEM experiments, in the range of secondary emitted electrons, to measure the variation of

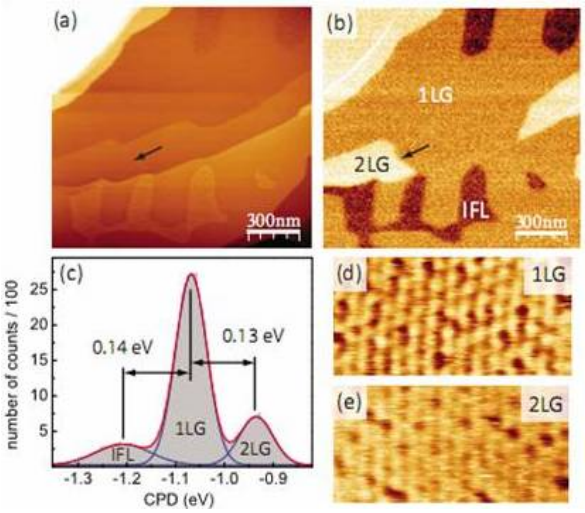

Figure C.5: (a) Topography image detailing the surface structure. (d) and (e) High-resolution topography images revealing the 6 × 6 superstructure on adjacent single and bilayer films. (b) CPD map identifying the interfacial layer zone and the 1LG and 2LG zones. (c) Histogram of the CPD map. From [168].

the local work function on graphene layers which thickness has been previously measured by LEEM technique. They demonstrated a monotonous increasing relationship between the graphene work function and the thickness of layers (see figure C.6).

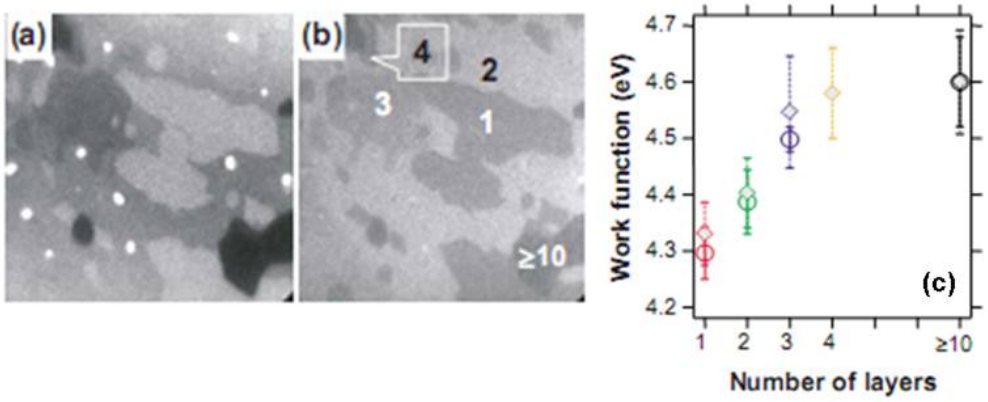

Figure C.6: (a)-(b) SE PEEM images of FLG grown on a 6H-SiC(0001) substrate. (c) The dependency of the work function of these FLG on the number of layers previously measured by LEEM on the regions indicated on the images (a) and (b). The work function of the bulk graphite is assumed equal to 4.6 eV. The error bars corresponds to the errors of the tangential fit of secondary electron spectra at the precised locations on the images. From [164]

Appendix D

Practical aspects for XPEEM and KFM coupled experiments

D.1 Sample orientation and referential elements

The ability to reproduce measurements on the same zone of interest over the surface of the sample in XPEEM and KFM experiments is a crucial point in the coupled studies. For this reason, an orientation elements are planned:

- First, we create a macroscopic feature on the sample by cleaving one of its corners. This way, it becomes easier to set the sample in the same orientation on both the XPEEM and the KFM sample holders.
- Second, we defined a microscopic referential feature somewhere in the central region on the surface of the sample by creating a cross mark using Focused Ion Beam (FIB) milling technique [1]. The shape and dimensions of the FIB cross mark are shown on figure D.1.
- Due to its microscopic dimensions, locating the referential cross mark using the KFM CCD camera system or the PEEM direct imaging becomes a difficult and time consuming problem. In order to avoid this difficulty an additional referential element can be featured. A small arrow shape can be made, by FIB milling, at one of the borders of the sample. Pointing toward the central cross mark, it helps to easily locate the cross mark by starting imaging around the borders of the sample.

D.2 Protocol steps

- Experiments should, first, start with XPEEM, after taking into account the points previously developed for the sample preparation. Therefore,

[1] FIB experiments were held on a FEI STRATA DB400

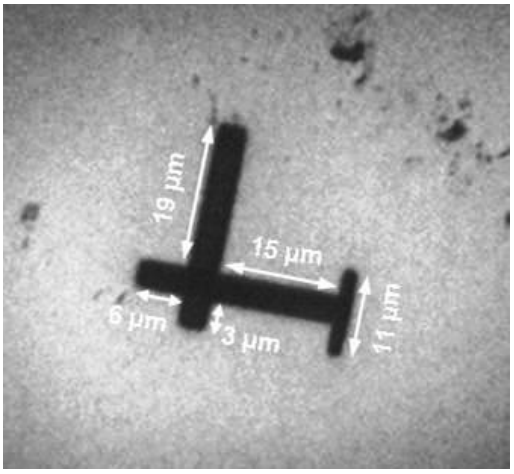

Figure D.1: A PEEM image of the cross mark showing its asymmetric geometry and dimensions as fabricated by FIB milling in the central region of the sample

XPEEM measurements can be done on a chosen field of view over the zone of interest which coordinates are defined with respect to the central referential cross mark.

- Second, the sample can be brought out of UHV and carefully positioned on the sample holder of the KFM experiment respecting the orientation instructions.
- For the sake of time gaining, the borders of the sample can be firstly imaged by KFM optical system in order to find the arrow mark. It becomes easier then to quickly find the position of the central cross mark and reposition the KFM probe over the defined zone of interest.

Bibliography

[1] John Bardeen. "theory of the work function. ii. the surface double layer". *Physical Review*, 49(9):653, 1936. 6, 8

[2] Wei W. Ashcroft and David N. Mermin. *"Solid state physics"*. Thomson Learning, 1976. 6, 9, 13, 14

[3] H. Luth. *"Solid Surfaces, Interfaces and Thin Films"*. Advanced Texts in Physics. Springer, 4 th edition, 2001. 6, 9, 10, 15, 16, 81, 82

[4] J. Holzl and F. Schulte. "work function of metals". In *Solid Surface Physics*, pages 1–150. 1979. 7, 10

[5] N. D. Lang and W. Kohn. "theory of metal surfaces: Charge density and surface energy". *Physical Review B (Condensed Matter and Materials Physics)*, 1(12):4555–4568, 1971. 7, 8

[6] G. Attard and C. Barnes. *Surfaces*. Oxford Chemistry Primers. Oxford University Press, Oxford, —1998—. 8, 9, 10

[7] K. Wandelt. "the local work function: Concept and implications". *Applied Surface Science*, 111:1–10, 1997. 8, 10

[8] R. Smoluchowski. "anisotropy of the electronic work function of metals". *Physical Review*, 60(9):661–674, 1941. 8, 9, 11

[9] O. Renault, R. Brochier, A. Roule, P. H. Haumesser, B. Kromker, and D. Funnemann. "work-function imaging of oriented copper grains by photoemission". *Surface and Interface Analysis*, 38(4):375–377, 2006. 9, 10, 11, 22, 25, 58, 59, 60, 61, 138

[10] Nicolas Gaillard, Mickael Gros-Jean, Denis Mariolle, Francois Bertin, and Ahmad Bsiesy. "method to assess the grain crystallographic orientation with a submicronic spatial resolution using kelvin probe force microscope". *Applied Physics Letters*, 89(15):154101–3, 2006. 9, 10, 11, 24, 42, 46, 48, 75, 80, 81

[11] R. L. Gerlach and T. N. Rhodin. Binding and charge transfer associated with alkali metal adsorption on single crystal nickel surfaces. *Surface Science*, 19(2):403–426, —1970—. 10

[12] R. Dianoux, F. Martins, F. Marchi, C. Alandi, F. Comin, and J. Chevrier. "detection of electrostatic forces with an atomic force microscope: Analytical and experimental dynamic force curves in the nonlinear regime". *Physical Review B (Condensed Matter and Materials Physics)*, 68:045403–6, 2003. 10, 74

[13] Olivier Douheret. *"High resolution electrical characterization of III-V materials and devices"*. PhD thesis, KTH, Microelectronics and Information Technology, 2004. 10, 15

[14] D. Cahen and A. Kahn. "electron energetics at surfaces and interfaces: Concepts and experiments". *Advanced Materials*, 15(4):271–277, 2003. 12, 14, 15

[15] D.P. Woodruff, T.A. Delchar, D.R. Clarke, S. Suresh, and I.M. Ward. *"Modern Techniques of Surface Science"*. Cambridge University Press, 2nd revised edition edition, 1994. 12, 16, 17, 189, 190

[16] N. A. Burnham, R. J. Colton, and H. M. Pollock. Interpretation of force curves in force microscopy. *Nanotechnology*, 4:64–80, —1993—. 12, 13, 14

[17] N. A. Burnham, R. J. Colton, and H. M. Pollock. "work-function anisotropies as an origin of long-range surface forces". *Physical Review Letters*, 69(1):144147, 1992. 13, 14, 75

[18] Russell D. Young and Howard E. Clark. Effect of surface patch fields on field-emission work-function determinations. *Physical Review Letters*, 17(7):351, —1966—. 14

[19] K. Kaja, N. Chevalier, D. Mariolle, F. Bertin, G. Feuillet, and A. Chabli. "effects of experimental parameters on the work function measurement: A kelvin force microscopy study". volume 1173, pages 224–228, Albany (New York), 2009. AIP. 14

[20] John Bardeen. "surface states and rectification at a metal semi-conductor contact". *Physical Review*, 71(10):717, 1947. 15

[21] S. M. Sze. *"Physics of Semiconductor Devices"*. BOOK. 1981. 15

[22] Rolf Enderlein and J. Norman Horing. *"Fundamentals of Semiconductor Physics and Devices "*. Work Scientific Publishing Co. Pte. Ltd., 1997. 15

[23] caspar Fall. *"Ab initio study of the work functions of elemental metal crystals."*. PhD thesis, Ecole Polytechnique Federale de Lazuanne, 1999. 16, 17, 21

[24] J. C. Riviere. "work function: Measurements and results". In Mino green, editor, *Solide State Surface science*, volume 1, pages 179–289. Marcel Dekker, London, 1969. 16

[25] Conyers Herring and M. H. Nichols. "thermionic emission". *Reviews of Modern Physics*, 21(2):185, 1949. 17

[26] Lord Kelvin. "contact electricity of metals". *Philosophical Magazine*, 46(82-120), 1898. 18

[27] Paul A. Anderson. "the contact difference of potential between tungsten and barium. the external work function of barium". *Physical Review*, 47(12):958, 1935. 20

[28] J. T. Jr. Yates. *"Experimental Innovations in Surface Science: A Guide to Practical Laboratory Methods and Instruments "*. Springer-Verlag New York Inc., 1997. 21

[29] Herbert B. Michaelson. "work functions of the elements". *Journal of Applied Physics*, 21(6):536–540, 1950. 21, 22

[30] H.B. Michaelson. "the work function of the elements and its periodicity". *Journal of Applied Physics*, 48(11):4729–4733, 1977. 21, 22

[31] H. L. Skriver and N. M. Rosengaard. "surface energy and work function of elemental metals". *Physical Review B*, 46(11):7157, 1992. 21, 22

[32] D. E. Eastman. "photoelectric work functions of transition, rare-earth, and noble metals". *Physical Review B*, 2(1):1, 1970. 21

[33] G. A. Haas and R. E. Thomas. "work function and secondary emission studies of various cu crystal faces". *Journal of Applied Physics*, 48(1):86–93, 1977. 21, 22

[34] S. C. Jain and K. S. Krishnan. "thermionic constants of metals and semiconductors. iii. monovalent metals". *Proceedings of the Royal Society of London. Series A. Mathematical and Physical Sciences*, 217(1131):451–461, 1953. 22

[35] W. M. H. Sachtler, G. J. H. Dorgelo, and A. A. Holscher. "the work function of gold". *Surface Science*, 5(2):221–229, 1966. 22

[36] A. A. Holscher. "a field emission retarding potential method for measuring work functions". *Surface Science*, 4(1):89–102, 1966. 22

[37] E. E. Huber Jr and C. T. Kirk Jr. "work function changes due to the chemisorption of water and oxygen on aluminum". *Surface Science*, 5(4):447–465, 1966. 22

[38] E. Gaviola and John Strong. "photoelectric effect of aluminum films evaporated in vacuum". *Physical Review*, 49(6):441, 1936. 22

[39] James J. Brady and Vincent P. Jacobsmeyer. "photoelectric properties of sodium films on aluminum". *Physical Review*, 49(9):670, 1936. 22

[40] R. Suhrmann and Joh Pietrzyk. "die anderung der lichtelektrischen elektronenemission beim ubergang reiner zink-, cadmium- und aluminiumschichten aus dem ungeordneten in den geordneten zustand und der einflub der temperatur auf die empfindlichkeit dieser metalle". *Zeitschrift fur Physik A Hadrons and Nuclei*, 122(9):600–613, 1944. 22

[41] E. W. J. Mitchell and J. W. Mitchell. "the work functions of copper, silver and aluminium". *Proceedings of the Royal Society of London. Series A. Mathematical and Physical Sciences*, 210(1100):70–84, 1951. 22

[42] J. C. Riviere. "contact potential difference measurements by the kelvin method". *Proceedings of the Physical Society. Section B*, (7):676, 1957. 22

[43] V.G. Bolshov. *J. Tech. Phys. U.S.S.R.*, 26, 1956. 22

[44] R. G. Wilson. "vacuum thermionic work functions of polycrystalline be, ti, cr, fe, ni, cu, pt, and type 304 stainless steel". *Journal of Applied Physics*, 37(6):2261–2267, 1966. 22

[45] A. Ertel. *Phys. Rev.*, 78, 1950. 22

[46] S. J. O'Shea, R. M. Atta, and M. E. Welland. "characterization of tips for conducting atomic force microscopy". *Review of Scientific Instruments*, 66(3):2508–2512, 1995. 22

[47] J. Giner and E. Lange. "elektronenaustrittsspannungen von reinem und sauerstoffbedecktem au, pt und pd auf grund ihrer voltaspannungen gegen ag". *Naturwissenschaften*, 40(19):506–506, 1953. 22

[48] O. Klein and E. Lange. *Z. Elektrochem*, 44, 1938. 22

[49] M. H. Nichols. "average thermionic constants of polycrystalline tungsten wires". *Physical Review*, 78(2):158, 1950. 22

[50] George A. Haas and Jr John T. Jensen. "thermionic studies of various uranium compounds". *Journal of Applied Physics*, 34(12):3451–3457, 1963. 22

[51] H. C. Rentschler, D. E. Henry, and K. O. Smith. "photoelectric emission from different metals". *Review of Scientific Instruments*, 3(12):794–802, 1932. 22

[52] L. Apker, E. Taft, and J. Dickey. "energy distribution of photoelectrons from polycrystalline tungsten". *Physical Review*, 73(1):46, 1948. 22

[53] M. Nonnenmacher, M. P. O'Boyle, and H. K. Wickramasinghe. "kelvin probe force microscopy". *Applied Physics Letters*, 58(25):2921–2923, 1991. 23

[54] E. Brüche. Elektronenmikroskopische abbildung mit lichtelektrischen elektronen. *Zeitschrift für Physik A Hadrons and Nuclei*, 86(7):448–450, —1933—. 24, 51

[55] E. Bauer, M. Mundschau, W. Swiech, and W. Telieps. Surface studies by low-energy electron microscopy (leem) and conventional uv photoemission electron microscopy (peem). *Ultramicroscopy*, 31(1):49–57, —1989—. 24

[56] G. Binnig, H. Rohrer, Ch Gerber, and E. Weibel. "tunneling through a controllable vacuum gap". *Applied Physics Letters*, 40(2):178, 1982. 28

[57] D. Maugis. *Contact, Adhesion and Rupture of elastic solids*. Springer, —2000—. 29

[58] G. Binning, C. F. Quate, and Ch. Gerber. "atomic force microscope". *Physical Review Letters*, 56(9):930–933, 1986. 29

[59] Y. Martin, C. C. Williams, and H. K. Wickramasinghe. "atomic force microscope-force mapping and profiling on a sub 100-a scale". *Journal of Applied Physics*, 61(10):4723–4729, 1987. 30

[60] Hans-Jurgen Butt, Brunero Cappella, and Michael Kappl. "force measurements with the atomic force microscope: Technique, interpretation and applications". *Surface Science Reports*, 59(1-6):1–152, 2005. 30

[61] J. E. Sader. "parallel beam approximation for v-shaped atomic force. microscope cantilevers". *Review of Scientific Instruments*, 66(9):4583–4587, 1995. 30

[62] M. Stark, R. W. Stark, W. M. Heckl, and R. Guckenberger. "spectroscopy of the anharmonic cantilever oscillations in tapping-mode atomic-force microscopy". *Applied Physics Letters*, 77(20):3293–3295, 2000. 30

[63] R. Garcia and R. Perez. "dynamic atomic force microscopy methods". *Surface Science Reports*, 47:197–301, 2002. 31, 32

[64] J.P. Aime, R. Boisgard, and G. Couturier. "microscopie de force dynamique". Technical report, CPMOH, Bordeaux, 2003. 31, 32

[65] F. Bertin. "cours de microscopie a force atomique - dea, universite joseph fourier". Technical report, 2005. 32, 36

[66] M. Skarabot and I. MuseviC. "atomic force microscope force spectroscopy study of the electric double layer at a liquid crystal interface". *Journal of Applied Physics*, 105(1):014905–6, 2009. 39

[67] L. Kantorovich, A. I. Livshits, and M. stoneham. "electrostatic energy calculation for the interpretation of scanning probe microscopy experiments". *Journal of Physics : Condensed Matter*, 12:795–814, 2000. 39, 186

[68] N. Gaillard. *"Etude des Proprietes Morphologiques, Electriques et Chimiques de l'Interface Metal / Isolant et de leur Impact sur les Performances de la Capacite TiN/Ta2O5/TiN"*. PhD thesis, University Joseph Fourier, 2006. 41, 46, 75, 77, 84, 103, 148

[69] N. Dompnier. *"Realisation d'une chaine de mesure KFM"*. PhD thesis, CNAM Grenoble, 2006. 45

[70] S. Hudlet, M. Saint Jean, C. guthmann, and J. Berger. "evaluation of the capacitive force between an atomic force microscopy tip and a metallic surface". *Europhysics Journal B*, 2:5–10, 1998. 46, 47, 76

[71] S. Belaidi, P. Girard, and G. Leveque. "electrostatic forces acting on the tip in atomic force microscopy: : Modelization and comparison with analytic expressions". *Journal of Applied Physics*, 81(3):1023–1030, 1997. 46, 47, 76, 78

[72] A. Gil. "electrostatic force gradient signal: resolution enhancement in electrostatic force microscopy and improved kelvin probe microscopy". *Nanotechnology*, 14:332–340, 2003. 47, 85, 86, 87, 97

[73] J. Colchero, A. Gil, and A. M. Baro. "resolution enhancement and improved data interpretation in electrostatic force microscopy". *Physical Review B (Condensed Matter and Materials Physics)*, 64, 2001. 47, 76, 85, 86, 87, 97, 98

[74] H. O. Jacobs, P. Leuchtmann, O. J. Homan, and A. Stemmer. "resolution and contrast in kelvin probe force microscopy". *Journal of Applied Physics*, 84(3):1168–1173, 1998. 47, 76, 86, 98

[75] A. Einstein. Über einen die erzeugung und verwandlung des lichtes betreffenden heuristischen gesichtspunkt. *Annalen der Physik*, 322(6):132–148, —1905—. 48

[76] N. Barrett and O. Renault. La spectromicroscopie xpeem avec le rayonnement synchrotron. *Mater. Tech.*, 97(2):101–122, —2009—. 49, 52, 57, 60

[77] Daniel Spanjaard, Claude Guillot, Marie-Catherine Desjonquères, Guy Tréglia, and Jean Lecante. Surface core level spectroscopy of transition metals: A new tool for the determination of their surface structure. *Surface Science Reports*, 5(1-2):1–85, —1985—. 50

[78] Carl Nordling, Evelyn Sokolowski, and Kai Siegbahn. Precision method for obtaining absolute values of atomic binding energies. *Physical Review*, 105(5):1676, —1957—. 50

[79] T. Koopmans. Über die zuordnung von wellenfunktionen und eigenwerten zu den einzelnen elektronen eines atoms. *Physica*, 1(1-6):104–113, —1934—. 50

[80] P.C. Deshmukh and S. Venkataraman. 100 years of einstein's photoelectric effect. *http://www.physics.iitm.ac.in/ labs/amp/*, —2006—. 51

[81] D. Briggs and John T. Grant. *"Surface Analysis by Auger and x-Ray Photoelectron Spectroscopy"*. IM Publications LLP, 2003. 50, 125

[82] W. Telieps and E. Bauer. An analytical reflection and emission uhv surface electron microscope. *Ultramicroscopy*, 17(1):57–65, —1985—. 51

[83] Elmitec. http://www.elmitec-gmbh.com/. 52

[84] Specs. http://www.specs.com/. 52

[85] focus gmbh. http://focus-gmbh.com/. 53

[86] Claus M. Schneider and Gerd Schonhense. "investigating surface magnetism by means of photoexcitation electron emission microscopy". *Reports on Progress in Physics*, 65(12):1785–1839, 2002. 53, 54, 68, 134, 190

[87] S. D. Kevan. Design of a high-resolution angle-resolving electron energy analyzer. *Review of Scientific Instruments*, 54(11):1441–1445, —1983—. 54

[88] M. Escher, N. Weber, M. Merkel, C. Ziethen, P. Bernhard, G. Schonhense, S. Schmidt, F. Forster, F. Reinert, B. Kromker, and D. Funnemann. "nanoesca: a novel energy filter for imaging x-ray photoemission spectroscopy". *Journal of Physics: Condensed Matter*, 17(16):S1329–S1338, 2005. 54, 55, 64, 65, 66

[89] M. Escher, K. Winkler, O. Renault, and N. Barrett. "applications of high lateral and energy resolution imaging xps with a double hemispherical analyser based spectromicroscope". *Journal of Electron Spectroscopy and Related Phenomena*, In Press, Corrected Proof, 2009. 54, 55, 61, 64, 65, 66

[90] A. Bailly, O. Renault, N. Barrett, L. F. Zagonel, P. Gentile, N. Pauc, F. Dhalluin, T. Baron, A. Chabli, J. C. Cezar, and N. B. Brookes. "direct quantification of gold along a single si nanowire". *Nano Letters*, 8(11):3709–3714, 2008. 58, 62, 66

[91] L. F. Zagonel, M. Baurer, A. Bailly, O. Renault, M. Hoffmann, S. J. Shih, D. Cockayne, and N. Barrett. "orientation-dependent work function of in situ annealed strontium titanate". *Journal of Physics: Condensed Matter*, 21(31):314013, 2009. 59, 61

[92] O. Renault, N. Barrett, A. Bailly, L. F. Zagonel, D. Mariolle, J. C. Cezar, N. B. Brookes, K. Winkler, B. Kromker, and D. Funnemann. "energy-filtered xpeem with nanoesca using synchrotron and laboratory x-ray sources: Principles and first demonstrated results". *Surface Science*, 601(20):4727–4732, 2007. 62, 66

[93] O. Renault. "high resolution xps spectromicroscopy". *in press*, 2009. 66

[94] S. Barbet, R. Aubry, M. A. di Forte-Poisson, J. C. Jacquet, D. Deresmes, T. Melin, and D. Theron. "surface potential of n- and p-type gan measured by kelvin force microscopy". *Applied Physics Letters*, 93(21):212107–3, 2008. 74

[95] G. Koley and G. Spencer. "surface potential measurements on gan and algan/gan heterostructures by scanning kelvin probe microscopy". *Journal of Applied Physics*, 90(1):337–344, 2001. 74

[96] Ralph M. Nyffenegger, Reginald M. Penner, and Rainer Schierle. "electrostatic force microscopy of silver nanocrystals with nanometer-scale resolution". *Applied Physics Letters*, 71(13):1878–1880, 1997. 74

[97] A. Liscio, V. Palermo, D. Gentilini, F. Nolde, K. Mullen, and P. Samori. "quantitative measurement of the local surface potential of pi-conjugated nanostructures: A kelvin probe force microscopy study". *Advanced Functional Materials*, 16(11):1407–1416, 2006. 74

[98] A. Liscio, V. Palermo, K. Mullen, and P. Samori. "tip-sample interactions in kelvin probe force microscopy: Quantitative measurement of the local surface potential". *Journal of Physical Chemistry C*, 2008. 74, 82, 152

[99] J. Lambert, C. Guthmann, and M. Saint-Jean. "relationship between charge distribution and its image by electrostatic force microscopy". *Journal of Applied Physics*, 93(9):5369–5376, 2003. 74

[100] B. D. Terris, J. E. Stern, D. Rugar, and H. J. Mamin. "contact electrification using force microscopy". *Physical Review Letters*, 63(24):2669–2672, 1989. 74

[101] J. E. Stern, B. D. Terris, H. J. Mamin, and D. Rugar. "deposition and imaging of localized charge on insulator surfaces using a force microscope". *Applied Physics Letters*, 53(26):2717, 1988. 74

[102] Guillaume Jourdan. *"Vers Un Microscope De Force De Casimir : Mesure Quantitative De Forces Faibles Et Nanopositionnement Absolu"*. PhD thesis, University Joseph Fourier, 2007. 75, 91

[103] Elmar Bonaccurso, Friedhelm Schonfeld, and Hans-Jurgen Butt. "electrostatic forces acting on tip and cantilever in atomic force microscopy". *Physical Review B (Condensed Matter and Materials Physics)*, 74(8):085413–8, 2006. 76

[104] Yongxing Shen, David M. Barnett, and Peter M. Pinsky. "simulating and interpreting kelvin probe force microscopy images on dielectrics with boundary integral equations". *Review of Scientific Instruments*, 79(2):023711–10, 2008. 78

[105] Yongxing Shen, Minhwan Lee, Wonyoung Lee, David M. Barnett, Peter M. Pinsky, and Friedrich B. Prinz. "a resolution study for electrostatic force microscopy on bimetallic samples using the boundary element method". *Nanotechnology*, 19(3):035710, 2008. 78

[106] S. Belaidi, F. Lebon, P. Girard, G. Leveque, and S. Pagano. "finite element simulations of the resolution in the electrostatic force microscopy". *Applied Physics A: Materials Science and Processing*, 66:S239–S243, 1998. 78

[107] S. Gomez-Monivas, J. J. Saenz, R. Carminati, and J. J. Greffet. "therory of electrostatic probe microscopy: a simple perturbative approach". *Applied Physics Letters*, 76(20):2955–2957, 2000. 79

[108] G. Mesa, E. Dobado-Fuentes, and J. J. Saenz. "image charge method for electrostatic calculations in field-emission diodes". *Journal of Applied Physics*, 79(1):39–44, 1996. 79

[109] E. A. Boer, L. D. Bell, M. L. Brongersma, and H. A. Atwater. "models for quantitative charge imaging by atomic force microscopy". *Journal of Applied Physics*, 90(6):2764–2772, 2001. 79

[110] P. Schmutz and G. S. Frankel. "characterization of aa2024-t3 by scanning kelvin probe force microscopy". *Journal of the Electrochemical Society*, 145(7):2285–2294, 1998. 80

[111] H. Sugimura, Y. Ishida, K. Hayashi, O. Takai, and N. Nakagiri. "potential shielding by the surface water layer in kelvin probe force microscopy". *Applied Physics Letters*, 80(8):1459–1461, 2002. 81

[112] Sheng Meng, E. G. Wang, and Shiwu Gao. "water adsorption on metal surfaces: A general picture from density functional theory studies". *Physical Review B*, 69(19):195404, 2004. 82

[113] Ulrich Zerweck, Christian Loppacher, Tobias Otto, Stefan Grafstrom, and Lukas M. Eng. "accuracy and resolution limits of kelvin probe force microscopy". *Physical Review B (Condensed Matter and Materials Physics)*, 71(12):125424, 2005. 85

[114] G. H. Enevoldsen, T. Glatzel, M. C. Christensen, J. V. Lauritsen, and F. Besenbacher. "atomic scale kelvin probe force microscopy studies of the surface potential variations on the tio2(110) surface". *Physical Review Letters*, 100(23):236104, 2008. 85

[115] Sascha Sadewasser, Pavel Jelinek, Chung-Kai Fang, Oscar Custance, Yusaku Yamada, Yoshiaki Sugimoto, Masayuki Abe, and Seizo Morita. "new insights on atomic-resolution frequency-modulation kelvin-probe force-microscopy imaging of semiconductors". *Physical Review Letters*, 103(26):266103, 2009. 85

[116] P. Girard, M. Ramonda, and D. Saluel. "electrical contrast observations and voltage measurements by kelvin probe force gradient microscopy". *Journal of Vacuum Science and Technology B: Microelectronics and Nanometer Structures*, 20(4):1348–1355, 2002. 85, 86

[117] Sergei Magonov. "advanced atomic force microscopy: Exploring measurements of local electric properties". Technical report, Agilent, 15-12-2008 2008. 85, 87

[118] X. D. Ding, J. An, J. B. Xu, C. Li, and R. Y. Zeng. "improving lateral resolution of electrostatic force microscopy by multifrequency method under ambient conditions". *Applied Physics Letters*, 94(22):223109–3, 2009. 85, 87

[119] D. Mariolle, K. Kaja, F. Bertin, E. Martinez, F. Martin, and R. Gassilloud. "protocol optimisation for work-function measurements of metal gates using kelvin force microscopy". *AIP Conference Proceedings*, 931(1):521–524, 2007. 86

[120] Lynda Cockins, Yoichi Miyahara, Romain Stomp, and Peter Grutter. "high-aspect ratio metal tips attached to atomic force microscopy cantilevers with controlled angle, length, and radius for electrostatic force microscopy". *Review of Scientific Instruments*, 78(11):113706, 2007. 86

[121] Dominik Ziegler, Jorg Rychen, Nicola Naujoks, and Andreas Stemmer. "compensating electrostatic forces by single-scan kelvin probe force microscopy". *Nanotechnology*, 18(22):225505–5, 2007. 87, 88, 101

[122] E. Palacios-Lidon, B. Perez-Garcia, and J. Colchero. "enhancing dynamic scanning force microscopy in air: as close as possible". *Nanotechnology*, 20(8):085707, 2009. 87, 88

[123] Roger Proksch. "multifrequency, repulsive-mode amplitude-modulated atomic force microscopy". *Applied Physics Letters*, 89(11):113121–3, 2006. 88, 101

[124] Robert W. Stark, Nicola Naujoks, and Andreas Stemmer. "multifrequency electrostatic force microscopy in the repulsive regime". *Nanotechnology*, 18(6):065502, 2007. 88, 91, 101

[125] R. W. Stark, N. Naujoks, and A. Stemmer. "detection of injected charges by kelvin probe and multimode electrostatic force microscopy". pages 725–728, 2005. 88

[126] N. F. Martinez, S. Patil, J. R. Lozano, and R. Garcia. "enhanced compositional sensitivity in atomic force microscopy by the excitation of the first two flexural modes". *Applied Physics Letters*, 89(15):153115–3, 2006. 88

[127] Jose R. Lozano and Ricardo Garcia. "theory of multifrequency atomic force microscopy". *Physical Review Letters*, 100(7):076102–4, 2008. 88, 99

[128] Robert W. Stark. "dynamics of repulsive dual-frequency atomic force microscopy". *Applied Physics Letters*, 94(6):063109–3, 2009. 88, 99

[129] F. Marchi, R. Dianoux, H. J. H. Smilde, P. Mur, F. Comin, and J. Chevrier. "characterisation of trapped electric charge carriers behaviour at nanometer scale by electrostatic force microscopy". *Journal of Electrostatics*, 66(9-10):538–547, 2008. 91, 186

[130] R. Dianoux. *"Injection et detection de charges dans des nanostructures semiconductrices par Microscopie a Force Atomique"*. PhD thesis, University Joseph Fourier, 2004. 91

[131] F. Varchon, R. Feng, J. Hass, X. Li, B. Ngoc Nguyen, C. Naud, P. Mallet, J. Y. Veuillen, C. Berger, E. H. Conrad, and L. Magaud. "electronic structure of epitaxial graphene layers on sic: Effect of the substrate". *Physical Review Letters*, 99(12):126805–4, 2007. 91, 116, 117, 118, 119, 128, 129, 131, 169, 171

[132] H. W. Kroto, J. R. Heath, S. C. O'Brien, R. F. Curl, and R. E. Smalley. C60: Buckminsterfullerene. *Nature*, 318(6042):162–163, —1985—. 10.1038/318162a0. 112

[133] Sumio Iijima. Helical microtubules of graphitic carbon. *Nature*, 354(6348):56–58, —1991—. 10.1038/354056a0. 112

[134] D. D. L. Chung. Review graphite. *Journal of Materials Science*, 37:1475–1489, —2002—. 112

[135] A. H. Castro Neto, F. Guinea, N. M. R. Peres, K. S. Novoselov, and A. K. Geim. The electronic properties of graphene. *Reviews of Modern Physics*, 81(1):109–54, —2009—. 112

[136] P. R. Wallace. The band theory of graphite. *Physical Review*, 71(9):622, —1947—. 112

[137] A. K. Geim. "graphene: Status and prospects". *Science*, 324(5934):1530–1534, 2009. 112, 113

[138] A. K. Geim and K. S. Novoselov. The rise of graphene. *Nat Mater*, 6(3):183–191, —2007—. 112, 113

[139] K. S. Novoselov, A. K. Geim, S. V. Morozov, D. Jiang, Y. Zhang, S. V. Dubonos, I. V. Grigorieva, and A. A. Firsov. "electric field effect in atomically thin carbon films". *Science*, 306(5696):666–669, 2004. 113

[140] K. S. Novoselov, A. K. Geim, S. V. Morozov, D. Jiang, M. I. Katsnelson, I. V. Grigorieva, S. V. Dubonos, and A. A. Firsov. Two-dimensional gas of massless dirac fermions in graphene. *Nature*, 438(7065):197–200, —2005—. 10.1038/nature04233. 113

[141] Yuanbo Zhang, Yan-Wen Tan, Horst L. Stormer, and Philip Kim. Experimental observation of the quantum hall effect and berry's phase in graphene. *Nature*, 438(7065):201–204, —2005—. 113

[142] Claire Berger, Zhimin Song, Tianbo Li, Xuebin Li, Asmerom Y. Ogbazghi, Rui Feng, Zhenting Dai, Alexei N. Marchenkov, Edward H. Conrad, Phillip N. First, and Walt A. de Heer. Ultrathin epitaxial graphite: 2d electron gas properties and a route toward graphene-based nanoelectronics. *The Journal of Physical Chemistry B*, 108(52):19912–19916, —2004—. 113, 115

[143] K. S. Novoselov, E. McCann, S. V. Morozov, V. I. Falko, M. I. Katsnelson, U. Zeitler, D. Jiang, F. Schedin, and A. K. Geim. "unconventional quantum hall effect and berry's phase of 2[pi] in bilayer graphene". *Nat Phys*, 2(3):177–180, 2006. 113

[144] K. S. Novoselov, Z. Jiang, Y. Zhang, S. V. Morozov, H. L. Stormer, U. Zeitler, J. C. Maan, G. S. Boebinger, P. Kim, and A. K. Geim. Room-temperature quantum hall effect in graphene. *Science*, 315(5817):1379, —2007—. 113

[145] Claire Berger, Zhimin Song, Xuebin Li, Xiaosong Wu, Nate Brown, Cecile Naud, Didier Mayou, Tianbo Li, Joanna Hass, Alexei N. Marchenkov, Edward H. Conrad, Phillip N. First, and Walt A. de Heer. Electronic confinement and coherence in patterned epitaxial graphene. *Science*, 312(5777):1191–1196, —2006—. 113

[146] F. Schedin, A. K. Geim, S. V. Morozov, E. W. Hill, P. Blake, M. I. Katsnelson, and K. S. Novoselov. Detection of individual gas molecules adsorbed on graphene. *Nat Mater*, 6(9):652–655, —2007—. 113

[147] Young-Woo Son, Marvin L. Cohen, and Steven G. Louie. Half-metallic graphene nanoribbons. *Nature*, 444(7117):347–349, —2006—. 10.1038/nature05180. 113

[148] Bjorn Trauzettel, Denis V. Bulaev, Daniel Loss, and Guido Burkard. Spin qubits in graphene quantum dots. *Nat Phys*, 3(3):192–196, —2007—. 113

[149] Takehito Yokoyama. Controllable spin transport in ferromagnetic graphene junctions. *Physical Review B*, 77(7):073413, —2008—. 113

[150] Vladimir Fal'ko. Graphene: Quantum information on chicken wire. *Nat Phys*, 3(3):151–152, —2007—. 113

[151] F. Rana. Graphene terahertz plasmon oscillators. *Nanotechnology, IEEE Transactions on*, 7(1):91 – 99, —2008—. 113

[152] Meryl D. Stoller, Sungjin Park, Yanwu Zhu, Jinho An, and Rodney S. Ruoff. Graphene-based ultracapacitors. *Nano Letters*, 8(10):3498–3502, —2008—. 113

[153] Xuan Wang, Linjie Zhi, and Klaus Mullen. Transparent, conductive graphene electrodes for dye-sensitized solar cells. *Nano Letters*, 8(1):323–327, —2008—. 113

[154] Konstantin V. Emtsev, Aaron Bostwick, Karsten Horn, Johannes Jobst, Gary L. Kellogg, Lothar Ley, Jessica L. McChesney, Taisuke Ohta, Sergey A. Reshanov, Jonas Rohrl, Eli Rotenberg, Andreas K. Schmid, Daniel Waldmann, Heiko B. Weber, and Thomas Seyller. Towards wafer-size graphene layers by atmospheric pressure graphitization of silicon carbide. *Nat Mater*, 8(3):203–207, —2009—. 113, 114, 115, 117, 121

[155] K. S. Novoselov, D. Jiang, F. Schedin, T. J. Booth, V. V. Khotkevich, S. V. Morozov, and A. K. Geim. Two-dimensional atomic crystals. *Proceedings of the National Academy of Sciences of the United States of America*, 102(30):10451–10453, —2005—. 113

[156] Peter W. Sutter, Jan-Ingo Flege, and Eli A. Sutter. Epitaxial graphene on ruthenium. *Nat Mater*, 7(5):406–411, —2008—. 113

[157] Yi Pan, Haigang Zhang, Dongxia Shi, Jiatao Sun, Shixuan Du, Feng Liu, and Hong-jun Gao. Highly ordered, millimeter-scale, continuous, single-crystalline graphene monolayer formed on ru (0001). *Advanced Materials*, 21(27):2777–2780, —2009—. 113

[158] Keun Soo Kim, Yue Zhao, Houk Jang, Sang Yoon Lee, Jong Min Kim, Kwang S. Kim, Jong-Hyun Ahn, Philip Kim, Jae-Young Choi, and Byung Hee Hong. Large-scale pattern growth of graphene films for stretchable transparent electrodes. *Nature*, 457(7230):706–710, —2009—. 113

[159] J. Hass, R. Feng, T. Li, X. Li, Z. Zong, W. A. de Heer, P. N. First, E. H. Conrad, C. A. Jeffrey, and C. Berger. Highly ordered graphene for two dimensional electronics. *Applied Physics Letters*, 89(14):143106–3, —2006—. 113

[160] K. V. Emtsev, F. Speck, Th Seyller, L. Ley, and J. D. Riley. Interaction, growth, and ordering of epitaxial graphene on sic0001 surfaces: A comparative photoelectron spectroscopy study. *Physical Review B*, 77(15):155303, —2008—. Copyright (C) 2010 The American Physical Society Please report any problems to prola@aps.org PRB. 113, 114, 115, 116, 117, 118, 119, 124, 125, 126, 127, 128, 129, 142

[161] Th. Seyller, A. Bostwick, K. V. Emtsev, K. Horn, L. Ley, J. L. McChesney, T. Ohta, J. D. Riley, E. Rotenberg, and F. Speck. "epitaxial graphene: a

new material". *physica status solidi (b)*, 9999(9999):NA, 2008. 113, 115, 116, 117, 118, 125, 126, 129, 130, 143, 168, 169

[162] J. Hass, W. A. de Heer, and E. H. Conrad. "the growth and morphology of epitaxial multilayer graphene". *Journal of Physics: Condensed Matter*, 20(32):323202, 2008. 113, 117, 195, 196

[163] C. Virojanadara, M. Syvajarvi, R. Yakimova, L. I. Johansson, A. A. Zakharov, and T. Balasubramanian. "homogeneous large-area graphene layer growth on 6h-sic(0001)". *Physical Review B (Condensed Matter and Materials Physics)*, 78(24):245403–6, 2008. 113, 114, 115, 124, 125, 127, 128, 130, 153, 154, 157

[164] H. Hibino, H. Kageshima, M. Kotsugi, F. Maeda, F. Z. Guo, and Y. Watanabe. "dependence of electronic properties of epitaxial few-layer graphene on the number of layers investigated by photoelectron emission microscopy". *Physical Review B (Condensed Matter and Materials Physics)*, 79(12):125437–7, 2009. 114, 115, 127, 130, 139, 140, 141, 142, 144, 166, 168, 169, 173, 201

[165] Taisuke Ohta, Aaron Bostwick, Thomas Seyller, Karsten Horn, and Eli Rotenberg. "controlling the electronic structure of bilayer graphene". *Science*, 313(5789):951–954, 2006. 114, 115, 129, 142, 143, 168, 169

[166] H. Hibino, H. Kageshima, F. Maeda, M. Nagase, Y. Kobayashi, and H. Yamaguchi. "microscopic thickness determination of thin graphite films formed on sic from quantized oscillation in reflectivity of low-energy electrons". *Physical Review B*, 77(7):075413, 2008. 114, 115, 116, 196, 197

[167] T. Ohta, F. El Gabaly, A. Bostwick, J. L. McChesney, K. V. Emtsev, A. E. Schmid, Th Seyller, K. Horn, and E. Rotenberg. Morphology of graphene thin film growth on sic(0001). *New Journal of Physics*, 10(2):023034, —2008—. 114

[168] T. Filleter, K. V. Emtsev, Th Seyller, and R. Bennewitz. "local work function measurements of epitaxial graphene". *Applied Physics Letters*, 93(13):133117–3, 2008. 115, 140, 141, 142, 152, 153, 155, 158, 174, 201

[169] Ekaterina A. Obraztsova, Alexander V. Osadchy, Elena D. Obraztsova, Serge Lefrant, and Igor V. Yaminsky. "statistical analysis of atomic force microscopy and raman spectroscopy data for estimation of graphene layer numbers". *physica status solidi (b)*, 9999(9999):NA, 2008. 115, 153, 199

[170] Sujit S. Datta, Douglas R. Strachan, E. J. Mele, and A. T. Charlie Johnson. "surface potentials and layer charge distributions in few-layer graphene films". *Nano Letters*, 2008. 115, 153

[171] Irene Calizo, Igor Bejenari, Muhammad Rahman, Guanxiong Liu, and Alexander A. Balandin. "ultraviolet raman microscopy of single and multilayer graphene". *Journal of Applied Physics*, 106(4):043509–5, 2009. 115, 121, 197, 198

[172] P. Lauffer, K. V. Emtsev, R. Graupner, Th Seyller, L. Ley, S. A. Reshanov, and H. B. Weber. "atomic and electronic structure of few-layer graphene on sic(0001) studied with scanning tunneling microscopy and spectroscopy". *Physical Review B (Condensed Matter and Materials Physics)*, 77(15):155426–10, 2008. 115, 153, 154, 155, 171, 199, 200

[173] P. Mallet, F. Varchon, C. Naud, L. Magaud, C. Berger, and J. Y. Veuillen. "electron states of mono- and bilayer graphene on sic probed by scanning-tunneling microscopy". *Physical Review B (Condensed Matter and Materials Physics)*, 76(4):041403–4, 2007. 115, 129, 199

[174] G. M. Rutter, N. P. Guisinger, J. N. Crain, E. A. A. Jarvis, M. D. Stiles, T. Li, P. N. First, and J. A. Stroscio. Imaging the interface of epitaxial graphene with silicon carbide via scanning tunneling microscopy. *Physical Review B (Condensed Matter and Materials Physics)*, 76(23):235416–6, —2007—. 115

[175] J. Hass, R. Feng, J. E. Millán-Otoya, X. Li, M. Sprinkle, P. N. First, W. A. de Heer, E. H. Conrad, and C. Berger. Structural properties of the multilayer graphene/ 4h-sic (000 1-bar) system as determined by surface x-ray diffraction. *Physical Review B*, 75(21):214109, —2007—. 115

[176] J. Hass, F. Varchon, J. E. Millán-Otoya, M. Sprinkle, N. Sharma, W. A. de Heer, C. Berger, P. N. First, L. Magaud, and E. H. Conrad. Why multilayer graphene on 4h-sic(0001-bar) behaves like a single sheet of graphene. *Physical Review Letters*, 100(12):125504, —2008—. 115

[177] C. Riedl, A. A. Zakharov, and U. Starke. "precise in situ thickness analysis of epitaxial graphene layers on sic(0001) using low-energy electron diffraction and angle resolved ultraviolet photoelectron spectroscopy". *Applied Physics Letters*, 93(3):033106–3, 2008. 115, 198

[178] I. Forbeaux, J. M. Themlin, and J. M. Debever. Heteroepitaxial graphite on 6h-sic(0001): Interface formation through conduction-band electronic structure. *Physical Review B*, 58(24):16396, —1998—. 115, 117

[179] Mingsheng Xu, Daisuke Fujita, Jianhua Gao, and Nobutaka Hanagata. Auger electron spectroscopy: A rational method for determining thickness of graphene films. *ACS Nano*, —2010—. 115

[180] F. Varchon, P. Mallet, J. Y. Veuillen, and L. Magaud. Ripples in epitaxial graphene on the si-terminated sic(0001) surface. *Physical Review*

B, 77(23):235412, —2008—. Copyright (C) 2010 The American Physical Society Please report any problems to prola@aps.org PRB. 116, 130, 131

[181] I. Forbeaux, J. M. Themlin, A. Charrier, F. Thibaudau, and J. M. Debever. Solid-state graphitization mechanisms of silicon carbide 6h-sic polar faces. *Applied Surface Science*, 162-163:406–412, —2000—. 118

[182] L. I. Johansson, Fredrik Owman, and Per Martensson. "high-resolution core-level study of 6h-sic(0001)". *Physical Review B*, 53(20):13793, 1996. 123, 124, 130, 131

[183] J. Penuelas, A. Ouerghi, D. Lucot, C. David, J. Gierak, H. Estrade-Szwarckopf, and C. Andreazza-Vignolle. "surface morphology and characterization of thin graphene films on sic vicinal substrate". *Physical Review B (Condensed Matter and Materials Physics)*, 79(3):033408–4, 2009. 124, 125, 130, 153

[184] E. Rollings, G. H. Gweon, S. Y. Zhou, B.S. Mun, J.L. McChesney, B. S. Hussain, A. V Fedorov, P. N.First, W. A. de Heer, and A. Lanzara. Synthesis and characterization of atomically thin graphite films on a silicon carbide substrate. *Journal of Physics and Chemistry of Solids*, 67(9-10):2172–2177, —2006—. doi: DOI: 10.1016/j.jpcs.2006.05.010. 124, 129

[185] N. Barrett, E. E. Krasovskii, J. M. Themlin, and V. N. Strocov. Elastic scattering effects in the electron mean free path in a graphite overlayer studied by photoelectron spectroscopy and leed. *Physical Review B*, 71(3):035427, —2005—. Copyright (C) 2010 The American Physical Society Please report any problems to prola@aps.org PRB. 128, 129

[186] Francois Varchon. *"Proprietes electroniques et structurales du graphene sur carbure de silicium Electronic and structural properties of graphene on silicon carbide"*. PhD thesis, University Joseph-Fourier - Grenoble I, 2008. 128, 129, 130, 171

[187] Alexander Mattausch and Oleg Pankratov. "ab initio study of graphene on sic". *Physical Review Letters*, 99(7):076802–4, 2007. 140, 141, 142, 143

[188] V. N. Strocov, P. Blaha, H. I. Starnberg, M. Rohlfing, R. Claessen, J. M. Debever, and J. M. Themlin. Three-dimensional unoccupied band structure of graphite: Very-low-energy electron diffraction and band calculations. *Physical Review B*, 61(7):4994, —2000—. 144

[189] T. Langer, H. Pfnur, H. W. Schumacher, and C. Tegenkamp. "graphitization process of sic(0001) studied by electron energy loss spectroscopy". *Applied Physics Letters*, 94(11):112106, 2009. 168

[190] L. D. Landau, L. P. Pitaevskii, and E. M. Lifshitz. *"Electrodynamics of Continuous Media: Volume 8 "*. A Butterworth-Heinemann Title, 2 nd edition, 1984. 185

[191] S. Halas. "100 years of work function". *Materials science-Poland*, 24(4), 2006. 189

[192] W. Schottky. *Physik Zeitschr*, 15:872, 1914. 189